OPTICAL COHERENCE TOMOGRAPHY:

EVALUATION AND CLINICAL APPLICATION

Sarah Muscat

**Thesis submitted to the University of Glasgow for
the Degree of Doctor of Philosophy**

This research was conducted in the Department of Clinical
Physics & Bio-Engineering and the Tennent Institute of
Ophthalmology, University of Glasgow

May 2003

ACKNOWLEDGEMENT

AUTHOR'S DECLARATION

The material presented in this thesis is the author's own work with the following exceptions:

Dr M Billson carried out histological analysis of the canine retinal specimens discussed in Chapter 3.

Ms N McKay assisted with the collection and analysis of normative corneal data discussed in Chapter 4.

The test object used to verify the accuracy and precision of measurements was commissioned from and constructed by a commercial company specialising in optical components. The high reflectance mirror used to measure axial resolution was purchased from the same company.

LIST OF CONTENTS

List of Contents (cont.)

List of Contents (cont)

LIST OF ILLUSTRATIONS

LIST OF TABLES

LIST OF PUBLICATIONS AND PRESENTATIONS

Publications

Material contained in this thesis has been published in the following five papers:

Muscat S, Fahad B, Parks S, Keating D. Optical coherence tomography and multifocal electroretinography of X-Linked juvenile retinoschisis. *Eye* 2001; 15: 796-99

Muscat S, Sathish S, Sampat V, Kemp E, Parks S, Keating D. Optical coherence tomography in the diagnosis of sub-clinical serous detachment of the macula secondary to a choroidal nevus. *Ophthalmic Surgery and Lasers* 2001; 32(6):474-6.

Muscat S, Parks S, Kemp E, Keating D. Repeatability and Reproducibility of Macular Thickness Measurements with the Humphrey OCT System. *Invest Ophthalmol Vis Sci.* 2002;43:490-495.

Muscat S, McKay N, Parks S, Kemp E, Keating D. Repeatability and Reproducibility of Corneal Thickness Measurements using optical coherence tomography. *Invest Ophthalmol Vis Sci.* 2002; 43:1791-1795.

Muscat S, Parks S, Kemp E, Keating D. Secondary Retinal Changes Associated with Choroidal Naevi and Melanomas documented by Optical Coherence Tomography. *The British Journal of Ophthalmology* [In Press].

Presentations

Material contained in this thesis has also been disseminated at local, national and international meetings. Details of oral and poster presentations are listed below:

Muscat S, Parks S, Kemp E, Keating D. In-vivo cross-sectional imaging of the retina using optical coherence tomography. Oral Presentation at the Research Workers Seminar, Tennent Institute of Ophthalmology. Glasgow, May 2000.

Muscat S, Fenton S, Parks S, Keating D. Functional and anatomical imaging of X-Linked retinoschisis using the wide-field multifocal electroretinogram and OCT. Poster presentation at the Annual Meeting for the Association for Research into Vision and Ophthalmology (ARVO). Fort Lauderdale Florida, May 2001.

Muscat S, Parks S, Keating D. Functional and anatomical imaging of X-linked retinoschisis using the wide-field mfERG and optical coherence tomography. Oral Presentation at the Research Workers Seminar, Tennent Institute of Ophthalmology. Glasgow, May 2001.

Fenton S, Sampat V, Muscat S, Parks S, Keating D, Kemp E. The role of optical coherence tomography in imaging choroidal melanoma. Poster presentation at the Annual Meeting of the Royal College of Ophthalmologists. Birmingham May 2001.

Muscat S. Optical Coherence Tomography in Ophthalmology. Didactic Talk at the Tennent Institute of Ophthalmology. Glasgow, March 2002.

Muscat S, Parks S, Kemp E, Keating D. The wide-field multifocal electroretinogram and optical coherence tomography in the assessment of choroidal nevi and melanomas. Poster presentation at the Annual Meeting for the Association for Research into Vision and Ophthalmology (ARVO). Fort Lauderdale Florida, May 2002.

Muscat S, Parks S, Kemp E, Keating D. The wide-field multifocal electroretinogram and optical coherence tomography in the assessment of choroidal naevi and melanomas. Oral Presentation at the Research Workers Seminar, Tennent Institute of Ophthalmology. Glasgow, May 2002.

Muscat S, Parks S, Kemp E, Keating D. The wide-field multifocal electroretinogram in the assessment of choroidal naevi and melanoma. Oral presentation at the IPEM Meeting on Recent Developments in Ophthalmic Electrophysiology. York, June 2002.

Muscat S, Parks S, Kemp E, Keating D. Functional and Anatomical Imaging of the Macula. Oral presentation at the Annual Meeting of the British and Eire Association of Vitreo-Retinal Surgery. Edinburgh, October 2002.

Muscat S, Parks S, Keating D. Cross-sectional Retinal Imaging in Ophthalmology. Presentation at the Department of Clinical Physics and Bio-Engineering Monthly Research Meetings. Glasgow, November 2002.

LIST OF ABBREVIATIONS

CCT   central corneal thickness

ERM   epiretinal membrane

IOP   intra-ocular pressure

mfERG   multifocal-electroretinogram

OCT   optical coherence tomography

RNFL   retinal nerve fibre layer

RPE   retinal pigment epithelium

SLO   scanning laser ophthalmoscope

ABSTRACT

The ability to examine the appearance of the retina is of paramount importance for the diagnosis and monitoring of ophthalmic disease and for the evaluation of treatment outcomes. Direct cross-sectional imaging of retinal structure could be useful for early diagnosis and more sensitive monitoring of a variety of retinal conditions such as macular oedema and glaucoma. The view of the fundus given by ophthalmoscopy provides very limited depth information and clinicians will often have to resort to additional techniques such as flourescein angiography or visual field testing for information on structural abnormalities within the retina. Other currently available imaging techniques do not provide sufficient depth resolution to produce useful cross-sectional images of retinal structure.

Optical coherence tomography (OCT) is a new imaging technique which is capable of producing cross-sectional images of the retina with a resolution that surpasses that of conventional imaging techniques. This new technique has axial resolution of around $10\mu m$ and can resolve individual retinal layers, thus providing information on retinal structure. In principle, OCT is very similar to ultrasound however it makes use of a light source rather than an acoustic one. The technique is non-contact and non-invasive and is generally well tolerated by patients. This thesis describes the evaluation of this new imaging technique with regards to its potential within routine clinical practice.

A number of investigations were performed to fulfil this evaluation. Tests were carried out to experimentally measure the system's resolution and the accuracy and precision of measurements made from the OCT scans. A number of factors that could affect the quality of the scans were identified and their effects were minimised wherever possible. The software provided with the system was rigorously tested and potential sources of error were identified. Various studies were undertaken to quantify the repeatability and reproducibility of measurements made from scans and normative values were established. These results were used to assess the ability of the technique to detect and quantify several retinal disorders. The potential of the technique for corneal imaging was investigated — a scanning protocol was established and customised software for processing corneal scans was developed. The relationship between OCT bands and retinal morphology was investigated by correlating scans from canine retina with corresponding light microscopy images and by observing the position of retinal abnormalities on scans from patients with a variety of conditions that affected different parts of the retina. Finally the clinical potential of OCT was investigated by carrying out various studies on a number of retinal conditions. Further clinical studies which combine anatomical information from OCT with functional information from electrophysiology are currently underway.

Current developments are aimed at improving the imaging processing features and user interface so as to provide a more robust, user-friendly system for routine clinical use.

Chapter 1

STRUCTURE OF THE EYE AND OCULAR IMAGING TECHNIQUES

This chapter gives an overview of the anatomy of the eye and takes a detailed look at the structure of the retina. This is followed by a description of various methods for imaging the retina.

1.1   Gross Anatomy of the Eye

The human eye is a structure which has two primary functions. Light rays incident on the eye are focussed onto the retina where an optical image is formed. The retina contains light-sensitive cells which translate the image into electrical signals. These are partially processed within the eye itself and the resulting information is coded for transmission to the visual cortex along the optic nerve. The structure of the eye is therefore determined by its optical and neurosensory functions.

The illustration of a cross-section through the human eye (Figure 1.1) shows:

- Three distinct layers:
    - The external layer, formed by the **sclera and cornea**
    - The intermediate layer, divided into two parts: anterior (**iris and ciliary body**) and posterior (**choroid**)
    - The internal layer, or the sensory part of the eye, **the retina**

- The lens which is a transparent body located behind the iris. The lens is suspended by ligaments (called zonule fibers), attached to the anterior portion of the ciliary body.

- Three chambers of fluid:
  - The anterior chamber (between cornea and iris), filled with aqueous humour
  - The posterior chamber (between iris, zonule fibers and lens), filled with aqueous humour
  - The vitreous chamber (between the lens and the retina), filled with vitreous humour

- The optic nerve which provides the connection between the eye and the visual cortex

Each eyeball is held in position in the orbital cavity by various ligaments, muscles and fascial expansions that surround it.
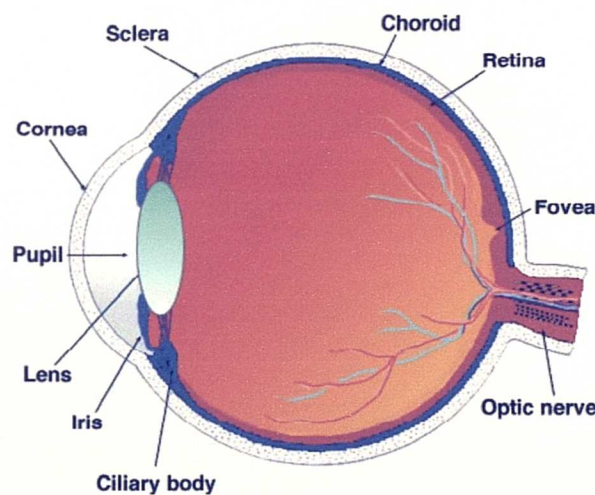
Figure 1.1   *Cross-sectional view through a human eye (adapted from Kolb H, Fernandez E, Nelson R.. Webvision Website: http://insight.med.utah.edu/webvision)*

1.1.1 The Sclera

The sclera is the white portion of the eye. Its radius of curvature is about 12mm and it varies from 0.4 to 1.0 mm in thickness. It is composed of obliquely arranged interlacing bundles of collagen fibrils and is tough and resists stretching. It gives rigidity and structure to the eye.

1.1.2 The cornea

The cornea is the first refractive surface of the eye and accounts for about two-thirds of the total refraction that light rays undergo within the eye. It has a refractive power of 43 dioptres (the whole eye has a combined refractive power of 60 dioptres) and a radius of curvature of about 8mm but is not truly spherical since the curvature is flatter at the periphery. It is covered by a tear film, approximately 8μm in thickness, which creates a reflecting surface. The corneal diameter is about 11.5mm and corneal thickness is typically in the region of 500 – 600 μm.

Histologically, the cornea is composed of five distinct layers:

- The *epithelium*, which is transparent. Cells of the epithelium can slide on each other and on the underlying Bowman's membrane and can promptly fill in any small defects in this layer.
- *Bowman's membrane*, which is a thin acellular layer of collagen fibrils.
- The *stroma* which accounts for most of the corneal thickness. It is composed of regular layers of parallel collagen fibrils embedded in a dehydrated ground substance of acid mucopolysaccharides. This regular arrangement, together with the reduced hydration and absence of blood vessels, accounts for the transparency of the stroma.
- *Descemet's membrane* is a thin, tough and elastic layer.
- The *endothelium*, which is a single layer of flat cells that have an important metabolic function in extracting water from the stroma.

1.1.3 The Iris

The iris is a diaphragm separating the anterior and posterior chambers. It has a central hole of variable size, called the pupil, through which light passes on its way to the retina and through which aqueous passes from the posterior to the anterior chamber. It consists of a vascular stroma covered on its anterior surface by mesothelium and on its posterior surface by two layers of epithelium which are both pigmented. The colour of the iris is determined by the number of melanin-containing pigment cells with the stroma which can vary from almost none (blue eye colour) to many (dark brown eye colour).

1.1.4 The ciliary body

The ciliary body is a band between 4 and 6mm wide and roughly triangular in section. It has two functions – the ciliary processes secrete the aqueous and the ciliary muscle alters the shape of the lens during accommodation.

1.1.5 The choroid

The choroid is a vascular layer applied to the outer surface of the retina. It is essentially a meshwork of blood vessels in which the arteries and veins are external and a dense network of capillaries (called the choriocapillaris) is internal. It is the indirect blood supply to the outer layers of the retina which are devoid of blood vessels. Cells containing melanin pigment are scattered throughout the choroid and give the choroid a purplish-brown colour. On the inner surface of the choroid is a thin sheet called Bruch's membrane.

1.1.6 The retina

The retina is a delicate layer, approximately 300 μm in thickness which lines the interior of the posterior two-thirds of the globe. It consists of two main parts, the transparent neural portion internally and the retinal pigment epithelium externally. The neural portion of the retina may be further sub-divided into several different

layers of cells. The structure and function of the retina are described in detail in section 1.2.

1.1.7 The lens

The lens provides the adjustable part of the eye's refractive power. It is biconvex with the curvature of the posterior surface being greater than the anterior. Externally there is an elastic capsule which encloses the lens fibres. During accommodation the curvature of the anterior and posterior surfaces is varied to change the shape, and hence the refractive power, of the lens.

1.1.8 The aqueous humour

The aqueous humour is a clear liquid which fills the anterior and posterior chambers. It is secreted by the ciliary processes into the posterior chamber from where it flows into the anterior chamber via the pupil. It is the nutritive medium for the lens and cornea.

1.1.9 The vitreous

The vitreous body is a transparent avascular jelly which fills the posterior segment. It is attached to its surrounds at two sites, the limits of the retina anteriorly and posteriorly around the margins of the optic disc.

1.1.10 The anterior chamber

The anterior chamber is the region between the posterior corneal surface and the iris and lens. The angle of the anterior chamber is the region where the aqueous leaves the eye and is of great clinical interest because if it becomes blocked the aqueous cannot escape and the intra-ocular pressure increases.

1.2   Morphology of the Retina

The retina consists of two main parts, the transparent neural portion internally and the pigment epithelium externally. A simplified diagram of retinal structure is shown in Figure 1.2.
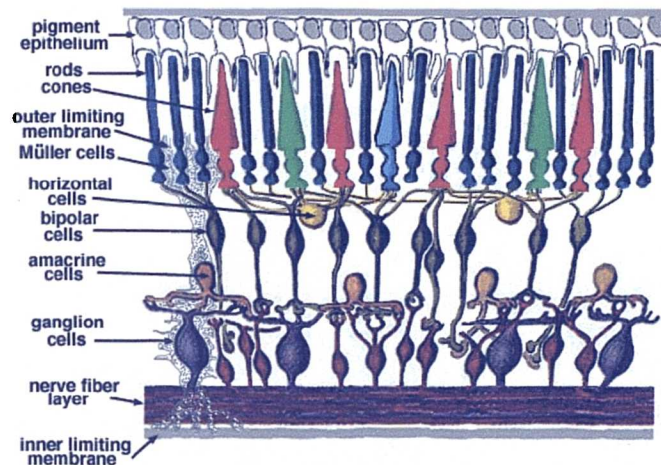
Figure 1.2   *Simplified representation of retinal structure (adapted from Kolb H, Fernandez E, Nelson R, Webvision website: http://webvision.med.utah.edu/)*

1.2.1   The retinal pigment epithelium

The retinal pigment epithelium (RPE) is a single layer of hexagonal cells which contain melanin. This pigment absorbs scattered light which would otherwise degrade the optical image. This light is converted into heat which is then dissipated by the blood flowing through the choroid. The RPE also selectively transports metabolites between the choroidal circulation and the outer retina but is able to prevent the diffusion of unwanted molecules from the choroid into the retina. It pumps water outwards from the vitreous and neural retina to the choroid which keeps the retina in contact with the outer layers of the globe. It transports vitamin A to the photoreceptors and synthesizes an acid-mucopolysaccharide which fills the spaces among the outer tips of the photoreceptors.

1.2.2   The neural retina

The neural retina is a complex structure composed of a variety of cells with specialised functions. It contains photoreceptors (rods and cones), five types of neurones (receptor nuclei, horizontal cells, bipolar cells, amacrine cells and ganglion cells), a specialised type of glial cell (Müller's cells) and many cell processes. Histology of the retina shows an organised layered structure as shown in Figure 1.3.

A   B
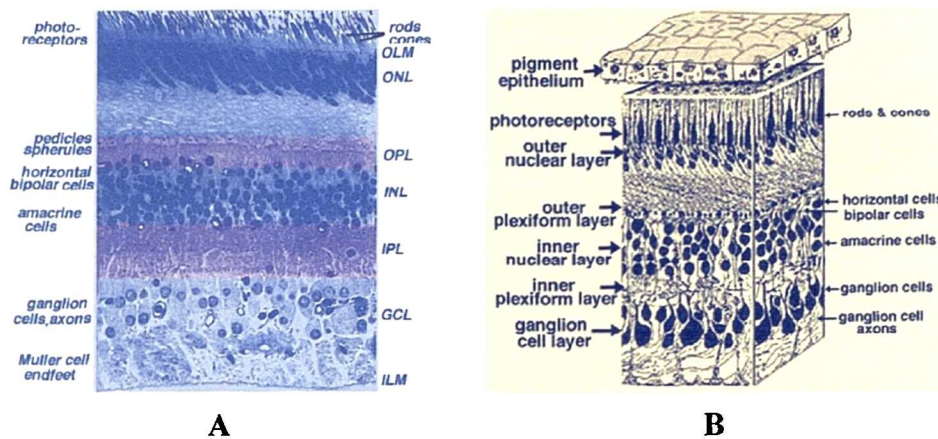
Figure 1.3   *Diagram of retinal morphology. (A) A light micrograph of a vertical section through the human retina. (B) Diagrammatic representation of retinal structure (adapted from Kolb H, Fernandez E, Nelson R, Webvision website: http://webvision.med.utah.edu/)*

The retina is composed of three layers of nerve cell bodies and two layers of synapses. The outer nuclear layer contains cell bodies of the rods and cones, the inner nuclear layer contains cell bodies of the bipolar, horizontal and amacrine cells and the ganglion cell layer contains cell bodies of ganglion cells and displaced amacrine cells. In between these nerve cell layers are two neuropils where synaptic contacts occur. In the outer plexiform layer (OPL) connections between rods and cones and vertically running bipolar cells and horizontal cells occur. The inner plexiform layer (IPL) is the second neuropil of the retina and it relays information from the bipolar cells to the ganglion cells. Further interactions occur between the horizontally- and vertically-directed amacrine cells, and these further influence and integrate the ganglion cell signals. After neural processing in the inner plexiform

layer, information about the visual image is transmitted to the brain along the optic nerve.

1.2.3   The central area of the retina

The central area of the retina, about 5 to 6mm in diameter has a somewhat different structure and function to the rest of the retina. It is has a higher concentration of cones than the peripheral retina. The central part of this region is the macula which appears slightly darker than the rest of the fundus because the underlying RPE contains heavier pigmentation. The central part of the macula is called the fovea, in the middle of which is a depression known as the foveal pit. In this region the retina is thinned to a layer of densely packed cones and all other layers are displaced concentrically (see Figure 1.4). This arrangement ensures that light incident on the fovea can strike the cones directly without having to travel through other retinal layers. Just outside the foveal pit, the displaced ganglion cells are piled into six layers, making this the thickest portion of the retina.
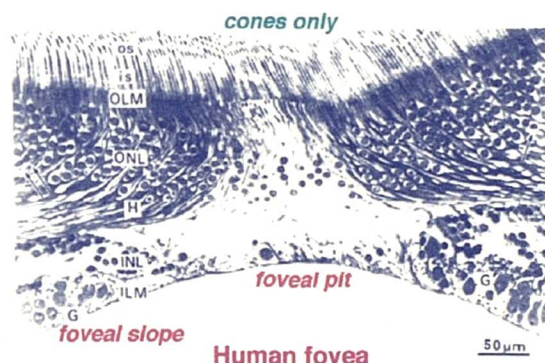
Figure 1.4   *Vertical section of human fovea (adapted from Kolb H, Fernandez E, Nelson R, Webvision website:*

http://webvision.med.utah.edu/webvision)

1.2.4   The optic disc

The disc is a relatively pale almost circular area, 1.5 to 2.0 mm in diameter. It is the point where the retinal retinal nerve fibre layers leave and the retinal vessels leave and enter the interior of the eye. The optic disc generally has a central depression

called the optical cup, the diameter and depth of which varies from individual to individual. The periphery of the disc is usually slightly higher than the surrounding retina because of bundling of the nerve fibres. This bundling is more marked in the superior and inferior areas.

1.3   Retinal Imaging Techniques

When a patient presents complaining of visual problems, one of the steps in attempting to establish a diagnosis involves examining the appearance of the retina for any obvious abnormalities. Clinicians first became able to view the retina in 1850 with the invention of the direct ophthalmoscope by Hermann von Helmholtz. Since then, technological advances such as the invention of the laser, have led to the development of more sophisticated retinal imaging techniques. This section gives an overview of some of these techniques.

1.3.1   The direct ophthalmoscope

The simplest instrument for examining the ocular fundus is the direct ophthalmoscope which is essentially a miniature flashlight held very close to the patient's eye and shone through the pupil. The fundus is viewed monocularly through a small peephole located just above the illumination source of the instrument producing an upright virtual image that magnifies the area of interest by about 15 times. There is also a dial containing neutralising lenses which is rotated to achieve the clearest retinal image. The basic optical arrangement of a direct ophthalmoscope is shown in Figure 1.5.

Although the magnification and resolution of the direct ophthalmoscope are quite good, there are number of shortcomings with this technique. These include:

- No depth information due to lack of stereopsis
- Limited field of view – images from the peripheral retina are distorted making it useful only for the central part of the fundus
- Degradation of images in cases where there are media opacities - due to insufficient illumination from the light source.

- May be impossible to examine patients with a high degree of astigmatism or spherical ametropia.

- Problems due to the corneal reflex (an image of the light source formed by the reflection of light from the cornea's front surface). This may be partially overcome by displacing the viewing and illumination axis or by restricting the illumination beam diameter, however these methods will restrict the field-of-view and reduce the intensity of the fundus image.

- Requires the examiner to be very close to the patient.

Some of these difficulties may be overcome by using the indirect ophthalmoscope.
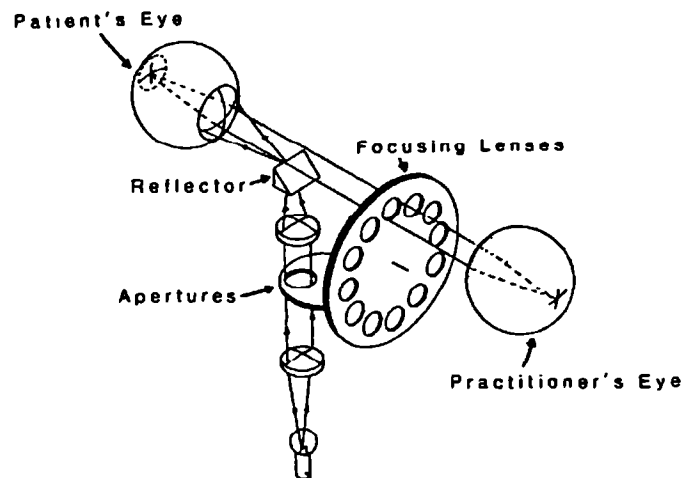
Figure 1.5   *Basic optical arrangement of the direct ophthalmoscope*

1.3.2   The indirect ophthalmoscope

Binocular indirect ophthalmoscopy offers a typical field of view of about 25° or more and excellent resolution of fundus details. Stereopsis is enhanced, allowing the examiner to detect variations in the elevation of the retinal contour. The ophthalmoscope is worn on a headband and a lens is held over the patient's eye to form a retinal image. The system is portable and examination may be carried out with the patient seated or lying down. The optical arrangement of the indirect ophthalmoscope is shown in Figure 1.6.
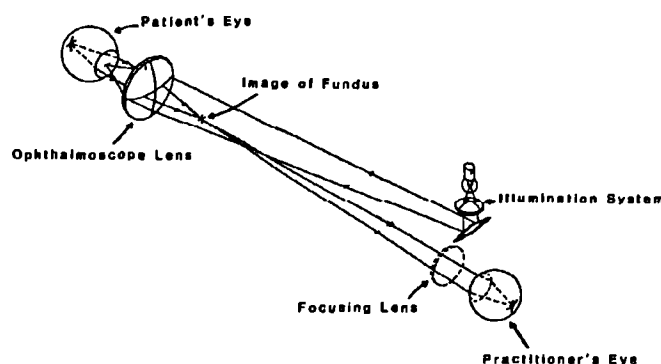
Figure 1.6   *Basic optical arrangement of the indirect ophthalmoscope*

Gullstrand modified the design of the basic indirect ophthalmoscope to eliminate the corneal reflex. He separated the illuminating and viewing paths as they pass through the cornea and lens. With such an arrangement, reflected light from the cornea and lens is directed away from the viewing system.

The indirect ophthalmoscope tends to have lower magnification than the direct which may limit its usefulness in detecting fundal anomalies. In clinical practice it is usual to use a combination of both techniques, indirect ophthalmoscopy to give a wide field-of-view and direct ophthalmoscopy to examine areas like the macula and optic nerve in greater detail.

1.3.3   The slit lamp biomicroscope

The slit lamp biomicroscope is an essential instrument for fundus examination particularly when a high degree of magnification is required. It consists of a moveable binocular biomicroscope mounted on a table and an intense illumination beam or slit beam of adjustable width that may be rotated 360° in the vertical plane. Focussing is accomplished by moving a joystick located on the microscope platform. The slit lamp is used in conjunction with a diagnostic contact lens or hand-held lens to provide a high quality magnified stereoscopic image of the fundus. Slit-lamp biomicroscopy is particularly useful in determining the location of a haemorrhage, detecting cystoid macular oedema and diagnosing clinically significant macular oedema.

The slit lamp also provides optical sections of the vitreous body to allow detection of posterior vitreous detachments, abnormal vitreous surfaces and floaters. Elevations are easily seen since these cause the slit beam to appear curved rather than straight. Macular holes and cystic spaces within the fovea can also be detected.

1.3.4 The fundus camera

The fundus camera makes it possible to store fundus images for future reference. The majority of fundus cameras are based on the optical arrangement found in the Gullstrand reflex-free indirect ophthalmoscope. They contain two light sources, a standard tungsten filament lamp for viewing the fundus and making focus adjustments and a flash source for taking photographs. Modern fundus cameras have a field-of-view ranging from around 50 to 100 degrees. Digital fundus cameras are also available making it very easy to store and transfer high quality images electronically.

Stereo photographs are useful for evaluating the depth or height of structures such as the optic nerve. Two photographs taken from slightly different angles, can be both stereographically viewed in a stereoviewer and processed to give quantified data on the depth of different structures.

1.3.5 The scanning laser ophthalmoscope

One of the main difficulties encountered when trying to image the fundus is the fact that both the illuminating and reflected beams need to pass through the same aperture. The scanning laser ophthalmoscope (SLO) is a fairly recent development which provides a solution to this problem and is also capable of giving information on different layers within the retina.

The principles and applications of the SLO have been explained in detail in several publications[1-4]. When compared with conventional fundoscopy, the illumination and observation apertures in the SLO are inverted. In conventional fundoscopy, the fundus is illuminated through the outer circumference of the dilated pupil and the fundus is observed through the central pupil as shown in Figure 1.7A. Since the exit

aperture is smaller than the entrance aperture, the amount of detectable light is significantly reduced, resulting in degradation of the image. In the SLO, a highly collimated narrow laser beam passes through a small aperture and is swept over the retina, illuminating a small area for a short period of time. The reflections from this spot are collected from the remaining large area of the pupil and decoded to form an image on a monitor. Thus, the exit aperture is larger than the entrance aperture, greatly improving the optical collection efficiency (Figure 1.7B).
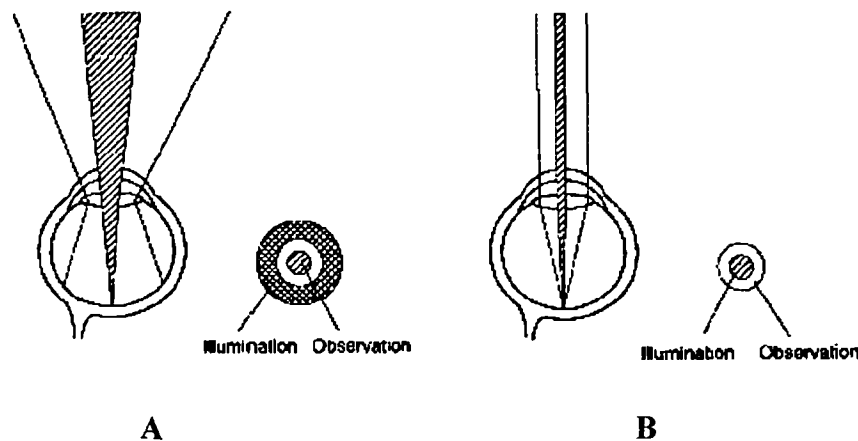
Figure 1.7   *Illumination and observation apertures in conventional fundoscopy (A) and in the SLO (B) (adapted from Mannivannan A, Sharp PF, Phillips RP, Forrester JV. Digital fundus imaging using a scanning laser ophthalmoscope. Physiol. Meas. 1993; 14:43-56.)*

The SLO may operate in three modes – direct, confocal and indirect. The mode of operation depends on the position of a confocal aperture situated in front of the detector. In the direct mode, the size of this aperture is very large compared to the size of the illumination spot and may allow scattered light that has undergone multiple reflections to reach the detector. This causes a reduction in contrast. Depth of focus is of the order of millimetres and the brightness of the image is high since it contains reflections from all the retinal layers.

In the confocal mode the aperture is smaller so light scattered from areas other than the illuminated point cannot reach the detector and contrast is improved over the direct mode, although at the expense of overall brightness of the image. In addition, the position of the aperture determines the layer from which the reflected light is

being collected, so tomographic imaging can be performed. The depth of focus will depend on the size of the confocal aperture.

Imaging in the indirect mode is achieved by using a large aperture with a central occluder. The effect of this set-up is that light from the central fundus is blocked and only scattered light reaches the detector. Clinically, this mode has been found to be useful for imaging drusen.

1.3.6   Scanning Laser Polarimetry

This imaging technique is designed to look specifically at the retinal nerve fibre layer (RNFL) around the optic disc. The thickness of the RNFL in this area is affected in glaucoma and its assessment is therefore important in the accurate diagnosis and monitoring of glaucoma.   Scanning laser polarimetry is based on the principle that polarized light passing through a form-birefringent medium undergoes a measureable phase shift directly proportional to the thickness of the medium. The RNFL consists of retinal ganglion cell axons containing microtubules which are several nanometres in diameter and are arranged in parallel bundles. Such a medium of parallel bundles, each smaller than the wavelength of the light passing through it, exhibits form-birefringence.

The birefringence causes a change in the state of polarization of an illuminating laser beam, known as retardation. Retardation of light that has doubly passed the optical media after being reflected from the retina is measured consecutively at each of 65536 (256 × 256) pixels in the field of view[5]. Clinical studies have demonstrated this method to be a promising one for assessing RNFL thickness in clinical practice[6,7].

1.3.7   Ophthalmic Ultrasound

Non-optical ocular imaging techniques are becoming more widely used in the clinical setting. Ocular ultrasound, in particular, has become a routine clinical tool

for measuring axial length of the eye and for the diagnosis and monitoring of ocular tumours.

In this imaging mode, a pulse of ultrasound is directed through the eye via a transducer, causing reflected echoes to be generated from boundaries within the eye. The depths of these boundaries can be calculated from the time taken for the reflections to return to the detector. Ultrasonic frequencies of 6-20 MHz are typically used for ophthalmic applications. These give resolutions ranging from around 0.25mm down to around 0.1mm for the higher frequencies.

The simplest form of ultrasound scanning is called A-Scan ultrasonography which essentially consists of depth information along a straight line parallel to the axis of the transducer. By moving the position of the transducer, it is possible to obtain a series of adjacent A-Scans which are combined to give a cross-sectional view of the eye, known as a B-scan (Figure 1.8).
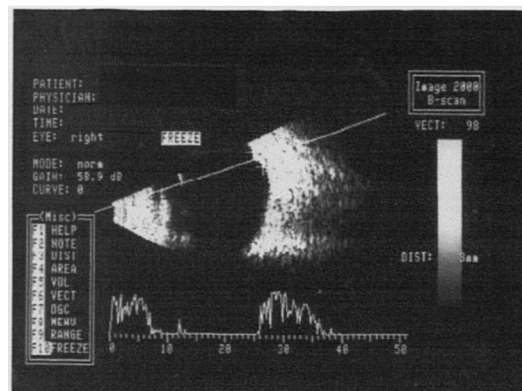
Figure 1.8   *An ultrasound scan of a patient with a small ocular tumour. This kind of ultrasound is used to make rough measurements of the dimensions of the naevus and to monitor any changes over time.*

1.3.8   Optical Coherence Tomography

Optical Coherence Tomography (OCT) is a relatively new technique which offers better depth resolution than any other technique currently available. OCT is the

subject of this project and the principles and applications of the technique will be explained in detail in subsequent chapters.

1.4   Conclusions

This chapter gives an overview of the structure of the eye and of the functions of the various structures within it. The structure of the retina is explained in detail since subsequent chapters will deal with the principles and clinical applications of an imaging system designed primarily to produce high-resolution cross-sectional images of the retina.

The ability to see depends on the health of the eye and when a patient presents with visual problems, it is important to examine the eye internally for any obvious abnormalities. Various imaging tools are available and, in the clinical setting, it is normal to use a combination of these techniques. The most basic ophthalmic imaging tool is the ophthalmoscope which presents the investigator with a magnified view of the illuminated retina. There are two types of ophthalmoscope, the direct and indirect. The indirect offers a number of advantages over the direct, such as a larger field of view but tends to have lower magnification so it may not be ideal for detailed examination of the macula or optic nerve.

When using an ophthalmoscope, the only way of recording findings for future reference is to draw and document the observations. The fundus camera offers a less subjective alternative. It functions essentially like an indirect ophthalmoscope and images may be recorded photographically for future reference. In recent years, digital fundus cameras, which store images electronically, are becoming increasing popular since digital images are very easy to transmit electronically. Digital fundus cameras are ideal for use in screening programmes since fundus photographs acquired from patients locally can be relayed to a specialist centre for analysis. Every ophthalmic clinic is also likely to have a slit lamp biomicroscope which has become an essential tool for examination of both the posterior and anterior eye.

Over the past decade a number of new ophthalmic imaging techniques have been developed and have been shown to be useful in the clinical setting. Amongst these are the scanning laser ophthalmoscope and the scanning laser polarimeter. The scanning laser ophthalmoscope uses a laser beam to produce high-resolution images of the retina and may be used confocally to give tomographic information. The scanning laser polarimeter is designed specifically for imaging the retinal nerve fibre layer around the optic disc and is useful in the diagnosis and management of glaucoma. Non-optical imaging techniques such as ultrasound, CT and MRI are often used in certain situations such as the diagnosis and monitoring of ocular or orbital tumours. Optical coherence tomography (OCT) is one of the most recent imaging tools to become commercially available and is rapidly gaining in popularity due to its ability to produce high-resolution cross-sectional images of the retina.

The aim of this thesis is the evaluation of a commercially available optical coherence tomography scanner for routine clinical use. To provide a thorough evaluation a number of investigations are required:

1. The basic parameters of the system such as its resolution and the accuracy and precision of measurements made from scans should be verified.
2. Factors affecting the quality of scans should be investigated and their effects minimised where possible.
3. A quantitative assessment of repeatability and reproducibility of the technique should be undertaken.
4. The correlation between OCT scans and retinal morphology should be investigated.
5. The characteristics of OCT scans in the normal population should be established and the normative ranges of parameters likely to be of use in the clinical environment should be determined from a control population.
6. An investigation of a selection of retinal disorders should be undertaken.

The next chapter gives an overview of the physical principles behind OCT technology and describes a typical scanner suitable for ophthalmic imaging.

Chapter 2

PRINCIPLES OF OPTICAL COHERENCE TOMOGRAPHY

Optical coherence tomography (OCT) is a relatively new imaging technique that permits in-vivo cross-sectional imaging of biological tissue. The technology was initially applied to in-vivo imaging of the eye since the eye is a transparent structure and is therefore ideal for imaging with an optical technique such as OCT. Further advances in technology have made it possible to image more scattering media, such as the skin.

2.1   Introduction

This chapter begins with a detailed description of the principles of operation and technology of optical coherence tomography. The main features of a typical ophthalmic OCT system are then described. A more detailed description of the principles and applications of OCT may be found in several publications[8-10].

2.2   Principles of Operation

In principle, OCT is very similar to ultrasonic imaging, the fundamental difference being that electro-magnetic radiation in the visible or infra-red portion of the spectrum is used instead of sound waves. An OCT 'A-Scan' is obtained by shining a beam from a super-luminescent diode onto the tissue to be imaged. As in ultrasound, the principle of echo delay is then employed to calculate the depth of the interfaces within the tissue. A series of adjacent A-scans can be combined to form a B-scan – a two-dimensional cross-sectional view through the structure. Successive B-scans may then be combined to give tomographic information on the structure.

2.2.1 Echo Delay

In both ultrasound and OCT, when the incident sound or light wave encounters an interface within the tissue, it is partly reflected back towards the emitter and partly transmitted deeper into the tissue. In ultrasound, the depth of an interface is calculated by measuring the time taken for the reflection, or echo, arising from that interface to travel back to the source. The depth of the interface can then be calculated, provided that the speed of the sound wave in the medium is known. Since the speed of light is several magnitudes greater than that of sound, measuring the echo time delay of a reflected light wave would require ultra-fast time resolution, of the order of femtoseconds. In OCT imaging, this problem is overcome by using low coherence interferometry to make high-resolution range measurements.

2.2.2 Low Coherence Interferometry

Figure 2.1 shows a schematic diagram of an optical interferometer. The light source of wavelength λ directs the incident optical wave $E_i(t)$ towards a beamsplitter. At the beamsplitter, one portion of the beam $E_S(t)$ is transmitted into the tissue sample and another portion $E_R(t)$ is reflected towards the reference mirror which is at a known spatial position. The beam which is incident on the tissue sample undergoes partial reflection whenever it encounters a structure or surface within the tissue. Thus, the reflected beam travelling back towards the beamsplitter contains multiple echoes from the interfaces within the tissue. The beam incident on the reference mirror is reflected back towards the beamsplitter. These two reflected beams are recombined in the beam splitter and the resulting beam $E_R(t) + E_S(t)$ is analysed by the detector.
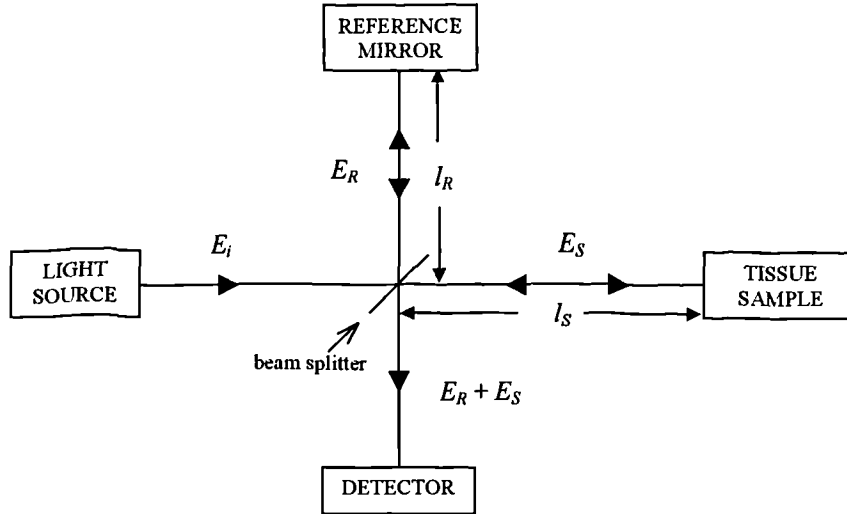
Figure 2.1   *Schematic diagram of a simple interferometer*

The intensity $I_0(t)$ measured by the detector is proportional to the square of the electromagnetic field. Because of interference effects, the intensity of the output from the interferometer will oscillate as a function of the difference between the path lengths of the reference and specimen beams. From electromagnetic theory, the intensity of the combined beam arriving at the detector is given by:

$$I_0(t) \approx \frac{1}{4}|E_R|^2 + \frac{1}{4}|E_S|^2 + \frac{1}{2}E_R E_S cos\left[2\left(\frac{2\pi}{\lambda}\right)\delta l\right]$$

(2.1)

Where l_r is the distance that light travels in the reference path of the interferometer

l_s is the distance that light travels in the measurement path (reflected from the specimen)

δl $= l_r - l_s$

Varying the position of the reference mirror changes the value of l_r and hence δl and will cause the two beams to interfere constructively or destructively. The intensity will oscillate between maximum and minimum each time the path length between reference and measurement arms changes by one optical wavelength (as the position of the reference mirror changes by half a wavelength).

If the light beam is coherent, constructive interference will be observed for a wide range of relative path lengths of the reference and measurement arms. However, in optical imaging, it is important to know the position of the structures within the specimen precisely, thus light with a short coherence length must be used. With short coherence length light, constructive interference is seen only when the paths travelled by the reference and measurement beams are nearly equal. If the paths are mismatched by more than the coherence length of the light, no interference effects are observed. The coherence length of the light therefore determines the spatial resolution of the imaging system. Since short coherence length light is composed of several different frequencies of light, it can be characterised by a frequency or wavelength bandwidth. It can be shown from electrodynamic and optical theory that the range resolution can be related to the bandwidth by the following equation:

$$\Delta L = \frac{2ln2}{\pi} \frac{\lambda^2}{\Delta\lambda}$$

(2.2)

Where ΔL is the ranging resolution

λ is the operating wavelength of the light source

$\Delta\lambda$ is the full width at half maximum of the spectral bandwidth

A typical OCT system for ophthalmic applications uses a superluminescent diode operating with a wavelength of around 850nm and an optical bandwidth of 30nm. From the above equation this gives an estimated range resolution of approximately 10μm. Experimental quantification of the range resolution of a typical OCT ophthalmic scanner is given in Chapter 4.

2.2.3   Spatial Resolution

The spatial resolution of an OCT system is determined by the spot size of the focussed beam. The minimum spot size to which a beam may be focussed is inversely proportional to the numerical aperture or the angle of focus of the beam. The spot size ω arising when a beam with diameter d is incident on a lens of focal length f is given by:

$$\omega = \frac{\lambda f}{\pi d}$$

(2.3)

Transverse resolution is therefore limited by the available focussing angle. In an ophthalmic OCT system used for retinal imaging, the focussing angle is limited by the pupil size and focal length of the eye. Spatial resolution in ophthalmic OCT systems is of the order of $10 - 15$ µm.

2.2.4 A Typical OCT Scanner

In practice, OCT scanners are built using fibre optics. The light source is a super-luminescent diode operating in the near infrared region of the E-M spectrum and having a short coherence length (~ 10µm). This is coupled directly into an optical fibre leading to the optical fibre coupler which functions as a beamsplitter. The resultant interference beam is analysed by a photodiode together with signal-processing electronics and computer data acquisition. A representative diagram of a typical OCT scanner is shown in Figure 2.2.
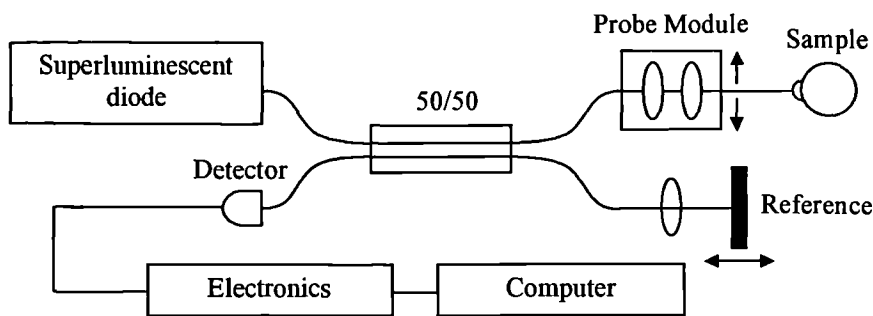
Figure 2.2   *Schematic diagram of a typical OCT scanner*

2.3   OCT in Ophthalmology

One of the first applications of OCT was in ophthalmology. In 1988 Fercher et al[11] showed that it was possible to measure the optical length of the eye with a precision of 30 µm using interferometric techniques. By 1991, Huang et al[12] had improved this resolution to 10 µm and, in the same year published images obtained from an in-vitro

sample of human retina in which the retinal nerve fibre layer (RNFL), retinal pigment epithelium (RPE) and blood vessels were easily identifiable[13]. Images obtained with this system correlated well with histological analysis of the same tissue sample. A couple of years later, the same group successfully acquired retinal scans in-vivo from a human volunteer[14]. This system could also process raw data scans and remove artefacts caused by patient motion and could be used to make measurements of retinal and retinal nerve fibre layer thickness. The only system that is currently commercially available, manufactured and marketed by Zeiss-Humphrey Medical Systems, evolved from the prototype system described in this publication. This commercial system is described in greater detail in Chapter 3. Izatt et al[15] showed that the same principles could be applied to imaging of the anterior segment of the eye.

Ophthalmic OCT systems generally make use of a superluminescent diode operating at approximately 850nm. The maximum signal power that is delivered onto the patient's eye must conform to safe ocular exposure standards and is typically in the region of 750 µW. The full-width-at-half-maximum (FWHM) spectral bandwidth of the source is around 30 nm and lateral and longitudinal resolutions of the order of 10 – 15 µm may be achieved. More recent developments in OCT technology have resulted in a system with resolution of about 3 µm[16]. This system is discussed in greater detail in Appendix A.

OCT can be used for imaging both anterior and posterior eye. In the healthy eye, scans of the retina can clearly distinguish at least three distinct retinal sections, giving more histological information than other available non-invasive ocular imaging techniques. OCT is also very useful in identifying abnormalities in the normal retinal architecture such as areas of retinal oedema, macular holes, retinal detachments and a variety of other conditions[17-20]. A more detailed description of clinical applications of OCT in ophthalmology may be found in Chapter 6. Figure 2.3 shows typical scans from the retina of a healthy volunteer. A detailed interpretation of these images will follow in the next chapter.

A	**B**	**C**
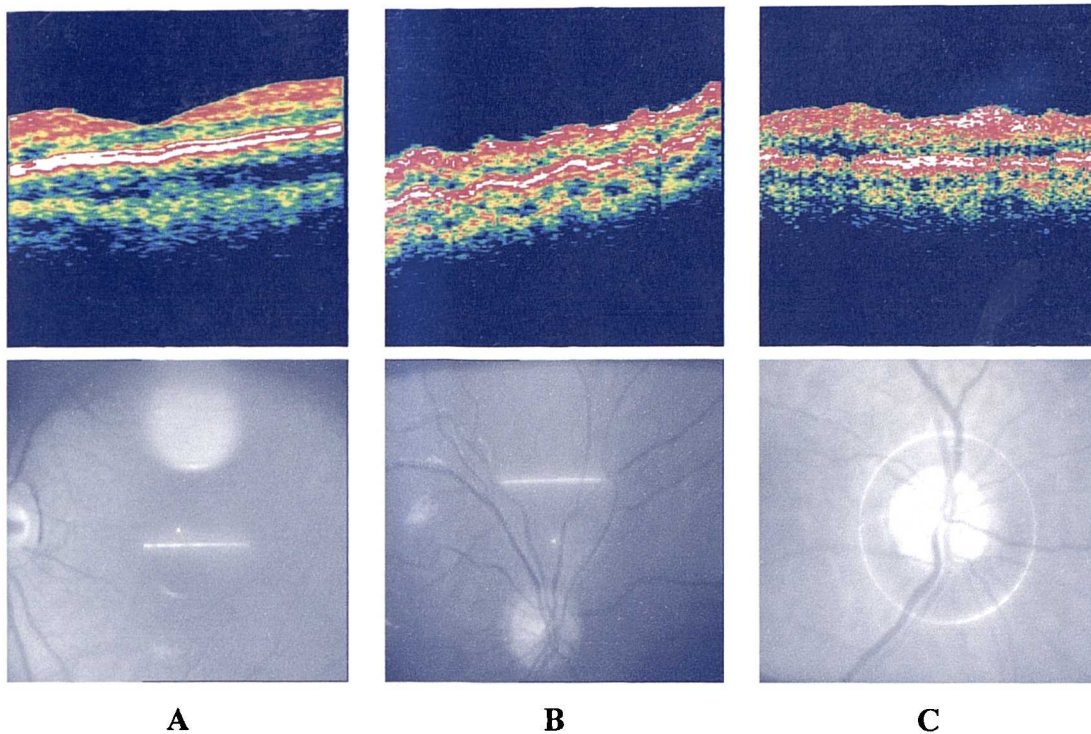
Figure 2.3 *Typical OCT images from the retina of a healthy volunteer. (A) Scan through the fovea showing the foveal contour. (B) Scan through a non-macular area of the retina showing clearly delineated retinal bands. (C) Circular scans around the optic nerve head. Corresponding fundus pictures demonstrating the position of the scan line are shown below.*

OCT has recently been gaining in popularity as a tool for imaging the anterior eye. Corneal OCT scans can differentiate between the corneal epithelium and the stroma. Measurements of central corneal thickness from OCT are an attractive alternative to other methods which often require contact with the cornea. OCT has been used successfully in a number of conditions which affect corneal health such as refractive surgery and corneal oedema [21-26.] A scan from a healthy cornea is shown in Figure 2.4A. OCT can also show other features of the anterior eye such as the lens and angle (Figure 2.4B).
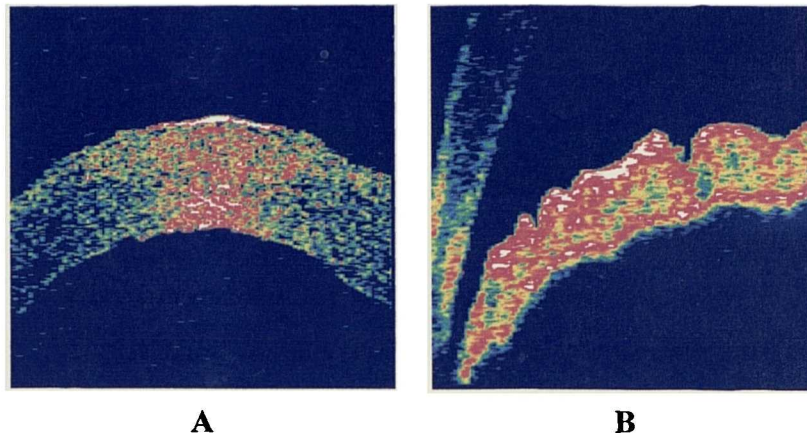
Figure 2.4   *(A) Scan through the cornea of a healthy volunteer. The distinction between the corneal epithelium and the stroma can be seen. (B) Scan showing the angle in the same volunteer.*

2.4   Conclusions

The basic operating principle behind OCT is quite simple. Short coherence length light from a superluminescent diode is incident on the tissue under investigation. At interfaces where there is a change in the optical properties of the tissue, the incident light is partially transmitted deeper into the tissue and partially reflected back towards the source. A Michelson interferometer combines the reflected beam with a reference one. The output of the interferometer contains information on the depth of structures and of the ocular properties of the tissue and may then be translated into a greyscale or pseudo-colour image.

Since the structures within the anterior eye are transparent, the retina is ideal for OCT imaging and the first successful clinical applications of OCT were, in fact, in ophthalmology. Imaging of turbid media such as skin is also possible and in recent years there have been a number of non-ophthalmic applications of the technology. Some of these non-ophthalmic applications are described in Appendix A. The resolution of OCT systems should continue to improve and it is likely that the technique will be applied successfully in several areas of medicine.

Chapter 3

THE ZEISS-HUMPHREY OCT SCANNER

A commercially available ophthalmic optical coherence tomography (OCT) scanner was used for this project. The hardware elements of this system are based on the operating principles described in the previous chapter. In addition, there are a number of software options provided for image processing and analysis. Retinal scans obtained from this system are very similar to those presented in the early publications on in-vivo ophthalmic OCT, which made use of a prototype system. The correlation between OCT scans and corresponding histology may be studied by scanning sections of animal retina which are similar in structure to human retina and comparing the OCT images with light micrographs of the same section of tissue.

3.1   Introduction

The scanner used throughout this project is the OCT 2 scanner manufactured by Zeiss-Humphrey Systems (Dublin, California, US). This chapter describes the key features of this scanner. The procedure for setting-up a patient for scanning is outlined and the various factors that could affect the quality of the OCT scans are discussed. An experiment to study the correlation between OCT images and corresponding histology in the retina of the dog is also described.

3.2   Technical Specifications

The OCT 2 scanner operates on the principles explained in the previous chapter. The light source is a super luminescent diode with a wavelength of 850 nm. The

operating power of this source is variable, reaching a maximum of 750 μW which conforms to the American National Standards Institution (ANSI) recommendations for safe exposure of the retina to light[27]. The scanning beam may move transversely either along a straight line of variable length or along a circle of variable diameter. In this model, the B-scan is composed of 100 A-scans regardless of the length of the scan. Each of these A-scans is composed of 500 pixels, thus giving a total of 50,000 data points per scan.

Longitudinal resolution is determined by the coherence length of the light source and in this model is between 10 and 15 μm. Transverse resolution is primarily dependent on the width of the spot size but in this system it will also be influenced by the length of the B-scan. In longer B-scans, the separation between successive A-scans increases so the resolution decreases. The best transverse resolution is therefore achieved with the shortest scan length and is of the order of 10 – 15 μm. If the longest available scan line is used (6.97 mm) the separation between successive scans is 70 μm and so the resolution that can be achieved decreases.

3.3 Acquiring a retinal scan

The Zeiss-Humphrey OCT 2 scanner is shown in Figure 3.1. Patients sit with their chin resting on the chin rest and their forehead pressed against the forehead bar. This helps to keep the head more stable and reduces motion artefacts. The viewing unit, shown on the far right, houses a fundus camera and the OCT components. For retinal scanning, the camera lens will typically need to be positioned at around 1 cm from the front of the eye. The monochrome monitor on the right shows a real-time image of the fundus. During scan positioning the light source traverses in rapid mode and the operator will see a continuous scan line which may be moved to any portion of the fundus visible on the screen. Scan length and orientation may also be modified at this stage. Once the position of the scan line has been selected, image acquisition may begin and the light source now traverses in slow mode.

To facilitate repeat scanning on future occasions, there is a landmark cursor which may be placed on an anatomical feature such as a bifurcation of blood vessels. The position of the scan line with respect to this landmark is saved along with the scan.
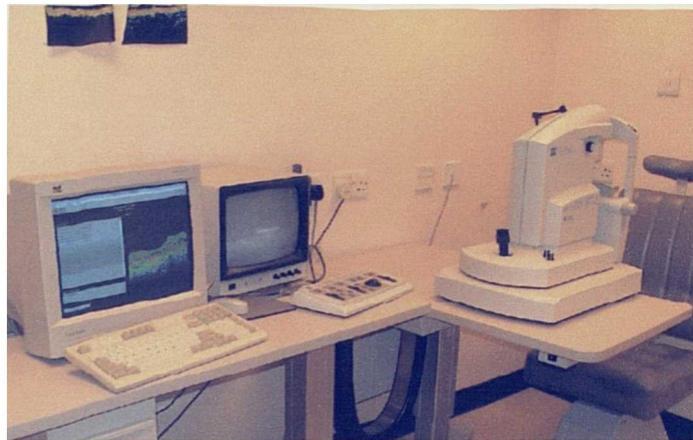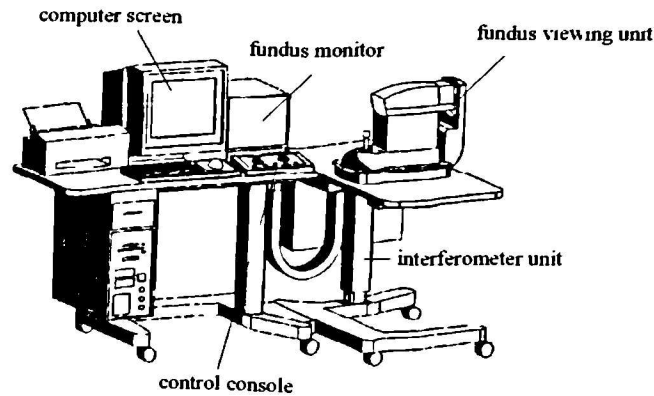
Figure 3.1   *Schematic representation and photograph of the Zeiss-Humphrey OCT 2 scanner.*

The scan acquisition time is always one second, regardless of the length or diameter of the scan line. The OCT image is continually updated on the computer screen on the left until scanning is stopped by the operator. At this point a fundus photograph is acquired and, if the operator is satisfied with the quality of the OCT scan, both the OCT scan and the corresponding fundus picture may be saved.

Retinal scans are best performed with a dilated pupil although in some subjects it is possible to obtain good quality scans of the central macula with an undilated pupil. The patient may be asked to fixate either on an internal fixation mark (a flashing green light) or on an external one (a flashing red LED mounted on a movable stand)

45

depending on the area to be imaged. The position of the internal fixation point can be varied in small increments and there is also a command that allows the operator to toggle the position of the fixation marker between the centre of the field of view (for foveal scanning) and the periphery (for imaging of the optic disc). With the internal fixation light, only the central 5-10° of the retina may be imaged. By using the external fixation light on the fellow eye, it is possible to image out to about 20° on the nasal side. Imaging non-central areas on the temporal side is harder since the movement of the external fixation light on this side is restricted by the viewing unit itself and can only be achieved in very co-operative patients.

The quality of the scan will depend on the clarity of the media and on the cooperation of the patient. If the media are not clear then a clear fundus view cannot be obtained, making it hard to position the scan. Unclear media will also reduce the intensity of the incident and reflected beams, thus degrading the quality of the scans. Scans marred by motion artefacts will occur if the patient is unable to fixate properly or sit still for the duration of the scanning session. In general, however, OCT scanning is relatively quick and easy to perform and is well tolerated by most patients.

3.4　Scanning Options

In order to create a B-scan, the OCT scanning beam can translate either along a straight line or along a circle. The software provided with this model offers a number of scanning options which are combinations of these basic scanning options.

Single Line: This permits scanning along a single straight line of variable length and orientation. Once the scan is saved the user is automatically taken from the scanning screen back to the scan selection screen.

Line Group: This is similar to the *single line* option, however when a scan is saved, the system allows more scans to be acquired and the operator must manually exit back to the scan selection screen once the scanning session is over.

Single Circle: This is similar to the *single line* option, however scanning is along a circle of variable diameter

Circle Group: This is similar to the *line group* option, however scans are circular rather than along straight lines.

Repeat: This option is designed for repeat scanning of a previously scanned patient. The previous scan that is to be repeated is selected. The landmark cursor is placed at the same position as in the original scan. The position of the scan line is set automatically from the relative positions of the landmark and scan line in the original scan, thus ensuring that the repeat scan is in the same position as the original.

Composite Circle: This option allows the operator to create a circular scan from four arc scans. This increases the number of A-scans within the complete circle to 400.

Raster 6 Lines: This option is designed for acquiring closely spaced tomographic line scans. The operator selects a rectangular area to be scanned and six equally spaced line scans across this region may be then be acquired.

Concentric 3 Rings: This is similar to the *raster 6 lines* option with 3 equally spaced circular scans positioned within a selected circular area.

Radial Lines: This scan option is designed for building retinal maps. A circular area to be scanned is selected. Six straight line scans running along the diameters of this area are then acquired. A software option may then be used to create a retinal thickness map from these scans.

Cross hair: Permits perpendicular vertical and horizontal scans through a selected point.

Rectangle: Two vertical and two horizontal scans along the sides of a rectangle of variable size.

Nerve Head 1.5R/Nerve Head 2.0R: This increases the radius of a selected circular scan by a factor of 1.5 or 2 respectively. These options are designed for scanning around the optic nerve head.

Nerve Head R=1.73mm: This option will set the radius of the circular scan to 1.73mm and is designed for scanning around the optic nerve head.

3.5   Interpretation of retinal OCT images

OCT can give information on the position and optical properties of structures and layers within the retina. The intensity of the backscattered optical signal in the OCT B-scan is displayed as a false-colour plot, where white represents the highest

intensity and black represents lowest. If two adjacent structures within the eye scatter light with different intensity, they will appear in different colours on the OCT scan. Thus, the OCT scan will consist of a number of differently coloured bands. In order to be able to use OCT as a diagnostic tool, it is essential to relate these OCT layers to actual retinal morphology. Some features on OCT scans are fairly straightforward to identify by simple comparison with textbook images of human retinal morphology and knowledge of the different reflective properties of retinal structures. A more scientific approach would be to compare the OCT scans and light micrographs of the same retinal sections. This first part of this section describes the appearance of various OCT scans acquired in-vivo from a normal volunteer – the interpretation of these images is based on comparison with published accounts of retinal morphology[28,29] and assumptions based on the different optical properties of substances such as melanin and haemoglobin. This is followed by a description of a study designed to directly compare OCT scans and light microscopy images obtained from the same section of canine retina.

3.5.1   Comparison of OCT scans and human retinal morphology

Typical scans at various locations in the normal human retina are shown in Figures 3.2, 3.3 and 3.4. In Figure 3.2 the fovea appears as a dip in the retinal contour – this is consistent with histological observations that, in this region, there is a lateral displacement of the photoreceptor synapses and inner retinal neurons, leading to thinning of the retina at this point. The retina appears as two highly reflecting bands (red and white) separated by a region of lower reflectivity (blue and green). The thin upper red band is thought to correspond to the retinal nerve fibre layer (RNFL)[13,14]. This band is very thin in Figure 3.2, close to the fovea, it is thicker in Figure 3.3, just above the optic disc and is even thicker in Figure 3.4 especially superior and inferior to the optic disc. Histologically, the RNFL is thinnest close to the fovea and thickest around the optic disc especially superiorly and inferiorly since bundling of the nerve fibres occurs at these points. Thus, the assumption that this red band corresponds to, or is related to the RNFL is reasonable. Further support for this theory is provided from the results of two clinical studies described in Chapter 6. The lower red and white band is thought to correspond to the retinal pigment epithelium (RPE) and the choriocapillaris[13,14]. The high reflectivity of this band is likely to arise from the

melanin in the RPE since melanin is a very strong scatterer of light at this wavelength. In some normal subjects this band may appear split into a thin portion anteriorly and a thicker portion posteriorly. This can clearly be seen in Figure 3.2 below. Often this split in the presumed RPE-choriocapillaris complex is best observed on the unprocessed OCT image as image processing may obscure it. The possible nature of these two distinct portions is investigated in Chapter 6. The lower intensity reflections between the RNFL and RPE-Choriocapillaris complex bands correspond to the mid- and outer retinal layers. In normal OCT scans, no specific layers are observed within this region. The apparent breaks in the RPE-choriocapillaris layer seen in Figure 3.4 are artefacts caused by the presence of the blood vessels. Haemoglobin absorbs light with wavelength of 850nm so blood vessels appear as black round structures which shadow reflections from structures beneath them.
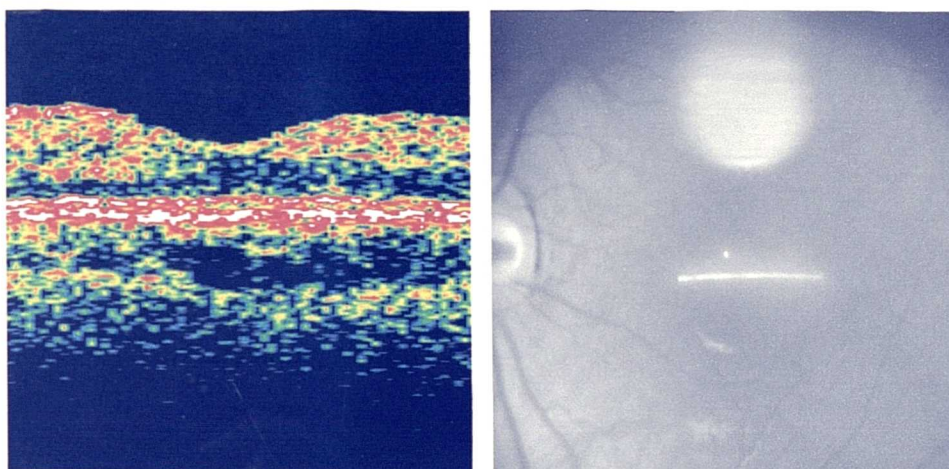
Figure 3.2 *Typical scan through the fovea of a normal volunteer and the corresponding fundus photograph.*
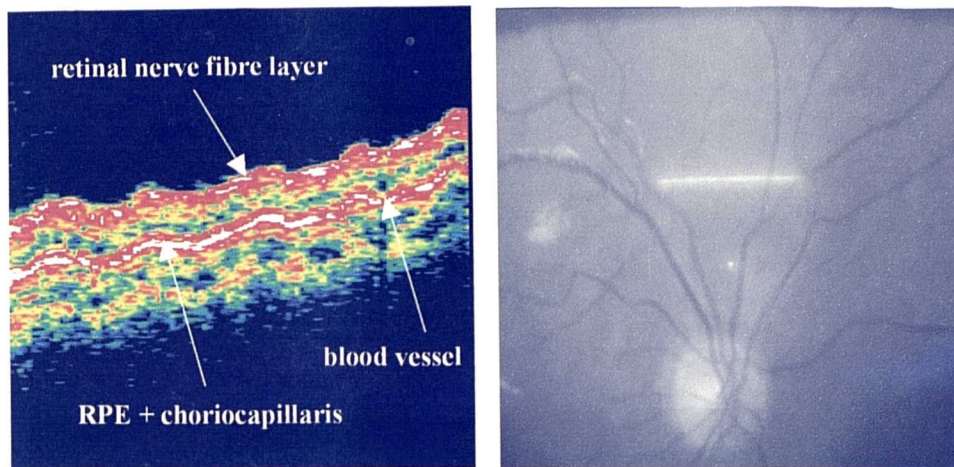
Figure 3.3   *Scan through a section just above the optic disc*
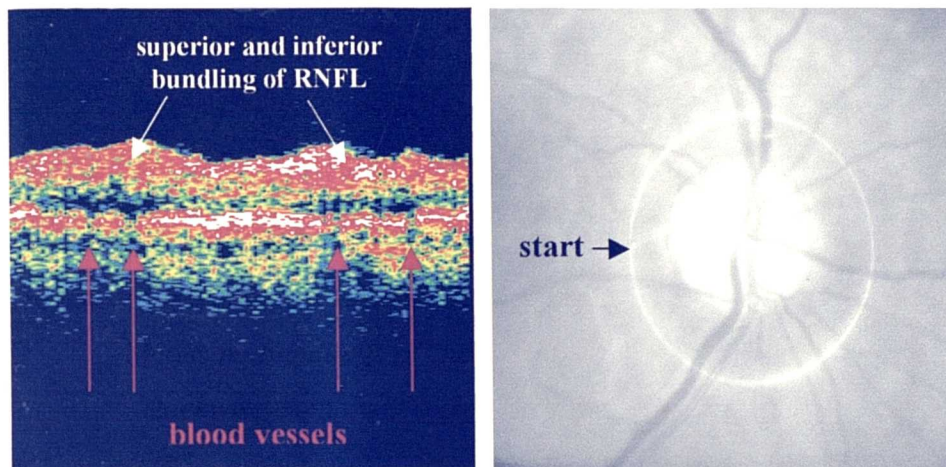
Figure 3.4   *Circular scan around the optic nerve head showing superior and inferior bundling of nerve fibres. The circular scan traverses clockwise from the 9 o'clock position.*

3.5.2 Direct correlation of OCT scans with histology in the canine retina

Direct correlation of OCT scans and corresponding histology was carried out on canine retina. Due to various ethical considerations, human retinal specimens were not available for direct comparisons. It was decided to use canine tissue for the following reasons:

- Post-mortem eyes from dogs were readily available soon after death
- The canine eye is roughly the same size as the human one so the scanning set-up was similar to that for humans

- A study on OCT scanning of canine eyes also served to evaluate the potential of OCT in veterinary applications.

One drawback of the study was that there are a few differences between canine and human retina, namely the absence of a fovea and the presence of a tapetal layer in the dog retina.

Methods

Retinal scans for this study were acquired from 8 eyes of 6 different dogs. These dogs were not laboratory animals but domestic pets that had to be put down for medical reasons. One or both eyes from each of these animals was enucleated following death after informed consent had been given by the dogs' owners. In all cases, there was no evidence to suggest that the animal had any ocular abnormalities in the enucleated eyes prior to death. All examined eyes had clear media.

OCT scans were acquired within two hours of death. The intact enucleated eyeball was placed in a custom-built holder for scanning. The eyeball was placed in a hollow hemispherical cup which had a diameter that was roughly equal to that of the eye. A small pump at the pole of the cup was used to create suction, which held the eyeball firmly in the cup. With this arrangement the eyeball could be positioned with the pupil directly in the line of the OCT scanning beam. Retinal scanning could then be performed in much the same way as in in-vivo human eyes.

A common cause of visual loss in dogs is glaucoma and thus, one of the potential veterinary applications of OCT is the analysis of retinal and retinal nerve fibre layer structure in the region close to the optic disc. In view of this, several vertical straight line scans were acquired nasally and temporal to the optic disc.

The retina was oriented for sectioning in the plane of the OCT scans. The fundus images exported from the OCT scanner were used to give an indication of the region that needed to be examined. Digital images of the sections were captured for correlation with OCT scans.

Histological analysis showed normal canine retinal structure in all 8 eyes. All OCT images were fairly similar in appearance and hence direct correlation was performed for only 2 eyes from 2 different dogs. Since some shrinkage of retinal tissue occurs during preparation of histological specimens, the light micrographs had to be scaled to match the dimensions of the OCT scan. In order to do this it was assumed that a red-white band observed on all scans corresponded to the RPE-choriocapillaris complex, as in human eyes. A study by Chauhan et al[30] looked at OCT scans of patients with retinitis pigmentosa which causes abnormal intra-retinal distribution of pigmented RPE cells. On OCT, these bone spicules appear as regions of high reflectivity. This suggests that melanin, a strong scatterer of light at 850nm, causes these intense reflections on OCT and that it is therefore plausible to assume that the highly reflecting band on OCT scans is caused by the melanin within the RPE cells. The retinal thickness was therefore taken to be the distance between the vitreo-retinal interface and the anterior surface of this band and the dimensions of the light micrograph were scaled accordingly.

The boundaries of the various retinal layers were marked on the light micrograph using Adobe Photoshop 5. These borders were then superimposed onto the corresponding OCT scan.

Results

Typical nasal and temporal scans acquired close to the optic disc in the canine eye are shown in Figure 3.5. The red-white band marked on both scans was visible on all the scans from all 8 eyes. Due to its location and intensity, it was assumed that this band corresponded to the RPE-choriocapillaris complex, as in human eyes. The split in this layer that is often observed in human OCT scans was not evident in any of the canine scans. In healthy human eyes, a relatively well-defined red band just beneath the vitreo-retinal interface is usually observed and this is thought to correspond to the retinal nerve fibre layer (RNFL). In some of the canine scans, such as Figure 3.5A, the reflectance of the anterior portion of the scan was relatively high, however, the posterior border of this region of higher reflectivity was not as well defined as in the human eye. In several other scans, such as Figure 3.5B, this region of increased reflectance is not apparent at all. In two of the specimens, the reflectivity of the

anterior portion of the OCT scan was observed to vary with the degree of corneal hydration, increasing in intensity as the cornea was re-hydrated. Figure 3.6 shows two images of the same region — Figure 3.6A was acquired immediately after corneal hydration and Figure 3.6B was acquired 5 minutes later with no changes to the scanning set-up. It can be seen that the reflectivity of the anterior portion of the scan was considerably more pronounced in the first case.

A

B
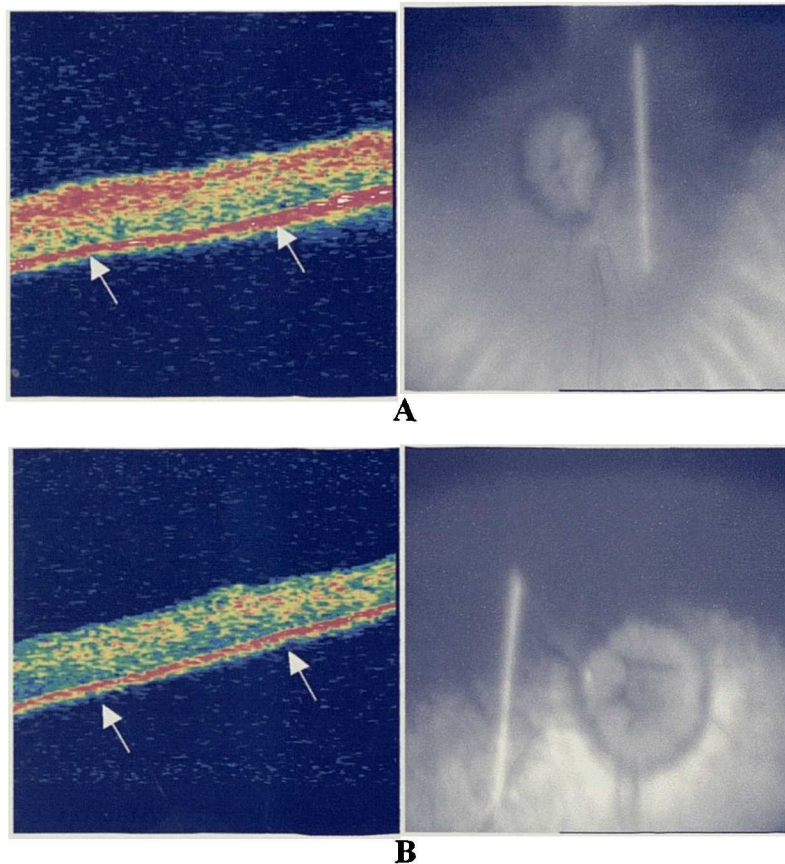
Figure 3.5   *Nasal and temporal OCT scans from two different canine eyes. (A) An anterior highly reflective band is clearly visible. (B) The highly reflective anterior band cannot be identified. The band believed to correspond to the RPE-choriocapillaris complex is marked by arrows in both cases.*

A   B
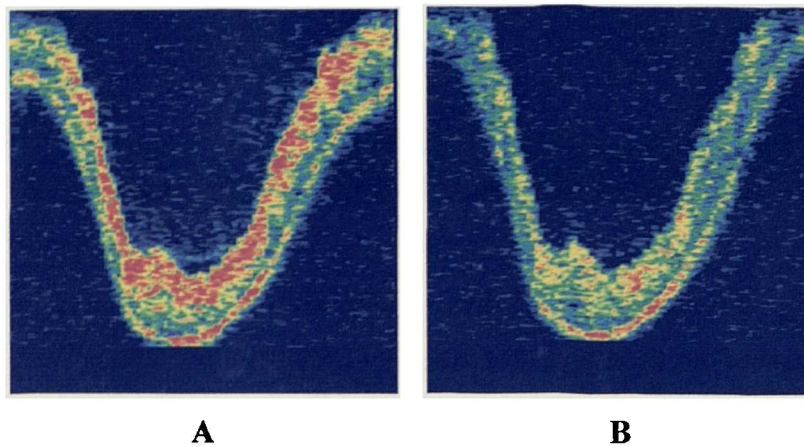
Figure 3.6   *An illustration of the effect of corneal hydration on the reflectivity of the anterior portion of the scan. (A) Scan acquired immediately after corneal hydration. (B) Scan acquired 5 minutes later.*

Histological analysis revealed normal canine retinal structure in all 8 eyes. A typical light micrograph from canine retina is shown in Figure 3.7.
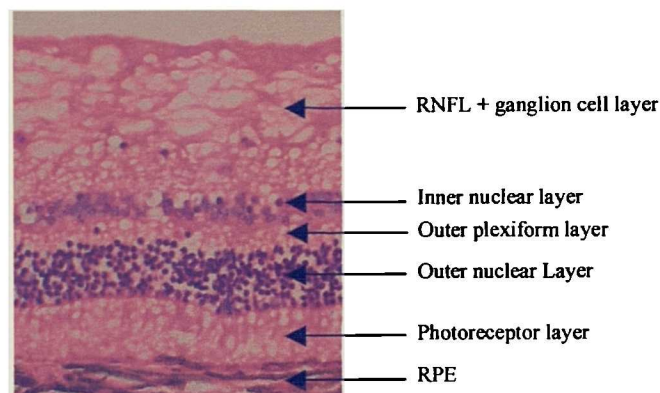
Figure 3.7   *Light micrograph of a vertical section through canine retina.*

Comparison between OCT scans and histology was carried out for the two scans shown in Figure 3.5 and the corresponding light micrographs. The results are shown in Figure 3.8.

The red anterior portion in Figure 3.8A clearly corresponds to more than just the RNFL. In this case it would appear to include at least up to the inner nuclear layer. In Figure 3.8B, the reflectance of the anterior 4 layers is very similar. In both cases, the photoreceptor layer appears darker than the layers above it, however none of the other layers could be isolated with any certainty.

RNFL + ganglion cell layer

Inner nuclear layer

Outer plexiform layer

Outer nuclear Layer

Photoreceptor layer

RPE

A

RNFL + ganglion cell layer

Inner nuclear layer

Outer plexiform layer

Outer nuclear Layer

Photoreceptor layer

RPE

B
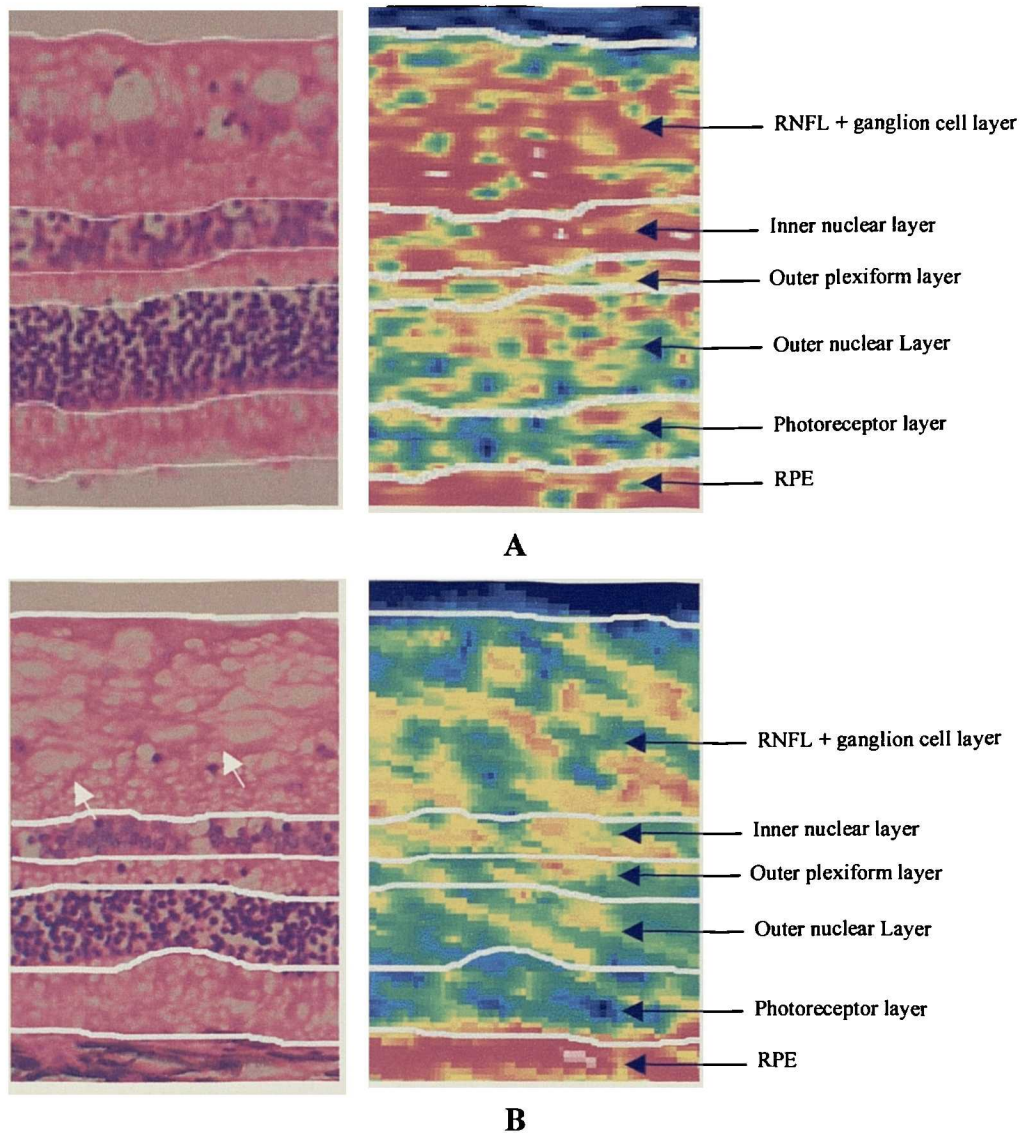
Figure 3.8 *Comparison of retinal morphology and corresponding OCT scans for the two scans shown in Figure 3.5*

Discussion

The main observation from this study is that the ability of light microscopy to differentiate between retinal layers is clearly superior to that of OCT. This is mainly due to the fact that OCT can only successfully differentiate between two adjacent structures if they have sufficiently different optical properties, whereas light microscopy depends on the different staining properties of retinal elements. Future generations of OCT scanners which use different light sources are likely to achieve greater differentiation between adjacent retinal layers.

The scans obtained from OCT were fairly consistent – all images from the 8 canine eyes were quite similar. The posterior red-white band was clearly identifiable and present on all scans. All the scans that were analysed in this study were acquired from the non-tapetal region where the RPE is pigmented. As with human retina, it seemed reasonable to assume that the high intensity reflections that form this band arose from a strong scatterer of light such as melanin. In order to scale the light micrographs to match the dimensions of the OCT scan, it was assumed that this layer corresponded to the RPE-choriocapillaris complex and, consequently, the posterior border of neurosensory retina. The reflectivity of the region anterior to this band varied considerably from eye to eye. This seemed to be partially dependent on corneal hydration and, in a few cases, was observed to increase considerably as the corneal surface was re-hydrated. Although some of the scans showed an anterior region of high reflectivity, this was not as well-defined as in human retinal scans in any of these cases. Correlation of one of these scans with a corresponding light micrograph showed that this region of high reflectance corresponded to considerably more than just the RNFL. One possible explanation for this could be differences between human and canine RNFL composition. On light micrographs, canine RNFL appears far less densely packed than human RNFL. If this is the case, it is not surprising that the reflectivity and definition of canine RNFL on OCT scans is poorer than that of human RNFL. A similar study carried out by Toth et al[31] also found considerable variation in reflectivity of the anterior portion of monkey retina and hypothesised that this could be due to variations in corneal hydration, however, this anterior portion was consistently more reflective than lower regions. In the primate study, the appearance of the retinal bands was similar to that observed in human OCT scans. This is likely to be due to the fact that the structure of monkey retina is closer to human retina than that of the dog. This study observed the properties of the anterior region of high reflectivity close to the fovea and concluded that it did indeed correspond to the RNFL. Conversely, a study by Chauhan et al[30] concluded that this signal was not RNFL-specific but was at least partially surface-related. This group based their conclusions on observations that a high reflectance anterior band persisted even when the RNFL was ablated. However, there is some difficulty in interpreting these findings and in reaching the definite conclusions that the authors of this study have come to. Firstly, this group made use of in-vitro retinal specimens and this may have affected the optical properties of the tissue and secondly, the act of

laser ablation is likely to have significantly changed the optical properties of the retinal specimens. Thus the persistence of an anterior red band may simply have been a result of laser-induced altered reflectivity. However, our own observation of the dependence of this reflectivity on corneal hydration suggest that, as Chauhan et al imply, this signal may be partially due to surface effects.

In the two scans shown in Figure 3.5 and Figure 3.8, a region of low reflectivity was observed immediately anterior to the RPE-choriocapillaris complex. Comparison with histology suggested that this corresponded to the photoreceptor layer. This dark layer was also evident on OCT scans of human retina and, as seen in Figure 3.2, increased in thickness at the fovea. It is known from human histology that, at the fovea, the inner and mid-retinal layers are displaced to leave only a layer of cones. This suggests that the dark band observed on OCT scans of both human and canine retina is likely to be the photoreceptor layer.

One of the aims of this study was to evaluate the potential of OCT in veterinary applications. OCT scans were easily obtained from whole enucleated dog eyes. Clearly, a number of modifications would be required to use OCT on animals in routine veterinary practice. Scanning times would need to be reduced to minimise motion artefacts and the fundus-viewing unit would need to be modified to accommodate the animal's head. Alternatively, a hand-held probe could be developed, as this would facilitate scanning. This pilot study has shown that the optics of the canine eye do not affect the ability of the OCT scanner to produce reproducible images of the retina. The two retinal borders are easily identifiable and retinal thickness measurements may be made in the same way as in human retina. This study has, however, also highlighted one important difficulty with imaging canine retina – the RNFL cannot be differentiated from underlying retinal layers and RNFL thickness cannot be measured from OCT scans. This implies that OCT in its present state would not be useful in the diagnosis of glaucoma in dogs.

This section has dealt with the interpretation of the OCT image. The interpretation of human retinal scans was based on textbook knowledge of retinal morphology and an appreciation of the different optical properties of retinal components. In Chapter 6, the relation between retinal layers on OCT and histological structure is investigated

further by analysing a number of clinical conditions which affect different portions of the retina. Direct correlation of canine OCT scans and corresponding light micrographs showed that the dark layer immediately anterior to the RPE-choriocapillaris complex is likely to represent the photoreceptor layer. However, no useful information on the nature of the anterior red band seen on human OCT scans could be obtained from this study. The resolution of current OCT systems is not sufficiently good to show the same amount of retinal detail as light microscopy, however, the major advantage of OCT over light microscopy is that it offers the possibility of observing retinal structure in vivo and does not suffer from artefacts caused by distortion and shrinkage. Future generations of scanners should be able to resolve retinal structures in greater detail, thus providing a unique view of in-vivo undistorted retinal histology.

3.6   Scanning the Anterior Segment

Although the OCT 2 scanner is designed for imaging the retina, images of the anterior eye can be obtained with very minor modifications to the system. In order to focus the laser beam onto the cornea for corneal scanning, patients need to be positioned slightly further away from the machine head than in the set-up for retinal imaging. This is easily achieved by attaching a small cushion to the forehead rest in order to move patients' eyes away from the machine by a few centimetres and still ensure comfortable and steady positioning of the head. Since the system has been designed to image a concave structure (the retina) and to display retinal scans as flat, it exaggerates the curvature of convex structures like the cornea so the curvature seen on corneal scans is an artefact. The lens and angle can also be imaged fairly successfully with this OCT system. Typical scans from the anterior eye are shown in Figure 3.9. The thin highly reflecting band situated anteriorly on the corneal scan is likely to correspond to the corneal endothelium and thus the region beneath it should correspond to the stroma.
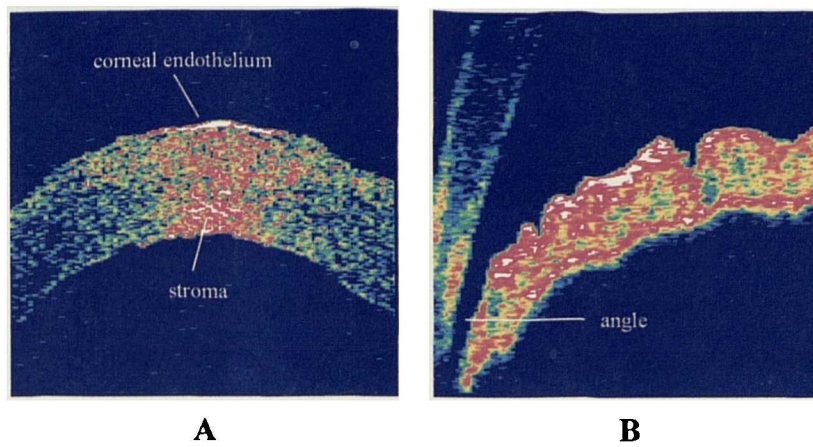
Figure 3.9   *(A) Scan through the cornea of a healthy volunteer. The distinction between the corneal epithelium and the stroma can be seen. (B) Scan showing the angle in the same volunteer.*

3.7   Image Processing

A number of options for enhancing the raw data scans are available with this system. The effect of some of these options on the same raw data scan is shown in Figure 3.10.

Normalize: This function is intended to display OCT data in a manner that is independent of noise and power settings. It is done by first finding the average noise level. Data having values less than or equal to the average noise are displayed as zero on a scale of 0-255. The maximum data value is then found and a fixed constant is subtracted. The resulting number is a "saturation" value and data values equal to or greater than this are displayed as 255. Thus the entire data range between the noise and saturation values is forced to display between 0 and 255 so the result should be independent of noise or power settings.

Align: This function attempts to correct the data for effects due to patient motion in the axial direction (Figure 3.10B). Small motions of the head towards and away from the instrument cause the data displayed during a scan to shift in the axial direction resulting in a wavy-looking scan. This function can also correct for scans in which the OCT beam is not perpendicular to the retina along its entire length. This leads to

a scan that is at an angle rather than horizontal. Each of the 100 longitudinal scans is aligned relative to its neighbour, based on the assumption that the RPE-choriocapillaris layer should be horizontal. This function, however, has no way of distinguishing between true retinal height changes and motion artefacts so in situations where the retina is raised because of, for example, a choroidal lesion, using the alignment option will result in an erroneous image of a flat retina.

Align & Normalize: Performs both the above functions together.

Gaussian Smoothing: This is used to average out noise. It enhances larger scale features but may cause smaller details to be lost. Gaussian smoothing works by performing a moving average of data points in a 3 × 3 region. The points are weighted according to a Gaussian function $e^{-k(x-x_0)^2}$, such that the outer points in the region are weighted less than the centre point (Figure 3.10C).

Median Smoothing: This is similar to Gaussian smoothing except that it is the median value of the 3 × 3 neighbourhood that is used not the weighted average. The advantage of this is that it effectively removes noise while still preserving small details in the data (Figure 3.10D).
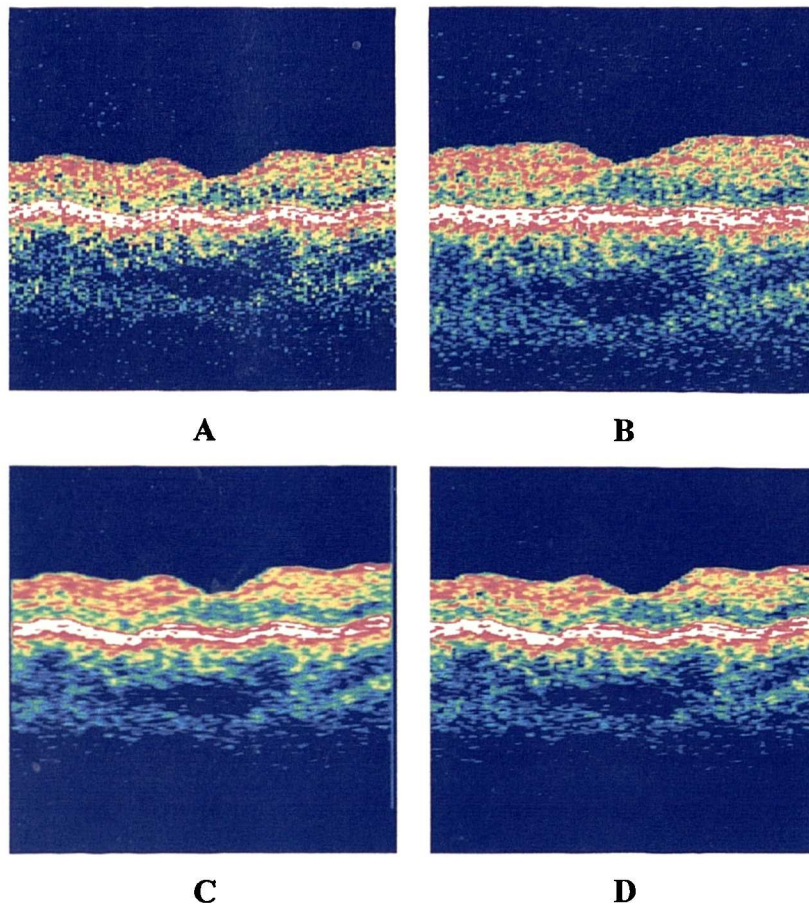
Figure 3.10   *The effect of various image-processing options on the same scan. (A) Raw data scan; (B) Align option which gets rid of the motion artefacts seen on the raw image; (C) Gaussian Smoothing: Enhances larger scale features – retinal bands are more defined; (D) Median Smoothing: Smaller features are preserved better than with Gaussian smoothing.*

3.8   Printing Results

The printing option provided with this system produces a report sheet which contains a single OCT scan, displayed both in raw data form and after image processing, the corresponding fundus picture and information about the patient and about the nature of the scan. A typical report sheet is shown in Figure 3.11.

Gaussian Smoothing

Gaussian Smoothing

Fundus Video

Raw Scan Data

Personal

Name
Birth Date

Scan
Scan Type   LineGroup
Scan Date   2-8-2000
Scan Length   4.20 mm

Eye Information
Eye   OS
Eye Length   24.46 mm
Refraction   0.00 D

ZEISS Humphrey
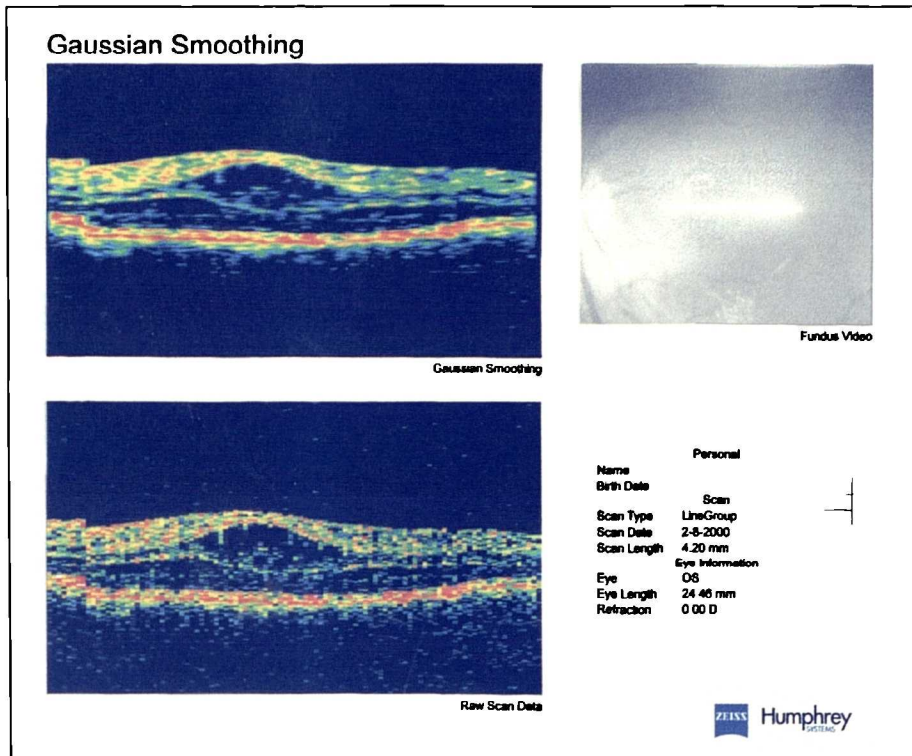
Figure 3.11   *Default OCT report sheet for a patient with macular oedema. Gaussian smoothing has been applied to the raw image.*

3.9   Image Analysis

This software provided with the OCT scanner has four image analysis options:

Retinal Thickness Tool: The retinal thickness is taken to be the distance between the vitreo-retinal interface and the anterior surface of the RPE-choriocapillaris. After aligning and smoothing the A-scans, these boundaries are detected by looking for the locations within each A-scan that have the greatest rate of change in the data. The retinal thickness measured from any individual A-scan may also be displayed. This option will work on any straight line or circular scan, provided that it does not pass through the optic nerve head (Figure 3.12).
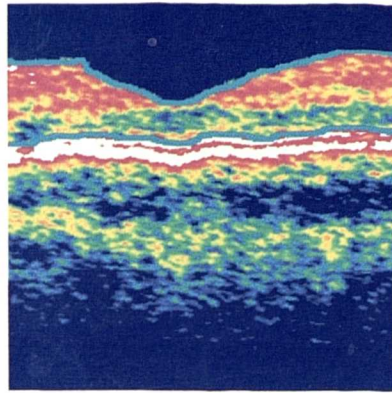
Figure 3.12   *The Retinal Thickness tool applied to a scan through the macula. The algorithm identifies the vitreo-retinal interface and the anterior surface of the RPE-choriocapillaris complex and measures the distance between them at all points along the scan.*

Retinal Map: This option is designed to function with the *Radial Lines* scanning option. The retinal thickness is computed for each of the 100 A-scans within each of the 6 radial line scans. This data is then used to construct a map of retinal thickness within the circular area spanned by the six line scans. Results are displayed graphically, as a colour-coded map divided into sectors where hotter colours indicate greater thickness, as well as numerically, where the average thickness for each sector is displayed. The centre value and associated error, found from the average and standard deviation of the six retinal thickness values at the crossing point of the six scans, is also displayed (Figure 3.13).

RNFL Thickness Tool: Identifying the posterior border of the RNFL is more challenging than identifying the interface between the neurosensory retina and the RPE. The RNFL is generally more reflective than the layers directly beneath it, but the border is often not sharply defined. Instead of using edge-detection algorithms, a threshold is defined for each A-scan, based on the maximum data value in that A-scan. Then, moving anteriorly from the dark band just above the RPE-choriocapillaris layer, the posterior border of the RNFL is defined as the point at which data values begin to exceed the threshold. This option is designed for use with circular scans around the optic nerve head, so data is displayed graphically as a plot of RNFL thickness against position, as averages over four sectors and as averages over clock hours. The *RNFL Thickness* measurement tool may also be used on

straight line scans, however the sector and clock hour averages which will be displayed will represent average RNFL thickness along a section of the line scan (Figure 3.14).

Normal

Diabetic macular oedema
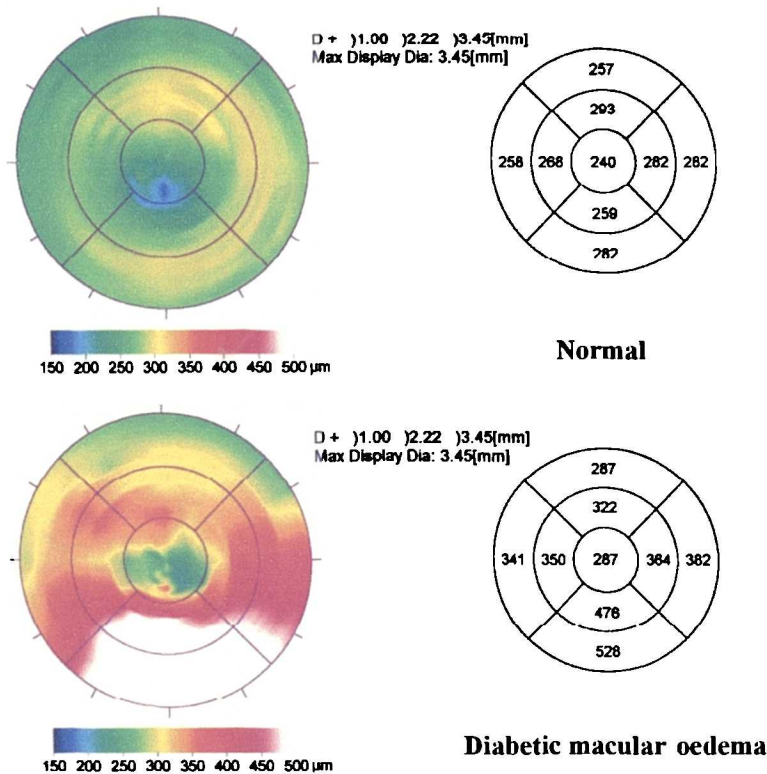
Figure 3.13   *Examples of macular maps in a normal volunteer (top) and in a patient with an abnormally thickened retina a result of diabetic macular oedema (bottom).*

Scan Profile: This displays the data from each individual A-scan graphically as a plot of intensity against position. Cursors may be placed at any point along the graph and the software will calculate the distance between them. When scanning retinal tissue, or anything with a similar refractive index, each pixel in the A-scan corresponds to 4μm. The OCT software automatically assumes the refractive index of retinal tissue so if anything with a different refractive index is scanned, the thickness displayed by the OCT software must be corrected for the different refractive index (Figure 3.15).
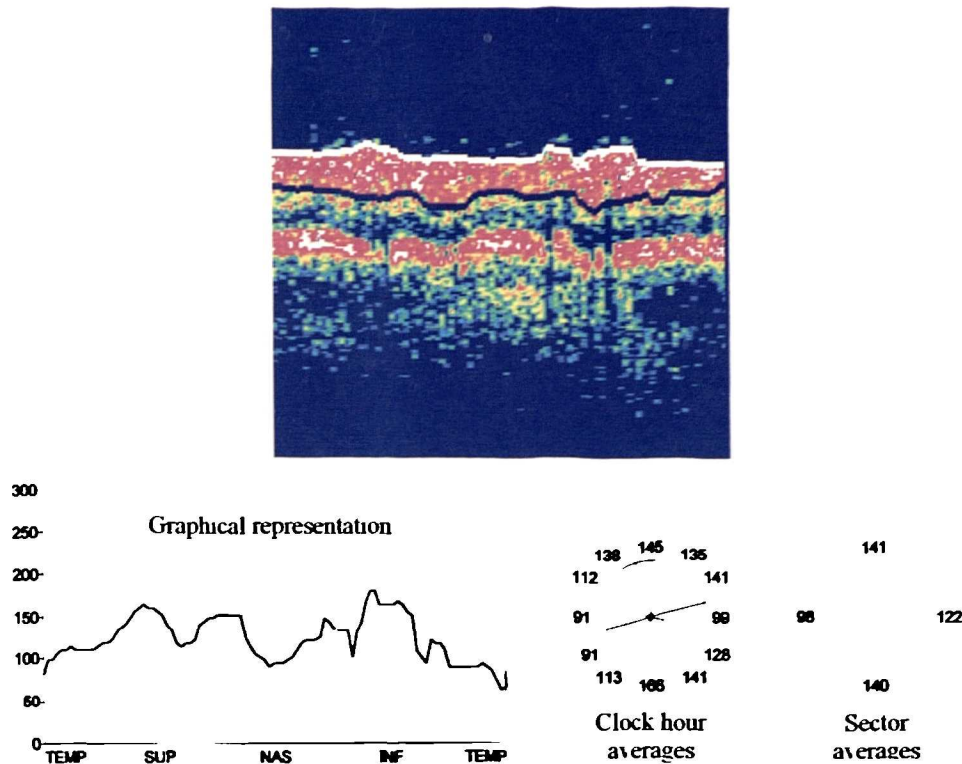
Figure 3.14   *The* RNFL thickness *tool applied to a scan around the optic disc. The algorithm attempts to identify the two borders of the RNFL and displays thicknesses graphically and numerically as averages per quadrant and over every clock hour*

3.10   Exporting Data

Processed OCT images and the associated fundus images may be exported as bitmap files. This gives users the option of designing their own reporting formats. The raw data may also be exported. This is saved in a file with extension *.raw* which essentially consists of 50,000 data points (500 points per A-scan and 100 A-scans per B-Scan). This gives users the flexibility to write their own software for performing image processing and analysis. Chapter 5 describes some software written specifically to work with exported OCT data.
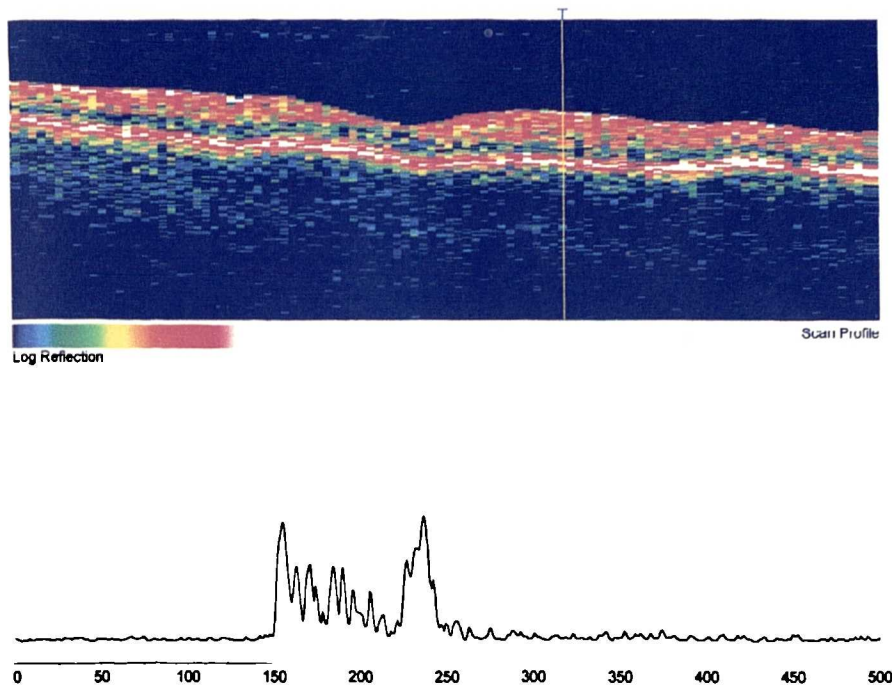
Figure 3.15   *Illustration of the* Scan Profile *feature for displaying raw reflectance data. The data from the A-scan at the position marked by the yellow line on the OCT scan is shown in the bottom half of the figure.*

3.11   Factors affecting the quality of OCT scans

3.11.1 Focussing

For optimum scanning, the focussing control on the viewing unit should be adjusted until a sharp image of the fundus is obtained on the fundus monitor. However, the focussing setting also affects the quality of the OCT scan. Changing the focussing setting by even slight amounts that do not affect the sharpness of the fundus image, can dramatically alter the appearance of the OCT scan. In practice, the focussing control is generally first adjusted to give a sharp image of the fundus and then fine-tuned to give the best quality OCT scan. Non-optimal focussing could result in poorer quality scans and, consequently, poorer performance from the thickness measuring algorithms. A study was therefore carried out to assess how different

focussing settings affect the quality of the OCT scan and the ability of the *Retinal Thickness* and *RNFL Thickness* algorithms to correctly identify the retinal layers.

Methods

Scans for this study were acquired from the macula and from around the optic disc of a healthy volunteer who gave his full consent for participation in the study. It was decided to use scans from a volunteer rather than from a test object since one of the aims of the study was to assess the performance of the *Retinal Thickness* and *RNFL Thickness* algorithms, which will only work on scans of retinal tissue. The drawback of this approach is that it is likely that there was a small degree of eye movement from one scan to the next.

The focussing control was initially set to give the best quality scan, centred on fixation, from the macula of the volunteer. Line scanning was used and the scan length was arbitrarily set at 2.5mm. A number of repeat scans were then acquired with different focussing settings. There is no numerical read-out to indicate the focussing setting and the focussing was therefore varied in roughly equal steps until no returning OCT signal could be recorded. A total of 6 straight-line scans (one optimal, and 5 non-optimal) with different focussing settings were acquired from the macula of the volunteer. The quality of the scans was assessed subjectively and the performance of the *Retinal Thickness* tool was assessed by running the algorithm for each of the 6 non-optimal scans and comparing the results graphically with those from the optimal scan.

The above procedure was then repeated with a series of circular scans centred on the optic nerve head in order to assess the performance of the *RNFL Thickness* tool. A total of 4 scans (one optimal, 3 non-optimal) were acquired in this part of the study.

Results

Macular straight-line scans: Figure 3.16 shows the effect of varying the focussing setting from its optimum position to a position where the returning OCT signal was very weak. The vitreo-retinal interface could only be reliably identified for the

optimal case and partially for settings 1 and 2. The intensity of the RPE-choriocapillaris layer was progressively reduced.
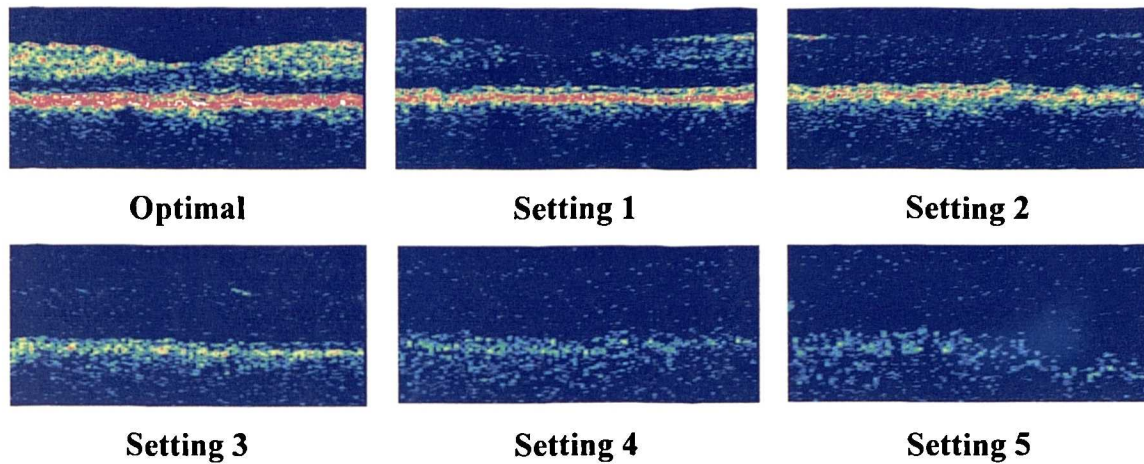
Figure 3.16 *Illustration of the effects of varying the focussing setting. Scans acquired from the same region of the macula of a normal volunteer showing the variation in the quality of the scans due to different focussing settings.*

The *Retinal Thickness* tool functioned only for the optimal case and for settings 1, 2 and 3. The retinal thickness was plotted graphically for each of these cases. No retinal thickness values were given by the algorithm for the scans with settings 4 and 5. Figure 3.17 shows the plotted retinal thickness for the first four cases.

As can be seen from this graph, the agreement between the retinal thickness from the optimal scan and the non-optimal ones became progressively worse. The retinal thickness measured from the scan with setting 1 agreed reasonably well with the optimal one until around A-Scan number 70, after which it under-estimated the retinal thickness. If it is assumed that the measurements made from the optimal scan are accurate, then those made from the scans with settings 2 and 3 were clearly inaccurate.
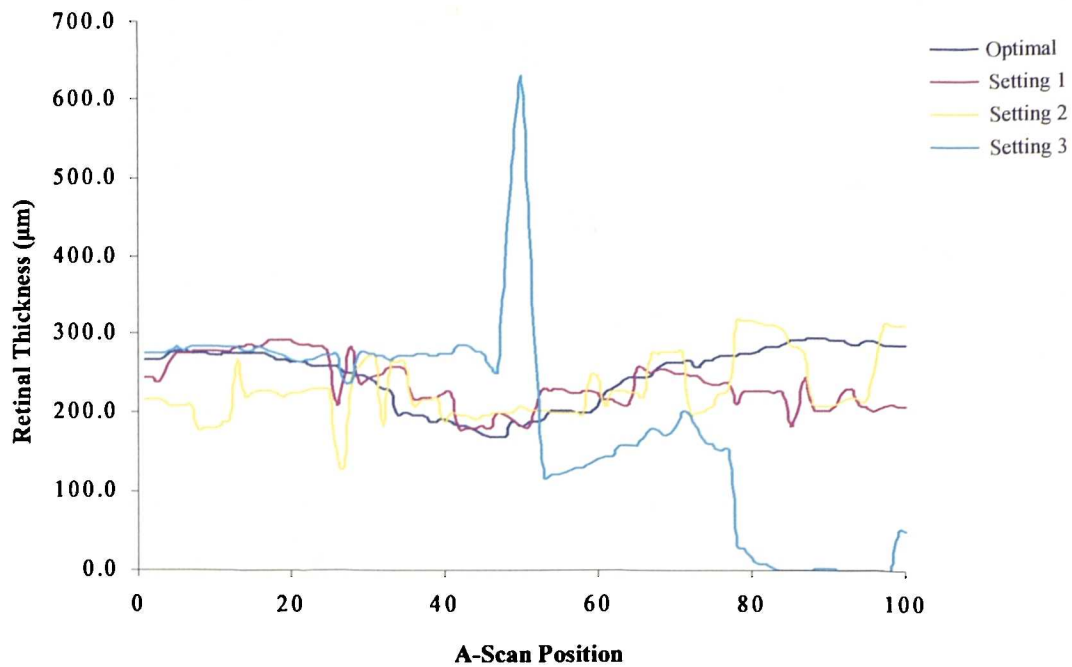
Figure 3.17   *Plot of retinal thickness, as measured by the* Retinal Thickness tool, *for the scan with optimal focussing setting and those with settings 1, 2 and 3.*

Circular scans around the optic nerve head: Figure 3.18 shows the effect of varying the focussing setting on the circular scans. The red band corresponding to the retinal nerve fibre layer was well-defined only in the optimal case.
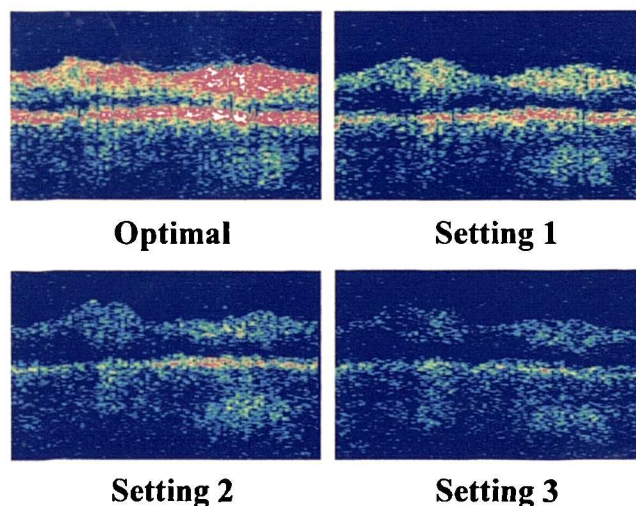
Figure 3.18   *Circular scans acquired from around the optic nerve head of a normal volunteer showing the variation in the quality of the scans due to different focussing settings.*

The RNFL thickness measured from each of these scans using the *RNFL Thickness* tool is shown in Figure 3.19. The RNFL thickness measured from the scan with setting 2 agreed reasonably well with that from the optimal scan until around scan 45. After this point it under-estimated the RNFL thickness. If it is assumed that the measurements made from the optimal scan are accurate, then those made from the scans with settings 2 and 3 were clearly inaccurate.
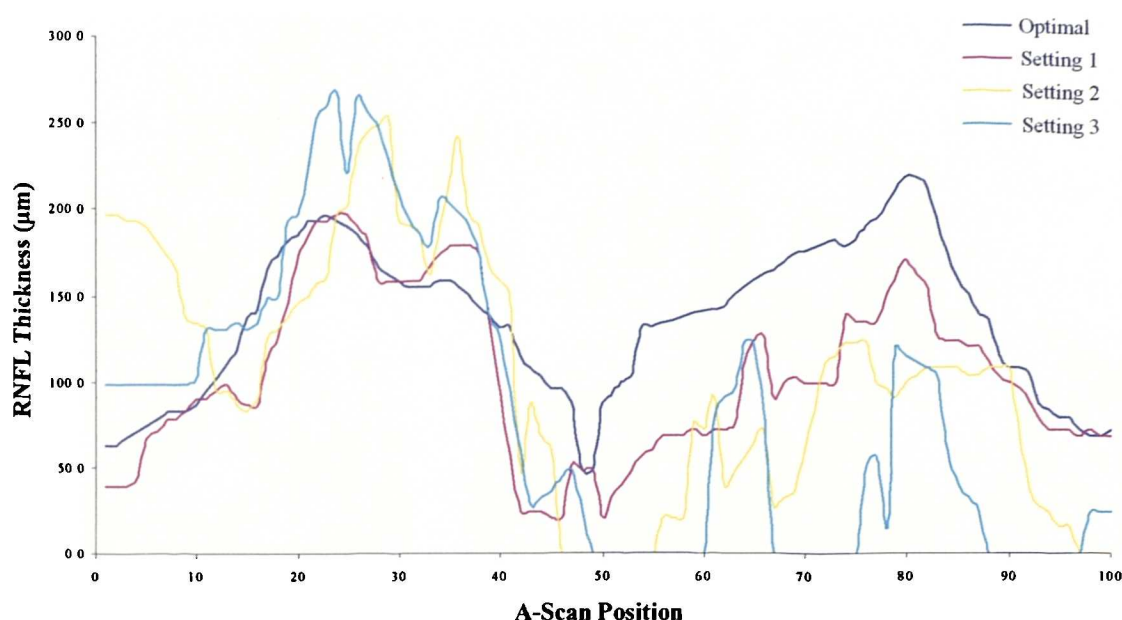
Figure 3.19 *Plot of RNFL thickness, as measured by* RNFL Thickness *tool, for the scan with optimal focussing setting and those with settings 1, 2 and 3.*

Discussion

The aim of the study described above was to investigate the effects of non-optimal focussing settings on the quality of OCT scans and on the correctness of measurements made from non-optimal scans. Scans from the macula and centred on the optic disc of a normal volunteer showed that, as the focussing control was varied from its optimal position, the quality of the scans varied quite dramatically. Both the vitreo-retinal interface and the band corresponding to the retinal nerve fibre layer lost definition. This caused the *Retinal Thickness* and *RNFL Thickness* tools to

misidentify the appropriate retinal layers, thus leading to erroneous measurements. One shortcoming of the study was that although every effort was made to ensure that the scans were acquired from the same area and were identical in every way apart from focussing setting, the possibility of slight movement between successive scans could not be ruled out. Thus, some of the variation between scans would have been due to small eye movements. However, as shown in the following chapter, the repeatability of retinal thickness measurements is very high. Thus, it is reasonable to assume that most of the variations in retinal thickness measurements from scans with non-optimal focussing settings were due to incorrect identification of the retinal boundaries. The repeatability of RNFL measurements is not as good as that of total retinal thickness. This is because the posterior border of the RNFL layer is more difficult to identify even on optimised scans. It is therefore not surprising that variations in the focussing settings had such a dramatic effect on RNFL thickness measurements.

This study has therefore highlighted the importance of adjusting the focussing control correctly. Unfortunately, in the present system, there is no numerical read-out to indicate the focussing setting. It is therefore down to the judgement and experience of the operator to decide on the optimal setting.

3.11.2 Polarisation

The polarisation adjustment is intended to optimise the OCT signal strength by matching the polarisation of the light reflected from the retina. In practice, adjusting the polarisation control slightly changes the intensity of the OCT signal and it is up to the operator to decide on the optimal setting. There is no numerical read-out for polarisation, thus when acquiring repeat scans it is not possible to be certain that the polarisation setting is identical to that of the original scan. In view of this it was considered necessary to investigate the effects of varying the polarisation on both the quality of the scan as well as on the performance of the *Retinal Thickness* and *RNFL Thickness* algorithms.

Methods

The design of this experiment is similar to that described in Section 3.11.1 above. Scans were acquired from the same volunteer. The system was initially set to acquire straight line scans of length 2.5mm centred on fixation. The polarisation control was adjusted to the optimal setting, as judged by the operator. A series of scans in the same position but with different polarisation settings were then acquired. A total of 6 scans (1 optimal, 5 non-optimal) were acquired for this part of the study. The *Retinal Thickness* tool was applied to each of these scans in order to investigate the performance of this algorithm in each situation.

The procedure was then repeated with circular scans centred on the optic nerve head. A total of 4 scans (1 optimal, 3 non-optimal) were acquired for this part of the study. The *RNFL Thickness* tool was applied to each of these scans in order to investigate the performance of this algorithm in each situation.

The quality of the scans was assessed subjectively and the performance of the two measuring algorithms was analysed graphically.

Results

Macular straight-line scans: Figure 3.20 shows the scans acquired with different polarisation settings. Inspection of the scans showed that, while there was clearly some reduction in intensity due to the change in polarisation, the vitreo-retinal interface and the RPE-choriocapillaris layer could easily be manually identified in all 6 scans.

Although the anterior retinal border can easily be identified manually in all the scans shown above, the ability of the *Retinal Thickness* tool to correctly identify this border appears to be have been affected by the different polarisation settings. As can be seen from Figure 3.21, the agreement between the measurements from the optimal scan and the scans at settings 1 and 2 was very close, however the agreement of the measurements from the scans with settings 3, 4 and 5 was poorer, especially in the region of the fovea.
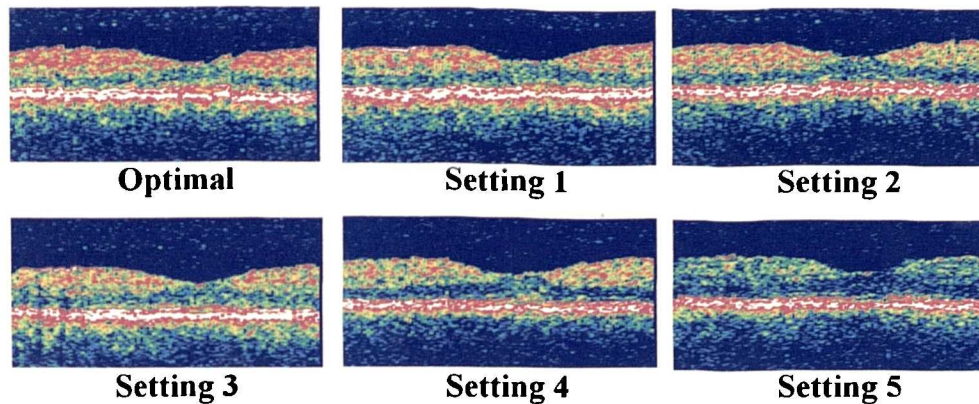
Figure 3.20   *Scans acquired from the same region of the macula of a normal volunteer showing the variation in the quality of the scans due to different polarisation settings.*
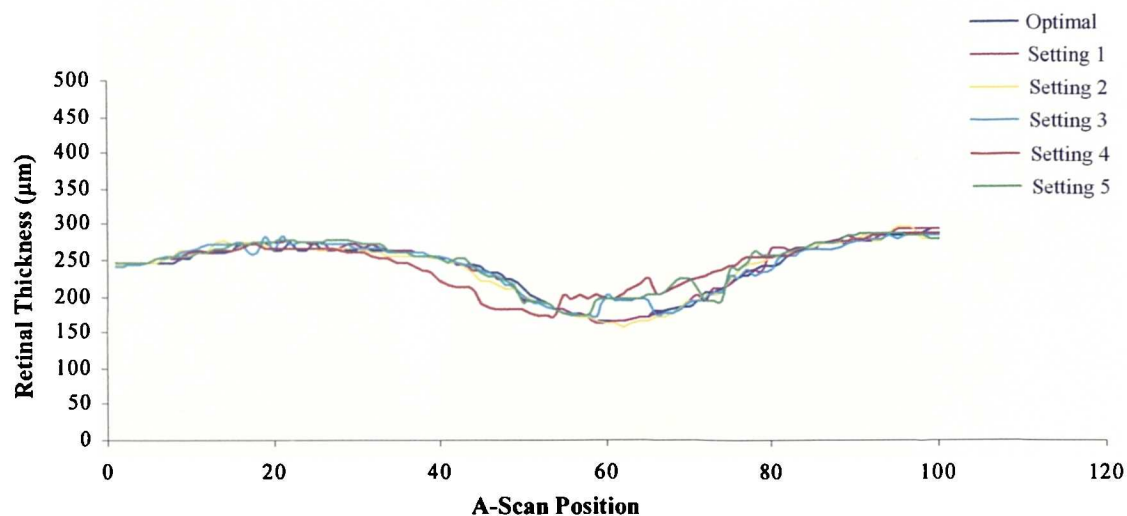
Figure 3.21   *Plot of retinal thickness, as measured by the* Retinal Thickness *tool, for the scan with optimal polarisation setting and those with settings 1, 2, 3, 4 and 5.*

Circular scans around the optic nerve head: Figure 3.22 shows the circular scans acquired with different polarisation settings. Inspection of these scans showed that the intensity of the red band corresponding to the RNFL decreased progressively, especially in the nasal and inferior portions. This was also evident from the plot of RNFL thickness measurements (Figure 3.23) where there was poor agreement on nasal and inferior RNFL thickness between the 4 scans.
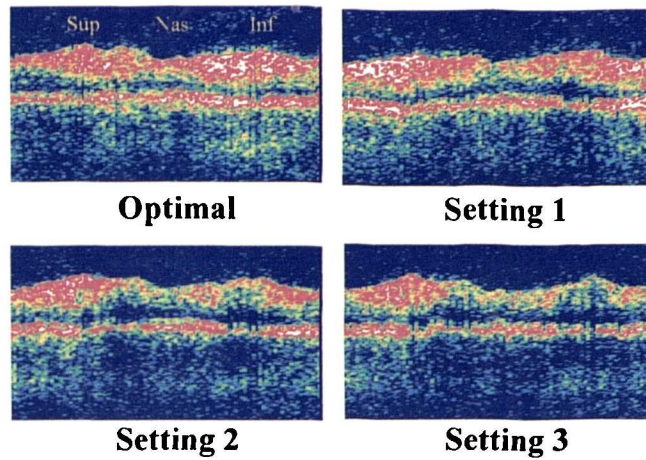
Figure 3.22   *Circular scans acquired from around the optic nerve head of a normal volunteer showing the variation in the quality of the scans due to different polarisation settings.*
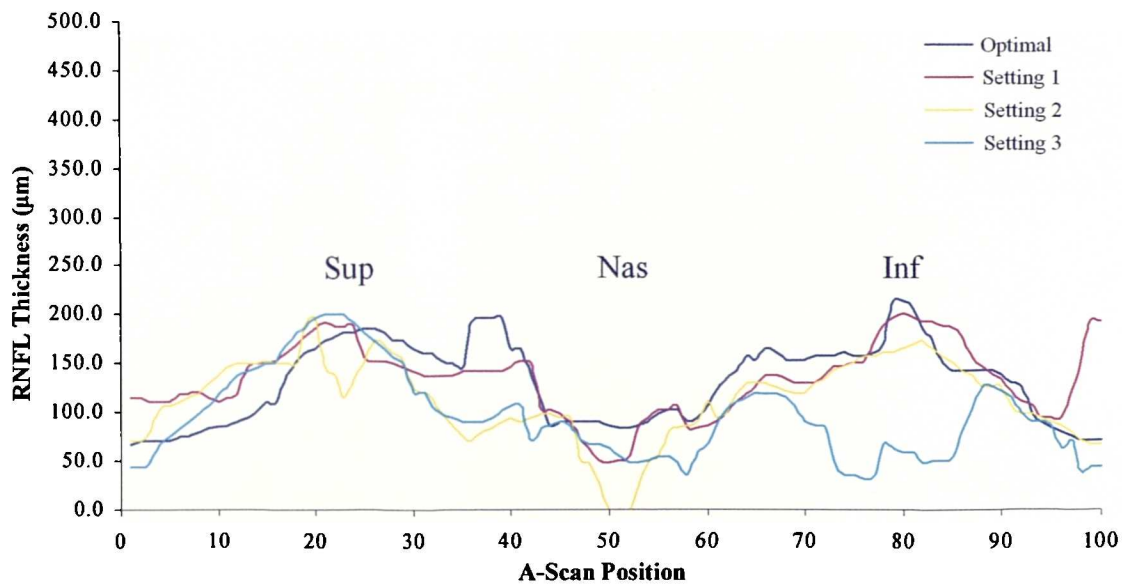
Figure 3.23   *Plot of RNFL thickness, as measured by* RNFL Thickness *tool, for the scan with optimal polarisation setting and those with settings 1, 2 and 3.*

Discussion

Although varying the polarisation setting certainly seemed to have caused some reduction in intensity of the scans, these effects were far less marked than those caused by non-optimal focussing settings. This indicates that the quality of the scan is less critically dependent on the polarisation than on the focussing.

RNFL thickness measurements were more severely affected by changes in the polarisation than retinal thickness measurements. As will be shown in Chapter 4, the repeatability of RNFL thickness measurements is poorer than that of total retinal thickness measurements, even with optimal polarisation and focussing settings. One possible explanation for this is that the intensity of this layer could be susceptible to small, undetectable eye movements. Thus the discrepancies in the measurements shown in Figure 3.23 are likely to have been due to a combination of errors arising from different polarisation settings and eye movement from one scan to the next.

This study has shown that although the polarisation setting is not as critical as the focussing, it is desirable to adjust the polarisation until the strongest OCT signal is recorded. This is especially important when acquiring scans that will be used for RNFL thickness measurements. As with the focussing setting, there is no numerical read-out, thus the decision on the optimal polarisation is largely down to the judgement and experience of the operator.

3.11.3 Noise Level

The noise threshold level of the OCT scanner may be set by the user. This threshold represents the lowest signal level that will be considered noise. Increasing this level converts more of the blue signal in the OCT scan to black. Arbitrary noise units are used by the OCT system. The default noise level is 0.10 units and noise settings can be varied from 0.02 to 5.00 units. A study was carried to assess how variations in the noise settings affected thickness measurements made from the scan and intensity values in the raw data.

Methods

Scans across a microscope slide were acquired for this study. It was decided to acquire scans from a test object, the microscope slide in this case, rather than from a human volunteer in order to avoid complications such as patient movement. Scans were acquired repeatedly with different noise settings. No other scan parameter apart from the noise level was varied between scans.

Thickness measurements were made from each of the scans acquired in order to assess whether thickness measurements were related to the noise level selected. Scans of the slide showed two highly reflecting signals corresponding to the front and back surfaces of the slide. The individual A-Scans that made up each of the B-scans showed two peaks corresponding to these two surfaces. For each scan, three thickness measurements were made directly from the three central A-Scans at locations 49-51. Graphs of the average thickness at this location against noise levels were plotted.

In order to investigate how different noise levels influenced the raw intensity values, an average noise value was calculated for each of the scans in the study. It was assumed that the first and last 50 pixels in each A-Scan in the image contained only background noise, since signals corresponding to the front and back surface of the slide were situated more centrally in the scan. An average noise value was calculated for each A-Scan within an image and these 100 values were then averaged to give a single noise value per B-Scan. These values were then plotted against the set noise level in order to investigate the relationship between noise setting and average noise intensity value.

Results

Relationship between thickness measurements and noise settings: Table 3.1 shows the relative average thickness of the slide measured from the 3 central A-Scans for different noise settings. Measurements are displayed in terms of the displacement distance of the interferometer mirror and are therefore not absolute thickness values. These values could be converted to absolute thickness values provided the refractive

index of the glass slide is known, however, for the purposes of this study, knowledge of the relative thickness was adequate.

Noise Level	Relative Thickness
0.00	283
0.06	280
0.12	283
0.18	282
0.24	282
0.31	280
0.37	281
0.43	283
0.53	279
0.57	281
0.63	280
0.67	278
0.71	279
0.76	279
0.82	279
0.88	280
0.92	280
0.98	279

Table 3.1 *Measured relative slide thickness from scans acquired with different noise level settings*

The relative thickness values ranged from 278 to 283 units (average: 280 units; SD: 1.6 units). The correlation coefficient was –0.70, which indicated poor correlation between noise level setting and measured relative thickness. The poor correlation was also evident when the data in Table 3.1 was plotted as shown in Figure 3.24.
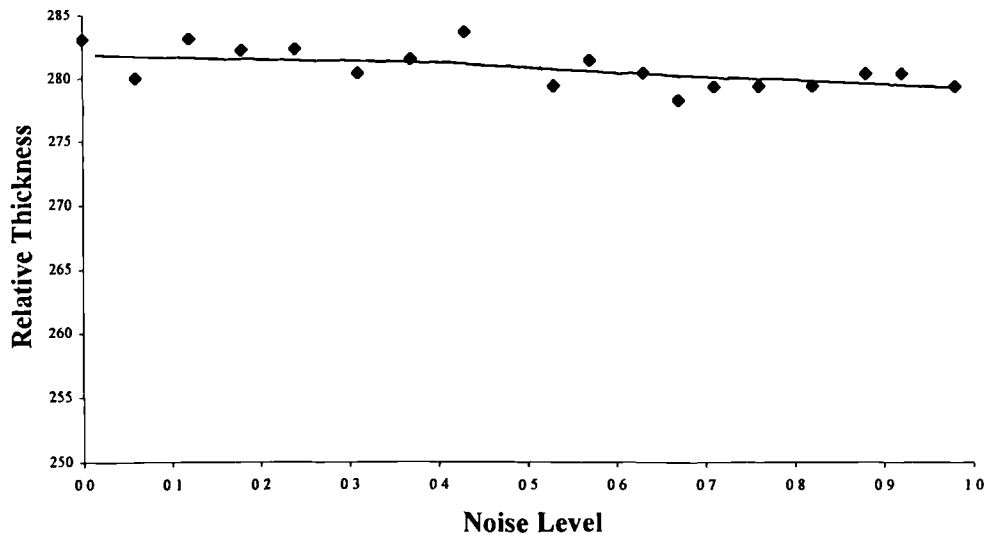
Figure 3.24 *Graph of noise level against measured relative thickness.*

Relationship between raw intensity data and noise level setting: Table 3.2 shows the average noise value calculated from the raw data as described above for scans acquired with different noise level settings. Data is shown only for scans with a noise setting of up to 0.57. For higher noise settings, the value of the noise pixels was automatically set to 0.

Noise Level	Average Noise
0.00	479
0.06	432
0.12	384
0.18	336
0.24	289
0.31	226
0.37	178
0.43	131
0.53	51
0.57	19

Table 3.2 *Average noise value for scans with different noise level settings*

This data is shown graphically in Figure 3.25 and a straight line was fitted to the data points. The relationship between noise level setting and average noise was clearly linear. The fitted line has equation $y = -813.3x + 418.25$ and R^2 of 0.9998.
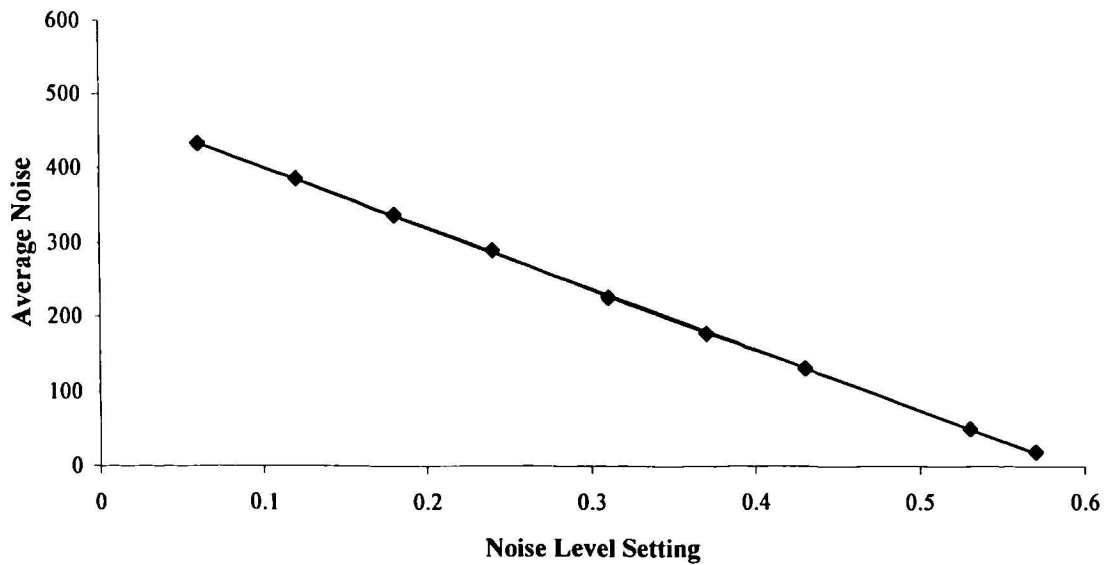
Figure 3.25   *Graph of average noise value against noise level setting.*

Figure 3.26 shows plots of the central A-Scan from each of the scans listed in Table 3.2. It can be seen from this graph that altering the noise level setting shifted the plot downwards.
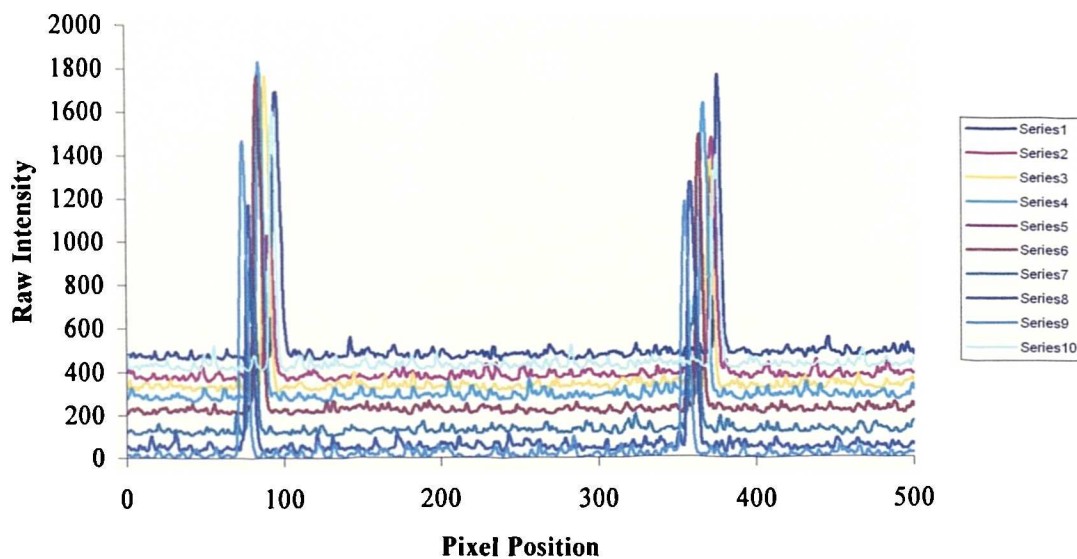
Figure 3.26   *Central A-Scan plots from scans with different noise settings (Series 1 had noise setting 0.00, Series 10 had noise setting 0.57).*

Since the intensity values in the raw data files are dependent on the noise level settings, it is essential to correct for variations in noise level settings between scans

before comparing intensity values. This may be easily done by using the equation of the straight line fitted to the data in Figure 3.25. The default noise level setting is 0.10 and this was therefore chosen as the reference noise level. Intensity values *in* scans acquired at different noise settings were converted to their equivalent reference value using the following equation derived from the straight line fit:

$$I_{0.1} = I_N - 813.3(0.10 - N)$$

(3.1)

Where $I_{0.1}$ is the equivalent intensity value with noise setting 0.10

I_N is the known intensity value with noise setting N

N is the noise setting

This equation was used to correct the intensity values in the A-Scans shown in Figure 3.26. The corrected data was then re-plotted as shown in Figure 3.27. The corrections ensured that the baseline line noise intensity values were the same regardless of the initial noise setting.
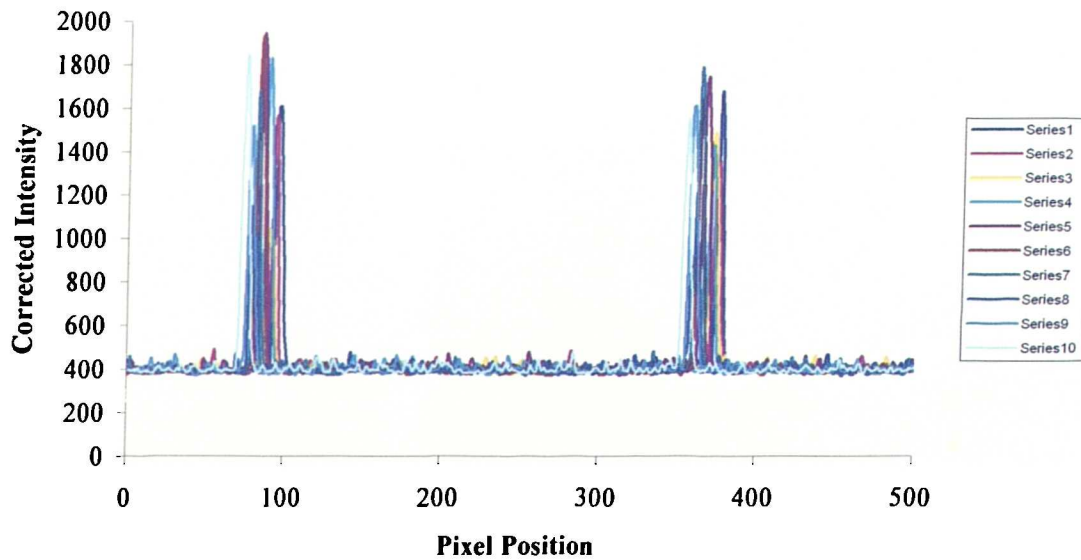
Figure 3.27   *Graph of central A-Scans after intensity corrections to correct for different noise levels had been applied.*

Discussion

The noise level in a particular scan may be adjusted by the user while scanning. Provided that the selected noise level is not high enough for signals from the actual tissue under investigation to fall beneath the noise threshold, altering the noise level does not appear to have any effect on thickness measurements made from the scans. Thus measurements from different scans may be compared without taking any differences in noise levels into account.

However the raw intensity values are dependent on the noise setting. This study has shown that the intensity values in the raw data file varied linearly with the selected noise settings. Thus, when comparing intensity values between different scans, the selected noise level must be taken into account. Scans acquired with different noise settings may be standardised to a reference noise settings by applying a simple equation to the raw data.

3.11.4 Age

The reflective properties of the retina may vary with age and since OCT is an optical technique, these changes may affect the quality of the OCT scans. A study was therefore carried out to assess whether the quality of OCT scans is related to age.

Methods

The study was carried out on a cohort of 77 subjects ranging in age from 16 years to 85 years (average: 52.5 years, standard deviation: 18.7 years). The inclusion criteria were the absence of any known ocular problems, and clear media. Subjects were excluded from the study if a clear view of the fundus could not be obtained with the OCT viewing unit or if their scans showed abnormalities in retinal or pre-retinal structure. One eye was chosen at random from each subject. In the selected eye, a scan of length 2.5mm centred on the fovea was acquired for each subject. It was decided to analyse scans through the fovea since the fovea provides an anatomical landmark. This made it easier to ensure that scans were acquired from the same location in all subjects. The 77 subjects described above satisfying the inclusion

criteria gave their consent for participation after the nature and intent of the study had been fully explained to them.

Each scan consisted of 50,000 pixels, each with a particular intensity value. Poor quality OCT images result when the intensity of the reflected OCT beam returning to the detector is reduced. Thus, in order to assess and compare the quality of the OCT scans in this study, the average intensity for each scan was calculated by finding the average of each of the 50,000 intensity values across the scan. Intensity values were corrected for any variations in noise level settings as explained in the previous section.

Results

Figure 3.28 shows a graph of age against corrected average intensity. The corrected average intensity was found to range from 420 to 537 units (average 471.1 units, standard deviation: 27.1 units). The correlation coefficient was found to be –0.25 indicating that there was no correlation between average intensity within the OCT scan and age.
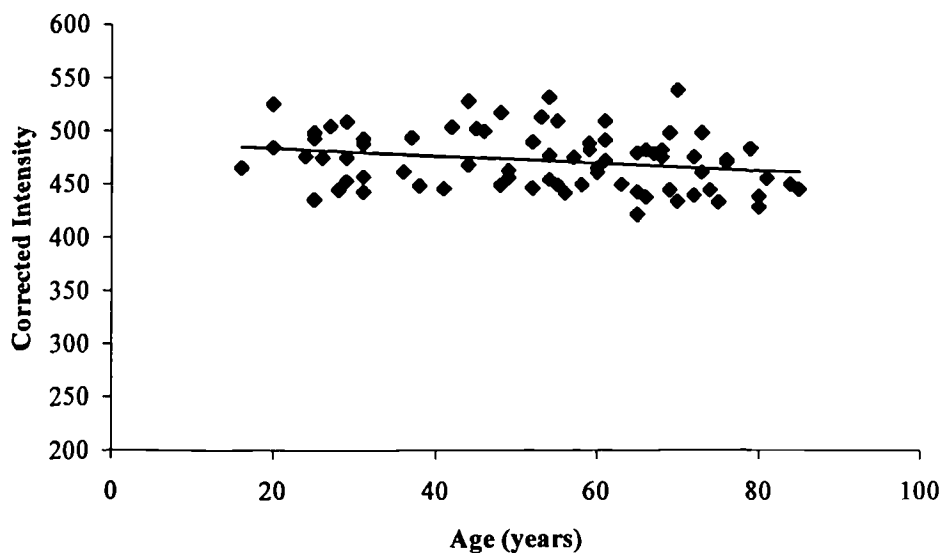
Figure 3.28   *Graph of age against corrected average intensity showing no correlation between the two*

Discussion

This study compared the average intensity of OCT scans acquired from the same location in a cohort of normal subjects of a range of ages. No correlation was found between age and average intensity. Thus, it can be concluded that, in healthy eyes with clear media, the quality of the OCT scan is not dependent on the age of the subject.

3.11.5 Clarity of Media

Cataracts or abnormalities within the vitreous, such as a vitreous haemorrhage, could limit both the intensity of the beam reaching the retina as well as the intensity of the returning reflection. This would degrade the quality of the OCT image. A study was carried out to quantitatively investigate the reduction in average intensity of retinal scans in a group of patients with cataracts. Average intensity values of scans from these patients were compared with those from the volunteers with clear media described in Section 3.11.4.

Methods

Patients with a mature cataract but no known retinal problems in the eye with the cataract were selected for this study. All of these patients had been scheduled for cataract surgery at the time of scanning. Patients were only selected if they could see the internal fixation light, positioned centrally, with the eye affected by the cataract. Ten patients who satisfied these inclusion criteria were selected for the study. In cases where both eyes satisfied the inclusion criteria, one eye was randomly selected for the study. Seven patients were female and 3 were male, with ages ranging from 65 to 81 years (average: 73.6 years, standard deviation: 5.9 years). All patients gave their consent for participation after the nature and intent of the study had been fully explained to them.

The same scanning protocol adopted in the study described in Section 3.11.4 was selected in order to facilitate comparison between the two groups. In all cases the fundus image viewed on the fundus monitor was of very poor quality because of the

cataract. However, all patients could see the internal fixation light when this was positioned centrally. Thus, patients were asked to keep their eye fixed on this light and scans were centred on the fixation light, which could be seen on the monitor. Scans were analysed as described in Section 3.11.4 in order to acquire a corrected value for average scan intensity for each patient.

Results

The average intensity values ranged from 404 to 437 units (average: 419.8 units; standard deviation: 10.4 units). Wilcoxon analysis (5% level of significance) showed that the average intensity of scans from patients with cataracts was significantly lower than that in patients with clear media.

Discussion

OCT scanning of patients with cataracts or other conditions which affect the clarity of the media presents two major problems. The image of the fundus is usually very poor, making positioning of the scan difficult and, in addition, the quality of the scan is degraded because the light from the OCT scanner is absorbed or diffracted on its way in and out of the eye. This study has shown that the average intensity of scans acquired from eyes with cataracts is significantly lower than that of scans acquired from eyes with clear media and has therefore highlighted one of the limitations of the current OCT scanner.

3.11.6 Other Factors

Other factors that could influence the quality of the OCT scans include the pupil size, ptosis, excessive blinking and inability of the patient to fixate.

When using the OCT 2 scanner, patients will generally need to be dilated for OCT scanning although scanning of the macular area is sometimes possible with an undilated pupil. The quality of the OCT scan in an undilated eye can be compromised because the smaller pupil may reduce the intensity of the OCT beam entering and leaving the eye. An additional problem with undilated scanning is that

the fundus image is not always clearly visible and, in such cases, the exact location of the OCT scan on the fundus cannot be established.

OCT scans in patients with ptosis may be difficult to acquire since the upper lid will severely reduce the amount of light that is able to enter the eye. The design of the machine makes it somewhat awkward for the operator to hold up the patient's eyelid while scanning – in such a situation the help of a second operator may be required.

The quality of the scan is also dependent on the patient's ability to keep the eye steadily fixed on the internal or external fixation light since even slight eye movements will cause significant motion artefacts in the scan. The OCT beam takes one second to traverse once along the scan line and produce an image, thus very rapid blinking will also lead to artefacts in the OCT scan.

3.12 Conclusions

This chapter presents a detailed analysis of the Zeiss-Humphrey OCT scanner. To date it is the only commercially available scanner. The system is fairly easy to use, although some experience is required since the quality of scans will be compromised if the set-up is not optimal. Scanning is not invasive and is very well tolerated by patients. Scans may be acquired from the majority of patients, although there may be some difficulties with patients who have non-clear media or ptosis or who are unable to fixate. Some of these problems may be overcome as the optics of the machine improve and scan acquisition times becomes faster. One of the strengths of the machine is the observation that the quality of OCT scans does not seem to be a function of age – this is important since many of the clinical applications of OCT are likely to involve conditions which predominantly affect the older population. Although the current scanner is designed for retinal scanning, with very slight modifications it may also be used for scanning the anterior segment, thus increasing the number of potential clinical applications of this technique.

The resolution of current OCT is not sufficient to demonstrate the same amount of retinal detail as light microscopy. However, the retinal borders are well-defined so

accurate retinal thickness measurements may be made from the scans. The exact nature of the anterior red band remains somewhat controversial although observation of the varying thickness of this band around the optic nerve head suggests that it is related to the RNFL. Even with better resolution, certain layers with similar optical properties may not be well differentiated. However, despite its limitations, the cross-sectional resolution of OCT surpasses that of other imaging techniques and provides useful in-vivo information which would otherwise be unavailable.

Chapter 4

PERFORMANCE TESTING AND NORMATIVE STUDIES

In order to successfully implement OCT scanning in the clinical environment, it must be shown that the commercially available OCT scanner is able to perform reliably. The performance of the system in a variety of situations should be rigorously tested before attempting to use OCT scans to influence clinical decisions. It is also important to establish the characteristics of OCT in the normal population and to determine the normative ranges of parameters such as retinal thickness as the potential of OCT as a diagnostic tool will depend, on its ability to distinguish between healthy and diseased states.

4.1   Introduction

This chapter deals with the testing of the system's basic parameters such as resolution, accuracy and precision and with the evaluation of its performance in terms of repeatability and reproducibility. The parameters which are most likely to be of use in the clinical environment are retinal thickness in the macula (for assessing a variety of macular conditions, such as diabetic macular oedema), retinal nerve fibre layer thickness around the optic nerve (for assessing glaucomatous or pre-glaucomatous states) and corneal thickness (for assessing a variety of corneal conditions) and consequently, normative data for each of these parameters is presented. Some of the studies presented in this chapter have been published[32,33].

4.2 Resolution

The longitudinal resolution of the OCT scanner is dependent on the coherence length of the light source as described in Chapter 2. The theoretical resolution calculated from the equation given in Section 2.2.2 is approximately 10μm. Longitudinal resolution may also be measured experimentally by scanning across the surface of a mirror. Since a mirror is a perfectly reflecting surface, it may be considered to be an object of negligibly small thickness.

Methods

OCT scans across the surface of a mirror were acquired for this study. The mirror used was a high precision flat mirror coated with a metallic gold layer. This type of mirror has very high reflectivity, typically greater than 98% for wavelengths in the infra-red region. The scan length was arbitrarily set at 2mm. This setting did not reflect the actual length of the scan across the mirror surface since the scan length read-out takes the optics of the eye into account. However, the true length of the scan line was not an important issue in this investigation. Three scans at different locations across the surface of the mirror were acquired.

Analysis

The raw data from each of the acquired scans was exported. The data in the exported *.raw* files was logarithmic and had to be converted back into its linear form in order to calculate the resolution of the system. Curves were fitted to the data using commercial curve-fitting software (DataFit V8.0.32, Oakdale Engineering, US). The resulting plots of the linear intensity data against mirror translation for each of the acquired A-scans showed a single peak which corresponded to the reflection from the surface of the mirror. A typical example is shown in Figure 4.1. The longitudinal resolution of the system could then be calculated from the full-width at half-maximum (FWHM) of the signal peak, which was calculated from the equation of the fitted curve. Three A-scans from each of the 3 scans acquired were randomly chosen and the FWHM was calculated from each of these 9 A-scans. An average

value for longitudinal resolution was computed from these 9 values. The mirror translated in fixed steps of 6μm in air.
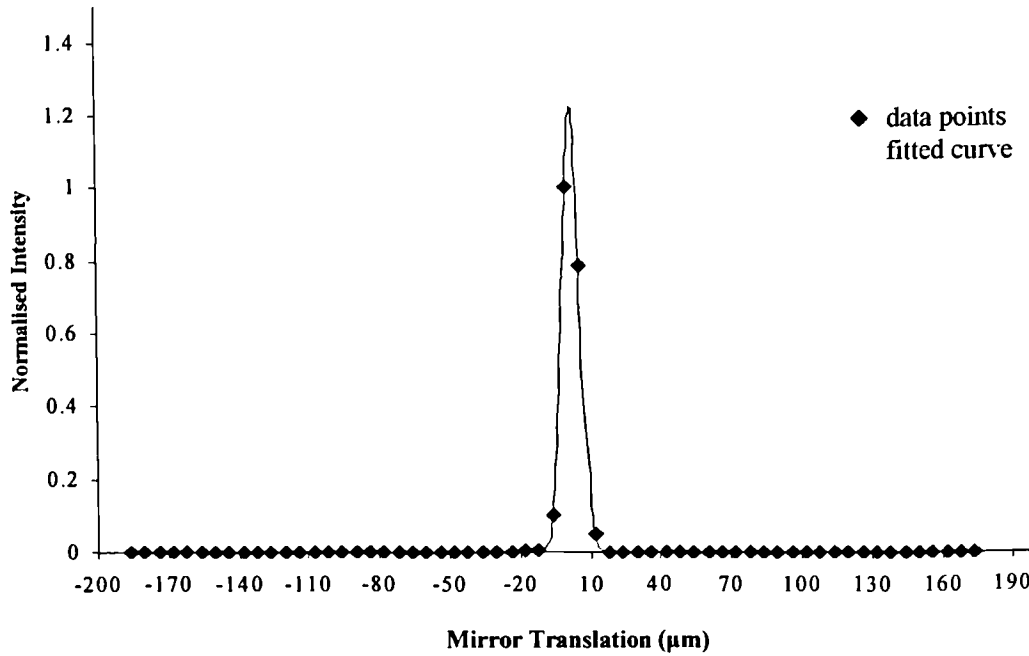
Figure 4.1   *Graph of a typical A-scan acquired from a scan across the surface of a highly reflecting mirror. The intensity data has been converted to its linear form and normalised with respect to the maximum value. A curve with equation $y = e^{(0.0002+0.1695x-0.0348x^2)}$ has been fitted to the data ($R^2 = 0.999$).*

Results

Curves of the form $y = e^{(a+bx+cx^2)}$ were fitted to each set of data (the coefficient of multiple determination, R^2, varied between 0.982 and 0.999). The FWHM calculated from each of the 9 selected scans is shown in Table 4.1. The average measured resolution was 11.3μm (standard deviation: 1.5μm).

Discussion

A similar method for experimentally assessing the longitudinal resolution of an early prototype OCT system was described by Huang and colleagues[12]. The measured FWHM of this system was found to be 10μm which compared well with the theoretical resolution of 10.6μm for the source used. The specifications of the commercially available OCT scanner, which was developed from this prototype system, quote a longitudinal resolution of 10-15μm. This study has shown that the experimentally measured resolution agrees with these specifications and is also in close agreement with the theoretical value of approximately 10μm. This study therefore confirms that the maximum achievable longitudinal resolution attainable with the commercial OCT system is of the order of 10-15μm. This method for assessing longitudinal resolution is fairly easy to carry out and may be used to regularly assess the performance of the OCT scanner.

Scan No	FWHM (μm)
1	12.3
2	10.1
3	13.6
4	9.4
5	11.7
6	10.3
7	9.8
8	13.3
9	11.5

Table 4.1   *Table of FWHM for each of the selected A-Scans*

4.3   Accuracy and Precision

Since one of the primary aims of OCT is to make accurate measurements from scans, it is necessary to investigate the accuracy and precision of measurements made by the system. One way of doing this is to make measurements from scans of an object with known dimensions and to compare the results from the OCT scans with the known values.

Materials and Methods

Equipment: A custom-built test object was commissioned for this purpose. This consisted of two 1cm-thick plates of glass separated by four 200μm-thick spacers. The thickness of the spacers was known to an accuracy of 0.5μm. A technique called optical contacting made it possible to attach the spacers to the glass plates without the use of any sort of adhesive. This technique is a process by which two surfaces are adhered through molecular attraction. The surfaces of the plates to be contacted are parallel to within 0.5 arc-second, extremely flat and cleaned to an exceptionally high degree. When brought together the surfaces then adhere with no adhesive. Using this technique ensured that the thickness of the gap corresponded exactly to the thickness of the spacers. This gap could also be filled with liquids. Scans of the test object resulted in two reflecting bands representing the glass-air or glass-liquid boundaries. The plates of the test object were made of fused silica with refractive index 1.452 at 850 nm. Thus imaging of the air-filled gap resulted in very strong reflections due to the large change in refractive index at the boundary. In the eye, reflections tend to be less pronounced and therefore, in order to model the *in-vivo* situation more effectively the experiment was repeated with the gap filled with water (refractive index 1.333) and glycerine (refractive index 1.473). This had the effect of making the glass-liquid boundary far less well defined and, consequently, the reflections from this interface were degraded.

Scanning: In each of the three cases, 10 line scans across the test object were acquired. The air gap thickness was calculated for each A-scan and the average gap thickness for each scan was calculated from these values. An overall average of these 10 values was then calculated.

The known distance between the plates of the test object assumes an incident beam normal to the sample. Thus tilting the sample would increase the distance travelled by the OCT beam, leading to a higher measurement. Each pixel within the A-scan represents a distance of 6μm in air, which corresponds to approximately 4.5μm in water and 4.1μm in glycerine, thus OCT measurements can only distinguish between measurements which vary by more than these amounts. From geometric calculations and experimentation it was found that tilts within 10° from the normal caused inaccuracies that were less than the intrinsic thickness resolution of the system. (Appendix C). Thus the positioning of the test object was not particularly critical for making accurate measurements. The focussing and polarization settings were adjusted to give the strongest possible signal. Several scans across the surface of the object were then acquired.

The degradation of the signal for the cases in which the gap was filled with water or glycerine was calculated. The object was first set up with an air-filled gap as explained above and then the liquid was introduced carefully without altering the position of the object or the polarization or focusing settings. Scans were acquired before and after the liquid was inserted so the reduction in intensity of the reflections could be assessed.

Analysis

A-scans of the test object showed two peaks corresponding to the edges of the air gap. The thickness of the gap was measured by considering the distance between the two maxima. A computer program which identified the peaks and calculated the distance between them was developed since the software provided with the OCT scanner could not perform these functions (this program is described in Section 5.4). When the gap was filled with air the gap edges were very well defined and the two maxima corresponding to the glass-air interfaces were easily identifiable on each of the A-Scans (Figure 4.2A). Filling the gap with either water or glycerine caused a reduction in the overall intensity of the reflections from the interfaces (Figure 4.2B and C). At some positions along the scan line, the returning reflection was so weak that it fell below the noise threshold and this meant that the gap edges no longer

appeared as continuous lines on the B-scan but had a more patchy appearance. At these positions, it was impossible to identify the two maxima corresponding to the gap edges from the A-scan. Thus thickness measurements were made only from the A-scans in which the two maxima could clearly be identified.

The OCT software assumes a refractive index of 1.38 for retinal tissue (this value was provided by the manufacturers of the system), thus measurements made from the A-Scan were multiplied by this value in order to convert them back into measurements in air. These values were then divided by the refractive index of the material within the gap to give a true value of gap thickness as measured from the OCT scan. The results were then compared to the known thickness of the gap. The same process was repeated for the water-filled and glycerine-filled cases.

A   B   C
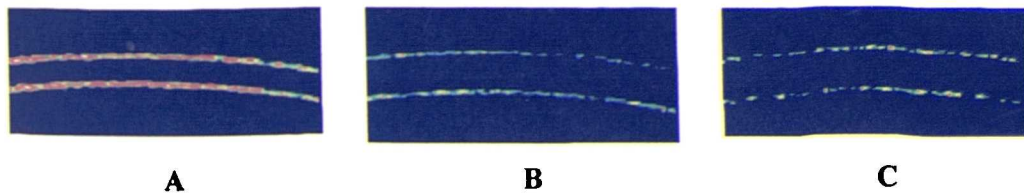
Figure 4.2   *OCT scans from the test object. (A) Air-filled gap. (B) Water-filled gap. (C) Glycerine-filled gap. The boundaries of the gap are poorly defined when the gap is filled with water or glycerine.*

In order to quantify the degradation of the signal caused by introducing a liquid into the air gap, the percentage reduction in reflectance was calculated. The A-scans in which the two maxima were clearly identifiable were selected from each acquired B-Scan and the intensity of the reflections from the interfaces was calculated. These values were then averaged over the entire B-scan. This value was then divided by the average intensity calculated from the scans acquired just before the liquid was introduced. For the water-filled case the intensity of the reflection from anterior edge of the gap (closest to the machine head) was found to be 48.5% of the air-filled case; for the posterior edge it was 57.0%. With glycerine in the gap, these values were 42.9% for the anterior edge and 47.7% for the posterior.

For the water-filled gap, an average of 97 A-scans per B-scan showed two easily identifiable maxima, whereas in the glycerine-filled case this value was 45 A-Scans per B-scan.

Results

The overall gap thickness values, obtained as described in the above section were found to be 197.7μm (standard deviation: 0.6μm) for the air-filled gap, 195.1μm (standard deviation: 0.7μm) for the water-filled gap and 196.1μm (standard deviation: 1.7μm) for the glycerine-filled gap.

Discussion

All three values are within 2.5% of the known thickness of 200μm and percentage errors are small. These results indicate that the measurements made from the OCT scanner are both accurate and precise.

4.4   Repeatability and Reproducibility

Rigorous assessment of the repeatability and reproducibility of the equipment was also necessary before using results from OCT scanning for diagnostic purposes. The definitions of repeatability and reproducibility adopted for the study were based on the standards set by the British Standards Institution and International Standards Organisation[34,35], as recommended by Bland and Altman[36].

Under repeatability conditions, independent test results are obtained with the same method on the same subject by the same operator and on the same set of equipment with the shortest time lapse possible between successive sets of readings. The repeatability limit was defined as a value *r* such that, in 95% of cases, the difference between an observed value and the true value of the measurement, estimated from the mean of all the measurements made under repeatability conditions, will be less than or equal to *r*. The value of *r* was therefore two standard deviations of the differences from the mean of the repeat measurements. The coefficient of

repeatability was found by dividing r by the mean of the repeated readings and expressing the result as a percentage.

Under reproducibility conditions sets of readings are obtained using the same method but with one variation in the experimental set-up, for example, a change of operator to investigate inter-operator reproducibility or a change in scanning session to investigate inter-session reproducibility. The reproducibility limit was defined as a value R such that in 95% of cases, the difference between measurements made on the same subject during different sessions or by different operators will be less than or equal to R. The value of R was therefore two standard deviations of the differences between pairs of measurements obtained during different sessions or by different operators. The coefficient of reproducibility was found by dividing R by the average of the means of each pair of readings and expressing the result as a percentage.

Repeatability and reproducibility of measurements were investigated first of all for the test object since it was reasonable to assume that the gap was non-varying, so any differences observed between scans could be attributed purely to the performance of the equipment. Repeatability and reproducibility were then assessed for situations likely to arise in the clinical setting. Since OCT may be used for quantifying retinal thickness within the macula, for assessing RNFL thickness around the optic nerve head or for measuring central corneal thickness, the repeatability and reproducibility of these measurements in normal subjects was assessed.

4.4.1 Repeatability and reproducibility of measurements from the test object

Methods

Repeatability for the test object was investigated by acquiring 10 scans in rapid succession, with as short a time lapse as possible between successive scans. Inter-session reproducibility for the test object was investigated by acquiring readings in the morning and afternoon on five consecutive days. The time separation between the morning and afternoon sessions was at least five hours and the OCT scanner was not switched off during this time period. The temperature of the room varied by approximately 2 degrees during this period of time. Both repeatability and

reproducibility were investigated for the air-filled, water-filled and glycerine-filled cases.

Analysis

Analysis of the A-scans in both cases was as described in Section 4.3 above. For each B-scan, the average gap thickness was computed by averaging values from the A-scans in which the two gap interfaces could easily be identified.

Results

Inter-session reproducibility: The average gap thickness was calculated from the individual A-Scan thicknesses for each morning and afternoon session. These values were then used to compute the overall coefficients of inter-session reproducibility which were found to be 1.3% (air-filled), 2.1% (water-filled) and 0.9% (glycerine-filled). The Wilcoxon paired measurement test (5% significance level) showed that there were no statistically significant differences between the measurements made from the morning and afternoon scanning sessions.

Repeatability: The coefficients of repeatability, calculated from the average gap thickness computed for each of the 10 consecutive scans, were found to be 0.6% (air-filled), 0.7% (water-filled) and 0.9% (glycerine-filled).

Discussion

The initial study on the air gap in the test object showed a high degree of repeatability (0.6%). Even with considerable degradation of the OCT signal and poorly defined interfaces, the coefficients of repeatability were still under 1%.

The overall coefficients of inter-session reproducibility were found to be between 0.9% and 2.1 % for the test object. These values indicate that variations in the temperature of the room or of the machine caused by leaving the machine switched on for a few hours did not significantly affect the reproducibility of measurements.

The results from the liquid-filled test object indicated that repeatable and reproducible measurements may also be made in cases where retinal pathology causes degradation of the OCT signal. Provided that the position of vitreo-retinal interface and the RPE-choriocapillaris complex can be identified in a least a few positions along the scan line, measurements of retinal thickness at these points should still show a high degree of repeatability and reproducibility.

4.4.2   Retinal Thickness within the Macula

A number of conditions, such as diabetes, may cause changes in the retinal thickness at the macula[37-39]. OCT measurements of retinal thickness in such cases are useful for monitoring the progression of the condition and for assessing the effects of treatment. It is therefore important to quantify the repeatability and reproducibility of macular thickness measurements and to find the percentile ranges of retinal thickness in the normal population. Repeatability and reproducibility of macular thickness measurements were investigated for a series of closely spaced straight line scans across the macula. In addition, inter-reproducibility of measurements within a macular map was also assessed since this scanning option is frequently used to map and monitor macular thickness. Establishing the normative ranges of foveal thickness was also considered important as visual acuity may be related to the thickness of the fovea in certain conditions.

Methods

Twenty volunteers (10 males and 10 females), ranging in age from 21 to 57 years (average age: 31.9 years, standard deviation: 19.6 years) participated in this study. The study was conducted according to the tenets of the Declaration of Helsinki and volunteers gave informed consent after the nature and intent of the study had been fully explained to them. The exclusion criterion was any history of known retinal disease. All scanning was performed in the right eye which was dilated with 1% tropicamide.

A series of horizontal single line scans across the fovea was acquired for each of the subjects. Scans were repositioned using the *Repeat Scan* feature which provides a landmark cursor to facilitate the repeat positioning of subsequent scans. Any scans in which the landmark cursor was not in the correct position were discarded, thus ensuring that all the saved scans were of exactly the same portion of retina. However, after careful analysis of the fundus pictures it was discovered that there was a degree of inaccuracy in the positioning of this landmark cursor. There was some displacement even between scans in which the landmark cursor appeared to be in exactly the same position. This average displacement was of the order of 0.2mm, reaching a maximum of 0.33mm (see Appendix B). In the region of the fovea where the thickness of the retina varies considerably over a small distance, a shift of this amount could cause considerable variations in the measured retinal thickness and this would lead to inaccuracies in the coefficients of repeatability and reproducibility. In an attempt to minimize the effects of landmark positioning errors it was therefore decided to scan across a band rather than across a single line. This was achieved by having a number of very closely spaced scan lines using the *raster six lines* option – this allowed six tomographic scans to be acquired in succession. In this scanning mode an aiming rectangle of adjustable dimensions was displayed on the fundus-viewing unit. The width of this rectangle determined the length of the scan lines whereas its height determined the spacing between the scans. In this case the width of the aiming rectangle was set at 4mm and its height was 0.5mm. Thus the spacing between successive scans was 0.1mm. The aiming rectangle was positioned such that at least four of the scans traversed and were centred on the foveal pit. These four scans therefore covered a vertical length of 0.3mm which corresponded to the maximum error in positioning found from the initial investigation. These four scans from each group were then used in subsequent calculations. The focussing and polarisation settings were adjusted so that the best quality image was obtained.

Repeatability of scans from the control group was investigated by obtaining 10 sets of 6 tomographic scans from the same subject. All scanning was carried out by the same operator. The time elapsed between successive sets of scans corresponded to the time taken to set up and position the aiming rectangle for a new set of tomographic scans and was always less than 1 minute. Repeatability was investigated for three different subjects.

Inter-session reproducibility was investigated by obtaining two sets of 6 tomographic scans from each of the 20 subjects on two separate occasions.

In the clinical setting, macular thickness is often assessed using a macular map. In this scanning option, an aiming circle is positioned over the area to be imaged and six straight line scans running along six equally spaced diameters of this circle are acquired in sequence. A software option then uses thickness values from each of these scans to compute an average retinal thickness for nine areas arranged concentrically within the aiming circle. Since this tool is becoming increasingly popular for assessing conditions such as diabetic macular oedema[38,39], inter-session reproducibility of macular maps was investigated for a sub-group of 10 volunteers (5 males, 5 females; ages: 21-50, average age: 37.9 years, standard deviation: 10.3 years). The radius of the aiming circle was set at 2.5mm and positioned such that the first scan of the set was centred on the fovea. The position of the subsequent scans in the set was not altered, however, only sets of scans in which all 6 scans traversed and were approximately centred on the fovea were included in the study. Inter-session reproducibility was investigated by acquiring by acquiring two sets of radial scans on two separate occasions. The macular map software was run to calculate the average retinal thickness in each of the nine sections.

Normative ranges for foveal thickness were also established. For each subject, the foveal thickness was measured from each of the four closely spaced scans across the fovea – measurements were made at the thinnest portion of each scan. The average foveal thickness was then calculated for each subject.

Analysis

Set of straight-line scans: The centre of each scan was taken to be the thinnest point of the retina, which was assumed to correspond to the deepest portion of the foveal pit. The A-scan at the centre of the scan was labelled A_0. Scans to the left of this were labelled A_{-1} to A_{-50} and scans to the right were labelled A_1 to A_{50}. Each scan was then divided into 8 sections each containing 10 A-scans. Sections to the left of the centre were labelled S_{-1} to S_{-4} and those to the right were labelled S_1 to S_4 as

shown in Figure 4.3. Thus, for each B-scan, only the 80 A-scans from A_{-39} to A_{40} were used in the calculations. The retinal thickness obtained from each of these 80 scans was averaged across the 4 levels in each set in an attempt to minimize the effects of errors in scan positioning, leaving a single set of 80 thickness values from each group of tomographic scans. The overall average retinal thickness (the average of these 80 thickness values) and the average retinal thickness per section were calculated for each group of data.
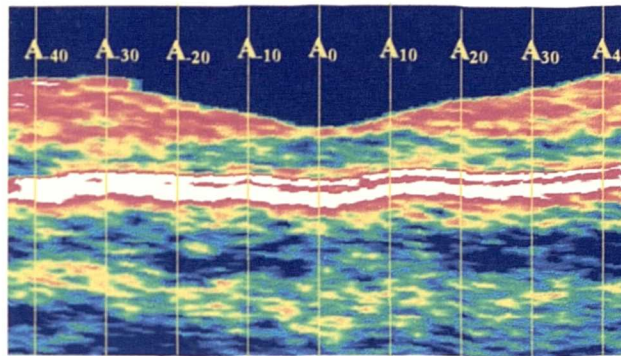
Figure 4.3   *Diagram showing the subdivision of the OCT scan into sections each containing 10 A-Scans*

The overall coefficient of inter-session reproducibility for the control group was calculated from the 20 overall average retinal thickness values. Coefficients of reproducibility were also calculated for each of the 8 retinal sections. A graph of differences against means was plotted both for the overall average retinal thickness as well as for each individual section. In both cases the Wilcoxon matched paired test ($5^0 o$ significance level) was also used to establish whether there was any statistically significant difference between measurements made during different sessions.

The coefficient of repeatability was calculated for each of the 3 subjects participating in the repeatability study.

In order to establish whether scanning across a 0.3mm band of retina rather than across a single line actually improved the repeatability, the coefficient of repeatability for each level was also computed and compared with the value obtained from the average over 4 levels.

Macular Maps: The *Retinal Map* software option was used to calculate the average thickness for each of the areas within the retinal map. The coefficient of inter-session reproducibility was then calculated for each of the 9 areas within the macular map. The system of labelling of the 9 areas is shown in Figure 4.4. For comparison with the data from Massin et al[42], the reproducibility limits (two standard deviations of the differences between inter-session measurements in the same subject), for each of the macular map areas were also calculated.
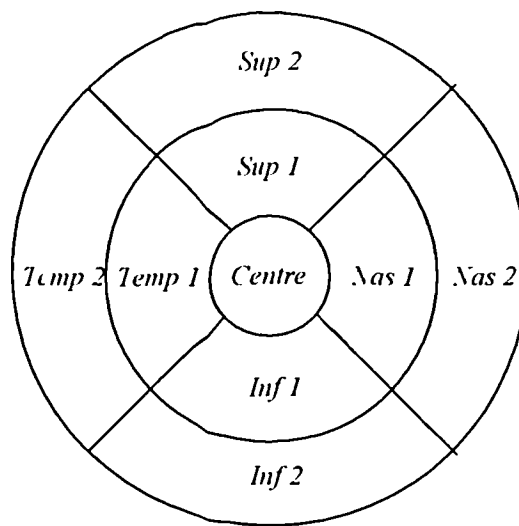
Figure 4.4   *System of labelling for macular map analysis*

Normative Thickness Values: The median, 5th and 95th percentiles of the overall retinal thickness, retinal thickness per section and foveal thickness were calculated for the sample as a whole as well as for females alone and for males alone.

Results

Inter-session reproducibility (straight line scans): For each subject the overall average retinal thickness was calculated for session 1 and session 2. The overall coefficient of reproducibility was then computed from these values and was found to be 3.0%. In addition, the average retinal thickness for each of the 8 sections was found and the coefficient of inter-session reproducibility for each section was computed. The results obtained are shown in Table 4.2. Graphs of differences against means were plotted for the overall average retinal thickness values as well as for each individual section. The graph of differences against means for the overall retinal

thickness (Figure 4.5) is shown below — the graphs for the individual sections were very similar in appearance. In all cases it was found that 95% (19 out of 20) of differences fell within 2 standard deviations of the mean. The Wilcoxon paired measurement test (5 % significance level) was also performed on the overall retinal thickness values and on the values for each retinal section. No statistically significant differences were found between the sets of data acquired during different sessions.

	Coefficient of reproducibility %
Overall	3.0
S_{-4}	4.0
S_{-3}	4.5
S_{-2}	7.0
S_{-1}	8.4
S_1	8.1
S_2	6.0
S_3	2.5
S_4	3.2

Table 4.2   *Coefficient of inter-session reproducibility   overall and for each section*
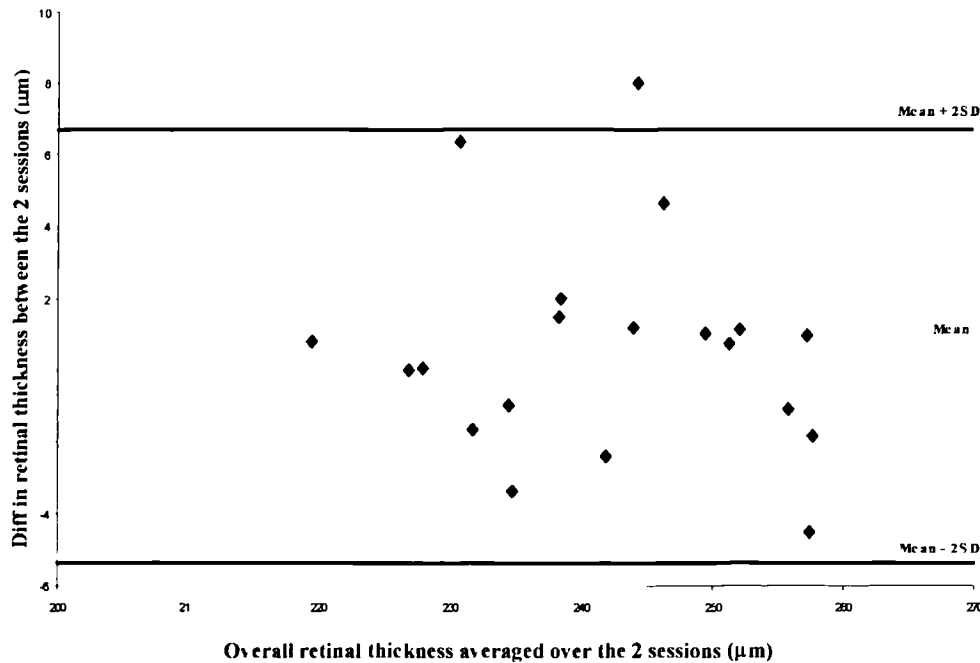
Figure 4.5   *Graph of data from inter-session reproducibility study. Mean retinal thickness for each subject is plotted against difference in retinal thickness between morning and afternoon scanning sessions. 95% of values (19 out of 20) fall within 2 standard deviations of the mean.*

Inter-session reproducibility (macular maps): The coefficients of inter-session reproducibility for each of the 9 areas in the macular map are shown in Table 4.3.

Repeatability: For each of the three subjects in the repeatability study the overall coefficient of repeatability was computed by analysing the overall average retinal thickness from each set of readings. The coefficient of repeatability for each of the 8 retinal sections was then computed. The results obtained are shown in Table 4.4.

In order to determine whether averaging over 4 levels had any significant effect on the repeatability of the measurements, the overall and per-section single-level coefficient of repeatability was also calculated for each of the 4 individual levels. These values were then averaged for each section and compared with the values obtained for the multiple-level case. The results for the single-level coefficients of repeatability are also shown in Table 4.4.

103

Normative Thickness Values: The median, 5th and 95th percentiles of the overall and sectional retinal thickness values are shown in Table 4.5. Foveal thickness ranges are also shown.

Area	Coefficient of Reproducibility	Reproducibility Limit (μm)
Centre	8.8%	13.7
Supl	6.0%	13.1
Nasl	8.4%	17.4
Infl	5.8%	12.4
Templ	15.4%	29.4
Sup2	4.8%	10.6
Nas2	6.4%	22.0
Inf2	9.4%	20.0
Temp2	5.2%	10.4

Table 4.3   *Table of Coefficients of Intersession Reproducibility for each of the areas within the macular map*

	COEFFICIENT OF REPEATABILITY %					
	Subject 1		Subject 2		Subject 3	
	ML	SL	ML	SL	ML	SL
Overall	2.1	3.2	2.5	3.5	4.0	5.8
S-4	3.9	4.7	1.5	2.7	3.2	4.8
S-3	2.6	3.7	2.2	3.5	3.2	4.8
S-2	3.4	6.1	6.4	8.6	4.3	6.4
S-1	7.1	11.4	8.1	11.2	8.3	14.0
S1	5.0	7.7	7.8	11.5	9.6	14.9
S2	2.5	4.3	8.7	10.5	3.7	6.3
S3	1.8	3.2	3.4	4.7	3.1	5.4
S4	2.1	3.7	2.1	3.1	3.1	5.8

Table 4.4   *Coefficients of repeatability: overall and for each retinal section and for the multiple-level (ML) and single-level (SL) case*

For comparison with the results of Koozekanani et al[40] the average retinal thickness for sections S_3 and S_4 together was calculated – this was found to be 271 ± 16 μm. The average retinal thickness for sections S_1 and S_{-1} together was also calculated and this was found to be 178 ± 18 μm for the female subjects and 190 ± 24 μm for the male subjects. Wilcoxon analysis (5% significance level) showed that there were statistically significant differences in the overall average retinal thickness for males and females (values were higher for the males subjects in the study). No significant differences in foveal thickness were found between males and females.

Retinal Thickness	Whole sample			Females			Males		
	Median	5th	95th	Median	5th	95th	Median	5th	95th
Overall	238	225	257	233	222	248	248	234	257
S_4	263	240	297	257	240	280	278	262	307
S_3	263	244	292	259	243	278	280	259	295
S_2	232	213	266	229	215	252	243	218	268
S_1	178	154	213	174	152	202	184	160	213
S_1	187	161	218	177	160	205	197	163	222
S_2	245	221	267	239	220	251	252	229	269
S_3	273	251	289	272	247	288	276	262	289
S_4	272	242	291	272	240	286	283	249	292
Foveal Thickness	162	137	194	159	134	186	168	145	191

Table 4.5   *Median, 5th and 95th percentile values for retinal and foveal thickness*

Discussion

For the control group, the overall coefficients of repeatability of the measurements across a 0.3mm band were between 2% and 4% and sectional coefficients of repeatability were all less than 10%. As expected, these values were slightly lower than for the test object due to the introduction of additional errors such as inaccuracies in positioning of scans but nevertheless show an acceptable degree of

repeatability in the clinical setting. This indicates that within the same scanning session, measurements made by the system are repeatable and hence for clinical applications, there is no need to take a large number of readings for accurate measures of retinal thickness.

The overall coefficients of inter-session reproducibility were found to be between 0.9% and 2.1 % for the test object and 3.0% for the control group. Sectional coefficients of reproducibility were all less than 9%. This indicates that variations of more than 9% in retinal thickness measurements from different scanning sessions are unlikely to be due to the performance of the scanner. Thus OCT may be used to monitor patients with conditions that affect the thickness of the retina in the macular region.

From Table 4.4 it is clear that the repeatability of the retinal measurements made over a band of 0.3mm is consistently better than when repeated scans are made across a single line. This confirms that slight errors in scan positioning do occur and consequently, that acquiring a series of scans across a 0.3mm band yields more repeatable measurements. These errors in positioning may be partly due to the fact that the quality of the fundus picture displayed on the fundus-viewing monitor is poor. Moreover, whilst in the slow scanning mode, the landmark cursor tends to lose its definition and thus it is very difficult to ensure that this remains in the correct position.

The methods used for quantifying repeatability and reproducibility of retinal thickness measurements in the foveal region differ slightly from those used in other publications, however the results obtained are quite similar. Koozekanani et al[40] analysed sets of scans obtained during independent measuring sessions. They found that there were no significant differences between different sessions or between different scans within the same session, however they do not specify which statistical test was used. The Wilcoxon matched paired test on the data obtained under reproducibility conditions showed that there were no significant differences between the sets of data acquired during different scanning sessions. This is true both for the overall retinal thickness as well as for the thickness in each retinal section.

The method of sub-dividing each scan into sections containing 10 A-scans for analysis is very similar to the system adopted by Baumann et al[41]. They divided their images into seven regions each containing 10 A-scans and computed the coefficient of variation for retinal thickness measurements made in each of these sections. They found that the greatest coefficient of variation occurred in the central section which covered a retinal length of 320μm centred on the foveal pit. Sections closest to the fixation point showed less reproducibility than those further away. Similarly, the coefficients of repeatability and reproducibility in this study tended to be highest for regions S_1 and S_{-1}, which correspond to the sections closest to the centre of the fovea. In this region the retinal thickness is varying and hence any errors in scan positioning will causes variations in the measured thickness of this region. Scanning across a 0.3mm band does compensate slightly for this, however, although it has been shown that this reduces the effects of errors in positioning, the higher coefficients of repeatability and reproducibility in these regions relative to other regions indicate that there is still a degree of inaccuracy in the positioning of scans.

The median, 5th and 95th percentiles for retinal thickness in the macular region were calculated in order to establish confidence intervals for retinal thickness in the normal population. The control group was not ideal since all subjects were relatively young. Nevertheless, the results obtained compare very well with those of other investigators.

The sample size and mean age were similar to those investigated by Baumann et al[41] and the sectional results are comparable to those quoted in this publication. The average retinal thickness for sections S_3 and S_4 together is 271 ± 16 μm. This represents an average over a 0.8mm section of retina at a distance of 0.8mm from the foveal pit and the result is almost identical to Koozekanani et al's[40] average retinal thickness of 274 ± 17 μm for a 1mm section at a distance of 0.75mm from the foveal pit. The average retinal thickness for sections S_1 and S_{-1} together is 178 ± 18 μm for females and 190 ± 24 μm for males. These values are higher than Hee et al's foveal thickness values of 169 ± 4 μm for females and 181 ± 4 μm for males[20]. This is probably due to the fact that this group analysed a circular region of diameter 500

μm whereas our study was performed on a larger rectangular region of 800 × 300 μm.

The coefficients of reproducibility of the areas in the retinal map are slightly higher than those calculated from the different sections in the straight-line scans and two of these values are greater than 10%. A study by Massin and colleagues[42] found that the reproducibility limit was under 7μm for all but two of the macular map areas. In our study, reproducibility limits were greater than this, with an average reproducibility limit of 15.7μm. Possibly, this group had stricter criteria for discarding sets of macular maps in which eye movement was detected between the six scans.

The studies described in this section have shown that retinal thickness measurements, whether made from a series of straight-line scans or from a macular map are both repeatable and reproducible. This indicates that OCT is a promising tool for monitoring changes in retinal thickness.

4.4.3   Retinal nerve fibre layer thickness around the optic disc

One potential application of OCT is in diagnosis and monitoring of glaucoma, a condition in which the retinal nerve fibre layer (RNFL) around the optic disc becomes thinner. Studies using OCT have suggested that these focal defects in the RNFL may be visualised using OCT and that there are significant differences in RNFL thickness between patients with glaucoma and control groups with no history of glaucoma or elevated intra-ocular pressure[43-46]. Since the algorithm used by the OCT system for identifying the RNFL is not the same as that used to calculate retinal thickness, it is necessary to separately determine the repeatability and inter-session reproducibility of RNFL thickness measurements.

Methods

Twenty volunteers (10 males and 10 females), ranging in age from 20 to 67 years (average age 37.8 years, standard deviation: 12.4 years) participated in this study. The study was conducted according to the tenets of the Declaration of Helsinki and

volunteers gave informed consent after the nature and intent of the study had been fully explained to them. The exclusion criterion was any history of known retinal disease, family history of glaucoma or history of elevated intra-ocular pressure (over 21mmHg). All scanning was performed in the left eye which was dilated with 1% tropicamide.

Circular scans around the optic nerve head were acquired, using the *Nerve Head R-1.73mm* scanning option. This particular scanning option was chosen over the other two options designed for scanning around the optic nerve head (*Nerve Head R-1.5R/2R*) since one study has shown this to be the most reproducible option of the three[47].

Repeatability was assessed by acquiring 10 consecutive circular scans from 3 volunteers. Inter-session reproducibility was assessed by acquiring scans on two separate occasions from all 20 volunteers.

Analysis

The OCT *RNFL Thickness* tool presents the data in three forms, as a graph of thickness against location (this data may be exported), as averages over clock hours and as averages of quadrants of the circle. The labelling system used in this study is shown in Figure 4.6. In the normal eye, RNFL thickness varies around the optic nerve head, with the greatest thickness in the superior and inferior quadrants due to bundling of the nerve fibres. Coefficients of repeatability and reproducibility of the averages per clock hour and per quadrant were calculated using the thickness values given by the OCT algorithm. The RNFL thickness computed from each individual A-Scan within a scan could also be exported. These values were used to compute an overall average RNFL thickness from each scan. The coefficient of variation for the overall RNFL thickness and thickness per clock hour and per quadrant was also calculated for comparison with published data[48, 49].
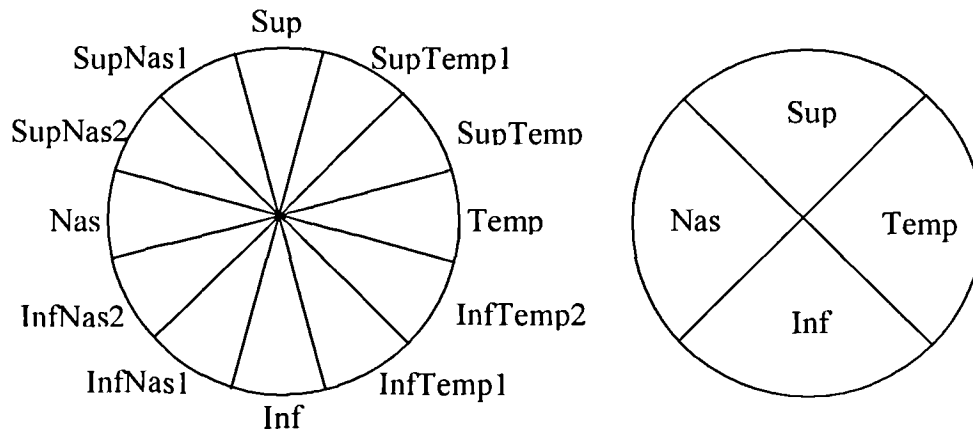
Figure 4.6   *Diagram showing the labelling system for the clock hour and quadrant analysis of circular scans centred on the optic disc.*

Results

Repeatability: The overall RNFL thickness was calculated from the exported thickness data and the average RNFL thickness value per clock hour and per quadrant were obtained from the available software features. Coefficients of repeatability of the overall mean thickness and thickness per quadrant and per clock hour were calculated for the 3 subjects in the repeatability study. The results are shown in Table 4.6.

Inter-session Reproducibility: The inter-session reproducibility of overall mean RNFL thickness, and RNFL thickness per clock hour and per quadrant was assessed. Figure 4.7 shows a graph of inter-session difference in mean RNFL thickness against mean RNFL thickness for each of the 20 patients in the study. This graph indicates that 100% of differences lie within 2 standard deviations of the mean. The coefficient of inter-session reproducibility for overall mean RNFL thickness was 12.8%.

	Region	Subject 1	Subject 2	Subject 3
	Overall	7.6%	11.6%	10.6%
Clock Hours	*Sup*	12.8%	7.0%	21.0%
	SupTemp1	11.4%	21.8%	37.8%
	SupTemp2	19.2%	37.0%	54.4%
	Temp	45.0%	57.8%	57.0%
	InfTemp2	11.8%	27.0%	56.8%
	InfTemp1	9.0%	15.4%	51.4%
	Inf	6.6%	25.0%	31.6%
	InfNas1	15.8%	32.2%	18.8%
	InfNas2	20.8%	25.8%	13.6%
	Nas	35.4%	31.4%	51.0%
	SupNas2	27.8%	13.2%	59.6%
	SupNas1	7.0%	6.2%	20.6%
Quadrants	*Nas*	7.2%	7.2%	23.8%
	Sup	20.2%	33.4%	36.2%
	Temp	7.2%	19.6%	11.0%
	Inf	21.8%	18.0%	40.0%

Table 4.6   *Coefficients of Repeatability of overall RNFL thickness and RNFL thickness per clock hour and per quadrant*
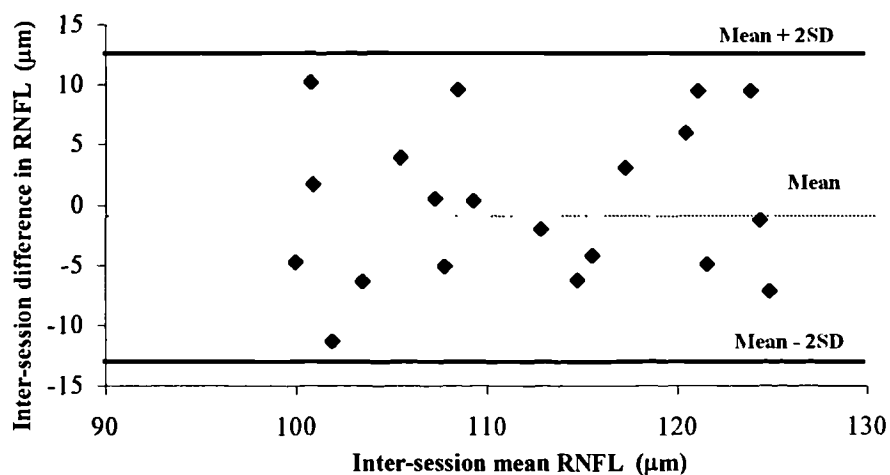
Figure 4.7   *Graph of data from inter-session reproducibility study. Mean RNFL thickness is plotted against difference in RNFL thickness between the different scanning sessions.*

Coefficients of inter-session reproducibility and coefficients of variation were also calculated for mean RNFL per clock hour and per quadrant. The results are shown in Table 4.7.

RNFL thickness: The median, 5th and 95th percentiles of the overall and sectional RNFL thickness values are shown in Table 4.8. Wilcoxon analysis (5% level of significance) showed no statistical significant differences between RNFL thickness in males and females, thus only results obtained from the whole sample are shown.

	Region	Coefficient of Reproducibility	Coefficient of Variation
	Overall	12.8%	3.8%
Clock Hours	*Sup*	26.6%	7.4%
	SupTemp1	30.6%	6.2%
	SupTemp2	40.2%	12.1%
	Temp	45.8%	10.2%
	InfTemp2	51.6%	11.4%
	InfTemp1	50.2%	7.1%
	Inf	36.2%	6.2%
	InfNas1	43.2%	5.8%
	InfNas2	47.2%	8.4%
	Nas	64.2%	13.6%
	SupNas2	21.8%	10.0%
	SupNas1	13.8%	5.7%
Quadrants	*Sup*	18.8%o	4.8%
	Temp	19.0%	8.6%
	Inf	25.2%	5.3%
	Nas	26.4%	8.2%

Table 4.7   *Coefficients of reproducibility and of variation of overall RNFL thickness and RNFL thickness per clock hour and per quadrant*

	Region	Median	5th	95th
	Overall	109	101	125
Clock Hours	*Sup*	136	98	169
	SupTemp1	126	95	173
	SupTemp2	98	74	133
	Temp	74	60	103
	InfTemp2	89	69	129
	InfTemp1	133	90	171
	Inf	127	88	173
	InfNas1	118	87	142
	InfNas2	89	76	117
	Nas	83	68	100
	SupNas2	118	96	141
	SupNas1	140	119	168
Quadrants	*Sup*	137	115	159
	Temp	84	69	122
	Inf	124	98	150
	Nas	95	82	116

Table 4.8   *Median, 5th and 95th percentiles of mean RNFL thickness and thickness per clock hour and per segment.*

Discussion

The RNFL has relatively high reflectance and is thought to correspond to the red band situated anteriorly on OCT scans. Its posterior border, however, is not as well defined as the posterior boundary of the neurosensory retina on OCT scans. Because of this, the edge-detection techniques used in the OCT retinal thickness algorithm cannot be used to identify the band corresponding to the RNFL and a different algorithm is used to establish the boundaries of the RNFL and measure its thickness. This study was conducted in order to evaluate the repeatability and reproducibility of RNFL thickness measurements using the *RNFL thickness* algorithm.

The coefficients of repeatability and reproducibility are not as good as those obtained in Section 4.4.2 for whole retinal thickness measurements. Coefficients of

repeatability and reproducibility for total retinal thickness were all under 10%, whereas the repeatability and reproducibility of RNFL thickness in some of the clock hour segments were close to 60%.

Although the RNFL is a relatively highly reflecting layer, small variations in the machine settings or in the patient's position can dramatically alter the appearance of this layer. Figure 4.8 shows two of the RNFL scans acquired from one of the subjects in the repeatability study. These two scans were acquired as part of the set of 10 scans acquired to assess repeatability and the time lapse between them was less than 1 minute. The scanning parameters were identical for the two scans and careful analysis of the scan position on the saved fundus images did not reveal any significant subject movement. However, the nasal portion of the RNFL appears much thinner in Figure 4.8B than in Figure 4.8A. Clock hour and quadrant RNFL thickness averages for this region are also dramatically different. There is no obvious reason for the differences between these two scans - one possible explanation is that they are due to very slight, undetectable movements of the eye. This observation confirms that the appearance of the RNFL is very susceptible to small changes in set-up and explains why coefficients of repeatability and reproducibility are higher for RNFL measurements than for total retinal thickness measurements. In the clinical setting, it is therefore important to take a number of repeated scans in order to measure RNFL thickness more accurately.

This study has also shown that the coefficients of reproducibility and of variation become worse as the scan is sub-divided into smaller areas. The reproducibility of clock-hour average RNFL thickness values is quite poor, with several values close to or exceeding 60%. This poor reproducibility could be partially due to the fact that there is considerable variation in the thickness of the RNFL in the region close to the optic disc. Thus even small variations in the position of the scan line could have quite a significant effect on the measured RNFL. Sub-dividing the scan into smaller sections would further accentuate these differences. Jones et al[48] reported similar findings when considering the mean coefficient of variation for global RNFL thickness, thickness per quadrant and thickness per clock hour segment. The coefficients of variation reported in this publication (5%, 8% and 9% for global, mean quadrant and mean clock hour segment respectively) and in another by

Blumenthal et al[49] (7% and 11.5% for global and mean quadrant RNFL thickness respectively) are comparable to those obtained in our study.
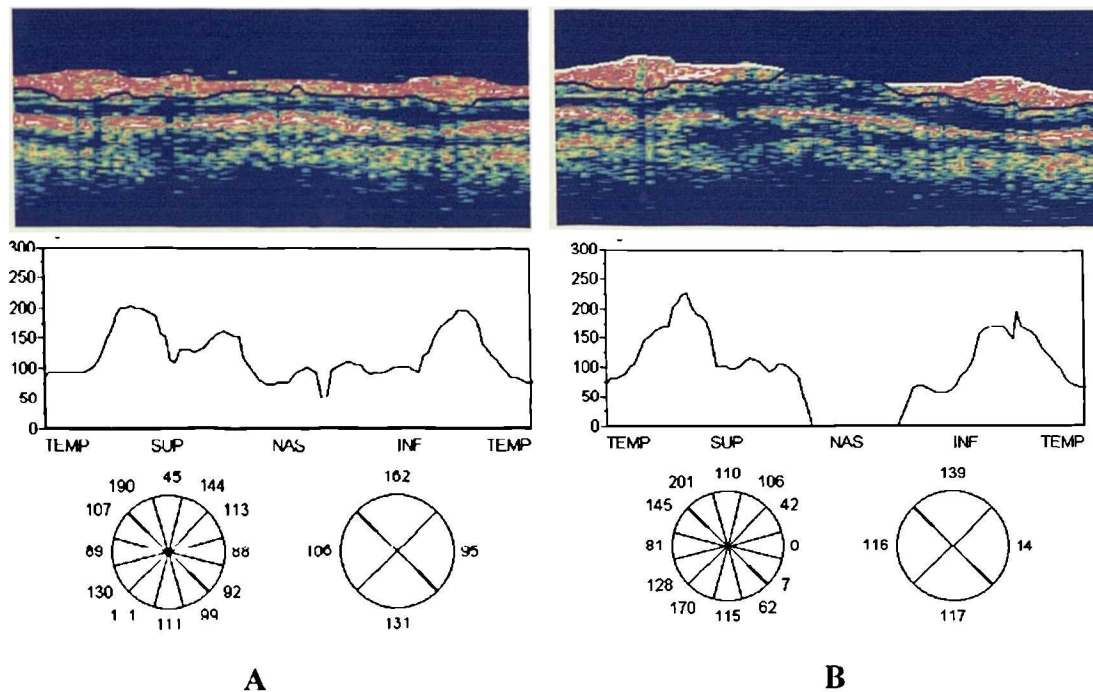
Figure 4.8   *RNFL Thickness measurements from two successive scans acquired less than 1 minute apart from one of the normal volunteers in the repeatability study. (A) RNFL thickness appears normal. (B) The RNFL reflectance from the nasal portion of the image appears reduced for no apparent reason. The RNFL thickness for the nasal clock hour segment and quadrant are consequently significantly different from those in the scan shown in (A).*

The 5th to 95th percentile range of RNFL thickness was found to be 101 – 125μm with a median of 109μm. A slightly higher average of 128μm is reported by Jones et al[48]. This could be due to the fact that the average age of subjects in this study was lower than in our study and indicates that RNFL thickness may be a function of age. RNFL thickness was greatest in the superior pole and least in the temporal. Jones et al[48] report a similar pattern of variation of RNFL thickness around the optic nerve head. This group also compared the OCT values with published histological data on RNFL thickness and found that although the variation in RNFL thickness as observed by OCT follows published histological data, the actual OCT values appear to underestimate the true RNFL thickness.

This study has shown that RNFL thickness measurements are not as repeatable and reproducible as total retinal thickness measurements. These differences may be due to the fact that the reflectance of the RNFL is more susceptible to changes in the set-up and that the posterior border of the RNFL is more difficult to identify than the boundary between the neurosensory retina and the RPE. Improvements to both the hardware and software features are therefore required for more accurate measurements of RNFL thickness.

4.4.4 Corneal Thickness

Although this model of OCT scanner was designed specifically for imaging the retina, a number of groups have shown that it can also be used for imaging the cornea[15,23,50]. Studies have shown that central thickness measurements made with OCT correlate well with those from established techniques such as pachymetry with the added advantage of being non-contact[50]. This ability of OCT to provide a simple, non-contact method for measuring corneal thickness has several potential clinical applications especially in the assessment of corneal health following refractive surgery which is becoming increasingly common[21-26]. Since the system and its software are designed for imaging the retina, it is important to separately assess the repeatability and reproducibility of corneal measurements and to establish the ranges of central corneal thickness in the normal population.

Methods

Corneal scans were easily obtained with very minor modifications to the system. In order to focus the laser beam onto the cornea for corneal scanning, patients needed to be positioned slightly further away from the machine head than in the set-up for retinal imaging. A small cushion was attached to the forehead rest in order to move patients' eyes away from the machine by a few centimetres and still ensure comfortable and steady positioning of the head.

Fourteen volunteers (7 males and 7 females), ranging in age from 21 to 58 years (average age 33.4 years; standard deviation 11.7 years) participated in this study. The study was conducted according to the tenets of the Declaration of Helsinki and

volunteers gave informed consent after the nature and intent of the study had been fully explained to them. The exclusion criteria were any ocular abnormalities, history of eye disease, prior refractive surgery and contact lens wear. All scanning was performed in the undilated left eye. During scanning, subjects were asked to fixate on the external fixation light with their right eye. The external fixation light was positioned so that the subject was looking straight ahead.

Repeatability was investigated by obtaining 10 horizontal and 10 vertical scans, ensuring that each scan bisected the pupil. All scanning was carried out by the same operator. The time elapsed between successive scans corresponded to the time taken to save the previous scan and adjust the position of the new scan if necessary, and never amounted to more than a few seconds. Repeatability was investigated for three different subjects. The scan length on the OCT system was set to 2mm, using the default axial length of 24.46mm. However, because the system is designed for retinal imaging this value is not the true length of the scan line on the cornea. The scan length was calibrated by projecting the scan line onto a ruler placed at the approximate position of the cornea and the true scan length was found to be approximately 2.5mm.

Both inter-session and inter-operator reproducibility were investigated. In both studies, sets of 6 radial scans centred on the centre of the pupil were obtained using the *Radial Lines* scanning option. The scan length set on the machine was 2mm (radial scan length set to 1mm), thus the true calibrated scan length was approximately 2.5mm. Inter-session reproducibility was investigated by acquiring readings on two separate occasions by a single operator. All scanning was performed during a specific time period, 11.00 to 14:00, in order to minimize the effect of diurnal variations in corneal thickness. Studies have shown that central corneal thickness is most stable during this time period[51-53]. To investigate inter-operator reproducibility, two operators each obtained a set of six scans on every subject during the same scanning session. The subject was asked to sit back and relax for a few minutes after the first set of scans while the first operator exited out of the OCT system. The second operator then re-positioned the subject and started the system once again before obtaining the second set of scans. Both inter-session and inter-operator reproducibility were investigated for a control group of 14 subjects.

Analysis

A typical OCT scan through the centre of the cornea is shown in Figure 4.9. The A-scan at the apex of the scan, marked by the white arrow in Figure 4.9A, is shown in Figure 4.9B. The anterior and posterior surfaces of the cornea are easily identified as the first and last spikes in the image, and corneal thickness is measured by calculating the longitudinal displacement between the positions of these two maxima. A computer program that identified these two peaks and calculated the distance between them was developed and is described in Section 5.4. After running this program, each individual A-scan was checked to ensure that the program had correctly identified the peaks. In the few cases in which the system had failed to identify the peaks correctly, the cursors were manually placed in the correct position, thus ensuring that all thickness measurements were correct.

A   B
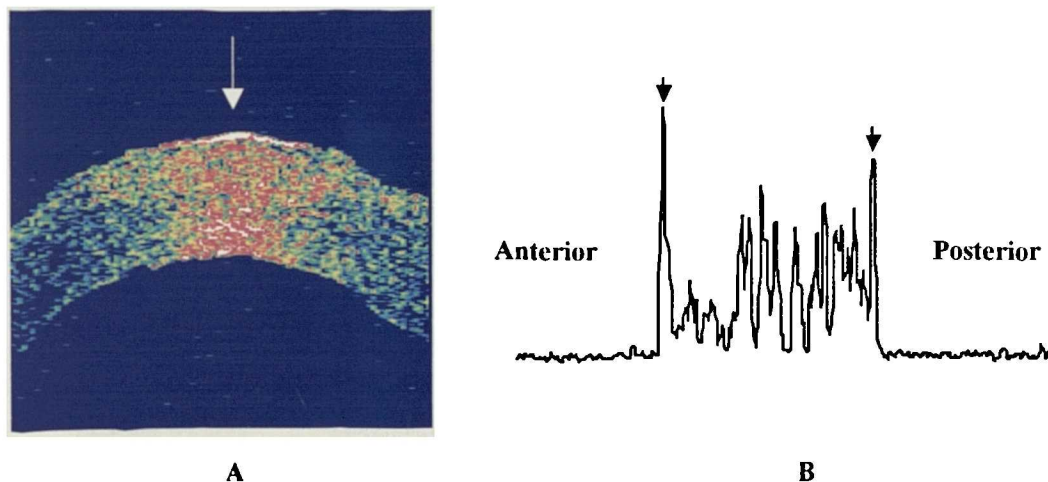
Figure 4.9   *(A) Typical scan through the centre of the cornea. (B) A-scan through the location marked by white arrow in (A). Anterior and posterior corneal surfaces are marked by arrows*

The OCT system is designed to image a convex structure, the retina, and has in-built correction factors to compensate for the curvature of the retina. Thus, when using the system to image a convex structure such as the cornea, the system exaggerates the curvature. Moreover, when the subject is looking straight ahead, the OCT beam is perpendicular to the surface of the cornea only at the centre so measurements made off-centre will overestimate the corneal thickness. In view of this, no attempt was made to quantify peripheral corneal thickness and the study was limited to measuring

only central corneal thickness. For each scan, the apical A-scan was identified, as shown in Figure 4.9, and this was taken to be the central A-scan. Corneal thickness was then quantified from the 21 central A-scans – the central one itself and 10 others on either side of it. Since the approximate length of the whole scan line was 2.5 mm and the scan consists of 100 equally spaced A-scans, these central 21 scans spanned a length of 0.5mm across the cornea. This 0.5 mm section was defined as the central cornea and it was assumed that the corneal surface was relatively flat and perpendicular to the OCT beam in this region. In the reproducibility study 6 scans arranged along the diameters of a circle centered on the center of the pupil were acquired for each subject during each session (using the *Radial Lines* scanning option). In this scanning mode the OCT system acquires a set of 6 scans of equal lengths arranged along 6 diameters of a circle of pre-determined size. Each of these scans takes 1 second to acquire and the system takes a couple of seconds to save each scan. Thus, assuming that there is no patient movement in between scans and thus, that no re-positioning of the scan lines is required, this set of 6 scans should take approximately 30 seconds to acquire. If any patient movement was detected in between scans the whole set was discarded and a new set was acquired. For each of these scans the central 21 A-scans were selected, as explained above, and corneal thickness measurements were made at each of these points. This yielded a total of 120 corneal thickness measurements for each patient arranged at different points along the radial scan lines and 6 repeated measurements at the center, at the point where the 6 scans intersect. This is illustrated in Figure 4.10.
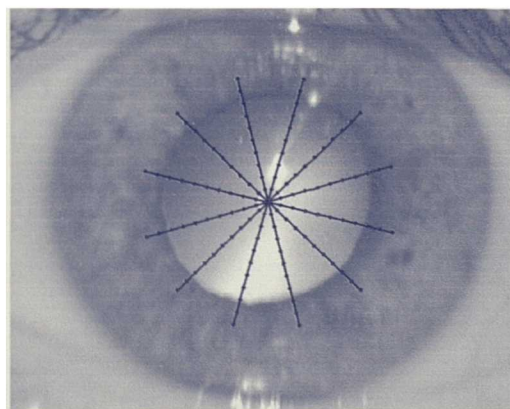
Figure 4.10   *Diagram illustrating the position of the six radial line scans and the locations of the 21 measurement points along each scan line (diagram is not to scale)*

For each patient in the reproducibility study one of the 6 values of corneal thickness at the intersection point of the 6 scans obtained during one session was randomly selected and then the overall average corneal thickness was calculated from this value together with the other 120 thickness values obtained along the radial lines. These results were used to calculate the coefficients of inter-session and inter-operator reproducibility. Graphs of differences against means were plotted for both the inter-operator and the inter-session studies. In both cases the Wilcoxon matched paired test (5% significance level) was also used to establish whether there was any statistically significant difference between measurements made during different sessions or by different operators.

Coefficients of repeatability were calculated from the ten consecutive vertical and horizontal scans for each of the 3 subjects participating in the repeatability study.

In order to establish the characteristics of OCT corneal scans in the normal population the overall mean and standard deviation of the corneal thickness measurements were calculated. The 5th to 95th percentile range was also calculated. Separate means for the males and females were also calculated in order to investigate whether there were any gender-related statistically significant differences in corneal thickness. Thickness values were not corrected for refractive index since the refractive index adopted by the system (1.38) and that of the cornea (1.376) are very similar.

Results

Inter-operator reproducibility: For each subject the overall average corneal thickness was calculated for operator 1 and operator 2. The coefficient of reproducibility was then computed from these values and was found to be 0.4 %. Figure 4.11 shows the graph of differences against means for the average corneal thickness. All values fall within 2 standard deviations of the mean. From this graph, the 95% limits of agreement (LoA), defined as mean inter-operator difference in thickness ± (2 × standard deviation of differences), were approximately – 3 to + 3 μm. The Wilcoxon paired measurement test (5% significance level) was also performed on the thickness values. No statistically significant differences were found between the two sets of data.

Inter-session reproducibility: Inter-session reproducibility was investigated in a similar way. The coefficient of inter-session reproducibility was found to be 2.2 %. From the graph of differences against mean for the inter-session data (Figure 4.12) it can be seen that 100% of the values fall within 2 standard deviations of the mean. The 95% LoA are approximately −16 + 7 µm. Wilcoxon analysis showed that there was no statistically significant difference between the two sessions.

Average of central corneal thickness values obtained by the two operators (µm)
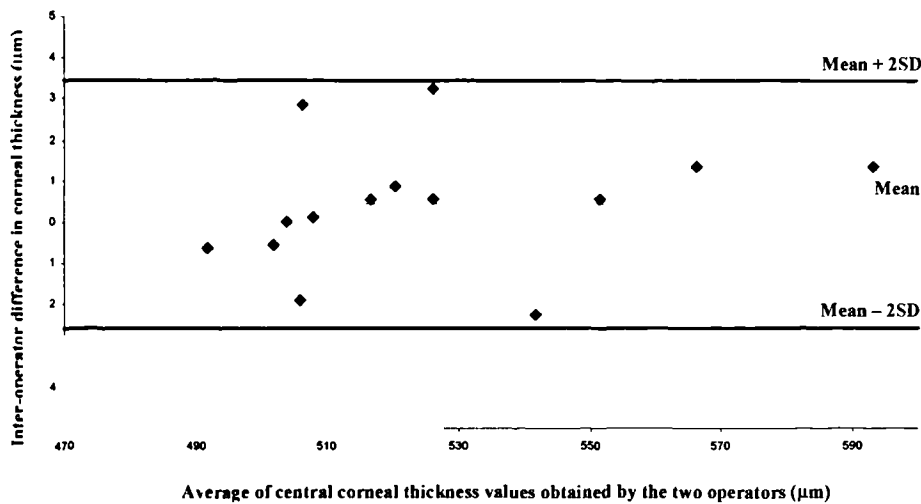
Figure 4.11   *Graph of data from inter-operator reproducibility study. Mean corneal thickness for each subject is plotted against difference in corneal thickness as measured by operator 1 and operator 2.*

Average of central corneal thickness values obtained from the two sessions (µm)

Figure 4.12   *Graph of data from inter-session reproducibility study. Mean corneal thickness for each subject is plotted against difference in corneal thickness as measured from session 1 and session 2.*

Repeatability: For each of the three subjects in the repeatability study, the coefficient of repeatability for the 10 horizontal and 10 vertical scans was calculated. The average for the horizontal sets was found to be 3.5 % whereas that for the vertical scans was 4.6 %. The individual results are displayed in Table 4.9.

Subjects	Horizontal coefficient of Repeatability	Vertical Coefficient of Repeatability
Subject 1	3.2 %	4.2 %
Subject 2	3.8 %	3.9 %
Subject 3	3.5 %	5.9 %

Table 4.9   *Vertical and horizontal coefficients of repeatability for the three subjects in the repeatability study*

Central corneal thickness: The overall mean central corneal thickness was found to be 526 + 28 μm (+ standard deviation). Mean central corneal thickness for males was 528 ± 25 μm, whereas for females the value was 524 ± 33 μm. The median, 5th and 95th percentiles of central corneal thickness were 519 μm, 498 μm and 576 μm respectively. Wilcoxon analysis (5% level of significance) showed that there was no statistically significant difference between the male and female groups. Intra-patient variability, the mean intra-patient standard deviation, was found to be 3.7 μm.

Discussion

With a few very minor modifications the commercially available Zeiss-Humphrey OCT system, originally designed for retinal imaging, can also be used to image the cornea. Several studies give examples of various situations in which OCT proved useful in the evaluation of corneal conditions especially after refractive surgery[21-26]. In addition, OCT may be used to make measurements of corneal thickness and has an advantage over more established methods of measuring corneal thickness in that it is a non-contact and non-invasive technique. Corneal thickness measured with OCT has been found to correlate very well with measurements from ultrasound pachymetry as shown by Bechmann et al[50] who found that in normal subjects values obtained using

OCT were consistently lower than those from ultrasound by a constant value of approximately 50 μm but that the actual correlation coefficient between the two methods was very high. Correlation was also high in a group of patients with corneal oedema, indicating the clinical potential of this technique. Since corneal imaging with OCT does not require contact with the patient's eye, OCT could be used immediately after corneal surgery.

The coefficients of repeatability for vertical and horizontal scanning were found to be less than 6% for all subjects in this part of the study. This indicates that during the same scanning session, corneal thickness measurements are repeatable and there is therefore no need to acquire a large number of readings for a reliable estimate of central corneal thickness.

Coefficients of inter-operator and inter-session reproducibility were 0.4% and 2.2% respectively. The observation that the inter-session reproducibility is slightly higher than the inter-operator reproducibility may be an indication of diurnal variation in corneal thickness between different sessions. Although efforts were made to acquire the second set of scans at approximately the same time of day, but on a different day from the first, it appears that there was nevertheless a small amount of variation. Marsich et al[54] investigated the performance of three devices for determining corneal thickness and found that the Orbscan slitlamp pachymetery system showed the best repeatability (what we have termed inter-session reproducibility) with 95% LoA of - 10 to + 17μm. We obtained 95% LoA of - 16 to 7μm from the inter-session data. This indicates that the performance of the OCT is comparable to that of established methods of evaluating corneal thickness.

The average value for central corneal thickness obtained was 526 ± 28μm. This value is almost identical to the value of 530 ± 32μm, obtained by Bechmann et al[26,50] for normal subjects. This group found that the intra-patient variability with OCT was 4.90μm whereas inter-patient variability was 32μm – these values are similar to our findings. No gender related differences in average values of corneal thickness were found however the sample sizes (7 males and 7 females) were rather small.

This study is limited to assessing only central corneal thickness. Peripheral measurements would have been inaccurate for two reasons. Firstly, at peripheral points the OCT beam would not have been perpendicular to the corneal surface so measurements would have had to be corrected for refraction at the air-cornea interface and secondly, the radius of curvature seen on the corneal scans is overestimated since the system is designed to image a concave rather than convex structure and hence exaggerates the curvature of the cornea. Central corneal thickness measurements, however, have been shown to be both repeatable and reproducible and this indicates that the commercially available OCT system in its present state and with practically no modifications is an accurate and useful tool in assessing and monitoring corneal conditions.

4.5   Conclusions

The performance characteristics of the OCT system must be well established before it can be used in the clinical environment. The studies carried out to scientifically assess the performance of the commercially available OCT system have been described in this chapter. The aim of the initial studies was to assess the fundamental characteristics of the scanner such as its longitudinal resolution and the accuracy and precision of measurements. The results from these studies showed that the experimentally measured resolution was in close agreement with the theoretical resolution and that measurements from the system were accurate and precise. The performance of the scanner in the clinical setting was then assessed by analysing the repeatability and reproducibility of measurements made from a test object and from groups of normal volunteers. In the clinical setting, the currently available OCT scanner is likely to be used for measuring total retinal thickness at the macula, for measuring retinal nerve fibre layer thickness around the optic disc and for measuring central corneal thickness. Different algorithms are used to make these measurements from the OCT data so repeatability and reproducibility were assessed separately for all three cases.

The system appears able to produce highly repeatable and reproducible retinal thickness measurements. This is an exciting finding since it implies that OCT could

be particularly useful in the diagnosis and management of conditions which cause changes in retinal thickness. Increased retinal thickness due to macular oedema is a fairly common sight-threatening complication in various conditions such as diabetes. Since OCT is able to make reproducible retinal thickness measurements with greater resolution than other ocular imaging techniques it is a promising technique for periodic quantitative assessment of retinal thickening in conditions such as diabetes.

The ability of the system to make repeatable and reproducible RNFL thickness measurements is somewhat poorer. The reflections arising from the RNFL appear to be quite susceptible to small variations in set-up and this may cause considerable variation in RNFL thickness from one scan to another. Nevertheless, the repeatability and reproducibility coefficients of global RNFL thickness measurements are both under 15%, which indicates that global RNFL thickness measurements are reasonably repeatable and reproducible. This may be of use in the clinical environment. A system that could reliably measure RNFL thickness to a high degree of accuracy is very desirable since it could improve the early diagnosis of glaucoma. There is therefore considerable incentive to improve the software and hardware features of the present OCT system in order to make it more capable of giving more reliable information on RNFL thickness.

Although the system has been designed for retinal scanning, our studies have shown that it also has potential in quantitative anterior segment imaging. Good quality corneal scans are easily acquired and corneal thickness measurements may be made from the raw data using custom-built software. Our studies on normal volunteers showed that the repeatability and reproducibility of central corneal thickness measurements is comparable to that for retinal thickness measurements. Moreover, these measurements correlate well with those from established methods for measuring corneal thickness and the reliability of the OCT system is comparable to that of these other techniques. This finding is important since, unlike most other methods for measuring corneal thickness, OCT does not require contact with the eye. This fact is likely to make it the technique of choice when measurements of central corneal thickness are required soon after surgery.

Chapter 5

ANALYSIS OF EXISTING SOFTWARE AND ADDITIONAL TOOLS

In the clinical setting it is useful to be able to measure total retinal thickness and thickness of the retinal nerve fibre layer (RNFL). The OCT 2 scanner is supplied with software designed for measuring these parameters from acquired scans. These tools have their limitations and it is important to identify these so as to avoid making incorrect measurements. Since the raw OCT data may be exported, it is also possible for users to write their own software for additional or improved image analysis. This software must be rigorously tested before it is put into clinical use.

5.1   Introduction

One of the main attractions of OCT technology is that the data may be analysed both quantitatively as well as qualitatively. This provides a permanent, numerical record of the anatomical structure of the retina of an individual on a particular occasion, a feature which makes OCT ideally suited for periodic assessment of conditions which affect the structure of the retina. The ability to accurately measure retinal thickness is highly desirable for monitoring conditions such as diabetic macular oedema, in which the extent of macular oedema directly influences the degree of visual loss, and for objectively assessing the efficacy of treatment designed to reduce the amount of macular oedema. There is also growing interest in imaging techniques that can give quantitative information on the retinal nerve fibre layer as this may improve the early diagnosis of glaucoma. In view of this, software algorithms designed to make retinal and retinal nerve fibre layer thickness measurements have been designed and are supplied with the scanner.

In the previous chapter, the repeatability and reproducibility of retinal and RNFL thickness measurements was assessed. The scans used in these studies were rigorously inspected to ensure that the algorithms for identifying the appropriate layers had functioned correctly, and any scans that did not meet these criteria were excluded from these investigations. This chapter deals with the performance of the actual algorithms and describes studies that were conducted to assess the capabilities of these two algorithms and to identify their limitations.

Some additional software was also developed to perform specific functions which could not be performed with the existing OCT software. These additional programs were rigorously tested before being used clinically. The algorithms and testing regimes for this additional software are also described in this chapter.

5.2   The *Retinal Thickness* Tool

5.2.1   Assessment of performance

As its name implies, the *Retinal Thickness* tool is designed for making retinal thickness measurements from an OCT scan. The aim of the algorithm is to identify the vitreo-retinal interface and the anterior surface of the red band corresponding to the RPE-choriocapilaris complex. These boundaries are assumed to be the borders of the neurosensory retina and the retinal thickness is the distance between them. Each pixel in the OCT image represents a longitudinal depth of $4\mu m$ in retinal tissue which is less than the inherent longitudinal resolution of the system, so measurements should be accurate to within around $10\mu m$.

Very little information is available on the algorithm used to identify the retinal borders. The only information supplied with the system states that, after aligning the A-scans and smoothing the data, the retinal borders are identified by looking for the regions of greatest rate of change of intensity in the A-scan as these areas are likely to correspond to the edges, or regions of high contrast. The OCT manual states that this tool cannot be used on scans which traverse the optic nerve head. When the *Retinal Thickness* tool is applied to a particular scan, the scan is smoothed and aligned and the borders identified by the algorithm are drawn on the scan in white.

The retinal thickness data is displayed in graphical format beneath. A study was carried out to assess the ability of the *Retinal Thickness* tool to identify the retinal borders, as accurate detection of these borders is crucial for correct retinal thickness measurements. It was assumed that the retinal borders did indeed correspond to the vitreo-retinal interface and the anterior surface of the RPE-choriocapillaris complex.

Methods

The *Retinal Thickness* tool was applied to 110 macular scans. Fifty scans were acquired from the macula of 10 normal volunteers (5 scans from each) in order to assess the success rate of the algorithm when applied to the normal retinal contour. A further 50 scans were acquired from 10 patients with a clinical diagnosis of macular oedema – this condition causes thickening of the retina, thereby altering the retinal contour. Since quantitative assessment of retinal thickness is of particular clinical importance in this group of patients, assessment of the performance of the algorithm in such situations was considered very important. Finally, 10 scans from 5 patients with clinically diagnosed full-thickness macular holes and 5 patients with pseudo or lamellar holes were included in the study in order to assess the performance of the algorithm in situations where the retinal structure is dramatically altered.

The performance of the algorithm was assessed qualitatively by observation of the retinal boundaries drawn on each of the scans. Successful identification was defined as correct identification of both retinal borders at each point along the scan line. Each instance of incorrect identification of the retinal borders at any point along the scan line was recorded.

Results

Normal scans: Out of the 50 normal scans analysed, the algorithm correctly identified the retinal borders at every point along the scan in 21 cases (from 9 different subjects). An example of correct identification of retinal borders is shown in Figure 5.1.
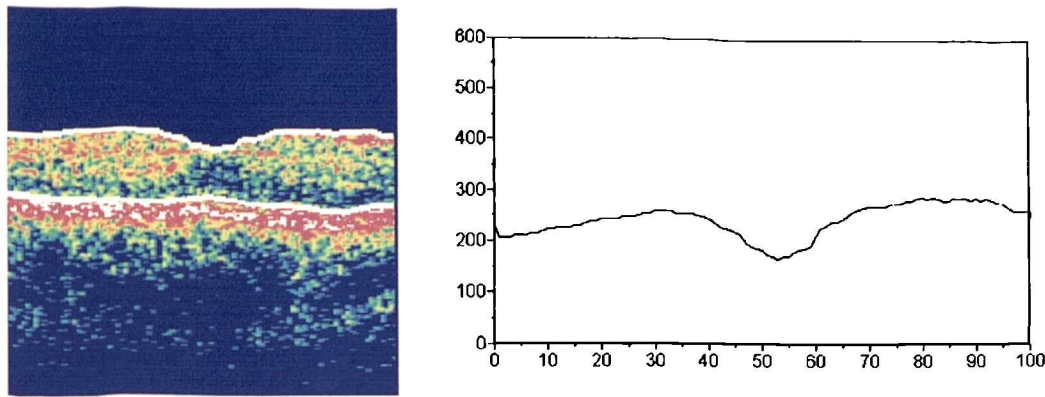
Figure 5.1   *Correct identification of retinal borders – OCT scan and corresponding retinal thickness plot*

In another 26 cases, there was misidentification of one or other of the retinal borders at some points along the scan. Although the retinal borders were misidentified in a few locations, these errors were small and did not affect the entire length of the scan, so useful measurements could still be made from these scans. There were three patterns of misidentification in these cases. In 11 out of the 26 cases (from 8 different subjects) the identified anterior retinal surface was rather jagged as shown in Figure 5.2A. The reason for this pattern of misidentification was not evident from examination of the raw data scans. In another 12 cases (from 9 different subjects), the algorithm failed to identify the borders at isolated locations along the scan, thus creating thickness 'glitches' on the retinal thickness plot (Figure 5.2B). These 'glitches' often seemed to be caused by small movement artefacts. In the remaining 3 cases (from 3 different subjects), the posterior border was incorrectly identified at the fovea, causing a falsely high foveal thickness reading (Figure 5.2C). These errors probably also resulted from small movement artefacts.

In 3 out of the 50 cases (from 2 different subjects), the algorithm completely failed to identify either the anterior or posterior retinal borders, leading to grossly erroneous retinal thickness measurements (Figure 5.3). Failure of the algorithm was not consistent - other scans acquired from the same area in both these subjects gave reasonable results when the *Retinal Thickness* tool was applied. In normal control subjects, spots of moderate reflectivity within the vitreous are frequently observed. These are likely to be small intra-vitreal floaters. If the reflectivity of these spots exceeds the noise threshold, the *Retinal Thickness* algorithm may erroneously

identify them as the retinal border. Although this is a plausible explanation for the failure of the algorithm in these two subjects, it should be noted that the intra-vitreal reflections in these 3 scans did not appear any more significant than in other scans in which the retinal thickness was correctly measured.

A   B   C
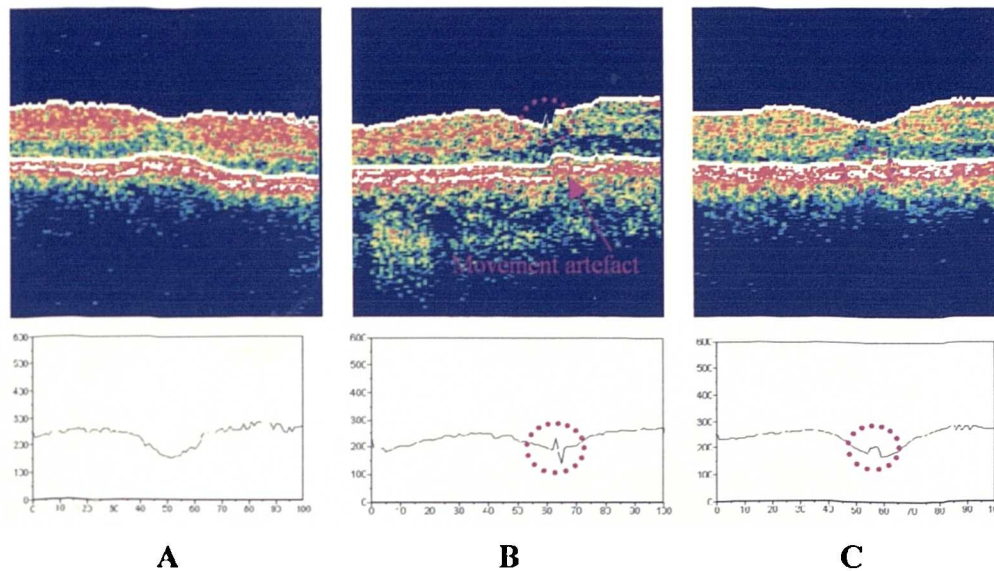
Figure 5.2   *Slight errors in identification of retinal borders. (A) The identification of borders is essentially correct however, the algorithm shows the retinal contour to be very jagged. (B) Incorrect identification of the anterior retinal surface at one point causes a glitch in the retinal thickness plot. (C) Misidentification of the posterior retinal border at the fovea, leading to falsely high foveal thickness*

Scans from patients with diabetic macular oedema: Out of the 50 scans in this category, the retinal borders were correctly identified in 17 cases (at least one from each of the 10 patients in this group). Correct identification of the anterior retinal surface occurred even in cases where the intensity of the scan was fairly low. In a further 24 cases (from 9 patients), there was slight misidentification of the borders, similar to the examples shown in Figure 5.2A and Figure 5.2B. In another 7 scans (from 6 patients) the algorithm failed to correctly identify longer tracts of retinal borders (Figure 5.4).
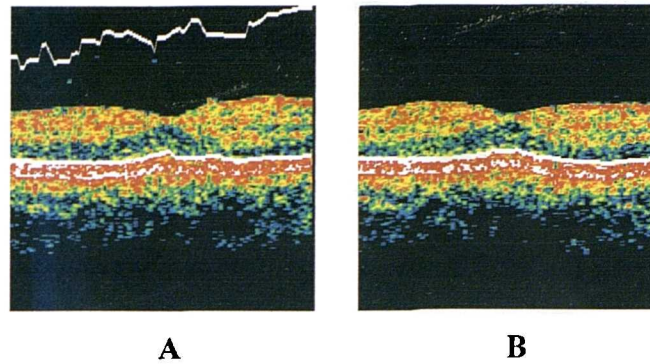
Figure 5.3   *Failure of the algorithm to identify the anterior retinal surface. (A) The algorithm erroneously selects intra-vitreal reflections as the anterior retinal surface. (B) In another subject, the algorithm completely fails to identify the anterior retinal surface.*
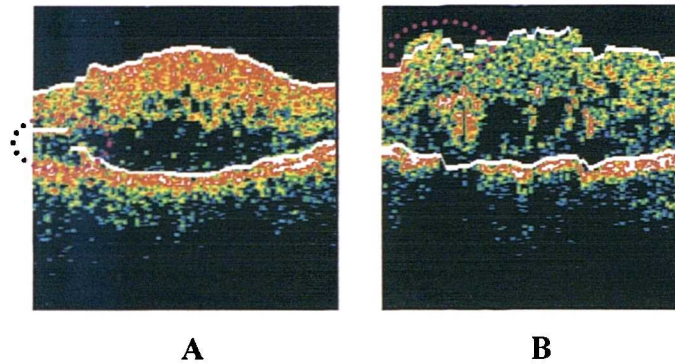
Figure 5.4   *Examples of failure of the algorithm to identify considerable amounts of the retinal borders in patients with macular oedema. (A) Misidentification of the posterior border. (B) Misidentification of the anterior border*

The algorithm completely failed to identify the anterior retinal surface in 2 scans (from 2 different patients). In one of these cases, the surface of the retina was severely puckered due to traction caused by a detaching vitreous face.

Scans from patients with macular holes: The *Retinal Thickness* tool could not cope with the discontinuity in the retinal structure caused by the macular hole. In three of the 5 patients with full-thickness macular holes, an operculum was present over the hole and the retinal thickness algorithm considered this to be the anterior retinal surface (Figure 5.5A). In the other 2 patients, there was a full thickness macular hole

with no operculum (Figure 5.5B). In these cases, the algorithm assumed that the anterior retinal border bridged across the macular hole. The algorithm also failed in the 5 patients with pseudo or lamellar holes (Figure 5.5C).

A   **B**
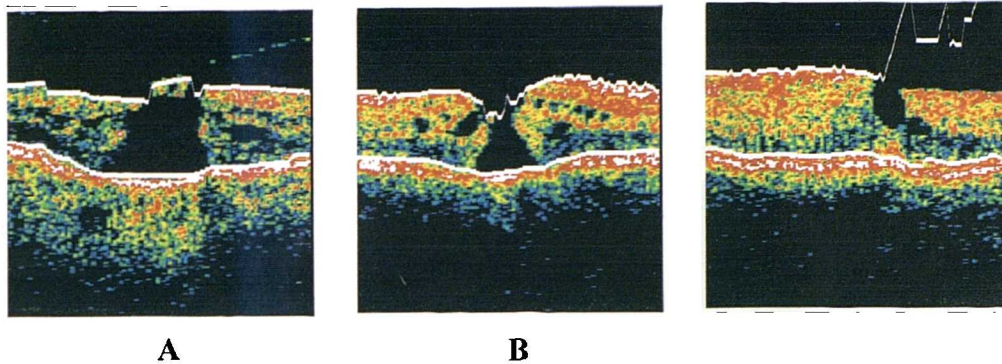
Figure 5.5   *Performance of the* Retinal Thickness *tool on scans from patients with macular holes. (A) Macular hole with operculum – the algorithm considers the operculum to be part of the retinal surface (B) Macular hole without operculum – the algorithm causes the anterior border to bridge across the hole. (C) Pseudohole – the algorithm fails when a perceived break in retinal tissue is encountered.*

Discussion

In the 50 scans from normal subjects, the *Retinal Thickness* tool completely failed in only 3 cases. The reason for failure in these cases was not evident from the scans although it was likely to be due to spots of relatively high reflectance within the vitreous. The *Retinal Thickness* tool was subsequently used successfully on repeat scans acquired from these same subjects – the fact that the algorithm seems to work on some scans but not on other almost identical ones suggests that the problem may be caused by particles such as floaters which may be present in one scan but not in another. Given that the problem does not seem consistent, it is unlikely to cause severe difficulties in the clinical setting.

Slight errors in the identification of the borders were observed to occur fairly frequently and were likely to be caused by small movement artefacts. Although, according to the documentation supplied by the manufacturer, the raw data is

smoothed and aligned prior to applying the edge detection algorithm, clearly the alignment feature needs to be improved. Misidentification of the retinal borders causes 'glitches' in the retinal thickness plot which are usually fairly easy to spot. The data in the thickness plot may be exported and thus, these errors may be manually corrected.

The performance of the *Retinal Thickness* tool in patients with macular oedema was found to be comparable to that in patients with a normal retinal contour. This is a reassuring finding since one of the main clinical applications of retinal thickness measurements is in the quantitative assessment of patients with macular oedema.

The *Retinal Thickness* tool cannot, however, cope with situations like full-thickness, lamellar or pseudo macular holes, which cause a real or apparent break in the normal retinal architecture. This is only likely to cause problems when attempting to distinguish between lamellar and pseudo holes (see section 6.2) which would require measuring the thickness of the residual retinal material within the hole. In these cases it is recommended to use an alternative measuring method such as the measurement callipers.

Overall, the performance of the *Retinal Thickness* tool is satisfactory, however there is clearly still room for improvement. The alignment of the individual A-Scans should be improved, as the residual movement artefacts seem responsible for many of the errors in edge detection. In addition, the algorithm should be able to determine whether the first region of high reflectance encountered is part of the retinal surface or whether it is simply a floater within the vitreous.

5.2.2 Comparison of different methods for measuring retinal thickness

Retinal thickness measurements may be made in three different ways. The *Retinal Thickness* tool, described above, automatically identifies the retinal borders, computes the retinal thickness and displays the retinal thickness along the scan in graphical form. The retinal thickness at any point along the scan, as computed by the *Retinal Thickness* tool, may be obtained by using the *Track* option. The measurement callipers offer an alternative method for measuring thickness – these may be placed anywhere on the scan and a readout of the distance between them is displayed. This

option is especially useful for making measurements from scans in which the *Retinal Thickness* tool has failed to correctly identify the retinal borders. One drawback of this method is that the calliper tool may only be used on the screen which displays the results from the *Retinal Thickness* tool. The size of the scan on which the callipers must be positioned is rather small and the retinal borders identified by the algorithm are drawn on the scan, thus obscuring part of it. This may make it difficult to correctly position the callipers. When the retinal thickness proves impossible to determine from these two methods, the only remaining alternative is to make measurements directly from the raw data. The *Scan Profile* option may be used to display the raw data plot for each of the A-Scans within a scan. Two cursors may then be placed anywhere along the A-Scan plot and the thickness of retinal tissue between the two cursors may then be computed from their relative positions. The *Retinal Thickness* algorithm assumes the retinal borders to be the vitreo-retinal interface and the anterior surface of the RPE-choriocapillaris complex. These are both regions of high contrast and the reflections from these two surfaces are generally fairly easy to identify on the A-scan plots. In Figure 5.6 these borders are marked by the two cursors.
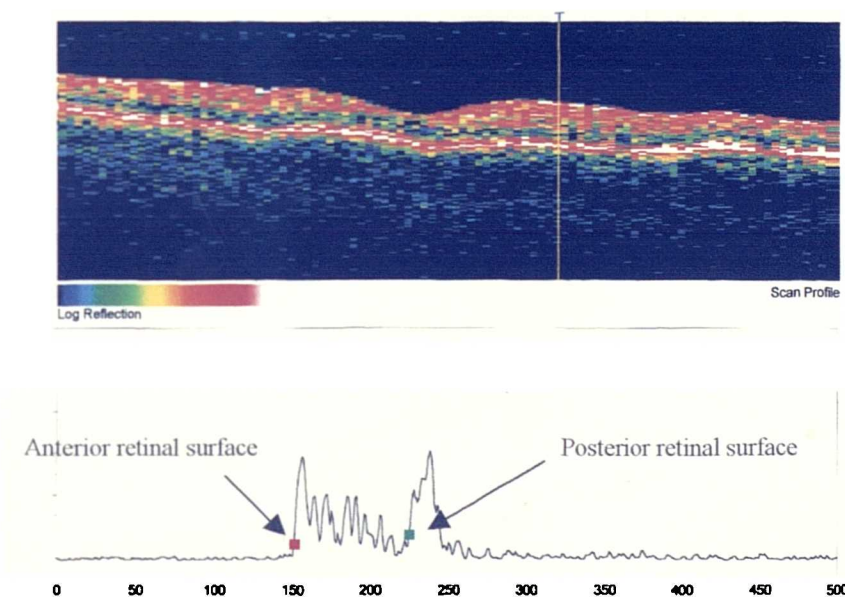
Figure 5.6   *Graphical representation of the data from the A-scan at the marked location. The vitreo-retinal interface and anterior surface of the choriocapillaris complex are marked by cursors.*

Since retinal thickness may be assessed in three different ways, a study was carried out to compare the results obtained from the three methods.

Methods

Ten scans through fixation acquired from 10 normal volunteers were used for this study. Retinal thickness measurements from three specific points along the scan line were made using each of the three different measuring methods. The three selected points were the deepest point within the foveal pit, corresponding to the thinnest part of the retina, and the two points on either side of the foveal pit where retinal thickness is at a maximum. These points were selected because they were easily identifiable anatomical landmarks which helped to ensure that measurements were made from approximately the same points on each scan.

The *Retinal Thickness* tool was applied to each of the scans in the study and the *Track* option was used to find the retinal thickness at each of the specified points. The A-Scan number at each of the three points of measurement was also recorded. Any scans in which the *Retinal Thickness* algorithm had clearly failed to identify the retinal borders at the measurement points were discarded from the study. The callipers were then placed at the vitreo-retinal interface and at the surface of the RPE-choriocapillaris layer on the scan and the thickness measurements were recorded. Finally the *Scan Profile* option was applied to the scan. Thickness measurements were made from the A-Scans whose positions had been recorded in the first part of the analysis. In order to maintain consistency with the definition of retinal surfaces used by the *Retinal Thickness* algorithm, the cursors were placed on the rising edge of the peaks corresponding to the reflections from the vitreo-retinal interface and surface of the RPE-choriocapillaris layer, as shown in Figure 5.6.

Analysis

A total of 30 sets of retinal thickness values were acquired for this study. Values obtained from the three techniques were compared using the techniques recommended by Bland and Altman[36]. Measurements were compared in pairs, callipers against *Retinal Thickness* algorithm, A-Scan measurements against

callipers, and A-Scan measurements against *Retinal Thickness* algorithm. The 95% limits of agreement for each pair of techniques were determined from the standard deviation of measurement differences and mean difference values.

Results

The average retinal thickness values at each of three measurement points obtained from the three techniques are shown in Table 5.1 and the 95% limits of agreement are shown in Table 5.2.

	Algorithm (μm)	Callipers (μm)	A-Scan (μm)
Fovea	170.9 ± 20.7	178.8 ±18.5	166.0 ± 17.8
Nasal	286.8 ± 26.0	280.3 ± 24.3	274.4 ± 31.2
Temporal	271.2 ± 25.8	271.7 ± 16.6	277.2 ± 26.1

Table 5.1   *Table showing the average retinal thickness at each of the three measurement points using the three different measurement techniques*

	Callipers vs Algorithm (μm)	A-scan vs Callipers (μm)	A-Scan vs Algorithm (μm)
Upper Limit	23.9	47.5	43.9
Lower Limit	-22.7	-56.3	-51.4

Table 5.2   *Table showing the 95% limits of agreement for each pair of techniques*

The average thickness values obtained from the three techniques are fairly similar, however the limits of agreement indicate that the best agreement is between the callipers and algorithm measurements. These results indicate that 95% of measurements made by the callipers will be up to 24μm above to 23μm below those from the algorithm, whereas those made directly from the A-Scan will be up to 48μm greater to 56μm less than those made with either the callipers or the algorithm.

Discussion

Measurements made with the callipers and those made from the algorithm may differ by up to approximately 24μm. In Chapter 4, the median retinal thickness was found to be 238μm, so the difference between methods is unlikely to differ by more than around 10%. Although this is a fairly reassuring finding, it should be borne in mind that there is a certain amount of subjectivity involved in positioning the cursors so this method should really only be used when measurements from the retinal thickness plot are not possible. One such clinical situation arises when attempting to distinguish between pseudoholes and lamellar holes. As shown in the previous section, the algorithm fails to give correct readings of the thickness of residual material at the hole, so in this situation it would be necessary to use the callipers.

Measurements made directly from the A-Scan are likely to differ from those made with the other two techniques by up to around 50μm or 20%. In the clinical setting, discrepancies of this order may be of clinical significance, so measurements made directly from the A-Scans should be used only as a last resort. There is a strong subjective element associated with the positioning of the cursors on the A-Scan plot and this is probably the cause of the larger difference observed with this method. It is therefore likely that experience and practice would enable the user to position the cursors more accurately and obtain results that agree more closely with those from the other two methods.

The study described in this section was designed to investigate the agreement of retinal thickness measurements made using three different methods. Measurements from two of these methods, using the callipers and directly from the A-Scan plot, are somewhat subjective, as they require the user to make a decision on where to position the callipers on the scan or the cursors on the A-Scan. The *Retinal Thickness* tool, on the other hand, identifies the retinal borders numerically and, provided it does this correctly, is the most objective method of the three. If it is not possible to make measurements from the retinal thickness plot, then it is acceptable to use the callipers. Measurements made directly from the A-scan are the least accurate. For correct results, the user needs to correctly identify the signals from the two retinal borders and then decide at which point along the slope to position the two cursors. In

scans of poor quality, this may be especially tricky. In view of this, measurements made directly from the A-Scan should be seen as a last resort.

5.3   The *RNFL Thickness* Tool

5.3.1   Assessment of Performance

The layer of relatively high reflectance which is situated just beneath the vitreo-retinal surface on typical OCT scans is thought to be the retinal nerve fibre layer (RNFL). In glaucoma, the RNFL around the optic disc becomes thinner and exhibits defects. Since glaucoma is a progressive condition which may be treated there is considerable incentive to develop more sensitive tools for early diagnosis of the condition. The ability of OCT to image the RNFL may therefore have diagnostic potential.

The scanner is supplied with a software feature, the *RNFL Thickness* tool, designed to identify the borders of the RNFL and measure its thickness. The front surface of the RNFL is taken to be the vitreo-retinal interface and the algorithm for identifying this is therefore the same as that used in the *Retinal Thickness* tool. Although the RNFL has higher reflectance than the layers immediately beneath it, its posterior border is not as well defined as the posterior retinal border and edge-detection techniques, as used in the *Retinal Thickness* tool, fail to detect it. The OCT 2 algorithm sets a threshold for each A-Scan based on the maximum intensity within that particular A-Scan. It then starts analysing pixels in turn, starting from the layer immediately anterior to the RPE-Choriocapillaris complex and moving upwards until it encounters the first pixel whose intensity rises above the threshold. This point is defined as the posterior border of the RNFL. The detected anterior and posterior borders are drawn on the scan in white and black respectively and the corresponding RNFL thickness plot is displayed in graphical format beneath. A study similar to the one described in Section 5.2.1 was conducted in order to assess the performance of the *RNFL Thickness* tool.

Methods

The *RNFL Thickness* tool was applied to 50 circular scans centred on the optic nerve head. These scans were acquired from 12 normal volunteers with no family history of glaucoma. The performance of the algorithm was assessed qualitatively by inspection of the RNFL boundaries drawn on the scan. Each instance of incorrect identification was recorded. It was decided not to analyse scans from patients with conditions affecting the RNFL as part of this study – the reason for this is given in the *Results* section below.

Results

Out of the 50 scans analysed, the algorithm correctly identified the RNFL borders at every point along the scan line in 33 cases (from 11 subjects). An example of correct identification of borders is shown in Figure 5.7. In the normal eye, the RNFL thickness around the optic nerve head varies quite considerably due to bundling of the nerve fibres superiorly and inferiorly, so even when the RNFL borders are correctly identified, the RNFL border appears somewhat jagged. It was therefore not possible to determine whether the observed jaggedness was due to the actual variation of the RNFL thickness or whether it was a result of small errors in boundary detection.
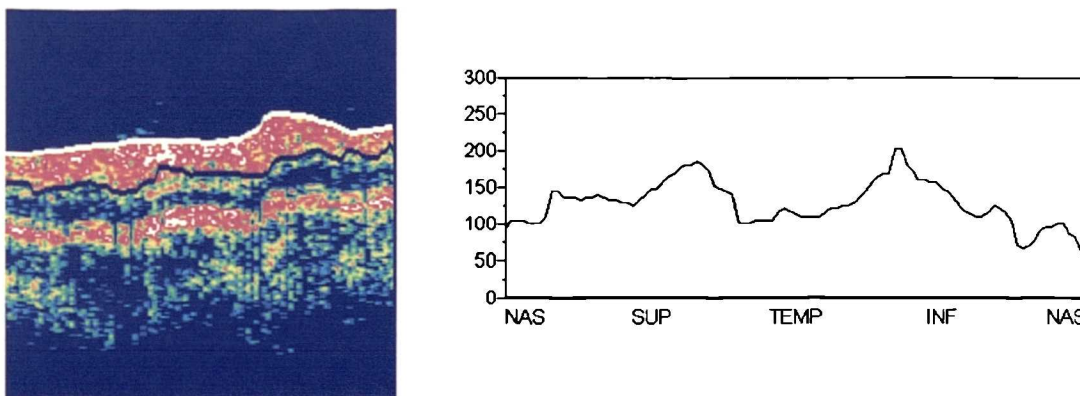
Figure 5.7   *Correct identification of RNFL borders – OCT scan with marked RNFL borders and corresponding RNFL thickness plot.*

In another 8 cases (from 6 subjects) the algorithm failed to identify a few points along the RNFL borders – these errors were fairly small and did not affect the entire

length of the scan, so useful measurements could still be made from the scans. These errors were probably caused by small movement artefacts. In a further case, portions of the anterior border were misidentified due to moderately reflective regions within the vitreous (Figure 5.8).
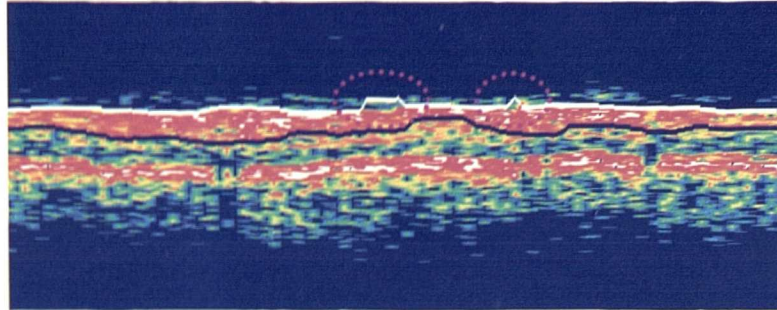
Figure 5.8   *Incorrect identification of the anterior RNFL border due to reflections from within the vitreous.*

In the remaining 8 scans (from 5 subjects) the algorithm erroneously showed zero RNFL thickness in part of the scan (Figure 5.9). Other scans from the same 5 subjects showed normal RNFL thickness. In Chapter 4 the reflectivity of the RNFL was shown to be highly susceptible to imperceptible eye movements. The observations from this study have shown that in some scans, the reflectivity of the RNFL at certain points fell below the threshold selected by the algorithm and thus no posterior RNFL border was identified. In the light of these findings it was decided not to include scans from patients with conditions such as glaucoma in this study. If a scan from a glaucomatous patient showed regions of zero RNFL thickness, it would be difficult to determine whether these were manifestations of true RNFL thinning or whether they were the result of low RNFL reflectance and poor boundary delineation.
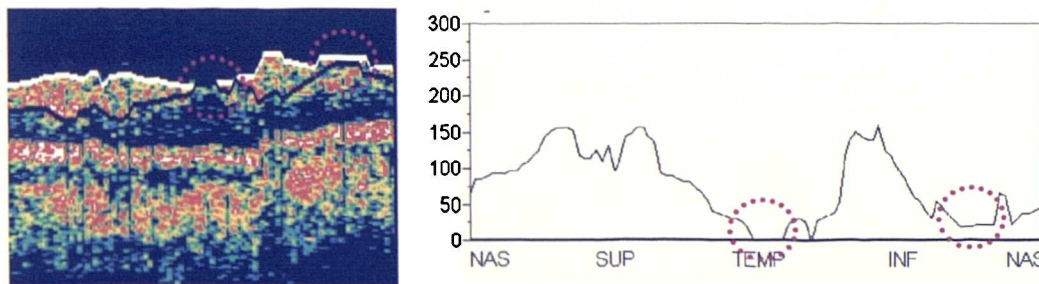
Figure 5.9   *Scan from a normal subject – the algorithm has erroneously detected zero or close to zero RNFL thickness at two locations*

Discussion

The initial impression from the results of this study is that the success rate of the *RNFL Thickness* tool (33/50 correctly identified scans) exceeds that of the *Retinal Thickness* tool (21/50 correct scans). However, one clear shortcoming of this study was the subjectivity associated with deciding whether the *RNFL Thickness* algorithm had correctly identified the RNFL borders. The posterior border of the RNFL is not sharply defined and, when studying a particular scan it was often difficult to determine its position with certainty. This implies that some of the scans that were judged to have correctly identified RNFL boundaries, may, in fact, have been subject to some errors. It was also hard to determine whether jaggedness in the RNFL thickness plot was due to real variations in RNFL thickness or errors in boundary detection. In view of these two points, it is likely that the number of scans with correctly identified borders has been slightly over-estimated in this study. Nevertheless, the number of apparently correctly identified scans is encouraging.

Since the anterior surface of the RNFL is considered to be the vitreo-retinal surface, the *RNFL Thickness* algorithm identifies this in the same way as the *Retinal Thickness* tool. It is therefore not surprising to observe the same types of errors - incorrectly identified points due to movement artefacts or reflections from floaters or other intra-vitreal particles. These errors were not consistent in any of the subjects examined, so in the clinical setting, the problem could be overcome by acquiring several repeat scans.

The *RNFL Thickness* algorithm runs into difficulties with scans that have reduced RNFL reflectivity. The reflections from the RNFL seem to vary considerably from one scan to another and this leads to inconsistencies in boundary detection and consequently, somewhat poor repeatability of RNFL measurements. It is also difficult to determine with certainty whether areas of zero RNFL thickness in glaucomatous patients are due to genuine RNFL thinning. It is clear from this, and other related studies described in Chapters 3 and 4, that imaging of the RNFL is not optimal in the OCT 2 system.

The overall conclusion from this study is that, provided the reflectance of the RNFL is not reduced by incorrect positioning or setting-up, the performance of the *RNFL Thickness* tool is comparable to that of the *Retinal Thickness* tool. Problems arise when the reflectivity of the RNFL is reduced either because of a clinical condition such as glaucoma, or because of non-optimal scanning set-up. In these situations, the algorithm often totally fails to identify the posterior RNFL border at several points along the scan line. When this happens, it is advisable to take several repeated readings in order to try to establish whether these observations are consistent or not.

5.3.2 Comparison of different methods for measuring RNFL thickness

RNFL thickness may be measured using the *RNFL Thickness* tool, the callipers and directly from the A-Scan. The RNFL Thickness tool described in Section 5.3.1 assumes that the vitreo-retinal interface corresponds to the anterior surface of the RNFL and identifies the posterior RNFL surface as the region anterior to the RPE-choriocapillaris complex where the pixel value rises above a calculated threshold. According to this algorithm the RNFL surfaces on a typical A-Scan would be roughly at the positions shown in Figure 5.10.

As with the *Retinal Thickness* tool, measurements may sometimes have to be made using the callipers or directly from the A-scans, if the algorithm has failed to correctly identify the RNFL borders. A study similar to that described in Section 5.2.2 was carried out to compare the performance of these three measuring tools.
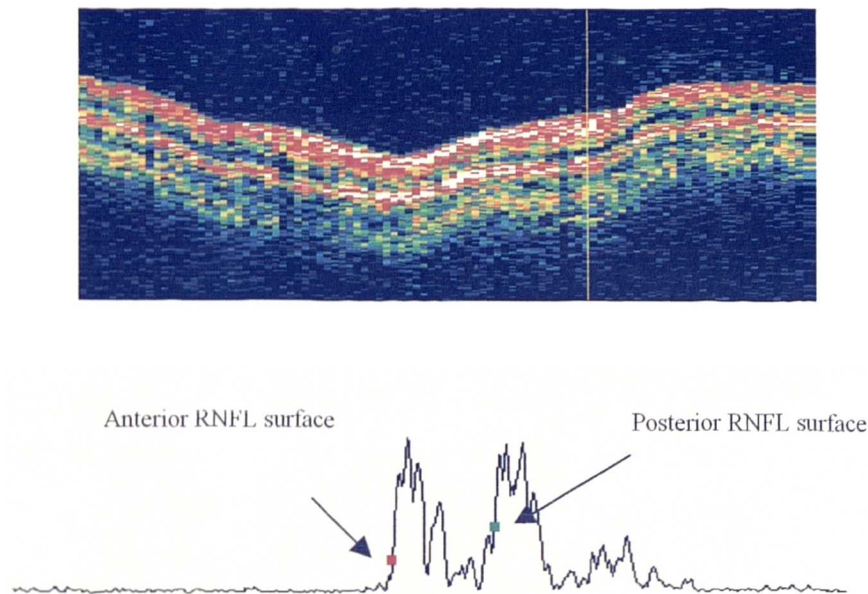
Figure 5.10   *Graphical representation of the A-scan at the marked location. The surfaces of the RNFL, as defined by the* RNFL Thickness *tool algorithm are marked by cursors.*

Methods

Fifteen circular scans centred on the optic nerve head were acquired from 15 normal volunteers. The *Nerve Head R= 1.73mm* scanning option was used. Measurements were made from two specific points along the scan line using the three measurement methods. The selected points were the superior and inferior points of the scan where the RNFL thickness was at a maximum. These points were chosen because they were fairly easy to identify, thus ensuring that measurements were made form approximately the same points on all scans.

The *RNFL Thickness* tool was applied to each of the scans and the *Track* option was used to find the thickness at the thickest superior and inferior points. The A-scan number at these two points was also noted. Any scans in which the algorithm clearly failed to correctly identify the RNFL borders at the measurements points were discarded from the study. The callipers were then placed at the presumed borders of the RNFL at the two measurement points and the readings were recorded. Finally the *Scan Profile* option was applied to the scan and thickness measurements were made

from the A-scans at the two measurement points by placing the cursors in the positions shown in Figure 5.10.

Analysis

A total of 30 sets of RNFL thickness values were acquired from this study. The comparison of the three measurement methods was carried out as described in the *Analysis* section of Section 5.2.2.

Results

The average RNFL thickness values at each of the two measurement points obtained from each of the three techniques are shown in Table 5.3. 95% limits of agreement are shown in Table 5.4.

	Algorithm (μm)	Callipers (μm)	A-Scan (μm)
Superior	185.7 ± 18.6	180.3 ± 17.1	219.6 ± 40.0
Inferior	177.7 ± 18.7	175.2 ± 16.2	208.8 ± 33.6

Table 5.3   *Table showing the average RNFL thickness at each of the three measurement points using the three different measurement techniques*

	Callipers vs Algorithm (μm)	A-scan vs Callipers (μm)	A-Scan vs Algorithm (μm)
Upper	20.2	110.6	96.5
Lower	-28.1	-37.7	-31.5

Table 5.4   *Table showing the 95% limits of agreement for each pair of techniques*

The agreement between the measurements made using the *RNFL Thickness* tool and those from the callipers is good. From Table 5.3 and Table 5.4, it can be seen that the average RNFL thickness measured by the two techniques are very similar and the 95% limits of agreement indicate that most measurements made by the callipers will range from up to 20μm greater to 28μm lower than those from the algorithm.

Measurements made directly from the A-Scan, on the other hand, are somewhat higher than those from the other two techniques. This is evident both from the average RNFL thickness values as well as from the 95% limits of agreement, which are clearly biased towards the upper limit.

Discussion

In Chapter 4, the median RNFL thickness values in the superior and inferior quadrants were shown to be 137μm and 124μm respectively. These values are lower than those in Table 5.3 because they represent the median from the entire quadrant as opposed to a single measurement at the thickest point within the quadrant. Using these median values, measurements from the callipers and the algorithm may differ by up to approximately 20%, which may be significant in the clinical context. The reason for this discrepancy is likely to be due to incorrect positioning of the posterior calliper. Correct identification of the posterior RNFL border by inspection of the scan is rarely straightforward and consequently, errors in positioning of the callipers are to be expected. The algorithm identifies this border numerically, and, provided it has worked successfully, should be used wherever possible. Although the limits of agreement between the two techniques are similar to those established for total retinal thickness, the discrepancy between these two techniques is more significant because RNFL thickness is considerably less than total retinal thickness. If periodic monitoring of RNFL thickness is required in the clinical setting, it is recommended to consistently use the same method for measuring the RNFL thickness.

Measurements made directly from the A-Scan clearly over-estimate the RNFL thickness, as measured by the other two techniques. There is also greater variability in measurements as shown by the higher standard deviation of the A-Scan measurements. The subjective element associated with positioning of the cursors is even greater than that associated with the positioning of the callipers. Correctly identifying the portion of the A-scan signal corresponding to the posterior RNFL face is more difficult than identifying the anterior surface of the RPE-choriocapillaris complex and consequently, RNFL thickness measurements made from the A-scan are less accurate than total retinal thickness measurements. The findings from this

study indicate that measurements of RNFL thickness directly from the A-scan should be avoided in the clinical setting.

5.4 An algorithm for measuring central corneal thickness

OCT is becoming increasingly popular for imaging the cornea. Since the currently available OCT scanner is designed exclusively for imaging the retina, no tools for measuring corneal thickness are provided. Corneal thickness measurements can, of course, be made using the callipers or directly from the raw A-Scan, however, measurements can only be made from one point at a time and are subjective since they require the user to decide on the location of the corneal surfaces. In order to facilitate central corneal thickness measurements, an algorithm was developed for automatically identifying the corneal surfaces and computing an average value for central corneal thickness based on measurements from the central 21 A-scans.

5.4.1 Description of the algorithm

The program prompts the user to enter the name of the exported *.raw* file containing the raw data from the corneal scan. It then displays the scan with the identified corneal borders marked in blue. Since the cornea is a convex structure, and the OCT scanner is designed to image a concave structure, the OCT beam is perpendicular to the corneal surface only close to the centre of the cornea. Meaningful measurements can therefore only be made from this portion. This algorithm is designed to automatically select the A-Scan at the apex of the cornea and to calculate the average CCT from this apex scan and the 10 scans on either side of it. The average central corneal thickness (CCT), calculated from these central 21 A-Scans is displayed on the results screen. The user has the option of viewing each of these 21 A-Scans individually. The location of the automatically identified corneal borders is marked by cursors on each A-Scan. The position of these cursors may be varied manually and the average CCT is updated accordingly. A text file containing the 21 corrected thickness values is also exported.

The algorithm may be broken down into the following steps:

1. **Read the raw data into a 100 × 500 array.**

   Data from a single scan is exported from the OCT system as a file with extension *.raw*, which consists of the 50,000 data points (500 points from each of the 100 A-Scans). This data was read into a 100 × 500 array of integers for processing.

2. **Identify the apex A-Scan.**

   The reflections from the corneal surface fall off quickly with distance from the apex and they tend to be strongest at the centre of the cornea. The algorithm used this fact to identify the apex scan. It first identified the anterior surface of the cornea and then looked at the combined intensity of the 10 pixels immediately beneath it. The scan with maximum intensity in this region was taken to be the apex scan. Subsequent steps were carried out only on this scan and 10 scans on either side of it.

3. **Find the corneal boundaries on the central 21 A-Scans.**

   A typical A-Scan from a corneal scan is shown in Figure 5.11. The two marked peaks were considered to be the front and back surfaces of the cornea. This was a reasonable assumption given that the strongest reflections occur at regions of large changes in refractive index. The first step in identifying these two peaks was to establish a background noise threshold. The average intensity from the first 50 and last 50 pixels from within each A-scan was calculated. If the operator had positioned the scan roughly in the centre of the screen, these 100 pixels would contain only noise. If the scan had been positioned at the top or bottom of the screen, then only the front or back 50 would contain only noise. The algorithm compared the averages from the front and back 50 pixels. If these values were found to be within 50 units of each

other, all 100 values were used to compute the noise threshold. If the difference exceeded 50 units, then the noise threshold was taken to be the smaller average. Starting from the first and last pixel in each of the selected A-Scans, the algorithm then identified the first pixel whose intensity exceeded 1.5 times the noise threshold. The maxima closest to this point were then considered to be the front and back surfaces of the cornea.

4. **Compute the corneal thickness from the 21 central A-Scans.**

The refractive index of the cornea is almost equal to that of the retina and hence, no corrections were made. As with retinal scanning, each pixel therefore corresponded to 4μm in corneal tissue. Corneal thickness was computed by multiplying the difference in position between the front and back corneal surfaces by 4.

5. **Compute the average CCT.**

The average central corneal thickness was calculated from the values computed from each of the central 21 A-scans.

6. **Display the average CCT and the corneal scan with marked boundaries.**

The result screen displayed the corneal scan in greyscale with the identified borders marked in blue across the central portion of the scan. The algorithm used for greyscale representation of OCT data is described in Section 5.5. During the testing phase, the program also displayed the position of the apex scan.

7. **Display the 21 A-scans with marked corneal borders if requested by the user.**

The raw data plot from the first of the 21 A-scans was displayed on the results screen just beneath the greyscale corneal scan and the user could similarly display any of the 21 central A-scans. The positions of the automatically identified corneal borders on

this scan were shown on each scan by two cursors and the corneal thickness computed from that particular scan was also shown. The position of the cursors could be modified by the user. The average CCT was updated every time the position of any cursor on any scan was altered.

8. Save the final thickness values in a text file for export.

The program also generated a text file containing the final 21 thickness values. This could then be used in programs such as Microsoft Excel for further analysis.
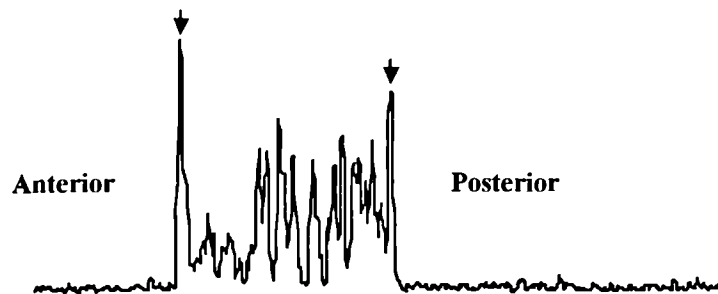
Figure 5.11   *A typical A-scan from a corneal scan showing the peaks assumed to correspond to the anterior and posterior corneal borders.*

5.4.2   Testing the algorithm

The program for automatically measuring CCT was tested before being used for the repeatability and reproducibility study described in Chapter 4.

Methods

Thirty corneal scans from 5 normal volunteers were used for testing purposes. The program was run on each of these scans. The position of the apex scan and uncorrected CCT value displayed on the results screen were recorded for each scan. Each individual A-Scan was then examined. If the cursors marking the boundaries

were in the wrong place, they were adjusted and a note of the error was recorded. The corrected CCT value, obtained after having corrected the positions of the boundary cursors as necessary, was also recorded and the discrepancy between the corrected and uncorrected CCT values was evaluated.

The apex scan may be approximately located by inspection of the corneal scan on the *Scan Profile* option of the scanner software. The approximate location of the apex scan was identified manually for each of the 30 test scans and these values were compared with those automatically computed by the program.

Results

The results from testing the algorithm are shown in Table 5.5. The position of the automatically identified apex scan differed from the manually-determined position by more than 2 A-Scans in 4 out of 30 cases. The maximum difference in position was 10 and the average difference was 1.4.

The identified borders needed no adjustments in 16 scans. Some modifications were required in the other 14 scans. Out of a total of 630 A-scans (21 from each of the 30 scans) the front corneal border was misidentified in 8 cases and the back one in 18 cases. The average uncorrected CCT was 539.7μm and the average corrected CCT was 539.6μm. The average of the differences between the 2 methods was 0.13μm. The maximum recorded difference between the corrected and uncorrected CCT was 17μm.

Scan No	Position of Apex		Uncorrected CCT (μm)	Corrected CCT (μm)	No of Misidentified Borders	
	program	*manual*			*Front*	*Back*
D6Z	47	46	568	567	0	2
D60	49	47	586	570	0	0
D61	50	49	565	565	0	0
D62	42	43	556	568	3	3
D63	54	53	564	565	0	1
D64	61	59	564	566	0	2
D7P	45	45	482	490	0	1
D7Q	49	49	488	491	0	5
D7R	45	45	481	491	1	0
D7S	55	53	490	492	0	0
D7T	60	59	487	488	0	0
D7U	59	58	484	487	0	1
D4H	58	57	595	595	0	0
D4I	55	54	609	593	0	1
D4J	57	52	593	593	0	0
D4K	39	40	592	593	0	0
D4M	41	42	597	597	0	0
D4N	53	52	599	599	0	0
D71	52	51	519	519	1	0
D72	58	53	516	515	0	0
D73	50	50	518	521	0	0
D74	68	60	525	524	2	0
D75	64	63	521	521	0	0
D76	52	51	509	512	0	1
D9W	55	53	531	530	0	0
D9X	60	50	529	529	1	0
D9Y	41	43	524	524	0	0
D9Z	46	45	526	526	0	1
D90	38	39	546	529	0	0
D91	40	40	530	530	0	0

Table 5.5   *Table of results from CCT program testing*

Discussion

As with the *Retinal Thickness* and *RNFL Thickness* tools, the corneal surfaces tended to be misidentified when there were regions of relatively high reflectance in front of or behind the cornea. Those in front of the cornea must have been artefacts and occurred in 8 out of 630 cases (1%). Those behind the cornea could have been artefacts or regions of higher reflectance within the aqueous and these occurred in 18 out of 630 cases (< 3%). The excellent agreement between the corrected and uncorrected CCT values indicates that these errors in boundary detection have practically no effect on the computed CCT. In practice, it is therefore unnecessary to track through the central 21 A-scans in order to adjust misdentified borders, as this will have little effect on the automatically computed CCT.

The program was also able to correctly identify the apex scan in most cases. The difference in position between the automatically identified apex scan and the approximate position found from inspection of the scan was less than 3 in all but 4 of the 30 cases. It should, however, be borne in mind that decision on the position of the apex from inspection of the scan is somewhat subjective and there is no way of determining the 'true' apex scan. The greatest difference between the manual and automatically-determined apex position occurred for scan D9X. The corrected CCT computed from this scan was 529μm, which is very similar to the values from the other scans from the same subject (Scans D9W, D9Y, D9Z, D90 and D91) in which the agreement between the manual and automatic position of the apex was excellent. This result indicates that either the manually-determined position was incorrect, or that misidentification of the apex scan by up to 10 positions does not appear to have a significant effect on the computed CCT.

The tests carried out on the program for measuring CCT from OCT scans showed that the algorithm performs satisfactorily on scans from normal subjects. The corneal boundaries are not always correctly identified, however, since the final CCT reading is an average of 21 values, a few errors in boundary detection seem to have a negligible effect on the computed CCT. On the basis of these results, it was decided that the program was robust enough for acquiring CCT measurements for the study

on repeatability and reproducibility described in Section 4.4.4. One shortcoming of this study was that the program was not tested specifically on abnormal corneas. In theory, it should function equally well since, whatever the state of the cornea, the contrast between the corneal surfaces and adjacent air or aqueous should still be sufficient for the borders to be detected correctly. However, before using this program in the clinical setting, its performance should also be tested for a number of corneal pathologies.

5.5 A program for greyscale representation of OCT data

The OCT software displays images as 16 colour false-colour plots. Each pixel within the image is assigned a colour based on its intensity value. The transition from one colour to the next and the sizes of the colour bands is somewhat arbitrary — Figure 5.12 shows an OCT plot, generated by the OCT 2 software, of an artificially created raw data file. The raw data file was created as follows: pixels 0 to 499 within each A-scan of this file were assigned a particular intensity value. The intensity of the pixels in first A-Scan was set at 350 (the approximate intensity of pixels which contain only noise) and this value increased in increments of 20 for each successive scan, such that the intensity within the last A-Scan was 2350. This raw file was then entered into the OCT system and displayed using the scanner software. As shown in Figure 5.12, the transitions between some colour bands such as green and yellow and red and white, is rather abrupt. This implies that tissues with similar optical properties may be displayed in different colours and this could lead to errors in the interpretation of the OCT scans. Conversely, the red and white colour bands alone represent approximately one half of all the intensities used, so intensity values which are quite different might be mapped onto the same colour. A study by Ishikawa et al[55] claimed that a group of 10 randomly selected retinal specialists agreed that greyscale OCT images presented more information than the false-colour images and were consequently, easier to interpret. In view of the suggestions in this study, a program was constructed to display exported raw OCT data in greyscale rather than false-colour mode.

Figure 5.12   *Spectrum of colours used by the OCT software*

5.5.1   Description of the algorithm

This program read the raw intensity values from the exported *.raw* OCT file and converted these intensity values into greyscale levels. The spectrum used consisted of 256 different greyscale levels ranging from black to white. In programming, hexadecimal numbers are often used to represent different colours – the hexadecimal code corresponding to a particular colour specifies the proportions of the three primary colours, red, green and blue that make up the colour.   The hexadecimal representation for black is $FFFFFF and that for white is $FFFFFF. A spectrum of 256 different greyscale levels is created by starting from colour $000000 (black) and increasing in equal increments of $010101 until $FFFFFF (white).

The steps in the algorithm are listed below:

1. **Read the raw data into a 100 × 500 array.**

   Data from a single scan was exported from the OCT system as a file with extension *.raw*, which consisted of the 50,000 data points (500 points from each of the 100 A-Scans). This data was read into a 100 × 500 array of integers for processing.

2. **Shift raw data.**

   In typical OCT scans the intensity of the background noise pixels is around 350 units. The raw data was shifted such that the background noise intensity was close to zero. This was done by finding the minimum intensity value within the whole scan and subtracting this value from every intensity value within the scan.

3. Align data points

Movement artefacts were removed by aligning the data. This was done by identifying the signal arising from the RPE-choriocapillaris complex and shifting each A-Scan such that this point was located at row number 250 in the intensity matrix. This ensured that the scan was aligned and centred within the scan window.

4. Apply smoothing algorithm

A median algorithm was used to smooth the raw, aligned data. The intensity value of each pixel was replaced by the median of the intensity values of a 3 x 3 array of pixels centred on the pixel in question. The smoothed data was written to a separate intensity array, so that the raw data was preserved.

5. Find the range of intensities per grey scale band

The maximum intensity within the entire scan was found. This value was then divided by the number of greyscale levels used, 256, in order to establish the range of intensities covered by a single greyscale level.

6. Assign a greyscale level to each pixel

The greyscale level corresponding to each pixel was found by dividing its intensity value by the intensity range covered by a single grey level and multiplying this value by $010101 to determine the hexadecimal representation of the assigned grey level.

7. Display the raw and median smoothed scan

Both the raw and the smoothed scans were displayed on the results screen. Bitmap files of these two images were also generated.

5.5.2 Application of the algorithm

A total of 20 scans from 20 normal volunteers were converted to greyscale as described above. The algorithm successfully displayed the greyscale images in all 20 cases and the greyscale scans were then compared subjectively with the corresponding false colour plots. Figure 5.13 shows two examples from two different normal volunteers. The raw and median smoothed scans are displayed together with the aligned image exported from the OCT 2 software. The last row of Figure 5.13 also shows scans with modified intensity data, created for comparison with those of Ishikawa et al[55]. This group modified each of the raw intensity values using the following equation:

$$Modified\ Intensity = a \times \sqrt{Original\ Intensity - Minimum\ Intensity}$$

$$(5.1)$$

The *Minimum Intensity* term represents the minimum intensity value in the whole scan and *a* is a user-defined constant. The authors of this study claimed that this modification gave better definition on OCT scans. In order to investigate this, the algorithm described above was also run with data modified according to equation 5.1. The data was modified before the shifting and aligning stages. The publication by Ishikawa et al[55] does not specify the value of *a* used. In our study it was found that the best scan definition was obtained with a value of 5 and the scans shown in Figure 5.13 were acquired with *a* at this value.

OCT 2 Scan
(Aligned)

Raw Data
(Aligned)

Raw Data with
Median Smoothing

Modified Data
with Median
Smoothing
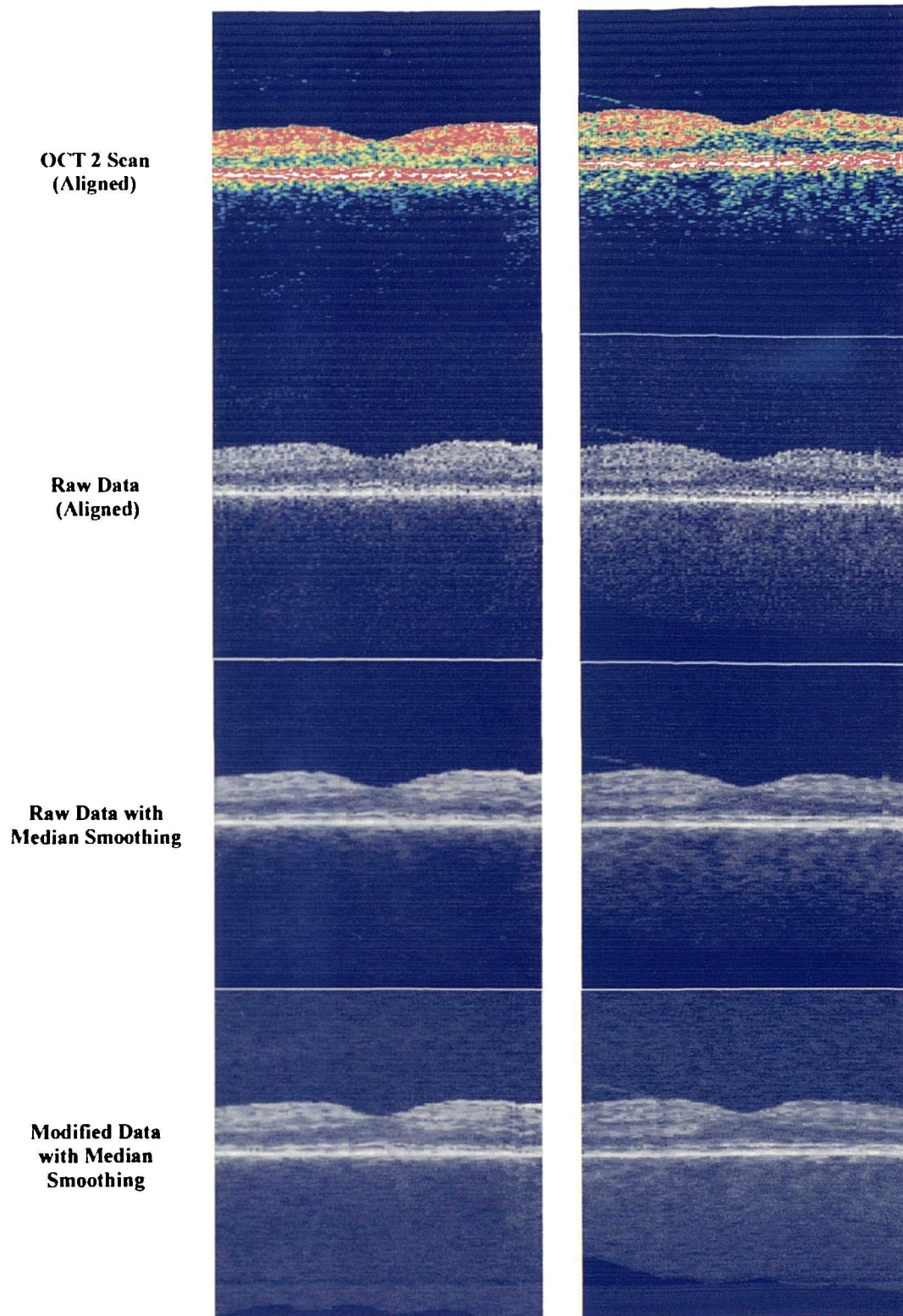
Figure 5.13 *Comparison of raw data greyscale OCT images with the corresponding false colour plots and greyscale plots with modified intensity data.*

157

5.5.3 Discussion

In the false colour plot generated by the OCT 2 scanner, intensities are mapped to a range of 16 colours. The range of intensities within a typical retinal scan is generally in the region of about 2000 so approximately 125 different intensity levels will map to a single colour. This implies that structures with different optical properties may be mapped to the same colour, thus making them indistinguishable. Conversely, since the colour variation from one band to the next may be quite abrupt, such as the transition from green to yellow or from red to white for example, two structures with very similar optical properties may fall within two different bands and may therefore be assigned very different colours. This would make them erroneously appear as two quite distinct structures. Moreover, in the spectrum used by the Humphrey software, the sizes of the colour bands are not equal, and in fact, the red and white bands seem to occupy around half of the spectrum, making the final colour image biased towards the regions of higher reflectivity. Thus, false colour representation of OCT scans may lead to misinterpretation of the OCT images. The greyscale images generated by the in-house algorithm described above provided a more balanced representation of the reflectivity of retinal structures than the false-colour plots since 256 levels of grey were used, meaning that each grey level covered only about 8 different intensity levels. In addition all the greyscale bands were of the same size, which eliminates the problem of the image being biased towards the regions of higher reflectivity.

One clear advantage of the greyscale plots was that the split in the choriocapillaris complex appeared easier to identify in the greyscale images than in the false-colour ones. This was useful in a study described in Section 6.5 designed to examine the nature of this layer. Modifying the raw data as suggested by Ishikawa et al[55] did not significantly alter the appearance of the scans, despite the claims of this group that this modification improved the definition of areas with medium reflectivity.

In theory, greyscale OCT images should give a more realistic representation of retinal anatomy. In view of this, an algorithm for displaying OCT images in greyscale was developed so that clinicians could have the option of viewing OCT data in either mode.

5.6   Conclusions

This chapter has taken a detailed look at the software tools provided with the Zeiss-Humphrey OCT 2 scanner, in particular, the *Retinal Thickness* and *RNFL Thickness* tools. The studies carried out showed that, while the overall performance of these tools was reasonably good, there were a number of situations which caused the algorithms to partially or completely misidentify the appropriate retinal layers. Clearly, more sophisticated edge detection techniques are required to make the two algorithms more robust.

Since the raw data may be exported from the OCT system, additional software tools for displaying and analysing the data may be created. Two such additional applications have been described. An in-house program for measuring central corneal thickness from corneal OCT scans was developed. This program was tested and found to perform well. Thus accurate central corneal thickness measurements can now be made automatically from the raw OCT data. A second in-house program was developed to give clinicians the option of viewing OCT scans in greyscale rather than false-colour mode. Although greyscale images may appear harder to interpret to users accustomed to the false-colour plots, they are actually more representative of the optical differences between retinal layers and it is therefore recommended to view images in both modes.

A future project, described in greater detail in Section 7.2.3 will combine these two in-house programs into a single enhanced OCT user interface which will provide the user with a greater range of image processing and analysis tools than the current OCT 2 software.

Chapter 6

CLINICAL STUDIES

This chapter describes the clinical evaluation of the Zeiss-Humphrey OCT 2 scanner for qualitative and quantitative assessment of conditions which affect the normal retinal architecture. The selected pathologies were chosen to evaluate the system's ability to give information about disorders affecting different retinal and sub-retinal layers and also to investigate the correlation between the bands seen on OCT and actual retinal layers.

Patients with epiretinal membranes were studied to investigate the hypothesis that the first high intensity signal on OCT scans arises from the vitreo-retinal interface and also to evaluate the ability of the OCT system to resolve a thin structure situated on the inner retinal surface. Patients with glaucoma were studied to assess the ability of the system to quantitatively assess conditions which cause a change in RNFL thickness. The rare hereditary disorder X-linked retinoschisis, which arises from a disorder of the Müller cells, was chosen to verify whether the red band situated anteriorly does in fact correspond to the retinal nerve fibre layer and to investigate the ability of the system to visualise conditions which cause a defect in the mid-retinal layers. Patients with rhegmatogenous retinal detachment or macular holes were investigated to determine the exact nature of the band thought to correspond to the RPE-Choriocapillaris complex. Cohorts of patients with choroidal melanoma and choroidal naevi were investigated to assess the ability of the system to give information on structures located beneath the retina and on the effects that these structures may have on the morphology of the overlying retina.

6.1   Introduction

Visual examination of the retina is one of the first steps in attempting to establish the cause for visual disturbances. As described in Chapter 1, there are various methods for examining the appearance of the retina. Since the more conventional methods such as ophthalmoscopy, fundus photography and biomicroscopy can only give limited depth information, the aim of newer imaging techniques such as optical coherence tomography is to provide tomographic information which will lead to a better three-dimensional understanding of the nature of retinal and sub-retinal pathologies.

Various ocular disorders were investigated in order to test the potential of the OCT 2 scanner within the clinical setting. The ability of OCT to give qualitative and quantitative information on pre-retinal, retinal and sub-retinal structures was investigated by selecting a number of conditions which specifically cause disorders in various layers ranging from the inner retinal surface anteriorly to the choroid posteriorly. Scans from some of these studies were also used to gain a better understanding of the relationship between the signals observed on the OCT scans and actual retinal anatomy. Findings from some of the studies described below have been published[56-58].

6.2   Analysis of the Inner Retinal Surface - Epiretinal Membrane

In any A-scan from an OCT scan of a normal eye, it is commonly accepted that the first peak on the scan is the signal arising from the reflection of the beam at the vitreo-retinal interface. Since there is a considerable difference in refractive index between the vitreous and the inner retina, it is likely that there will be a strong reflection arising from this interface. A cohort of patients with a clinical diagnosis of epiretinal membrane were investigated in order to verify that this interface on OCT scans does indeed correspond to the vitreo-retinal interface and to investigate the ability of the system to separately resolve two adjacent structures with similar reflective properties.

An epiretinal membrane (ERM) is a fibrocellular membrane which proliferates on the inner retinal surface in the macular area. It may occur in otherwise healthy eyes or secondary to retinal breaks and rhegmatogenous retinal detachment, retinal vascular diseases, intra-ocular inflammation, blunt or penetrating trauma, and other ocular disorders. It is widely believed that idiopathic epiretinal membranes are produced by retinal glial cells that migrate through defects in the internal limiting membrane to proliferate and contract on the inner retinal surface. RPE cells are the main cell type in many cases of idiopathic epiretinal membrane. Other cellular elements that may be present include fibrous astrocytes, fibrocytes, and macrophages. Most of the cell types found in epiretinal membranes have the capacity to assume myofibroblastic properties, which allows them to change shape and cause the membrane to contract. Visual symptoms associated with epiretinal membranes range in severity, depending on the opacity of the membrane and the amount of macular distortion induced by the contracting fibrocellular tissue.

The clinical appearance of an epiretinal membrane depends on its thickness and the extent to which it has undergone shrinkage or contraction. The diagnosis of epiretinal membranes is clinical, based on biomicroscopic observation of physical features such as abnormal glistening reflexes and striae caused by shrinkage or contraction of the membrane The presence of a defect in the prefoveolar portion of an epiretinal membrane may simulate the appearance of a full-thickness macular hole on biomicroscopic examination. This is generally referred to as a pseudohole and may be difficult to distinguish from a lamellar hole or true macular hole from clinical examination. Macular oedema may also be present as a result of tractional effects of the membrane on the retina.

Since epiretinal membranes are located on the inner retinal surface, this condition was chosen to investigate the validity of the assumption that the first high intensity reflection on OCT scans corresponds to the anterior surface of the retina. A further aim of the study was to establish whether OCT could successfully resolve the epiretinal membrane from the underlying retinal tissue.

cases will be referred to as "possible ERM detected ". In the remaining 6 cases, there was no evidence of an ERM on the OCT scans. These cases are referred to as "no ERM detected" (Figure 6.1C).

A   B   C
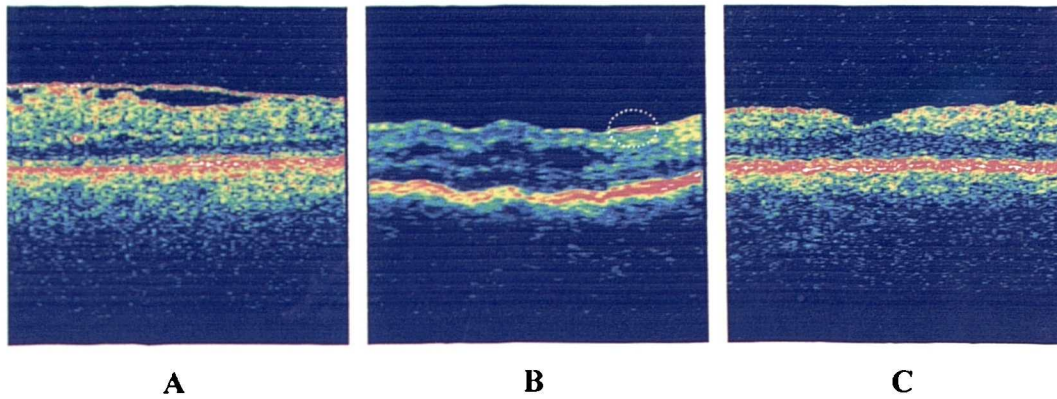
Figure 6.1   *(A) Example of a definite ERM detected. The ERM appears as a thin highly reflective band partially adherent to the inner surface of the retina. (B) Example of a possible ERM detected. The thin band shown encircled may be an ERM which is totally adherent to the inner retinal surface. (C) Example of a case in which the ERM could not be detected by OCT.*

Macular oedema or macular thickening was observed in 6 out of the 22 eyes – 4 of these eyes had a definite ERM (Figure 6.2A) 1 had possible ERM (Figure 6.2B) and 1 had no ERM visible on OCT (Figure 6.2C). The maximum retinal thickness was measured from the scans. Maximum retinal thickness ranged from 385-796µm (mean: 541.4µm; standard deviation: 163.5µm). These values are significantly higher than retinal thickness measurements in the same area in normal subjects (Chapter 4). Macular oedema had been detected clinically in 4 of these cases.

Methods

Twenty-two eyes from 19 patients with a clinical diagnosis of epiretinal membrane were included in the study. Clinical diagnoses were established with slit-lamp biomicroscopy, fundus photography and fluorescein angiography. Nine patients were male and 10 were female and the average age was 67 years (standard deviation = 10.2 years). OCT was performed through a dilated pupil – several scans across the macula were acquired in each case. The characteristic appearance of normal scans from the macular region has been established in previous chapters. Scans in this study were analysed for an abnormality that could correspond to the epiretinal membrane. The position of this abnormality was used to establish the location of the vitreo-retinal interface on OCT scans.

Results

In 9 out of 22 cases, OCT scans of patients with ERM differed from scans of normal subjects due to the presence of an additional thin red band that appeared to be partially attached to the interface commonly believed to represent the vitreo-retinal interface (Figure 6.1A). It was therefore concluded that this signal arose from an ERM which was partially attached to the inner retinal face and consequently, that the interface immediately below the ERM band corresponded to the vitreo-retinal interface. Thus in normal eyes, without an ERM or other pre-retinal abnormalities, the first significantly reflecting structure encountered by the OCT beam must be the vitreo-retinal interface These 9 cases in which the ERM is clearly distinguishable from the underlying retina will be referred to as "definite ERM detected". The thickness of this band ranged from 37-47μm (mean: 40.7μm; standard deviation: 3.0μm). In another 7 cases, a thin reflective band on the anterior surface of the retina was observed (Figure 6.1B). This band was globally adherent to the retinal surface with no observed area of separation. The thickness of this band ranged from 35-54μm (mean: 45.0μm; SD: 6.9μm). In these 7 cases, it is possible that the observed bands corresponded to the ERM since they were similar in appearance and thickness to the bands seen in the 9 definite ERM cases. These
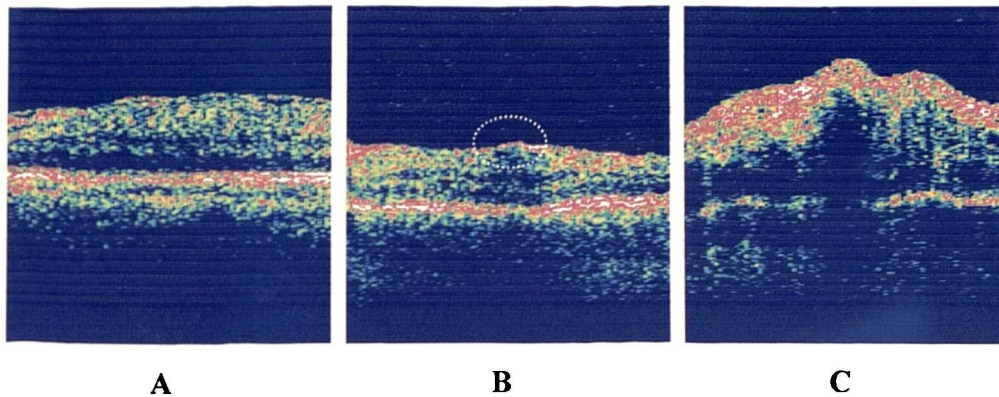
Figure 6.2   *(A) Definite ERM (partially adherent) and associated macular oedema. (B) Possible ERM (encircled) with macular oedema. (C) No ERM can be detected but macular oedema is evident*

In 4 eyes an abnormal indentation of the retinal structure was observed at the fovea. This was not thought to be a macular hole since there was clearly retinal tissue still present beneath the indentation (Figure 6.3). The retinal thickness beneath the indentation was measured in each of these cases. Foveal thickness ranged from 144-169µm (mean: 161.5µm; standard deviation: 11.7µm). These values fall within the normal range of foveal thickness (137-194µm) established in Chapter 4. Thus it was concluded that no loss of retinal material had occurred and that this was therefore a pseudohole rather than a lamellar hole. The 4 presumed pseudoholes and the corresponding foveal thicknesses are displayed in Figure 6.3. In this figure, cases A, B and C were found to have a possible ERM. Although the possible ERM is not evident on the scans shown in Figure 6.3, it was observed on other scans from the same patients. In case D, no ERM was detected on any of the scans acquired. In 2 of these a diagnosis of macular pseudohole had been established from the clinical investigation, however in the other 2 cases, the clinical examination could not establish whether there was a lamellar or pseudohole present.
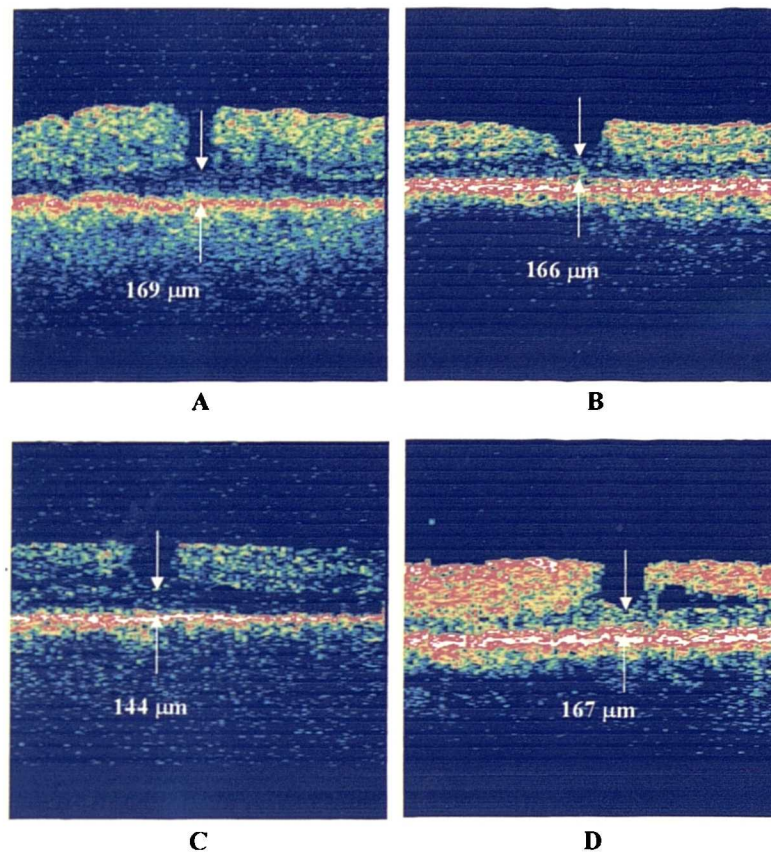
Figure 6.3   *OCT scans from the 4 patients with a presumed pseudohole showing the foveal thickness in each case. In cases A, B and C a possible ERM was detected. In case D, no ERM was detected.*

Discussion

In this study OCT was able to unequivocally detect the presence of an ERM in 9 out of 22 (41%) cases. In these cases the ERM was partially detached from the inner retinal surface and could therefore easily be distinguished from the underlying retina. Analysis of these scans also confirmed the position of the vitreo-retinal interface on OCT scans. In these 9 cases the ERM appeared as a highly reflective structure with an average thickness of 41μm. Our values are similar to those of Massin and colleagues[59] who detected a definite ERM in 42% out of 62 eyes investigated. However, a study by Wilkins and colleagues[60] on 186 eyes with an ERM found that the diagnosis of ERM

could be made unequivocally from the OCT scans in only 26% of the cases. The difference in results could be due to the fact that Wilkins and colleagues studied a much larger population.

In another 7 cases a thin highly reflecting structure adherent to the inner retinal surface was observed. The average thickness of these structures was found to be 45μm. It is possible that this structure is the ERM since it is similar in thickness and reflectivity to the definite ERMs observed in the 9 patients described above. In the remaining 6 cases no ERM could be detected on the OCT scans. These findings indicate that the ability of OCT to distinguish between adjacent structures with similar reflective properties is somewhat limited.

Complications arising from the ERM, such as associated macular oedema, were well visualised with OCT even in cases where the macular oedema was not observed clinically. This indicates that the OCT can identify retinal thickening due to macular oedema before this becomes clinically apparent and that the technique is therefore suitable for monitoring changes in retinal thickening.

Unusually deep foveal contours were identified in 4 eyes. The foveal thickness in these cases ranged from 144-169μm, thus all values fall within the range of normal foveal thickness established in Chapter 4. These findings indicate that there was no loss of retinal material in these cases and that these were therefore more likely to be pseudoholes rather than lamellar macular holes. In 2 of these cases, the diagnosis of pseudohole due to ERM contraction had been made on the basis of clinical examination, however in the other two cases a definite clinical diagnosis could not be made. This indicates that OCT could be useful in distinguishing between lamellar and pseudoholes.

This study has shown that in normal eyes with no pre-retinal abnormalities, the first significantly reflecting surface encountered by the OCT beam is the vitreo-retinal interface. However, highly reflecting structures closely adherent to the inner surface of the retina may be hard to distinguish from the underlying RNFL since these two

structures have similar optical properties when investigated with the OCT beam. This implies that the diagnostic capabilities of OCT in relation to ERM are limited. However, changes in the neurosensory retina arising from contraction of the ERM are well documented by OCT.

6.3   Analysis of the Retinal nerve fibre layer (RNFL) - Glaucoma

In OCT scans of the normal eye the red band situated immediately beneath the vitreo-retinal interface is thought to correspond to the retinal nerve fibre layer (RNFL). Circular scans centred on the optic disc show a thickening of this layer superiorly and inferiorly. Histological studies have shown that there is bundling of the nerve fibres superior and inferior to the optic disc and these observations support the theory that this red band is in fact related to the RNFL (further support for this theory is provided in Section 6.4). Since glaucoma causes defects in the RNFL, a cohort of patients with diagnosed glaucoma was examined with OCT in order to establish the ability of the system to monitor progressive changes of the RNFL.

The word glaucoma is used for a group of ocular diseases with the common features of abnormally elevated intraocular pressure (IOP) and ultimate loss of vision if left untreated. Several categories of the condition exist:

 Primary glaucoma: increased IOP for no clinically apparent reason. There are two kinds – open angle, which is the commoner type and angle closure.

Secondary glaucoma: the raised IOP is due to local causes such as iritis, injury or occlusion of the central retinal vein.

Congenital glaucoma: glaucoma which occurs during the first three years of life.

Low tension glaucoma: a condition in which there are features similar to those seen in open angle glaucoma without an abnormally high IOP.

Ocular hypertension: a condition in which the IOP is abnormally high but there are none of the other features of glaucoma.

Primary open angle glaucoma is the most common type of glaucoma and is the subject of the study described below. This is a bilateral, slowly progressive condition which causes no symptoms until considerable visual impairment has occurred. Early treatment can prevent or delay visual loss and screening is therefore extremely important. The aetiology of the condition is not fully understood. It is believed that there is a reduction in the facility of aqueous outflow due to changes in the trabecular meshwork, Schlemm's canal or the efferent veins. This may cause an elevation of the IOP which will eventually damage the optic nerve.

There are no symptoms at all in the early stages and the patient usually notices no abnormality until much of the peripheral visual field has been destroyed. Clinically there is pathological cupping of the optic disc in which the cup becomes wider and deeper and the remaining rim of disc tissue becomes atrophic. The retinal nerve fibre layer is generally affected and may appear abnormal on stereoscopic photography. The IOP is raised (except in low tension glaucoma) – normal IOP is in the region of 21mmHg and readings over 25mmHg are usually considered to be abnormally high. Visual field changes are evidence of impaired visual function. Initially these are always peripheral and therefore central vision and visual acuity are not affected. Nerve fibre bundle defects are characteristic (arcuate scotoma).

The red band thought to correspond to healthy RNFL on scans of normal subjects is well-defined on OCT scans since this layer is quite reflective and the axons are positioned perpendicularly to the OCT beam. This has led to considerable interest in the potential of OCT as a tool for screening glaucoma[43]. Studies have shown that focal defects of the RNFL can be visualised using OCT[44,45] and a number of groups have shown that the RNFL thickness in glaucomatous patients is significantly less than in an age-matched control group[46,61-65]The ability of OCT to assess glaucomatous damage is comparable to that of other methods such as photography, scanning laser polarimetry and retinal tomography[61-65].

Although there have been a number of studies that make use of the ability of OCT to visualise the RNFL and make measurements of its thickness in glaucomatous patients, there has been very little research into the ability of the system to reliably quantify the RNFL thickness in normal subjects and glaucomatous patients. In Chapter 4, it was shown that the coefficients of repeatability and reproducibility of RNFL measurements in the normal eye are worse than those for total retinal thickness measurements. A study by Jones and colleagues[48] reports similar findings. There are a number of possible explanations for this. In Chapter 3 we showed that the signal from the RNFL is very susceptible to slight variations in the focussing and polarimeter settings. With this model of the OCT scanner there are no means of ensuring that focussing and polarimeter settings are identical from one session to another, so there is the possibility that scans acquired during different sessions will yield different measures of the RNFL thickness. To make matters worse, the studies described in Section 4.4.3 showed that there were clear differences in the appearance of the RNFL in successive scans acquired from the same normal subject. These observed differences may have been the result of small, undetectable eye movements. It has been suggested, in a study by Pons and colleagues[66], that the RNFL reflectivity in glaucomatous patients is lower than in normal subjects due to the reduced number of axons, so correct detection of the RNFL borders is likely to be even more difficult in this group. One of the aims of this study was therefore to establish whether the coefficients of inter-session reproducibility of RNFL measurements in a cohort of glaucomatous patients are similar to those for a group of normal volunteers.

Since the RNFL becomes thinner with the progression of glaucoma, the overall retinal thickness should also decrease. The posterior retinal border on OCT scans is much better defined than that of the RNFL and therefore easier to identify using edge-detection techniques. As shown in Chapter 4, measurements of retinal thickness are more repeatable and reproducible than RNFL thickness measurements. A second aim of this study was to establish whether total retinal thickness in glaucomatous patients is significantly different to that in normal subjects. The coefficient of inter-session reproducibility of retinal thickness in glaucomatous patients was also calculated and compared with that for normal subjects.

Methods

The circular scan options available with this version of the OCT scanner are specifically designed for scanning around the optic nerve head. A study by Schumann and colleagues[47] examined the reproducibility of various scanning options and established that the best reproducibility was achieved using a circular scan of diameter 3.4mm centred on the optic disk. Thus, from the various circular scanning options available, the $R - 1.73mm$ option gives the most reliable results. In this mode, scanning is performed along a circle of radius 1.73mm centred on the optic nerve head. It was therefore decided to adopt this scanning option for the study. Three identical scans were obtained for each subject and any scans that were not properly centred on the optic nerve head were discarded. RNFL measurements for the superior, inferior, temporal and nasal quadrants were obtained from the OCT *RNFL Thickness* tool. The average RNFL thickness was calculated from the exported RNFL thickness data. Retinal thickness measurements were exported using the OCT retinal thickness tool – average retinal thickness and retinal thickness per quadrant were calculated from this data. All values were averaged over the three scans acquired for each subject. In order to calculate the inter-session reproducibility, two sets of scans were acquired on two separate occasions.

Ten patients attending the Glaucoma Review Clinic were recruited for this study. All these patients had a measured intra-ocular pressure of 24mmHg or more on at least 2 occasions, glaucomatous appearance of the optic disc and abnormal visual fields results. Informed consent was obtained from each of these patients. One eye from each subject was randomly chosen for the study. Data for the control group of normal subjects was obtained from the study described in Chapter 4.

Results

RNFL Thickness: The overall average RNFL thickness values and average values for each quadrant are shown in Table 6.1. These values are averages of the values obtained in each of the 2 scanning sessions.

	Normal (μm)*	Glaucoma (μm)*
Overall average	111.7 ± 9.7	61.7 ± 9.8
Superior	135.4 ± 15.1	72.3 ± 18.2
Temporal	90.4 ± 18.3	36.5 ± 22.2
Inferior	125.5 ± 18.7	70.9 ± 24.7
Nasal	97.0 ± 12.3	59.9 ± 17.7

*Values shown are averages across the group ± standard deviation

Table 6.1   *RNFL thickness values for the two study groups.*

Wilcoxon analysis (5% level of significance) showed that there were statistically significant differences in overall RNFL thickness and thickness within each quadrant between the two groups.

The coefficients of inter-session reproducibility for each quadrant are shown in Table 6.2.

	Normal	Glaucoma
Overall average	12.8%	38.4%
Superior	19.0%	28.8%
Temporal	18.8%	51.2%
Inferior	25.2%	31.8%
Nasal	26.4%	56.2%

Table 6.2   *Coefficients of inter-session reproducibility of RNFL thickness measurements for the 2 study groups*

Retinal thickness: The overall average retinal thickness values and average values for each quadrant are shown in Table 6.3. These values are averages of the values obtained in each of the 2 scanning sessions.

	Normal (μm)*	Glaucoma (μm)*
Overall average	246.7 ± 30.7	233.4 ± 18.4
Superior	267.6 ± 30.7	239.9 ± 20.2
Temporal	233.7 ± 18.1	217.1 ± 15.9
Inferior	243.0 ± 19.8	211.3 ± 24.3
Nasal	241.9 ± 25.9	225.3 ± 28.3

* Values shown are averages across the group ± standard deviation

Table 6.3   *Retinal thickness values for the two study group*

Wilcoxon analysis (5% level of significance) showed that there were statistically significant differences in overall retinal thickness and thickness within each quadrant.

The coefficients of inter-session reproducibility for each quadrant are shown in Table 6.4.

	Normal	Glaucoma
Overall average	4.4%	5.0%
Superior	7.6%	7.4%
Temporal	3.4%	7.8%
Inferior	7.2%	8.2%
Nasal	13.6%	7.0%

Table 6.4   *Coefficients of inter-session reproducibility of retinal thickness measurements for the 2 study groups*

Discussion

As shown in Table 6.2, inter-visit reproducibility of RNFL thickness measurements is considerably worse in glaucomatous patients than in normal controls. In this group of patients the RNFL may be less reflective than in normal subjects. This could lead to poorer delineation of the posterior border of the RNFL and more errors in RNFL

thickness measurements. If the whole retinal thickness rather than just the RNFL thickness is considered in the same group of patients, the coefficients of inter-session reproducibility are similar to those in normal subjects. These results suggest that the performance of the RNFL Thickness tool is adversely affected by the reduced RNFL reflectivity in glaucomatous patients.

As expected, the RNFL was significantly thinner in the glaucoma group than in the normal group. Results from this study correlate well with findings from other studies[46,61-65]. Since we have shown that retinal thickness measurements are more reproducible than RNFL thickness measurements, the total retinal thickness from the scans was also calculated for the two study groups. It was shown that the total retinal thickness in glaucomatous patients was also significantly less than that of the control group.

This study has shown that although OCT can show differences in RNFL thickness between normal and glaucomatous patients, these measurements have somewhat poor coefficients of reproducibility. Since total retinal thickness measurements are more reproducible than RNFL measurements, it is preferable to use total retinal thickness measurements in studies involving conditions that cause progressive thinning of the RNFL.

6.4   Analysis of the Mid-Retinal Layers - X-Linked Retinoschisis

The yellow-green region between the red RNFL layer and the red-white RPE/choriocapillaris complex on OCT scans should correspond to the mid- and outer retinal layers. With the resolution currently available, it is impossible to distinguish between different layers in this region. In order to investigate whether the anterior red band corresponds to the RNFL and whether the region immediately posterior to this band corresponds to the mid-retinal layers, OCT findings in patients with X-linked retinoschisis were investigated.

X-linked juvenile retinoschisis (also called congenital hereditary retinoschisis, congenital vitreous veil, cystic disease of the retina, and juvenile retinoschisis) is a rare

bilateral hereditary condition which affects almost exclusively males. The condition is linked to a mutation in the short arm of the X-chromosome which is thought to lead to a defect in the Müller cells. In practically all cases the condition manifests itself as cystic-like, stellate maculopathy or 'foveal schisis'. Peripheral schisis is also present in about 50% of cases[67,68].

Histopathological studies[69-71] have shown that the inner retina splits at the level of the retinal nerve fibre layer. The inner layer balloons into the vitreous cavity and unsupported retinal vessels may lead to recurrent vitreous haemorrhages from associated vitreous traction. Occasional bridges of tissue are sometimes seen bridging the schisis cavity – these are though to be defective, excessively elongated Müller cells.

Since this condition causes splitting at the level of the RNFL and affects the mid-retinal layers, a study using OCT was carried out on a group of patients with the condition in order to use the position of the observed split on OCT scans to confirm the position of the RNFL layer and to investigate the ability of the technique to visualise abnormalities of the mid-retina.

Methods

5 eyes from 3 unrelated male patients were examined using OCT. Details of these patients are shown in Table 6.5. In all three cases the diagnosis of X-linked retinoschisis had been made on the basis of clinical findings, family history, electroretinographic findings and genetic analysis. Clinical examination and fundus photography confirmed the classic stellate appearance of foveal schisis in all cases. Peripheral schisis was seen in 1 eye (LE of patient 2).

OCT scans were acquired from both eyes of two of the patients. No scans could be obtained from the right eye of Patient 3 due to a vitreous haemorrhage which prevented the OCT beam from penetrating to the retina. A series of straight line scans was acquired across the area of foveal schisis in all cases. An attempt was made to scan in

the region of the peripheral schisis in the LE of patient 2, however this was too peripheral for OCT scanning.

The level of the split on the OCT scans was used to establish the location of the RNFL on OCT scans.

	Patient 1	**Patient 2**	**Patient 3**
Age	35	29	31
Clinical characteristics	Foveal schisis, no peripheral schisis	Foveal schisis, peripheral schisis in LE	Foveal schisis, no peripheral schisis. Vitreous haemorrhage in RE
VA	RF: 6/60; LE: 6 36	RE: 6/18; LE: 6/18	RE: 1/60; LE: 6/12
Secondary complications	None	None	Squint, vitreous haemorrhage and persistent retinal detachment in RE
Affected family members	Brother, maternal uncle, maternal grandfather	Male cousins, maternal uncle, maternal grandfather	Maternal uncle

Table 6.5 *Patients included in the X-linked retinoschisis study*

Results

Figure 6.4 shows a scan through the fovea of each eye in the study. Splitting was observed in all cases. In Figure 6.4B and D it is clear that the red band thought to correspond to the RNFL was still relatively intact and that the splitting is occurring beneath this layer. Bridges of tissue were also seen bridging the schisis cavity in Figure 6.4A and Figure 6.4B. The size and appearance of the schisis cavity varied considerably from one case to another. Functional information from multifocal-ERG (mfERG) recordings is also shown and is discussed in a later section.

P1 Amplitude:	46 nV
P1 Latency:	50 ms
P1/N1:	1.3

P1 Amplitude:	40 nV
P1 Latency:	47 ms
P1/N1:	1.5

P1 Amplitude:	32 nV
P1 Latency:	50 ms
P1/N1:	1.2

P1 Amplitude:	17 nV
P1 Latency:	42 ms
P1/N1:	1.0

P1 Amplitude:	25 nV
P1 Latency:	54 ms
P1/N1:	1.3
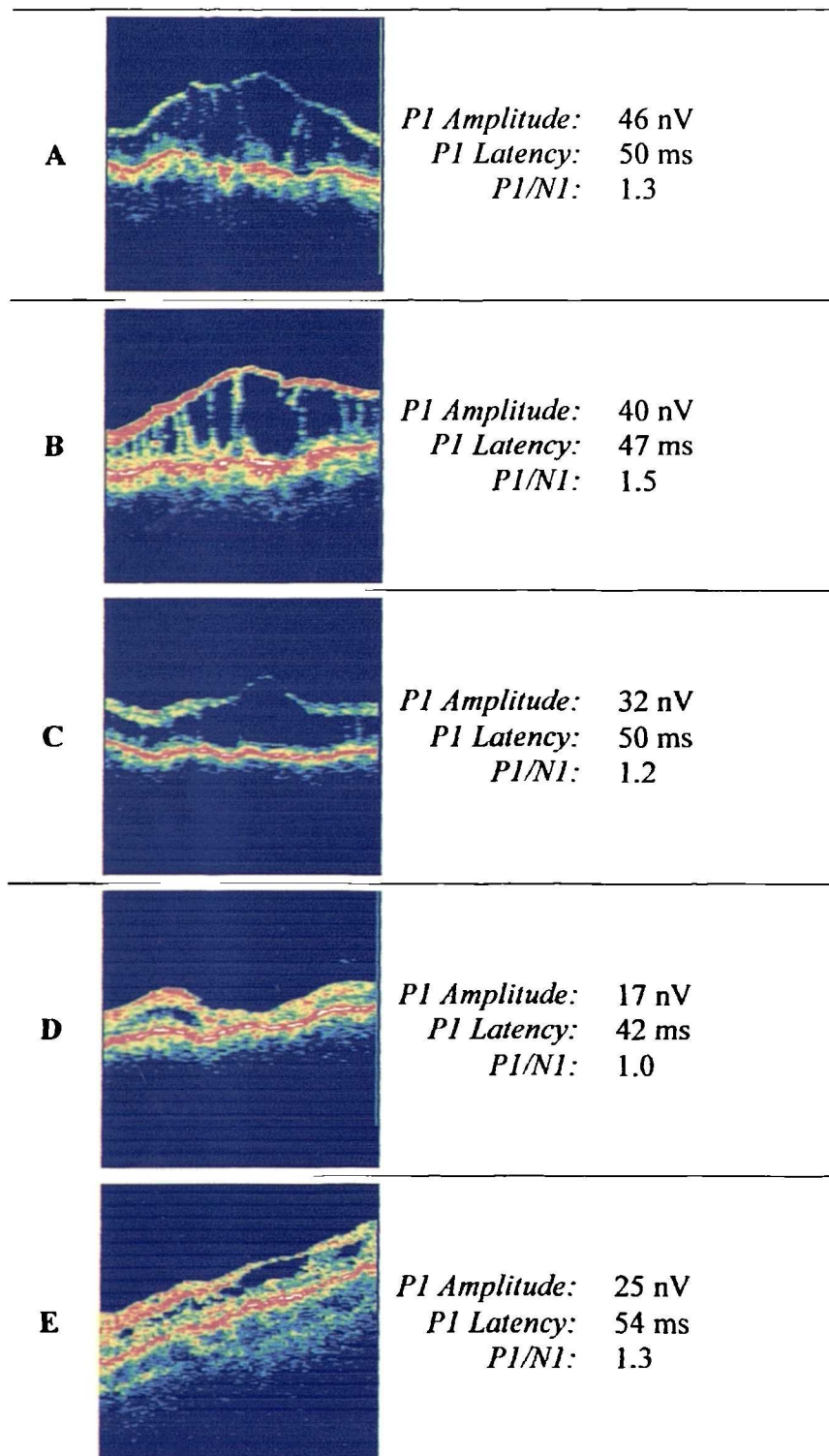
Figure 6.4 *OCT scan through fixation and corresponding mfERG functional information obtained from each eye in the study. (A) RE of Patient 1. (B) LE of Patient 1; (C) RE of Patient 2; (D) LE of Patient 2; (E) LE of Patient 3.*

Discussion

This OCT study of patients with X-linked retinoschisis has shown that the technique can clearly visualise disorders of the mid-retina. Figure 6.4 shows that the splitting has occurred just beneath the anterior red band that is normally seen on OCT scans. Histopathological studies on cases of X-linked retinoschisis have shown that splitting occurs at the level of the RNFL and thus, this finding lends further support to the belief that this anterior red band corresponds to the RNFL. From this figure it can also be seen that the splitting does not involve the entire region between the two red bands and that there is a residual green-yellow region beneath the schisis cavity and immediately anterior to the red band thought to be the RPE-Choriocapillaris complex. This region must therefore correspond to the outer retinal layers and this study therefore shows that the outer retinal layers appear as yellow-green on OCT scans. In OCT scans of normal retina, the whole region between the two red band appears to be of more or less uniform reflectance and appears as a single green-yellow area with no well-defined layer structure. From this study, we have established that this region corresponds to the mid- and outer-retinal layers. Since these layers appear to have similar reflective properties for the wavelength of light used, the OCT scanner cannot distinguish between various layers in this region.

In Figure 6.4A and Figure 6.4B strands of tissue are seen traversing the schisis cavity. The retinal splitting in X-linked retinoschisis is thought to arise from defective Müller cells which become more elongated, consequently becoming less able to function normally. These elongated Müller cells are often seen bridging the schisis cavity. It is therefore likely that the strands of tissue seen on the OCT scans are elongated Müller cells.

Since this disease is very rare and almost never leads to enucleation, very few histopathological studies have been carried and the mechanisms of the condition are not well understood. If it were possible to observe these histological changes in-vivo and non-invasively, much more data would be available for analysis. Although small, this

study has shown that the resolution of OCT is sufficiently high to give information on this mid-retinal disorder which is not inconsistent with histopathological findings. OCT offers new possibilities for studying rare conditions such as X-linked retinoschisis and may lead to a better understanding of their mechanisms.

Further Work

Since X-linked retinoschisis affects the macula, there is an associated degree of visual impairment which may vary from moderate to severe. The correlation between observed retinal damage and the degree of corresponding visual impairment in patients with this condition is somewhat vague. The amplitude of the scotopic ERG b-wave is often severely reduced in these patients, even in cases where only foveal schisis has been observed[72]. This would suggest retinal damage that extends beyond the macula. The multifocal-ERG (mfERG) is able to give more localised information on retinal damage than the conventional ERG which is a single global response. We have shown that in a case where the conventional ERG responses in a patient with this condition were normal, the mfERG was sensitive enough to show abnormal P1 responses in several areas[56].

The OCT study on patients with X-linked retinoschisis described above was extended to investigate the correlation between anatomical damage and associated abnormalities in retinal function.

Methods

In addition to OCT scanning, electrophysiological testing of the patients was carried out using wide-field mfERG techniques. The mfERG was performed using a custom-built system with a 61 hexagonal display digitally back projected onto a polysilicon screen[73]. For analysis, mfERG recordings from specific areas were grouped and averaged in three different ways. Grouping 1 consisted of the central hexagon, grouping 2 consisted of the central 3 hexagons, grouping 3 included 13 central hexagons and grouping 4 consisted of a ring of 22 peripheral hexagons as shown in Figure 6.5. The amplitude and latency of

the first positive peak (P1) and the ratio of the amplitude of the first positive peak to the first negative trough (P1/N1 ratio) were assessed in all cases.

Grouping 1	**Grouping 2**
Grouping 3	**Grouping 4**
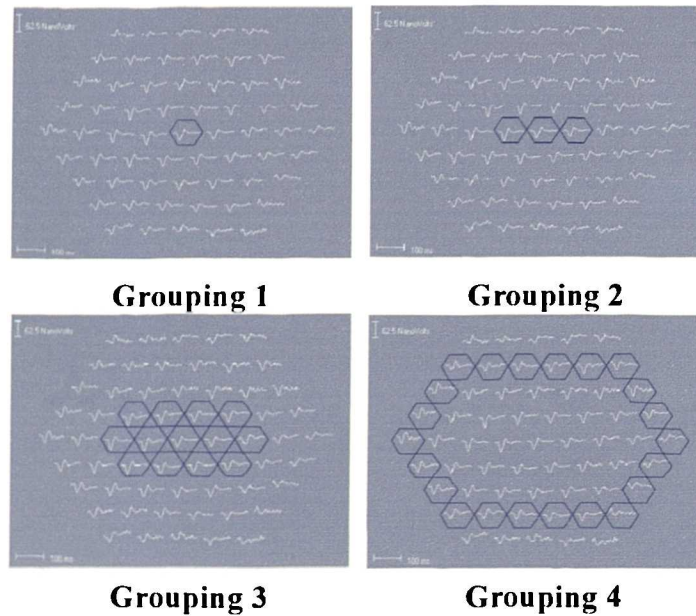
Figure 6.5   *Figure showing the 4 groupings used to analyse the mfERG recordings*

In order to investigate the relationship between anatomical abnormalities and loss of retinal function, the areas of the mfERG recording that corresponded to the location of the scans were assessed by calculating the amplitude, P1 latency and P1/N1 ratio from the mfERG responses. The correlation between the maximum height of the schisis cavity within the macula, measured from the OCT scans, and the response from the central areas in the mfERG recording was also assessed.

Results

Table 6.6 shows the height of the schisis cavity measured from the OCT scans and the results from the mfERG recordings for the 5 eyes. The 5th and 95th percentile values obtained from an age-matched cohort of normal volunteers are also shown.

	Pt 1 RE	Pt 1 LE	Pt2 RE	Pt 2 LE	Pt 3 LE	Normal
Height of Schisis Cavity (μm)	568	600	95	462	120	-
Grouping 1 *Amplitude (nV)*	41	44	33	15	27	*80-190*
Latency (ms)	50	49	40	46	45	*38-41*
P1 N1	1.5	1.6	1.4	1.0	1.2	*2.3-2.8*
Grouping 2 *Amplitude (nV)*	46	40	32	17	25	*60-170*
Latency (ms)	50	47	50	42	54	*37-41*
P1 N1	1.3	1.5	1.2	1.0	1.3	*2.2-2.7*
Grouping 3 *Amplitude (nV)*	51	44	37	26	34	*53-180*
Latency (ms)	49	50	50	49	58	*38-44*
P1 N1	1.5	1.3	1.2	1.1	1.7	*2.0-2.5*
Grouping 4 *Amplitude (nV)*	45	31	41	27	32	*47-138*
Latency(ms)	47	50	50	50	56	*38-44*
P1 N1	1.5	1.2	1.5	1.4	1.8	*2.0-2.4*

Table 6.6   *mfERG results for patients with X-linked Retinoschisis*

The data in the above table shows that P1 amplitude and latency and P1/N1 ratio are abnormal in all areas for all eyes. This implies that there is a global reduction in retinal function even in patients 1 and 3 who only appear to have foveal schisis.

Comparison of OCT and mfERG data showed that areas that did not show any splitting on OCT also had abnormal retinal function. There was negative correlation between the degree of splitting, measured by the height of the schisis cavity and the amplitude of the mfERG response from the macular area (correlation coefficient: 0.93) – larger schisis cavities were associated with higher mfERG response amplitudes. No correlation was found between the size of the schisis cavity and the latency of the mfERG responses (correlation coefficient: 0.12).

Discussion

Although the number of patients in this study is very small, the results are interesting and shed some light on the mechanisms of this rare condition. The results from the mfERG confirm that there is a global reduction in retinal function. Abnormal retinal function was evident even in areas which did not show signs of retinal splitting on OCT.

These findings indicate that retinal function is reduced before schisis develops. The association between the extent of retinal splitting and the degree of abnormality in retinal function is also interesting. Surprisingly, analysis of retinal function at the centre of the macula showed that larger schisis cavities were associated with higher mfERG amplitudes and in fact, the left eye of patient 2 (Figure 6.4D), which showed the least amount of foveal splitting on OCT was found to have the lowest mfERG response amplitude. A larger study is required to further investigate this relationship.

This study has shown that a combination of results from anatomical and functional imaging can give valuable new information about the mechanisms of conditions such as X-linked retinoschisis.

6.5 Analysis of the RPE/Choriocapillaris Complex - Retinal Detachment and Macular Holes

The red-white band situated posteriorly on OCT scans is thought to correspond to the RPE-Choriocapillaris complex. However, as was observed in Section 3.5, in some normal subjects this layer appears split into two fairly distinct portions – a thinner one anteriorly and a thicker one posteriorly. The aim of this study was to attempt to establish the nature of these two distinct portions, in particular to establish whether the thinner anterior portion of the band is part of the neurosensory retina or part of the RPE-choriocapillaris complex.

Initially, the prevalence of an observed split in the RPE-choriocapillaris complex in the normal population was investigated. A group of patients with a rhegmatogenous retinal detachment were then investigated since this condition results in fluid accumulation between the neurosensory retina and the RPE. Patients with macular holes were also investigated since this condition results in a full-thickness defect of the neurosensory retina.

A rhegmatogenous retinal detachment is a condition in which fluid from the vitreous cavity passes through a full-thickness retinal defect into the subretinal space to cause separation of the neural retina from the underlying RPE. The vast majority of retinal breaks are located at the equator or more anteriorly. Sub-retinal fluid initially accumulates in the retinal periphery, where it causes a corresponding loss of peripheral vision in the area that is related inversely to the location of the retinal detachment. The loss of peripheral vision (a 'curtain effect') increases as the detachment enlarges and central visual acuity is lost when subretinal fluid passes beneath the macula. Frequently, patients do not notice any symptoms until the macula becomes involved. The diagnosis is generally made on the basis of clinical examination if the retina can be visualised well. In eyes with opaque media, the retinal detachment can often be visualised ultrasonographically.

A macular hole is a full-thickness defect of retinal tissue involving the anatomic fovea, thereby affecting visual acuity. Macular holes were originally believed to arise exclusively following ocular trauma, however it was later realised that traumatic macular holes in fact account for only a small percentage of macular holes and that the majority of diagnosed macular holes are idiopathic, age-related holes. The pathogenesis of these idiopathic holes remains somewhat controversial. Recently Gass[74,75] has described an updated biomicroscopic classification of holes and postulated that tangential vitreous traction may play a role. Diagnosis is generally made on the basis of careful contact lens biomicroscopic evaluation of the lesion. Histopathologic examination shows a round, full-thickness defect through all neural retinal layers. The underlying retinal pigment epithelium is intact.

These two conditions have been selected for this study since they result in either a clear separation between the neurosensory retina and underlying RPE (rhegmatogenous retinal detachment) or a full-thickness defect involving all the retinal layers but leaving the RPE intact (macular hole).

Methods

23 normal subjects (11 male, 12 female. Age range: 19-65 years; mean: 42 years, standard deviation: 7 years) were recruited to investigate the prevalence of an apparent split in the RPE-choriocapillaris complex in the normal population. One eye was randomly selected for the study and a 3mm-long scan through the fovea was acquired from each subject. Each scan was analysed for the presence of a split in the RPE-choriocapillaris complex.

5 patients (2 male, 3 female. Age range: 31-55 years; Mean: 40 years, standard deviation: 10 years) with a clinical diagnosis of rhegmatogenous retinal detachment were recruited in order to investigate the location of fluid accumulation on OCT scans. In one patient the detachment was long-standing. In these cases at least one scan traversing from an intact, unaffected portion of the retina across to a detached portion was acquired. The scans were studied in order to determine whether the anterior thinner part of the red-white RPE-choriocapillaris complex was contained within the detached portion of the retina.

16 patients (5 males, 11 females. Age range 52-76 years; Mean: 67 years, standard deviation: 9 years) with a clinical diagnosis of a full-thickness macular hole were recruited in order to investigate whether this full-thickness retinal defect had affected any part of the red-white choriocapillaris complex. Scans were analysed for the presence of a split in the RPE-choriocapillaris complex close to the edges of the hole. In cases where a split was observed, the appearance of the base of the hole was studied in order to determine whether the anterior thinner portion of the RPE-choriocapillaris complex was still present at the level of the hole.

All patients and normal controls gave informed consent for participation in the study after the full nature and purpose of the study had been fully explained to them.

Results

Normal subjects: All 23 normal subjects were observed to have a split in the red-white RPE-choriocapillaris complex. The split was seen most easily on the unprocessed scans and in all cases it was observed that there was a thin portion anteriorly and a thicker portion posteriorly.

Rhegmatogenous Retinal Detachment Group: In 3 out of the 5 patients in this group, the thin anterior portion of the posterior red-white band appeared detached along with the rest of the retina (Figure 6.6). In the other 2 patients, no red line was observed in the detached portion. One of these patients had a long-standing retinal detachment.

A   **B**
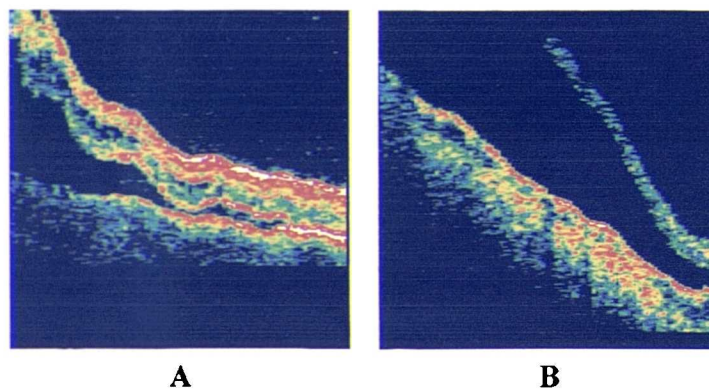
Figure 6.6   *(A) Rhegmatogenous retinal detachment in which part of the red-white choriocapillaris complex has clearly separated along with the detached neurosensory retina. (B) Long-standing rhegmatogenous retinal detachment. No red line is seen in the detached portion*

Macular Hole Group: In 11 out of 16 patients a split in the RPE-choriocapillaris complex was observed close to the edges of the hole (Figure 6.7). Only a single line was observed beneath the hole in each of these patients. In the remaining 5 patients no split was observed in the RPE-choriocapillaris complex close to the edges of the hole and only a single line was observed beneath the hole.
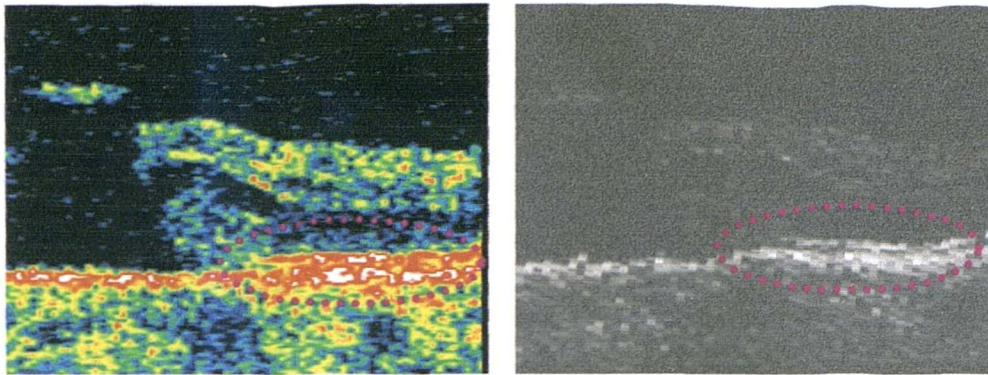
Figure 6.7   *Detail of a scan of a patient with a full-thickness macular hole, shown in false colour and greyscale modes. The encircled area shows a split in the RPE-Choriocapillaris complex. This split is not evident beneath the hole.*

Discussion

The highly reflecting band situated posteriorly is generally considered to correspond to the RPE-choriocapillaris complex and the algorithm used to calculate retinal thickness considers the anterior surface of this band to be the posterior boundary of neurosensory retina. In normal subjects this band often appears split into two portions, a thinner one anteriorly and a thicker one posteriorly. All normal subjects investigated in this study were observed to have this split and it is therefore reasonable to assume that this is the characteristic appearance of this band in scans of normal subjects. To date, it has not been established whether the thinner anterior portion of this band represents part of the neurosensory retina or whether it is part of the RPE-choriocapillaris complex.

Patients with a clinical diagnosis of rhegmatogenous retinal detachment were investigated in order to determine whether the anterior thinner layer formed part of the detached portion of retina or whether it was observed in the underlying non-detached portion. In 3 out of 5 patients, it was clearly within the detached portion. In this condition fluid accumulates between the neurosensory retina and the retinal pigment epithelium so the results from these 3 patients indicate that the thinner red portion forms part of the neurosensory retina since it appears to have detached with the rest of the

186

retina. In the remaining 2 patients a single red line was observed in the non-detached portion, but no red line was observed in the detached portion. One of these patients was known to have a long-standing retinal detachment. In cases where the retinal detachment has existed for a long period of time, retinal degeneration especially death of the photoreceptor layer frequently occurs. It is therefore possible that no red line is seen on the detached retinal portion in this patient because damage to the photoreceptor layer has occurred.

In most of the patients with full-thickness macular holes a split in the RPE-choriocapillaris complex was observed close to the edges of the hole. The appearance of this was similar to that in normal subjects with a thinner portion anteriorly and a thicker one posteriorly. At the base of the hole, only a single line was observed in all cases. A macular hole is a full-thickness defect which affects all the layers of the neurosensory retina but leaves the RPE intact. The findings in macular hole patients lend further support to the fact that only the posterior thicker portion of the RPE-choriocapillaris complex actually represents part of the RPE-choriocapillaris complex.

This study offers some evidence to support the hypothesis that the layer that has been considered to represent the RPE-choriocapillaris complex may in fact contain an element of neurosensory retina. If this is the case, then the retinal thickness algorithm which is based on the assumption that the whole layer is non-neurosensory retina, slightly underestimates retinal thickness. This is unlikely to cause problems in the clinical environment since OCT is generally used to make relative rather than absolute retinal thickness measurements.

This study has also shown that OCT is capable of visualising rhegmatogenous retinal detachment and macular holes and may therefore be useful in the diagnosis and management of these conditions.

6.6   Analysis of the Choroid - Choroidal Naevi and Melanomas

The region posterior to the RPE-choriocapillaris complex on OCT scans appears as a green, blue and yellow area and is thought to correspond to the choroid. The relatively low reflectivity of this region is partly due to the fact that the choroid is located behind the highly reflecting RPE-Choriocapillaris complex and partly due to the vascular nature of the choroid (haemoglobin is a strong absorber of light at this wavelength). In order to confirm that this region does indeed correspond to the choroid and to investigate the ability of OCT to image structures originating within it, a cohort of patients with either choroidal naevi or choroidal melanomas was investigated with OCT.

A choroidal melanoma is a malignant neoplasm that arises from neuroectodermal melanocytes within the choroid. It is the most common primary intraocular neoplasm in adults. Metastases are fairly common, often favouring the liver and the prognosis for patients with metastases is poor. Clinically, a choroidal melanoma appears as a dark brown to golden mass. Many of these tumours do not produce any visual symptoms and are often noticed during a routine eye test. At the time of detection, tumours are generally around 7mm or greater in basal diameter and over 2mm in height.

A choroidal naevus is a benign neoplasm that arises from melanocytic cells. Naevi are by far the most common intraocular tumour, affecting around 20% of persons over the age of 50. Clinically naevi appear as fairly small grey or pale lesions, usually less than 5mm in diameter and under 1mm high at the time of detection. While many naevi are benign and show no signs of malignant transformation during the lifetime of the individual, there is evidence to show that around 1 in 4000-5000 naevi may become malignant. In general, small, relatively flat choroidal naevi are unlikely to cause any changes in surrounding and overlying retinal tissue. Thus, OCT scans of patients with small naevi should simply show a slight elevation of all the layers anterior to the choroid. Analysis of these scans should give information on the exact location of the choroid on OCT scans. One aim of this study is to use scans of small naevi to determine the location of the choroid.

The classification of small, pigmented lesions in the posterior pole is not always straightforward. Most of these lesions are likely to be benign naevi, however some may be small choroidal melanomas. Various studies have identified a number of clinical factors which are thought to indicate greater likelihood for malignant potential. These include: tumour height greater than 2mm, associated sub-retinal fluid, tumour location within 1 disc diameter of the optic disc, the presence of orange pigmentation over the surface of the tumour, associated visual symptoms and the absence of surface drusen or changes in the underlying retinal pigment epithelium. However, to date there is no single clinical factor or test that can be performed to reliably distinguish between benign and malignant small tumours at first presentation. In view of this, the recommended management of these suspicious lesions is photographic and ultrasonographic documentation coupled with regular periodic reassessment for signs of growth. The diagnosis of choroidal melanoma is generally made only after documented changes or growth in these small lesions since it is assumed that growth is an indication of malignancy. Most ophthalmologists will only treat small lesions that have shown signs of growth or change. This approach is somewhat controversial since it means that treatment in some small melanomas may be delayed by a few months which could affect the management of the lesion and prognosis for the patient[76,77]. There is therefore a need to find a more efficient way of distinguishing between benign and malignant small lesions at first presentation. Histologically, naevi and melanomas are composed of different kinds of cells. An imaging technique which could give information on the cellular structure of sub-retinal lesions would be useful for distinguishing between the benign and the malignant. A second aim of this study was therefore to investigate the ability of OCT to give information on the histological structure of choroidal lesions.

Choroidal melanomas and some naevi are known to cause specific changes in the surrounding and overlying retinal tissue. A further aim of this study was to establish the appearance of these secondary changes on OCT and to investigate whether this information could be used to distinguish between benign and malignant lesions.

Methods

Study Group: The study was carried out prospectively on a total of 60 patients, 34 male and 26 female, attending the Ocular Oncology Service at the Tennent Institute over a period of 36 months. Ages ranged from 31 to 95 years (average: 65.9 years, standard deviation: 11.7 years). The inclusion criteria were the presence of a choroidal lesion which was untreated at the time of OCT scanning and located such that OCT scans around its base and across its surface could be easily acquired, no history of other conditions which could affect retinal structure and clear media to ensure good quality OCT scans. Patients were excluded if they had a choroidal melanoma which had previously been treated in any way since treatment may have affected retinal structure, if they suffered from any other condition which could affect retinal structure, if they had non-clear media which would reduce the quality of the OCT scans or if they had very peripheral lesions which could not imaged using OCT. Ethics committee approval for this study was obtained and all participating patients gave their full consent after the nature and aims of the study had been fully explained to them.

All patients included in the study underwent wide-field binocular fundal examination as well as ultrasound assessment. The location of the tumour, basal diameter and tumour thickness were recorded. Measurement of tumour thickness was made from the ultrasound scans which were assessed by an experienced radiologist. Tumours were classified as choroidal melanomas or naevi on the basis of these clinical findings, mainly size, with tumours under 1mm thick being classified as naevi and those over 3mm being diagnosed as choroidal melanoma. Some tumours under 3mm were classified as choroidal melanomas following documented growth during the observation period. Out of these 60 cases, 20 tumours were classified as malignant choroidal melanoma and 40 were classified as naevi. All tumours diagnosed as choroidal melanoma were treated whereas those classified as naevi were kept under regular observation for any signs of growth. Several clinical factors have been associated with increased risk of growth in small choroidal tumours. Studies have shown that tumour thickness greater than 2mm, the presence of sub-retinal fluid, visual symptoms, orange pigmentation, proximity to

the optic disc and the absence of drusen or RPE atrophy are factors which may be predictive of growth[83-85]. A record of any of these features noticed during clinical examination was also kept for both categories of tumours.

Scanning Protocol: No formal scanning protocol was designed for this study since the sizes and locations of tumours varied considerably between patients, making it impossible to design a scanning protocol that would be applicable to all cases. The longitudinal depth of an A-scan acquired by the OCT scanner is 3mm in air, approximately 2mm in retinal tissue, meaning that any structures separated by more than 2mm in the longitudinal direction could not be seen entirely on a single scan. In the case of lesions under 2mm high, at least one scan which extended from a flat, unaffected portion of the retina to the highest point of the lesion that could be imaged was acquired. For larger lesions it was not possible to have both the flat portion of the retina close to the base of the lesion and the surface of the lesion in focus at the same time. In these cases scans were first acquired around the base of the lesion, then the focussing control was re-adjusted until a clear image of the surface of the lesion was visible on the fundus monitor and a few scans across the surface of the lesion were acquired.

Scan Analysis: Scans from 10 patients with flat naevi were selected to establish the position of the choroid on OCT scans. These patients had lesions which showed none of the features associated with increased risk of growth. It was therefore very likely that the lesions in these patients were benign naevi.

The ability of OCT to give information on the histological structure of the tumour was investigated by analysing the reflectance pattern arising from within the bulk of the lesion for all patients in the study. Scans were also analysed to assess whether the appearance of retinal tissue around or overlying the lesion differed from the normal appearance of retinal tissue on OCT scans. Scans across the surface of the tumour and around its base revealed three distinct patterns of abnormalities – serous retinal detachments around and overlying the tumour, intra-retinal splitting or cystic spaces in the overlying retina and loss of normal retinal architecture overlying the tumour. A

serous retinal detachment was identified as an area of low-reflectance that did not cause shadowing of underlying structures and was situated immediately anterior to the RPE-choriocapillaris band, which was still well defined. Typical examples are shown in Figure 6.8A and Figure 6.8B. Intra-retinal splitting and cystic spaces were identified as regions of low reflectance within the neurosensory retina as shown in Figure 6.8C. In these cases, the bands corresponding to the RNFL and RPE-choriocapillaris complex were still well defined. Loss of normal retinal architecture was identified in cases where the retinal tissue overlying the tumour no longer showed the characteristic appearance of retinal tissue on OCT. Scans that no longer showed this well-defined layer structure were considered to be abnormal. In these cases, the band corresponding to the RPE-choriocapillaris complex could no longer be identified. Figure 6.8D shows an example of loss of normal retinal architecture – scans across the surface of the tumour showed a structureless highly reflecting signal.

No measurements were made from the OCT scans. Measuring the height of the lesion from OCT seemed unnecessary since this information was available from conventional ultrasound, which was performed on all patients attending the clinic. Moreover, as explained above, for lesions thicker than 2mm, it was impossible to have both the base and the surface of the tumour on the same scan. Thus, measuring the height of larger lesions from OCT was not possible. In a study by Schaudig et al[86] measurements of retinal thickness across the surface of the tumour were made. However, in the current study there were several cases in which the retina overlying the tumour no longer had the appearance of normal retinal structure and the layers corresponding to the RNFL and RPE-choriocapillaris complex could no longer be identified. This made it impossible to determine the positions of the retinal boundaries and to make accurate measurements of retinal thickness.
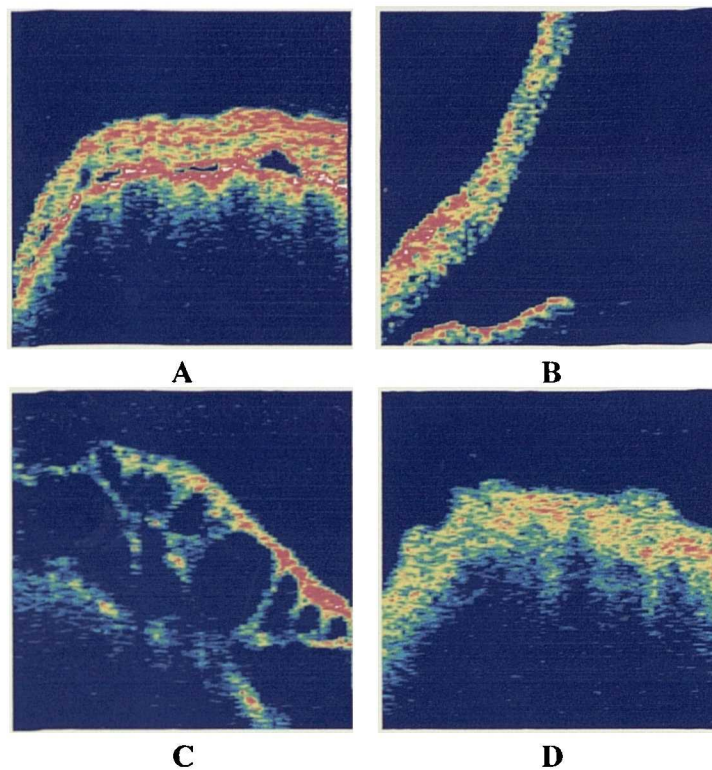
Figure 6.8 *(A) Scan across the surface of a choroidal melanoma showing small serous detachments of the retina overlying the tumour. (B) Serous detachment of the retina at the base of a choroidal melanoma. (C) Intra-retinal splitting overlying the tumour (D) Highly abnormal structure of retinal tissue overlying the tumour.*

Results

Clinical Findings: 20 patients were diagnosed with malignant melanoma. 14 of these 20 patients were diagnosed with malignant choroidal melanoma at their first visit to this centre and they proceeded to immediate treatment. The tumour thickness in this group of 14 patients ranged from 3 to 7.3mm (average: 5.6mm, standard deviation: 1.6mm) and basal diameter ranged from 5 to 15mm (average: 10.7mm, standard deviation: 3.3mm). On clinical examination, 8 of these patients were found to have associated serous detachments, 13 had visual symptoms, 8 had orange pigmentation over the tumour surface and none had drusen.

The other 6 patients with choroidal melanoma were diagnosed following documented growth or changes in their lesions. Tumour thickness and basal diameter at diagnosis ranged from 1.4 to 5.4mm (average: 3.1mm, standard deviation: 1.4mm) and from 6 to 14.9mm (average: 9.9mm, standard deviation: 3.5mm) respectively. The average increase in tumour thickness during the observation period was 1.7mm. OCT scans were performed on more than one occasion during follow-up for 4 of these patients. In the other two cases, this was not possible since the patients had been initially managed at other centres and were only referred to our centre after changes in the lesion were observed. At the time of diagnosis, 4 had serous detachments, 4 had visual symptoms, 3 had orange pigmentation over the tumour surface and 5 had no drusen.

9 of the 20 patients with choroidal melanoma were treated with ruthenium plaque only, another 4 received proton beam therapy only, and another 4 had local resection followed by Ruthenium plaque brachytherapy. 3 patients, 2 who had received proton beam therapy and another who had been treated with Ruthenium plaque had to undergo enucleation of the eye because of further growth of the tumour despite the initial treatment. Histological analysis of the tumour was therefore available in 7 cases. In all cases, the diagnosis of malignant melanoma was confirmed by histological analysis. 5 tumours were of mixed cell type (epitheloid and spindle-B) and 2 were of Spindle-B type.

The remaining 40 patients in this study currently have a diagnosis of choroidal naevus and are being managed by regular observation. Tumour thickness ranged from 0mm (flat) to 2.5mm (average: 0.8mm, standard deviation: 0.8mm) and basal diameter ranged from 2mm to 7.5mm (average: 5.1mm, standard deviation: 1.8mm). The number of risk factors associated with increased risk of growth was calculated for each patient. 7 patients (17.5%) had lesions over 2mm in thickness, 12 (30%) had lesions within 1 disc diameter of the optic disc, 1 (2.5%) had clinically detected sub-retinal fluid associated with the lesion, 5 (12.5%) had associated visual symptoms, 13 (32.5%) had no drusen and 5 (12.5%) had orange pigmentation within the lesion. 2 patients (5%) had 6 risk factors, 2 (5%) had 5, 1 (2.5%) had 4, 3 (7.5%) had 3, 7 (17.5%) had 2, 11 (27.5%) had

1 and the remaining 14 (35%) had none of the risk factors associated with increased risk of tumour growth.

Position of the choroid: Scans across the 10 flat naevi selected for this part of the study showed similar patterns of reflectance. In all cases, the retinal structure appeared intact. In 7 out of 10 cases there was increased reflectance in the region of the scan traversing the naevus. This increased reflectance appeared beneath the RPE-Choriocapillaris complex as shown in Figure 6.9 and is likely to be due to concentrations of melanin with the naevus. Thus, these findings show that the naevus is located beneath the RPE-Choriocapillaris complex and that this region therefore must correspond to the choroid.
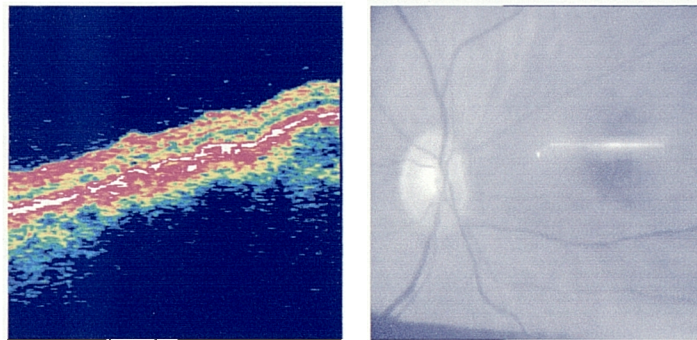
Figure 6.9   *OCT scan across a flat naevus. There are increased reflections beneath the choriocapillaris complex in the region where the scanning beam traverses the pigmented lesion. Retinal structure appears intact.*

Reflectance pattern from within the tumour: In all cases, it was found that reflections from beneath the band corresponding to the RPE-choriocapillaris are very weak. Since the RPE contains melanin, which is a strong scatterer of light at this frequency, very little light can penetrate to layers beneath the RPE and thus, the reflections from within the tumour mass are weak and do not give any useful information on the histological composition of the tumour.

Changes in the surrounding and overlying tissue: In the group of patients with malignant melanoma, OCT showed serous retinal detachments surrounding or overlying

the tumour in all 20 cases, including 8 cases in which no serous detachments had been noted on clinical examination. Only 2 patients had no evidence of intra-retinal splitting or abnormal retinal structure in the tissue overlying the tumour. All of the other 18 patients had at least one of these abnormalities. 8 had only intra-retinal splitting, 7 had only abnormal structure and 3 had abnormal retinal structure with low reflectance areas within, suggestive of cystic spaces.

The repeat scans from one patient who was diagnosed with choroidal melanoma 15 months after initial presentation, following enlargement of the lesion from 1 mm to 2mm, are interesting. The initial scan across the surface of the lesion showed a raised, but essentially normal retinal structure with a few very small serous detachments (Figure 6.10A). Repeat scans of the same region were acquired at a follow-up visit 15 months later. These scans were made using the *Repeat Scan* option and the corresponding fundus pictures were analysed to ensure that the same regions had been scanned on both occasions. These scans (Figure 6.10B) showed cystoid spaces which had not been evident from the first set of scans. Repeat scans from the other patients whose naevi showed growth during the period of observation were acquired at shorter intervals and showed no appreciable inter-visit differences other than an increase in elevation.

In cases where OCT identified sub-clinical serous detachments of the retina, the maximum separation between neurosensory retina and the RPE-choriocapillaris complex was measured from the OCT scans. These separations ranged from 15 to 120 microns (average: 75.3 microns, standard deviation: 23.8 microns).

| A | B |
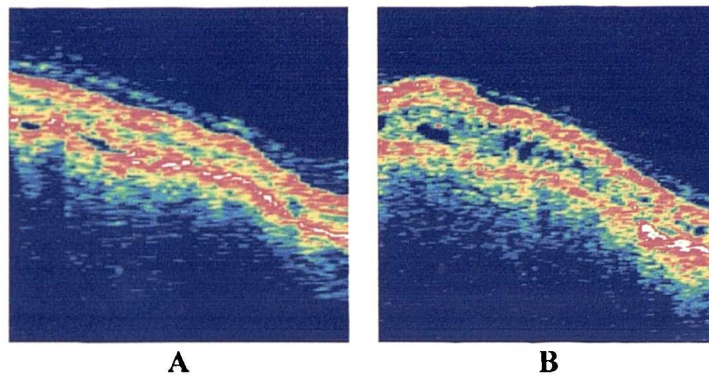
Figure 6.10   *Scan across the tumour surface a patient with a lesion that increased in size. (A) Scan at presentation showing a few areas of sub-retina fluid but normal retinal architecture. (B) Scan of the same area obtained 15 months later, after documented growth of the tumour. Subtle intra-retinal splitting was observed.*

Scans from the 40 patients with naevi were analysed for changes similar to those observed in the melanoma group. 27 patients (67.5%) showed none of these abnormalities - no serous detachments at the base of the lesion or in the retinal tissue overlying the lesion, no intra-retinal splitting and no structural abnormalities. Out of the remaining 13 (32.5%), 12 had serous retinal detachments. Serous detachments had been noticed clinically in only 1 of these patients. The separation between neurosensory retina and underlying RPE-choriocapillaris in these cases of sub-clinical serous detachments was similar to that observed in the melanoma group ranging from 17 to 118 microns (average: 68.2 microns, standard deviation: 26.6 microns). 2 patients were found to have intra-retinal splitting in the tissue overlying the lesion (Figure 6.11A). Changes in the retinal structure, similar to those found in the melanoma group, were observed in 1 patient (Figure 6.11B).

A   B
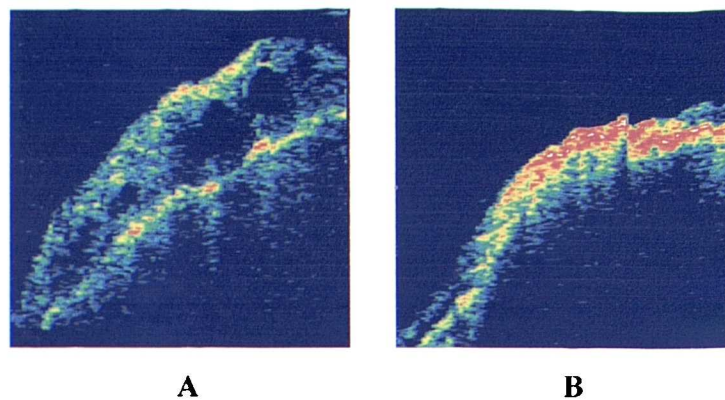
Figure 6.11   *Secondary retinal changes in patients with naevi. (A) Intra-retinal splitting. (B) Abnormal retinal structure.*

Discussion

Analysis of scans from patients with flat naevi showed that the retina had the characteristic band structure and that increased reflectance was visible beneath the RPE-choriocapillaris complex in most cases. This confirms that the choroid is the low reflectance region situated beneath the red band corresponding to the RPE-Choriocapillaris complex on OCT scans.

In the normal retina, reflections from the choroid tend to be rather weak since they are shadowed by strong reflections arising from the RPE. If the scan line traverses a choroidal naevus or melanoma, this shadowing effect tends to be even more pronounced since many of these lesions are pigmented. Thus currently available ophthalmic OCT systems cannot give any information on the internal structure of choroidal naevi and melanomas meaning that OCT cannot be used for in-vivo histological analysis of these lesions. In order to acquire information on the internal composition of such lesions, an OCT system that makes use of a more penetrating wavelength would have to be designed. Similar findings were reported in a smaller study by Schaudig et al[86].

It is known that malignant choroidal melanomas and choroidal naevi may cause secondary retinal changes[78,79]. To date, there is little information on the OCT appearance

of these secondary changes and an additional aim of this study was therefore to establish the characteristic appearance of secondary retinal changes associated with choroidal melanomas and naevi when imaged with OCT.

Clinical and histopathological studies on patients with choroidal tumours have shown that common associated secondary changes include serous retinal detachment extending beyond the limit of the tumour, atrophy of the RPE, atrophy of the retina starting in the photoreceptor layer, cystoid retinal degeneration leading to retinoschisis and invasion of the sensory retina by the tumour[78,79] This study showed that serous detachments, cystoid retinal degeneration and retinoschisis could be visualised in-vivo using OCT. In some patients, the retina overlying the tumour appeared to have lost the characteristic band structure associated with normal retinal tissue on OCT. Since the RPE-choriocapillaris layer could not be identified in these patients, it is possible that atrophy of the RPE had occurred. This study shows that although OCT in its current state cannot give any in-vivo information on the histology of choroidal tumours, this imaging technique can clearly demonstrate retinal changes in the tissue surrounding and overlying choroidal tumour.

An interesting observation from our study was the fact that the majority of patients with diagnosed choroidal melanoma in our study group were found to have cystic degeneration, retinoschisis or abnormal retinal structure suggestive of RPE or retinal atrophy. By contrast, only a small percentage of patients with presumed naevi showed these changes. Out of the three patients with presumed naevi who did have these changes, 2 have been under observation for less than 2 years and have some of the risk factors associated with increased risk for growth, so the possibility that these are in fact small choroidal tumours cannot be ruled out at this stage. The third patient has been under observation for over 30 years but has recently developed visual symptoms in the affected eye. Thus it is possible that the lesion in this case was a dormant melanoma that has recently become active.

The case presented in Figure 6.10 shows repeat OCT scans of a lesion that grew from just under 1mm at first presentation to 2mm during a 15-month period. At presentation,

the lesion was classified as suspicious due to its proximity to the optic disc, the presence of sub-retinal fluid accumulation at the macula, visual symptoms, absence of drusen and clumps of orange pigmentation over the tumour surface. It was therefore decided to re-examine the lesion at frequent intervals. The initial scans (Figure 6.10A) showed an elevated area over which the retinal structure appeared relatively intact. There were a few small regions of sub-retinal fluid accumulation, but both the retinal nerve fibre layer and retinal pigment epithelium layer were still well defined. The follow-up scans acquired 15 months later showed cystic spaces within the retina overlying the tumour. This cystic degeneration could have simply been a result of chronicity, however, given that similar cystic degeneration was observed in several patients with diagnosed choroidal melanoma but in very few of those with naevi, some of which were long-standing, it is possible that the development of cystic spaces in this particular patient was due to the probable malignant nature of this tumour. This particular case indicates that OCT can document the development of secondary retinal changes and could therefore be a useful tool in the follow-up of patients with suspicious naevi.

The majority of serous retinal detachments observed on OCT scans of patients with presumed naevi had not been noticed clinically. Since the presence of sub-retinal fluid has been associated with a greater risk of growth[83-85], this finding could be of value in the differential diagnosis of small choroidal lesions.

Investigation, using OCT, of patients with diagnosed choroidal melanoma has shown that the majority of these patients have associated secondary retinal changes. The incidence of similar changes in patients with presumed choroidal naevi appears to be much lower. Long term follow-up of the patients with presumed naevi that show changes similar to those of patients with melanomas is required to establish whether these findings are of diagnostic value.

6.7   Conclusions

Various ocular conditions were studied with OCT in order to gain a greater understanding of the correlation between OCT images and histology and also to investigate the ability of the system to document disorders occurring at different locations within the retina and choroid.

The position of the vitreo-retinal interface was established by analysing scans of patients with epiretinal membranes. Studies on patients with glaucoma and X-linked retinoschisis showed that the red band situated immediately below the vitreo-retinal interface corresponds to the RNFL. The yellow-green region between the two red bands was found to correspond to the mid- and outer- retinal layers, as shown from the study on patients with X-linked retinoschisis. A deeper understanding of the nature of the two sections often visible within the posterior red-white band resulted from the study on patients with either rhegmatogenous retinal detachments or macular holes. Finally, analysis of scans of patients with choroidal naevi showed that the region beneath this posterior red-white band corresponds to the choroid. These results from studies have helped to identify the nature of the various bands that appear on OCT scans.

Some of the limitations of the OCT system used became apparent through these studies. The study on epiretinal membranes showed that OCT was not always able to resolve two adjacent structures with similar reflective properties. Measurements of the RNFL thickness in glaucomatous patients were not as reproducible as those in normal patients due to problems with correctly identifying the posterior border of the RNFL in conditions that affect the health and reflectivity of this layer. Since the reflectivity of the mid- and outer-retinal layers appears similar for the wavelength of the light source, these layers cannot be individually resolved in current OCT systems. An additional problem with the light beam is that it is strongly reflected by the melanin within the RPE, thus the choroid and any structures within it are not well visualised with the current system. Preliminary studies on OCT system with improved longitudinal resolution have indicated that some of these limitations will be overcome in future generations of OCT

scanners. These developments are discussed in Appendix A. Changing the wavelength of the light source may also improve the ability of the system to give higher resolution images of retinal and sub-retinal structures.

Despite these limitations, it is clear from these studies that OCT in its present state is nevertheless a useful tool in ophthalmology. Differentiating between pseudoholes, lamellar holes and macular holes is not always straightforward using conventional methods of visualising the retina such as slit-lamp biomicroscopy and fundus photography. The appearance of each of these conditions on OCT is quite distinctive and OCT can therefore be used to establish a definitive diagnosis in situations where a clinical diagnosis is not clear. In X-linked retinoschisis, a combination of anatomical information from OCT and functional information from electrophysiology has led to a deeper understanding of the mechanisms of the condition. OCT is able to document epiretinal membranes, macular holes and rhegmatogenous retinal detachments and is therefore a useful tool for assessing the outcome of surgery for these conditions. The results from the study on choroidal lesions suggest that OCT may also be of value in differentiating between benign and malignant tumours.

Analysis of OCT scans acquired from a range of clinical studies has led to a more accurate interpretation of the OCT image. Although these studies have highlighted some of the limitations of the current technology, they have nevertheless shown that OCT can provide useful additional information on a variety of ocular conditions.

Chapter 7

CONCLUSIONS AND FURTHER WORK

7.1   Conclusions

This thesis describes the evaluation of a new ophthalmic imaging technique – Optical Coherence Tomography (OCT) designed to produce high-resolution cross-sectional images of the eye. The purpose of this research was the evaluation of a commercially available OCT scanner, the OCT 2 scanner manufactured by Zeiss-Humphrey Medical Systems, in the context of a routine clinical setting. In Chapter 1, (Section 1.4) the framework of research was devised to quantitatively assess this technique. The conclusions from this research are discussed in the following six sections.

7.1.1   Assessment of Performance

Various tests were carried out to test specific aspects of the performance of the scanner. One of the main attractions of OCT technology is that it can give axial information on ocular tissue with a resolution that surpasses that of other ophthalmic imaging systems. The longitudinal resolution of the system is determined by the coherence length of the scanner. In the OCT 2 scanner, which uses a light source operating at 850nm and an optical bandwidth of 30nm, the theoretical resolution of the system is around 10μm. The resolution was measured by analysing images from a highly-reflecting mirror. The reflection from the surface of the mirror resulted in a single high-intensity peak, the width of which gave a measure of the true longitudinal resolution of the system. The average full-width-at-half-maximum (FWHM) measured from the reflections at several points along the scan line was 11.6μm which was in close agreement with the theoretical longitudinal resolution.

The OCT 2 scanner is supplied with software designed for making absolute measurements of retinal thickness and thickness of the retinal nerve fibre layer (RNFL). The calibration of the system and accuracy and precision of measurements were investigated by acquiring scans of a glass test object that contained a gap of width $200 \pm 0.5\mu m$. Scans were acquired with this gap filled with air, which gave rise to very intense reflections at the edges of the gap, and also with water or glycerine in the gap. Both water and glycerine have a refractive index which is quite similar to that of glass, so reflections from the glass-liquid interface were much weaker than those arising from the glass-air interface. When compared with the known gap thickness, measurements made from the scans in all three cases were found to have a high degree of accuracy and precision. When the gap was filled with water or glycerine, the reflections from the interfaces did not appear as continuous lines, however, the gap edges could be identified at a number of locations along the scan. Measurements made at these locations were also accurate and precise.   This observation has important clinical implications since it shows that accurate and precise measurements may be made even from scans of relatively poor quality at locations where the retinal or RNFL borders can be identified.

One of the potential clinical applications of OCT is the monitoring of changes in retinal or RNFL thickness in patients with conditions such as diabetic macular oedema or glaucoma. It was therefore important to quantify the repeatability and reproducibility of OCT measurements. The definitions of repeatability and reproducibility used throughout the project were derived from documents issued by the British Standards Institution[34,35] and the related statistical analysis was carried out according to the guidelines of Bland and Altman[36]. Reproducibility and inter-session repeatability were initially assessed using the test object. The studies showed that measurements of gap thickness were highly repeatable and reproducible and that any changes in room temperature caused by the OCT scanner being left switched on for long periods of time did not affect the measurements. The repeatability and reproducibility of retinal, retinal nerve fibre layer and corneal thickness in normal volunteers were also assessed and the results are discussed in Section 7.1.4 below.

7.1.2   Factors affecting scan quality

Since OCT is a non-invasive technique, scanning was well tolerated by the majority of patients and, in general, it was found that an experienced operator could acquire good quality scans quite quickly and easily from most patients. A few factors could, however, affect the quality of the OCT scans.

It was observed that scan quality could be considerably compromised by non-optimal scan set-up. The focussing control on the viewing unit serves two purposes - it is used to obtain a sharp fundus image on the fundus imaging unit and it may also be varied to optimise the intensity of the OCT signals. Varying the focussing control even by very small amounts was observed to have an appreciable effect on the intensity of the OCT signals. As the intensity of the signals decreased, the retinal interfaces became less clearly defined and consequently the measurement algorithms were more likely to misidentify these borders and give erroneous readings. While scanning, the operator may also adjust the polarisation control which attempts to optimise the strength of the OCT signal by matching the polarisation of the light reflected from the tissue. The quality of scans was also somewhat affected by adjustment of the polarisation setting although the effects of this were not as severe as those observed for non-optimal focussing settings. These studies showed the importance of optimising both the focussing and the polarisation settings as non-optimal settings could lead to poor identification of retinal layers by the OCT software.

The operator also has control over the noise level setting of a particular scan. Raising the noise level changes the appearance of the scan as more of the lower-intensity signal is converted to black. A study carried out on repeat scans with different noise level settings showed that, provided that the signals from the interfaces of interest did not fall below the noise threshold, thickness measurements were not influenced by different noise settings. The actual intensity values, on the other hand, were found to be linearly related to the noise level setting. Thus comparison of intensity values between different scans is meaningful only if the scans were acquired with the same noise level settings. If this is not the case, intensity values must first be converted to a reference noise level using a simple linear equation.

Other factors which affect scan quality are patient-related. As OCT is an optical imaging system which constructs transverse retinal images from light reflected within the eye, any factors which affect the ability of light to travel through to the retina are likely to compromise the quality of the scans. A study of scan quality in patients with mature cataracts did, in fact, show that the overall intensity per pixel in these scans from these patients was significantly lower than that from patients with clear media. This is one of the limitations of the OCT 2 scanner. There was also some concern that the quality of the scans could be affected by the age of the subject. However, a study carried out to investigate this relationship established that, provided the subject had clear media, the quality of retinal images was not related to the age of the subject. Clinical experience also showed that good quality scans were difficult to acquire in patients with small pupil size, ptosis, those unable to maintain fixation and those prone to excessive blinking.

7.1.3   Interpretation of Retinal OCT Images

Good quality OCT scans of normal retinal tissue have a distinctive characteristic appearance. OCT scans from normal subjects show two regions of relatively high reflectivity which appear as red or red and white bands. The more posterior of these two bands is more clearly delineated and often appears split into two portions, a thinner one anteriorly and a thicker one posteriorly. In the literature related to OCT, it is generally assumed that the more anterior of these two bands corresponds to the retinal nerve fibre layer (RNFL) whereas the more posterior represents the RPE-choriocapillaris complex. The *Retinal Thickness* and *RNFL Thickness* tools supplied with the OCT 2 scanner work on these assumptions. These bands are separated by a region of lower reflectivity which generally appears as yellow and green. Sometimes the region immediately anterior to the lower red-white layer appears as a region with very low reflectivity (dark blue or black). Scans through fixation in normal subjects show a clear dip in the retinal contour.

The relationship between the characteristic OCT bands and histological retinal layers was investigated in three different ways. In the first instance, OCT images were compared to textbook images of histological sections of retinal tissue, as seen under a light microscope. This was followed by direct correlation between OCT scans and

histological images of canine retina. Finally, scans from patients with a variety of retinal conditions of known pathology were studied. The locations of the abnormalities on the OCT scans gave further information on the nature of the various OCT bands.

It was observed that the anterior red band was at its thickest around the optic nerve head, especially in the superior and inferior regions and became progressively thinner with increasing proximity to the fovea. From histological studies, the retinal nerve fibre layer (RNFL) is known to be at its thickest around the optic nerve head, especially superiorly and inferiorly where bundling of the nerve fibres occurs. At the fovea, all the retinal layers above the photoreceptors are displaced concentrically. This pattern of RNFL thickness matches the variation in thickness of the red band on OCT scans. Two of the clinical studies carried out also suggest that this red band may be related to the RNFL. In patients with glaucoma, a condition in which the RNFL becomes thinner and exhibits defects, the thickness of the anterior red band was found to be significantly less than that measured from a cohort of normal volunteers and in patients with X-linked retinoschisis, which manifests as splitting of the retina beneath the RNFL, the splitting on the OCT scans was observed to occur just behind the anterior red band. These observations suggest that there is a relationship between the anterior red band on OCT scans and the RNFL. The direct correlation between canine OCT scans and corresponding light microscopy images was somewhat inconclusive. The anterior red band was not present on all the specimens studied and, in the cases in which it was visible, it was not as well-defined as in scans from human subjects. This could have been due to the differences in anatomy between dog and canine retina but may also have been caused by the fact that the canine eyes that were examined were enucleated. Direct comparison of OCT scans and light micrographs showed that this red band corresponded to more than just the RNFL. The region on the scans corresponding to the photoreceptor layer appeared as a region of lower intensity in the two cases examined. This region of low intensity is often seen on scans of normal human volunteers and this study suggests that it may be related to the photoreceptor layer. Another interesting observation from this study was that the intensity of the anterior region of the scan varied with corneal hydration in a couple of cases. This finding merits further investigation as it may have clinical implications.

The more posterior high reflectance band is generally believed to correspond to the retinal pigment epithelium (RPE) together with the choriocapillaris because of the high reflectivity of this region. The RPE contains melanin which is a strong scatterer of light of wavelength 850nm and in fact, scans across regions of bone spicule pigmentation in patients with retinitis pigmentosa show white areas of high intensity. This band is generally split into two portions in normal subjects and clinical investigations were carried out on patients with rhegmatogenous retinal detachment or macular holes in order to determine the nature of these two distinct portions. In several of the patients with rhegmatogenous retinal detachment, the thinner anterior portion of this layer was observed to have detached along with the neurosensory retina. This suggests that this portion is more likely to form part of the neurosensory retina rather than the RPE-choriocapillaris. Similarly, in most patients with full-thickness macular holes, a condition which affects all layers of the neurosensory retina but leaves the RPE intact, only one portion of the RPE-choriocapillaris band was observed at the base of the hole but both portions were present at the edges of the hole and elsewhere in the retina. This observation lends further support to the theory that this portion of the posterior highly reflecting band is actually part of the neurosensory retina rather than the RPE-choriocapillaris complex.

7.1.4   Normative Studies

The performance of the OCT scanner in the clinical setting was investigated and normative data was acquired. The repeatability and reproducibility of measurements of total retinal thickness, RNFL thickness and central corneal thickness were assessed and normative ranges for these parameters were established. The normative range of foveal thickness was also established as this parameter is often useful to know in the clinical environment.

Measurements of all three parameters were found to be repeatable and reproducible, however, coefficients of repeatability and reproducibility of RNFL thickness measurements were poorer than those of retinal or corneal thickness measurements. The posterior boundary of the RNFL is not very well-defined and the intensity of the returning signals from this layer is susceptible to very small eye movements.

Consequently the RNFL Thickness tool may fail to correctly identify this border at all locations along the scan. Nevertheless, provided that several repeat scans are acquired during a scanning session and that the RNFL thickness is averaged across these scans, the repeatability and reproducibility of these measurements should be at a level that is clinically acceptable. The ability of OCT to produce repeatable and reproducible measurements implies that is it a useful tool in the periodic assessment of conditions which cause variations in retinal, RNFL or corneal thickness.

7.1.5   Analysis of supplied and additional software

The performance of the *Retinal Thickness* and *RNFL Thickness* tools was rigorously assessed. Both tools were found to perform reasonably well in normal subjects as well as in patients with macular oedema, however, small errors in border detection were frequently present at points along the scans. These were likely to be caused by small movement artefacts. The algorithms ran into more serious difficulties when reflective particles were present in the vitreous. These caused the algorithms to completely mis-identify the anterior surface of the retina and give erroneous retinal thickness and RNFL thickness measurements. It was observed, however, that these problems were not consistent and that other scans acquired from the same subjects were correctly analysed by the thickness measuring tools. In the clinical environment, it is therefore recommended to run the thickness measuring tools while the patient is still in clinic so that repeat scans may be acquired if necessary. The retinal thickness also failed to function properly in patients with conditions that caused a break in the retinal contour, such as macular holes – this is one of the limitations of the current software. Measurements made using the callipers are comparable to those generated automatically by the measuring software, however, measurements directly from the A-scans are very subjective and should be avoided unless there is no alternative.

The OCT 2 scanner is not designed for corneal scanning, although this is possible with minor modifications to the system. Consequently no software for measuring corneal thickness is supplied with this model. In-house software which read raw data from corneal OCT scans and computed central corneal thickness was therefore developed. This program identified the apex of the scan and measured corneal

thickness from the 21 scans centred on the apical one. It then computed an average central corneal thickness. The software was tested and found to perform well on corneal scans from normal subjects.

Another in-house program was developed to display images in greyscale rather than as false-colour plots. The program was written to use 256 bands of greyscale ranging from black to white in even increments. It has been suggested that greyscale representation of OCT data is easier to interpret than the standard false colour plots and the OCT 3 scanner, the most recent model, includes an option for greyscale representation of data. Since the option was not available with the OCT 2 scanner used in this project, the in-house software was developed so as to give clinicians the option of viewing scans in either mode.

7.1.6 Clinical Studies

The clinical studies carried out for this project served two purposes – to give information about the correlation between the retinal bands observed on OCT and histological layers (discussed in Section 7.1.3 above) and additionally to assess the potential clinical role of OCT imaging. The selected pathologies were chosen to evaluate the system's ability to give information about disorders affecting different retinal and sub-retinal layers.

A study on patients with a clinical diagnosis of epiretinal membrane showed that OCT could clearly demonstrate the presence of the epiretinal membrane if this was not totally adherent to the surface of the retina. In these cases, the membrane appeared as a thin, highly reflecting band, partially attached to the vitreo-retinal interface. Epiretinal membranes were more difficult to identify if they were totally adherent to the retinal surface. In some of these cases, thin, highly reflecting areas were observed in the anterior portion of the retina, however, it could not be concluded that these signals were definitely arising from the epiretinal membrane. The RNFL is also highly reflecting so these signals may have arisen from this layer rather than from the membrane. One limitation of OCT that it cannot adequately resolve adjacent structures with similar optical properties. Complications associated with the presence of an epiretinal membrane, such as macular oedema, were well

documented with OCT. Measurements of residual foveal thickness were also useful for distinguishing between pseudoholes and lamellar holes. OCT may be useful in the diagnosis of epiretinal membranes and associated complications as well as for follow-up after surgery.

Several research groups have shown that the RNFL thickness measured from OCT scans is significantly lower in glaucomatous patients than in normal subjects and these findings suggest that OCT could be a valuable tool in the diagnosis of glaucoma. However, one of the shortcomings of current OCT scanners is their inability to produce RNFL thickness measurements with the same degree of repeatability and reproducibility as measurements of total retinal thickness. The studies carried out in this project showed that while the coefficients of repeatability and reproducibility of total retinal thickness were similar in normal and glaucomatous subjects, those for RNFL thickness measurements were considerably worse in the glaucoma group. Moreover, total retinal thickness in glaucomatous patients was significantly lower than in normal subjects. These findings suggest that retinal thickness is a more accurate parameter than RNFL thickness for distinguishing between normal and glaucomatous patients.

OCT was able to show splitting in the mid-retinal layers in patients with X-linked retinoschisis. These images were correlated with localised functional information acquired from multifocal-ERG (mfERG) recordings, thus giving interesting information on the relationship between anatomical abnormalities and corresponding retinal function. The results from this study showed that retinal function was abnormal throughout the retina even in cases were no peripheral schisis had been observed clinically or on OCT, which indicates that loss of retinal function occurs before mid-retinal splitting develops. The relationship between the degree of retinal splitting and the amplitude of the central mfERG responses was surprising as the eyes with smaller schisis cavities tended to have more reduced amplitudes. The latencies of the central responses were similar in all cases and were not correlated to the size of the schisis cavities. Although the individual mid-retinal layers are not well resolved with the OCT 2 scanner, abnormalities occurring in this region may be seen on the scans, as demonstrated by this study. The correlation of anatomical OCT information with functional data can give interesting information on disease

processes. Other conditions which are well visualised on OCT include retinal detachments and macular holes, as shown by the studies carried out on patients with these conditions. Differentiating between full thickness macular holes, lamellar holes and pseudoholes is often fairly straightforward if OCT scans are available. Another potential clinical application is the evaluation of anatomical recovery following surgery for these conditions.

One limitation of current OCT technology, highlighted by the study on patients with choroidal tumours, is its inability to give any information on structures located beneath the RPE-choriocapillaris complex. This layer is highly reflecting because of the melanin within the RPE and as a result of this, reflections from the layers beneath it tend to be very weak. OCT was therefore unable to give any information on the histological composition of choroidal tumours. A different wavelength of light with greater penetrating power would be required for imaging structures beneath the RPE-choriocapillaris complex. Secondary retinal changes associated with the tumours were, however, well documented. Histological studies on choroidal melanoma have shown that these tumours may cause serous retinal detachments, macular oedema, retinal splitting cystic degeneration and atrophy in the overlying and surrounding retina. These could all be observed with OCT and the majority of patients with choroidal melanomas were found to have at least one these secondary retinal changes. Patients with naevi under observation were also assessed with OCT. In several cases, sub-retinal fluid that was not visible clinically was present on the scans. As the presence of sub-retinal fluid is one of the factors believed to indicate greater risk of malignancy, it is useful to have a technique that can show these serous detachments before they become clinically apparent. Very few of the patients with choroidal naevi included in this studied show secondary changes similar to those observed in the melanoma group. Follow-up of patients with these changes should show whether this observation is useful in differentiating between naevi and melanomas.

The overall conclusion from the work described in this thesis is that OCT is an imaging technique which can give repeatable and reproducible information on axial retinal and corneal structure with a resolution that is better than that of other available techniques. The OCT 2 scanner is easy to use and scanning is well-

tolerated by patients. Despite some limitations with the currently available system, OCT in its current state has many potential clinical applications in ophthalmology and its popularity is likely to increase over the next few years. The following section gives details on future projects designed to overcome some of the limitations of the current system and to continue to investigate the clinical potential of this new imaging technique.

7.2 Further Work

7.2.1 Correlation with functional information

The study on patients with X-linked retinoschisis, described in Section 6.4, showed that combining anatomical images from OCT with localised, objective, functional information from the multifocal-ERG (mfERG) gave a fascinating insight into the relationship between retinal changes and corresponding retinal function in different parts of the retina. Since our unit is one of the few to have access to tools for localised functional and anatomical retinal imaging, several future projects that combine information from the two techniques have been planned. Two of these future projects are discussed briefly below.

Project 1: Combined functional and anatomical information for improved diagnosis of small choroidal melanoma

The study on patients with choroidal naevi and melanomas, described in Section 6.6, indicated that secondary retinal changes associated with these lesions and demonstrated by OCT might be useful in differentiating between benign and malignant tumours. In addition to this study using OCT, a pilot study to investigate the retinal function in a sub-group of the 60 patients in the OCT study was also carried out.

A total of 20 patients, 10 with diagnosed choroidal melanoma and 10 with presumed choroidal naevi of various sizes were included in the study. The wide-field mfERG was used to acquire functional information in all cases. The initial results from this study indicate that abnormal retinal function was present in the quadrant containing

the tumour in all patients with diagnosed choroidal melanoma. Figure 7.1 illustrates a typical case. This patient had a relatively small choroidal melanoma (height: 2mm; basal diameter: 4mm) situated superior to the left optic disc. The patient had no other known ocular conditions in either eye. The mfERG recording clearly showed that the implicit time of the recording from the affected quadrant in the left eye was delayed with respect to the other quadrants in the same eye and to the corresponding quadrant in the fellow eye. A similar pattern of retinal abnormalities was seen in all other 9 patients with diagnosed choroidal melanoma. In some cases, the responses from the affected quadrant were also reduced in amplitude as well as delayed. By contrast, only one of the patients with a presumed choroidal naevus showed delayed mfERG recordings in the region corresponding to the location of the naevus. This patient had three of the risk factors associated with increased likelihood of growth (sub-retinal fluid around the lesion, height greater than 2mm and associated visual symptoms).

The results from this pilot study indicate that the wide-field mfERG may give information on retinal function that could be useful in distinguishing between patients with choroidal naevi and choroidal melanomas. However, it is clear that a larger study with more patients and longer follow-up times is required in order to make any valid conclusions. The study using OCT showed that some patients with presumed choroidal naevi had secondary changes similar to those seen in patients with diagnosed choroidal melanoma. It will certainly be interesting to investigate whether these patients also have abnormal retinal function in the affected regions and conversely, whether patients with naevi and functional abnormalities also have structural abnormalities. The combination of anatomical and functional information in a larger group of patients with choroidal naevi and choroidal melanomas will be the subject of a future study to determine the efficacy of these two combined techniques in distinguishing between benign and malignant tumours.
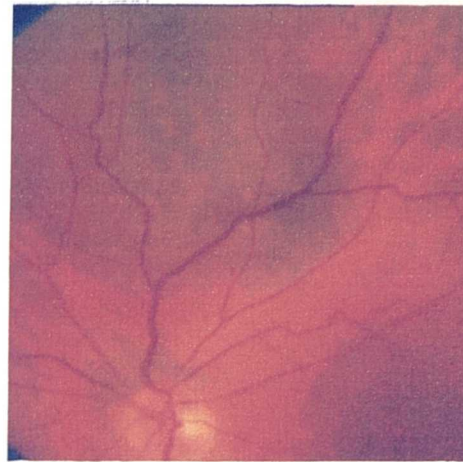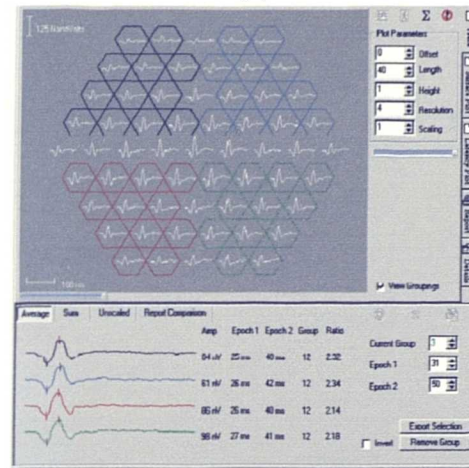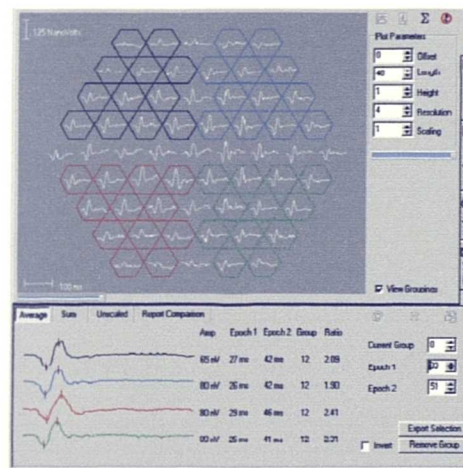
Figure 7.1   *mfERG recordings from a patient with a small choroidal melanoma. (A) Fundus photograph showing the location and appearance of the tumour. (B) Recording from the unaffected right eye. (C) Recording from the affected left eye. The recording from the affected quadrant, shown in red, is clearly delayed with respect to other quadrants in the same eye and the corresponding quadrant in the right eye.*

Project 2: Combined functional and anatomical information for early diagnosis of impending macular holes

Significant new information on the early stages of macular holes has emerged from several studies using OCT[87-92]. A study by Haouchine et al[87] offers evidence that supports the theory that a foveal cyst is the first stage in macular hole development and another study by Gaudric et al[89] showed that OCT could show the presence of these foveal cysts in some fellow eyes of patients with macular holes even when biomicroscopic examination of the fellow eyes revealed no indication of an impending macular hole.

In an interesting study by Birch et al[93], focal electroretinography was performed on the fellow eye of patients with a unilateral full-thickness macular hole. Abnormal fellow eye foveal electroretinography amplitude was significantly related to subsequent macular hole formation compared with eyes that did not go on to develop a macular hole, suggesting that electroretinography can provide an objective measure for identifying eyes at risk for macular hole formation.

These studies suggest that both OCT and focal electroretinography are potentially useful in the early diagnosis of macular holes, yet to date, there has not been a study in which both investigations are carried out on the same group of patients. The combined information from OCT and multifocal electroretinography will provide a means for assessing whether the presence of a foveal cyst, thought to be the first stage in macular hole formation, is correlated with abnormal foveal mfERG results.

7.2.2 Estimating Scleral Curvature

A planned future project will investigate the potential of OCT in estimating scleral curvature. We have recently been approached by a group carrying out research on the physiological functions of the tears and the preocular tear film. This group is interested in measuring the evaporation from the surface of the eye on a loss per unit area basis and have developed a computer-assisted method of estimating exposed wetted area of cornea and sclera from 2-dimensional images of the eye[94]. However, this program requires an estimate of both corneal and perilimbal curvature.

Measuring corneal curvature is fairly straightforward, however, estimating the curvature of the exposed portion of sclera has proved to be more challenging. The observation that the sclera is easy to visualise on OCT has led to interest into investigating whether scleral OCT scans may be used to estimate scleral curvature.

Since the current OCT system is designed to display scans acquired across a concave surface as flat images, when imaging a convex surface such as the sclera, the degree of curvature is exaggerated. The first step in this study will be to determine the reproducibility of direct curvature measurements made from OCT scans. Scans will be acquired from a number of cylindrical objects and volunteers during several independent scanning sessions. If the curvature measurements are found to be reproducible, the next part of the study will concentrate on devising methods of estimating the true scleral curvature from the OCT scans. There are two potential ways of doing this and both will be investigated.

The first approach is to compare OCT curvature with true curvature for a number of cylindrical test objects of known size. The scleral radius of curvature is typically in the region of 12.5 to 14.4mm so a set of objects ranging in radius from around 10mm to around 20mm in steps of around 0.5mm is desirable. The relationship between OCT radii of curvature and true curvature will be investigated. Provided a clear relationship exists, this information could then be used to estimate true curvature from OCT scans. Since corneal curvature can be estimated by other methods, this method will first be tested on corneal scans.

An alternative, and more scientific approach would be to quantify the extent of 'false' curvature caused by the OCT software. This information is probably readily available from the manufacturers. Once this is known, it should be fairly straightforward to estimate true corneal or scleral curvature.

If this project proves successful it would provide a solution to the problem of estimating scleral curvature.

7.2.3   An Enhanced User Interface

This project has highlighted a number of limitations of the OCT 2 software. Work is currently in progress to construct an enhanced and more user-friendly OCT user interface which will include more efficient image display, analysis and export features. The main features of this enhanced user interface are described below.

Platform

The current OCT software runs on a Windows 3.1 platform which is out-dated and somewhat limiting. The new interface is being constructed to run on a Windows 2000 platform. The advantage of this is that recent versions of software packages such as statistical packages may be run on the same machine and this would facilitate data analysis. The new system is designed to work with the exported raw intensity data, scan information file and fundus bitmap images. It is planned that the computer attached to the OCT scanner and the one running the enhanced interface will eventually be linked together to facilitate data transfer.

Image Display

The current OCT system can only display images in false-colour mode. As explained in Section 5.5, there are advantages to displaying the data in greyscale mode. The new interface will incorporate the program described in Section 5.5 for converting raw data into 256-level greyscale images. At present this program can display the data in raw and median-smoothed mode but work is currently underway to include other smoothing options.

In the present system, OCT images are scaled to fit in a window of fixed size regardless of the original length of the scan and consequently, the lateral scaling factor will vary for scans of different lengths. This can be quite misleading as the same feature will appear larger on a shorter scan than on a longer one. The new system will therefore be designed to read the scan length from the scan information file and will display all images with the same lateral scaling. In addition, a zoom

function will be included so sections of the scan may be displayed in greater detail. This will facilitate the positioning of the measurement cursors.

Image Analysis

As highlighted in Chapter 5, the algorithms used in the *Retinal Thickness* and *RNFL Thickness* tools are not infallible. Now that the major problems with these algorithms have been identified, work is underway to design algorithms that overcome these problems. A detailed publication by Koozekanani et al[95] describes an alternative algorithm for identifying retinal borders and the tests carried out on this algorithm show it to be considerably more reliable than the Zeiss-Humphrey one. The guidelines in this publication are being used as the basis of the new algorithms being designed.

In the present system, it is not possible to alter the automatically identified retinal contours, even when these have clearly been incorrectly identified. In the new system, the user will be able to manually adjust borders that have been incorrectly identified.

The only way of measuring corneal thickness with the Humphrey OCT software is by using the callipers. Since OCT corneal scanning is becoming increasingly popular at our centre, an algorithm for automatically identifying corneal borders and measuring average central corneal thickness was designed (see Section 5.4). This function will be incorporated into the enhanced user interface.

Printing Options

With the present system, only a single OCT image may be printed per page. This is not ideal since it is often preferable to view images of multiple slices on the same report. With the new interface, the user will have the option to choose from a number of different report formats, depending on the number of images to be displayed. The user will also be able to decide whether images are to be printed in smoothed or raw version and whether in greyscale or colour mode.

Data Export

In the present system the raw data is exported in a format which cannot be directly read into graphical or statistical packages such as Excel or SPSS. The new interface will read the raw data from the exported *.raw* file and automatically write it to a text file which can be read by most commercial software packages.

Another limitation of the existing software is that the option for exporting retinal and RNFL thickness data after running the Retinal Thickness and RNFL thickness tool is not part of the integral OCT software. This feature was supplied by the company as an additional program running directly from the DOS screen following demands by users. Although this feature functions well, it is quite cumbersome to use as the user must toggle between the OCT and DOS screens, type in an export command for every set of exported data and rename the created thickness file to prevent it from being over-written by the next set of exported data. With the new user interface, the option to export thickness data will be available from the main operating screen at the click of a button.

With the current OCT system, unprocessed OCT scans cannot be exported. This is a drawback in situations where certain features are best viewed on the unprocessed image. One typical example is of scans in which the vitreous is partially detached. In these cases, the vitreous appears as a thin blue line partially attached to the retinal surface. When alignment and smoothing procedures are applied to the scan, the weak signal corresponding to the vitreous is often obscured. The new system will therefore also allow users to export unprocessed as well as processed images.

Appendix A

RECENT DEVELOPMENTS IN OCT TECHNOLOGY

OCT technology has advanced at a rapid pace during the last decade. Zeiss-Humphrey Medical systems were the first to produce a commercially available scanner, based on the prototype developed at the Massachusetts Institute of Technology and the scanner described in this project belongs to the second generation of scanners to be produced by this company. Spurred on by the first successful applications of OCT in clinical practice, several Applied Optics research groups have turned their attention to OCT techniques and the past few years have seen a dramatic improvement in both the resolution and quality of OCT images as well as in the range of applications of OCT imaging techniques. This appendix gives a brief overview of some of these recent developments.

A.1 Recent Developments in Ophthalmic OCT

A.1.1 High-resolution imaging

One of the most exciting recent advances in OCT technology has been the development of an ultra-high resolution OCT system. This system is described in detail in reference 16. When compared with the currently available OCT system, this new system has significantly higher resolution. The current system, described in this project has a longitudinal resolution of 10-15μm – this resolution is dependent on the light source used, a super-luminescent diode with an optical bandwidth of approximately 30nm. The fundamental change in the new system is the use of a different light source, a state-of-the-art broadband Ti:Al$_2$O$_3$ laser which can generate ultra-short laser pulses. Ultra-short pulse laser sources are ideal for OCT imaging

because they have very broad spectral bandwidths and high single-mode power. The Ti:Al₂O₃ laser used in the ultra-high resolution OCT system produces pulses as short as 5.4 femtoseconds, which corresponds to bandwidths of up to 350nm centred on 800nm (the wavelength required in order to prevent absorption in the ocular media). This enables a longitudinal resolution of 2-3μm in the new system.

Some modifications in the internal design of the scanner were required. The fibre-optic interferometer and optical components were designed to transmit broad optical bandwidths. Optical dispersion in the sample and reference paths of the interferometer had to be balanced, as significant dispersion mismatch would have led to broadening of the axial resolution. Dispersion was balanced by using variable thicknesses of fused silica and BK7 and the dispersion of ocular media was compensated for using 25-mm water. The chosen spot size in this system was approximately 15μm, slightly larger than that in the conventional system. This larger spot size, however, improved the depth of focus and facilitated imaging through an undilated pupil.

The advantages of the improved resolution are clear from Figure A.1, which shows scans extending from the macula to the optic nerve head acquired from the conventional and ultra-high resolution OCT systems. The most obvious improvement is the much better definition of the RNFL. The variation in thickness from the fovea to the optic disc is far more evident from the new system than from the conventional one. There is also much better definition of the mid- and outer retinal layers. In the conventional system these layers appear as a single yellow-green band which cannot be separated into its various component layers. In the new system, however, many more layers are clearly visible. The split in the red band corresponding to the RPE-choriocapillaris complex is also well-defined. The upper, thin portion is labelled as the RPE and the lower as the choriocapillaris and choroidea. The various retinal layers visible on the ultra-high OCT scan were identified by comparison with text book images of normal retinal pathology and segmentation algorithms using boundary detection techniques were developed to identify the various layers and make thickness measurement. Direct comparison of a scanned specimen of human retina and its corresponding pathology was not carried out.
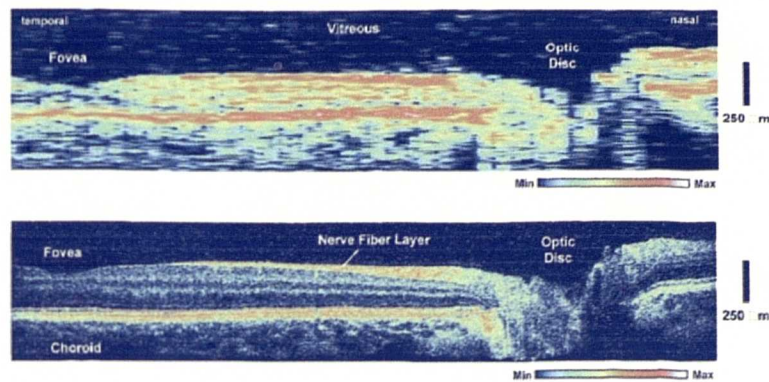
Figure A.1   *Comparison of conventional OCT (top) and ultra-high resolution OCT (bottom). Re-printed from Drexler W, Morgner U, Ghanta RK et al. Ultrahigh-resolution ophthalmic optical coherence tomography. Nature Medicine 2001;7(4):502-507.*

Improved corneal imaging is also possible with the new system. The corneal epithelium, Bowman's layer, intrastromal morphology and endothelial surface were clearly differentiated using the prototype ultra-high scanner (Figure A.2). Descement's membrane, however, could not be resolved, possibly because of insufficient contrast between the endothelium and stroma.
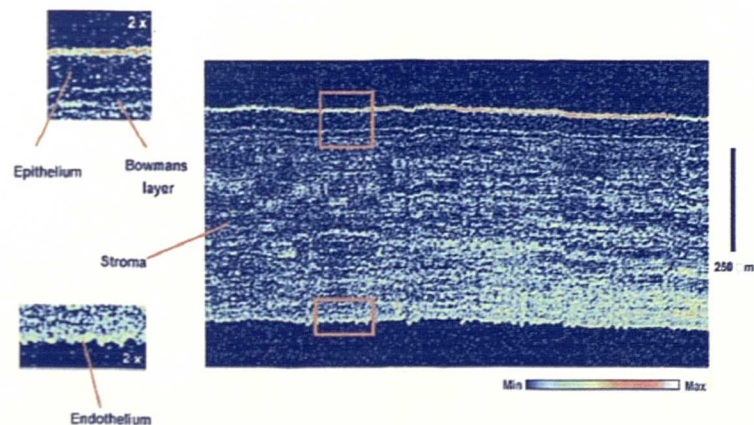

Figure A.2   *A corneal scan acquired with the ultrahigh resolution OCT scanner. Re-printed from Drexler W, Morgner U, Ghanta RK et al. Ultrahigh-resolution ophthalmic optical coherence tomography. Nature Medicine 2001;7(4):502-507.*

Ultrahigh resolution OCT scanners are not yet commercially available – the primary limitation, at present, is the high cost of the laser source. As laser technology improves, solid-state lasers should become more compact, cheaper and more readily available. It is therefore likely that ultra-high resolution OCT scanners will become available in the not too distant future. The significantly improved resolution of these new systems will be comparable to that of microscopy. The ability to acquire in vivo information of histological quality will certainly lead to very exciting new areas of research as disease processes will be able to be visualised with unprecedented clarity. Better delineation of the retinal layers should also lead to greater repeatability and reproducibility of intra-retinal thickness measurements, making OCT a better tool for monitoring variations in retinal morphology.

A.1.2   Improved Anterior segment imaging

The potential of OCT in imaging of the anterior segment has been recognised in recent years and imaging of the cornea with the currently available retinal OCT system has been performed successfully by a number of research groups. One drawback of the current system is the relatively long scan acquisition time of 1 second. This may introduce movement artefacts and scan misalignment. In order to overcome these problems and be able to carry out imaging of dynamic ocular events, Radharkrishnan and colleagues have developed a new, high-speed OCT system designed specifically for anterior segment imaging[96]

This system makes use of a light source with wavelength of 1310nm. The advantage of this higher wavelength is that the amount of scattering and absorption in ocular tissue is considerably lower than at 850nm, which is the wavelength used in most ophthalmic OCT systems, and the absorption in water increases sharply. Since the primary constituent of the vitreous humour is water, this implies that light at this wavelength will be mostly absorbed before reaching the retina, thus much higher illumination power may be used. The system uses a semiconductor optical amplifier light source capable of emitting 22mW of low-coherence light. The longitudinal resolution and lateral resolution achievable with this source is 8.1μm and 15μm respectively. Imaging rates range from 4 to 16 frames per second. Instead of the

usual slit-lamp set-up, this system makes use of a hand-held probe, which makes the scanner portable and permits scanning in any position.

Numerous examples of anterior segment scans acquired with this system are presented in the publication by Radhakrishnan et al[96]. Corneal scans from this system are fairly similar to those attainable from the current system – the corneal epithelium and stroma can easily be differentiated however the various components of the stroma cannot be individually resolved. In the iris, the stroma and pigment epithelium are well-delineated and real-time visualisation of dynamic events such as pupillary constriction is possible due to the high scanning speed. The deeper penetration of the 1310nm wavelength relative to the conventional 850nm, makes it possible to visualise the ciliary body and angle of the anterior chamber in greater detail.

In addition to non-invasive quantitative assessment of the cornea, there are several additional potential clinical applications for this new OCT system. Visualisation of the angle is important in evaluating the structural causes of angle-closure glaucoma syndromes. It is also possible to visualise, in real-time, anatomical changes in the angle in response to light and accommodation. Real-time corneal imaging could also be applied in the field of refractive surgery. Corneal flap thickness could be measured intra-operatively, which could improve the predictability of these procedures. Continuous monitoring of the ablation process and determination of the ablation rate would also be possible.

As the interest in anterior segment imaging using OCT is growing, more sophisticated systems, like the one described in this section are becoming available. This newer system offers a number of advantages over the conventional OCT system, which was designed primarily for retinal imaging, and consequently, there are several additional potential applications. The ability to perform high speed imaging is particularly interesting as it solves the problem of movement artefacts and allows changes in the anatomical structure to be viewed in real time.

A.1.3 *En-Face* OCT Imaging

The Applied Optics Group at the University of Kent in Canterbury, England have been working on an OCT system which acquires depth information in a different way to the conventional systems. Instead of imaging in the longitudinal x-z or y-z planes, the Kent system scans transversely (*en-face*), in the x-y plane[97] (Figure A.3). One of the main advantages of this approach is that scanning is in the same plane as in the scanning laser ophthalmoscope (SLO), which clinicians are likely to be well accustomed to. Thus the experience acquired in interpreting SLO images may be transferred more directly to the interpretation of the OCT images. This group has recently teamed up with Ophthalmic Technologies Inc. (Toronto, Canada) to produce a clinical *en-face* OCT system which can also produce SLO images. This system is often referred to as the OCT Ophthalmoscope and is currently being tested clinically in a few ophthalmic centres. It is likely to become commercially available in the near future.
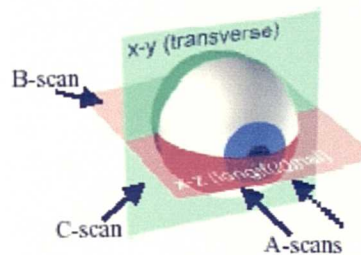
Figure A.3   *Relative orientation of the axial scan (A-Scan), longitudinal slice (B-scan), and en-face or transversal slice (C-Scan). Re-printed from Rogers, Podoleanu et al. Topography of volume measurements of the optic nerve using en-face optical coherence tomography. Optics Express. 2001;9(10):533-545*

The apparatus for this system comprises an interferometer excited by a superluminescent diode operating at 850nm with a bandwidth of 20nm. The OCT depth is adjusted by changing the optical path of the reference arm using computer-controlled translation in 1μm steps. The system also captures a confocal image simultaneously with the OCT image and both are displayed via a frame grabber. A

galvanometer scanning pair driven by ramp generators makes it possible to scan in both the transverse and longitudinal planes. Three-dimensional information may be collected by acquiring many en-face OCT images at different depth positions. The 3D information may be displayed in movie format or as a rotatable volume. The currently achievable depth resolution with this system is in the region of 20μm.
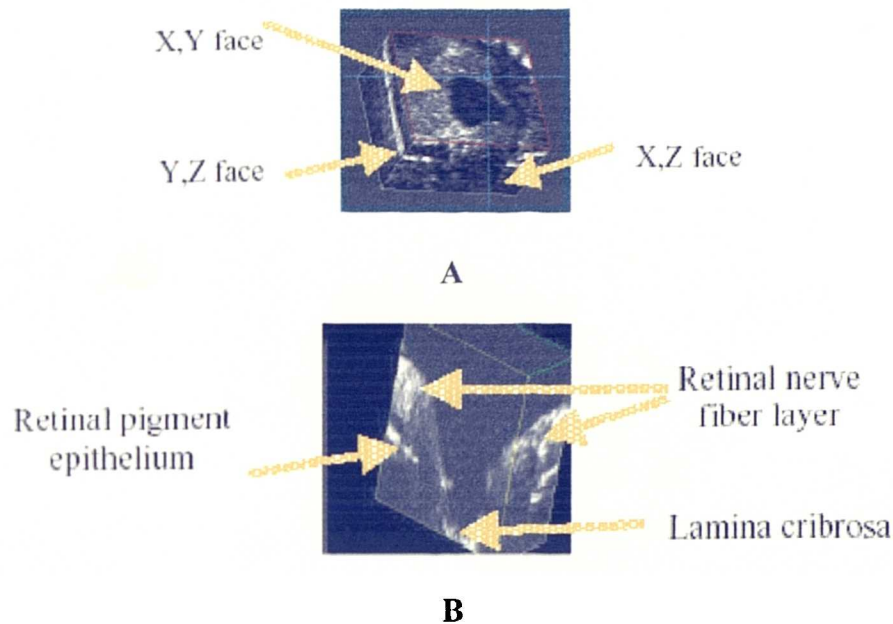
Figure A.4   *Tomographic Imaging of the optic nerve head. Re-printed from Rogers, Podoleanu et al. Topography of volume measurements of the optic nerve using en-face optical coherence tomography. Optics Express. 2001;9(10):533-545*

So far, this system has been used successfully for tomographical imaging of the optic nerve head from which area and volume measurements could be made[98] (Figure A.4). Since a prototype OCT Ophthalmoscope is now in clinical use in a few ophthalmic centres, it is likely that this new technology will be applied to the study of various other ocular conditions.

A.2   Non-Ophthalmic applications of OCT

OCT imaging is not restricted only to ophthalmic applications. The eye is a transparent layered structure which makes it ideal for OCT imaging, however it is

also possible to apply the technology to scattering turbid media. In 1991, Huang et al[13] published images from an in-vitro section of the coronary artery and showed that the reflections arising from fatty-calcified plaque were distinct from those arising from broatheromatous plaque and normal arterial wall. These initial experiments showed the potential value of OCT in imaging scattering media. Over the past few years OCT has emerged as a useful imaging tool in several different areas of medicine.

When imaging scattering tissue, the wavelength of light used is generally higher than that for ophthalmic applications since more penetration is required. Typical wavelengths used are in the region of 1300nm.

A.2.1 Endoscopic Imaging using OCT

Since OCT is based on technology used in optical communication, systems can be constructed with common optical fibre components and can easily be integrated with conventional endoscopes. This form of imaging has found many applications in urology and gastro-intestinal medicine.

Tearney[99,100] et al and Kobayashi et al[101] carried out in vitro studies on samples of gastrointestinal tissue and urologic tissue and compared the OCT scans with corresponding histological analysis. They showed that OCT could delineate microstructure in different urological tissue such as the prostatic urethra, prostate, bladder and ureter as well as differentiate between different tissue layers (mucosa, submucosa and muscolaris) in the colon and oesophagus.

In recent years, a number of in vivo investigations have also been carried out. Sivak et al[102] used a 2.4mm diameter OCT probe inserted through an endoscope to provide 360-degree radial scans. With the probe held 1mm above the mucosal surface, structures such as colonic crypts, gastric pits and duodenal villi could be imaged. With the OCT probe held directly against the wall, the mucosa, muscolaris mucosae and submucosa could easily be identified.

A pilot study by Seitz et al[103] showed that in vivo imaging of the human bile duct is also possible with OCT. This group presented four cases of intraductal OCT in which the OCT probe was inserted through the working channel of a duodenoscope. In these cases, the connective tissue layer and underlying retroperitoneal tissue could clearly be demonstrated.

OCT imaging in the GI tract is comparable to that achieved with other imaging techniques, as shown by Das et al[104] who compared the performance of OCT with that of a high frequency catheter probe EUS (CPEUS). They found that the depth of penetration of the CPEUS system (10 –20 mm) was superior to that achieved with the OCT system (0.7-0.9 mm). However, OCT could demonstrate microscopic detail in the mucosa and submucosa whereas with the CPEUS system these appeared as thin layers with no microscopic detail. This suggests that the two systems could be used complementarily for clinical imaging.

A.2.2   Applications in Dermatology

Since the majority of skin diseases are known to be accompanied by structural alterations, OCT is particularly useful in this area of medicine since it has been shown to be capable of detecting specific features of thin and thick skin and of identifying OCT patterns typical of certain pathological processes in skin. Structures of the stratum corneum, the living epidermis and papillary dermis can be distinguished. A few research groups have investigated the potential of OCT in dermatological applications[105,106]. A typical example of dermatological OCT images is shown in Figure A.5.

In dermatology OCT offers a number of advantages over other imaging techniques – it can resolve structures to within 10 – 15μm, it has a maximum imaging depth of 1.5mm - 2mm, which is sufficient for dermatological applications, it can provide in vivo information also on some specific features in the functional state of tissue and it is non-invasive, compact and relatively inexpensive.
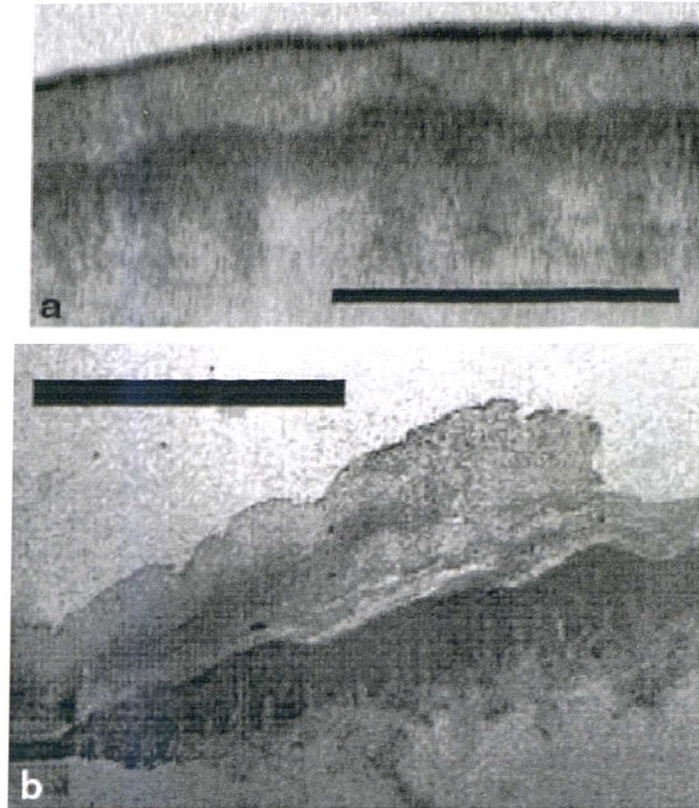
Figure A.5   *Comparison of OCT image (top) and corresponding histological section through a sample of skin from the palm of a healthy individual. Clearly differentiated are the poorly backscattering (light) horny layer, highly backscattering (dark) cellular layers of the epidermis with appendages, and the poorly backscattering (light again) papillary layer of the dermis. The epidermal appendages are well visualized since they are large enough to be spatially resolved by OCT. The size of the bar shown on each OCT image is 1 mm, and the vertical scale is normalized using the assumption that the average refractive index of skin is 1.4. (re-printed from Gladkova ND et al. In vivo optical coherence tomography imaging of human skin: norm and pathology. Skin Research and Technology 2000;6:6-16)*

A.2.3   Applications in Dentistry

A prototype OCT system for in vivo dental imaging is described by Otis et al[107]. This system can clearly depict anatomical structures that are important in the diagnostic

evaluation of hard and soft oral tissue. Periodontal tissue contour, sulcular depth and connective tissue attachment can be visualized and the technology shows potential for periodontal assessments and for identifying active periodontal disease before significant alveolar bone loss occurs.

In addition, OCT is useful in evaluating restored teeth. It is able to identify recurrent caries around existing restorations with greater sensitivity than intraoral radiographs and can be used to visualize the internal aspects and marginal adaptation of porcelain and composite restorations. Figure A.6 shows an example of a dental OCT image.
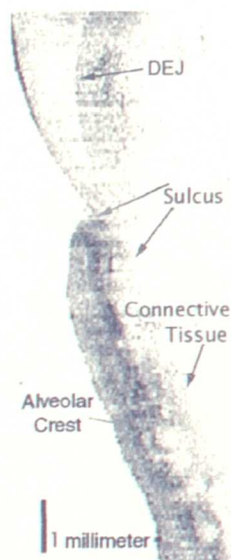
Figure A.6   *OCT image of the facial surface of a mandibular premolar. OCT signals are high at tissue interfaces like the gingival sulcus. OCT images provide a visual recording of periodontal structure. DEJ: dentino-enamel junction. (reprinted from Otis LL et al. Optical coherence tomography: a new imaging technology for dentistry. Journal of the American Dental Association. 2000; 131:511-514.)*

A.2.4 Other Applications

The feasibility of OCT imaging has been investigated in a number of other areas such as developmental biology[108,109], respiratory medicine[110], otolaryngology[111] and gynaecology[112]. In all cases, OCT appears to be a potentially valuable method for

high resolution in vivo imaging that offers a number of distinct advantages over more conventional imaging techniques. As the resolution of OCT systems improves, it is likely that OCT will become a valuable in vivo imaging tool in many areas of medicine.

.

QUANTIFICATION OF REPEATABILITY OF SCAN POSITIONING USING THE *REPEAT SCAN* OPTION

B.1   Introduction

The *Repeat Scan* option is designed for acquiring scans at the same location in different scanning sessions. For optimal repeat scanning, the landmark cursor should be placed on a well-defined anatomical landmark, for example, at the bifurcation of a prominent blood vessel. The scan line is then placed where required and the system will record the relative positions of the scan line and landmark cursor. In *Repeat Scanning* mode, the landmark cursor and scan line positions are locked together with the same relative coordinates as the original scan. If the landmark cursor is placed at the same anatomical position as in the original scan, the new scan line should be in the same place as the original.

For the repeatability study described in Section 4.4.2, it was necessary to first quantify the repeatability of scan re-positioning using the *Repeat Scan* option.

B.2   Methods

Scan Acquisition: This study was carried out on a cohort of 10 normal volunteers. For each subject, one eye was randomly chosen for the study and the landmark cursor was placed on a prominent anatomical landmark. A horizontal straight line scan of length 3mm and centred on the fovea was then acquired. A further 9 scans for each subject were then acquired using the *Repeat Scan* option. Before each of these scans, the subject was asked to sit back and blink. Meanwhile the OCT system was

taken back to the opening screen and the fundus viewing unit was pulled away from the subject and the focussing control was randomly re-adjusted. This was done to ensure that subjects needed to be set up again for each of the repeat scans. For each of the repeat scans, the landmark cursor was re-positioned on the same anatomical landmark. At the end of the scanning session, the fundus images of the 9 repeat scans were analysed carefully by two independent operators. If both operators agreed that the landmark cursor on a particular scan did not appear to be accurately positioned on the anatomical landmark, that scan was discarded. If more than 2 scans for any particular subject needed to be discarded, the entire scanning session was repeated for that subject so that each subject had at least 8 suitable scans included in the study.

Scan Analysis: The analysis was carried out on the saved fundus images corresponding to each of the OCT scans. These bitmap images were exported and analysis was performed using composite layered images in Adobe Photoshop version 5. In the layered imaging mode, the user may paste several images on to each other as different layers. The transparency of these layers may be varied so that the underlying layers may be viewed simultaneously. Any layer may also be turned on and off as required.

The original image was used as the background for the composite image and a line running through the OCT scan line was drawn. Each of the repeat scan fundus images was then pasted onto the background as a separate layer and a line was again drawn through the OCT scan line. The transparency of each of the repeat scan fundus images was set to 60% so that the underlying background could also be seen. The repeat scans were positioned such that the optic disc and prominent blood vessels were coincident. Once all the repeat scans had been pasted onto the background, such that the positions of the optic disc and prominent blood vessels were coincident on all scans, the variation in position of the scan line could be assessed. This was done by measuring the greatest vertical and horizontal displacement of the scan line. The maximum and average vertical and horizontal displacements for the group were recorded. In order to quantify the scaling factor for measurements, the scan length was measured from all the individual fundus images and an average length was computed. The true length of the scan line was known to be 3mm, so a scaling factor could be computed.

B.3   Results

Some degree of horizontal and vertical displacement was observed for all 10 subjects in this study. The maximum vertical displacement recorded was 0.33mm and the greatest horizontal displacement was 0.21mm. The average vertical displacement was 0.19mm (standard deviation: 0.11mm). The average horizontal displacement was 0.11mm (standard deviation: 0.06mm).

B.4   Discussion

The amount of displacement in both the vertical and horizontal directions was relatively low, with average displacements of under 0.2mm. This indicates that reasonably accurate re-positioning of the scan line in *Repeat Scanning* mode is readily achievable. Small differences in scan positioning are unlikely to cause significant differences in retinal thickness measurements provided that the region scanned is not close to the fovea. In the foveal region, the retinal thickness varies rapidly because of the foveal dip so foveal thickness measurements made at points that are 0.2mm apart may be significantly different. In the repeatability and reproducibility study described in Section 4.4.2, repeated measurements across the foveal contour were required, thus, in order to minimise errors due to variations in the position of repeated scans, it was decided to make measurements from an average of four closely spaced scans rather than from a single scan.

Appendix C

DETERMINATION OF THE EFFECT OF TEST OBJECT ORIENTATION ON THICKNESS MEASUREMENTS

C.1 Introduction

For optimal scanning set-up and accurate gap thickness measurements, the test object used in Section 0 should be aligned so that the glass plates are perpendicular to the incident OCT beam. Theoretically, if the object is not perfectly perpendicular to the OCT beam, the gap thickness will be overestimated. However, in practice, it is impossible to know whether the test-object is perfectly perpendicular to the OCT beam. A study was therefore carried out to assess how varying the orientation of the test object with respect to the incident beam affected the gap thickness measured from the scan.

C.2 Methods

Measurements of gap thickness were made from a series of scans positioned at 3° intervals relative to each other. A template was designed to facilitate the positioning of the test object. This template consisted of a series of lines at 3°angles to each other. This template was taped to a platform attached to the head of the OCT viewing unit, onto which the test object would be placed for scanning. One of the lines was arbitrarily selected as the reference orientation and the test-object was positioned such that its front edge ran along this line. Scans were acquired in this position with the polarisation and focussing setting adjusted to their optimum positions. The test-object was rotated in a

clock-wise direction so that its front edge ran along the next line on the template. This procedure was repeated in both the clockwise and anti-clockwise direction until the test object had been rotated through 15° in both directions.

The gap thickness was measured from each of the scans. The scan position which yielded the smallest gap thickness was assumed to be the scan in which the test-object was closest to being perpendicular to the incident beam. Scans acquired in positions clockwise to this scan were labelled 3°, 6° etc. and those anti-clockwise were labelled - 3°, -6° etc. The percentage difference between the measured gap thickness at each position and the reference thickness was calculated.

C.3   Results

The least measured gap thickness was found to be 197.1μm and this occurred with the test object in the selected reference orientation. Table C.1 shows the gap thickness measured at various orientations to this scan and the percentage difference between each scan and the reference one.

Orientation	Gap Thickness	% Difference	Orientation	Gap Thickness	% Difference
3°	197.7	0.30%	-3°	197.8	0.36%
6°	198.3	0.61%	-6°	198.1	0.51%
9°	198.6	0.76%	-9°	198.4	0.66%
12°	198.9	0.91%	-12°	198.7	0.81%
15°	202.1	2.54%	-15°	201.6	2.28%

Table C.1   *Table of measured gap thickness with the test object at various orientations relative to the reference scan*

C.4   Discussion

This study has shown that that varying the position of the glass object by up to 12° causes a change in measured thickness which is under 1%. In practice, it is impossible to align the test-object to be exactly perpendicular to OCT beam, however it is easy enough to position it within 12° of the optimal position, simply by inspection. This study has shown that the positioning of the test object is not critical and will not lead to any significant inaccuracies in the measured gap thickness.

REFERENCES

1.   Webb RH, Hughes GW, Delori FC. Confocal laser ophthalmoscope. *Appl Opt.* 1987; 26:1492-9

2.   Mannivannan A, Sharp PF, Phillips RP, Forrester JV. Digital fundus imaging using a scanning laser ophthalmoscope. *Physiol. Meas.* 1993; 14:43-56.

3.   Mannivannan A, Sharp PF, Forrester JV. Performance measurements of an infrared digital scanning laser ophthalmoscope. *Physiol. Meas.* 1994; 15:317-324.

4.   Sharp PF, Mannivannan A. The scanning laser ophthalmoscope. *Phys. Med. Biol.* 1997; 42:951-966.

5.   Dreher AW, Reiter K. Scanning laser polarimetry of the retina retinal nerve fibre layer. *SPIE Proc.* 1992; 1746:34-38.

6.   Weinreb RN, Sakiba S, Zangwill L. Scanning laser polarimetry to measure the retinal nerve fibre layer of normal and glaucomatous eyes. *Am J Ophthalmol.* 1995; 119:627-636.

7.   Tion-Fo-Sang MJ, de Vries J, Lemij HG. Measurement by nerve fibre analyser of retinal nerve fibre layer thickness in normal subjects and patients with ocular hypertension. *Am J Ophthalmol.* 1996; 122:220-227.

8.   Puliafito C, Hee MR, Schuman JS, Fujimoto JG. *Optical coherence tomography of ocular diseases.* 37-368 (Slack Incorporated, Thorofare, New Jersey, 1996).

9.   Fercher AF, Drexler W, Hitzenberger CK, Lasser T. Optical coherence tomography - principles and applications. *Rep. Prog Phys.* 66(2): 239-303.

10.   Bouma BE, Tearney GJ. *Handbook of Optical Coherence Tomography.* (Marcel Dekker Publications, New York, 2002.)

11.   Fercher AF, Mengedoht K, Werner W. Eye-length measurement by interferometry with partially coherent light. *Optics Letters.* 1988; 13(3):186-188.

12.   Huang D, Wang J, Lin CP, Puliafito CA, Fujimoto JG. Micron resolution ranging of cornea anterior chamber by optical reflectometry. *Lasers in Surgery and Medicine.* 1991; 11:419-425

13.   Huang D, Swanson EA, Lin CP, et al. Optical coherence tomography. *Science* 1991; 244:1178-1181

14. Swanson EA, Izatt JA, Hee MR et al. In-vivo retinal imaging by optical coherence tomography. *Optics Letters.*1993; 18(21):1864-1866.

15. Izatt JA, Hee MR, Swanson EA et al. Micrometer-scale resolution imaging of the anterior eye in vivo with optical coherence tomography. *Arch Opthalmol.* 1994; 112:1584-1589.

16. Drexler W, Morgner U, Ghanta RK et al. Ultrahigh-resolution ophthalmic optical coherence tomography. *Nature Medicine* 2001; 7(4):502-507.

17. Hee MR, Izatt JA, Swanson EA, et al. Optical coherence tomography for ophthalmic imaging. *IEEE Eng Med Biol* 1995; 14:67-76

18. Baumal CR. Clinical applications of optical coherence tomography. *Current Opinion in Ophthalmology* 1999; 10:182-188.

19. Puliafito CA, Hee MR, Lin CP, Reichel E, Schuman JS, Duker JS, Izatt JA, Swanson EA, Fujimoto JG. Imaging of macular diseases with optical coherence tomography. *Ophthalmology.* 1995; 102(2):217-29.

20. Hee MR, Izatt JA, Swanson EA, Huang D, Schuman JS, Lin CP, Puliafito CA, Fujimoto JG. Optical coherence tomography of the human retina. *Arch Ophthalmol.* 1995; 113(3):325-32.

21. Maldonado MJ, Ruiz-Oblitas L, Munuera JM et al. Optical coherence tomography evaluation of the corneal cap and stromal bed features after laser in situ keratomileusis for high myopia and astigmatism. *Ophthalmology.* 2000; 107(1):81-9.

22. Hirano K, Kojima T, Nakamura M, Hotta Y. Triple anterior chamber after full-thickness lamellar keratoplasty for lattice corneal dystrophy. *Cornea.* 2001; 20(5):530-3.

23. Hirano K, Ito Y, Suzuki T, Kojima T, Kachi S, Miyake Y. Optical coherence tomography for the non-invasive evaluation of the cornea. *Cornea.* 2001; 20(3):281-9.

24. Ustundag C, Bahcecioglu H, Ozdamar A et al. Optical coherence tomography for evaluation of anatomical changes in the cornea after laser in situ keratomileusis. *J Cataract Refract Surg* 2000; 26:1458-62.

25. Wirbelauer C, Scholz C, Hoerauf H et al. Corneal optical coherence tomography before and immediately after eximer laser photorefractive keratectomy. *Am J Ophthalmol* 2000; 130(6):693-9.

26. Bechmann M , Thiel MJ, Roesen B et al. Central corneal thickness determined with optical coherence tomography in various types of glaucoma. *Br J Ophthalmol* 2000; 84:1233-1237.

27. American National Standards Institute. *Safe use of lasers.* ANSI Z136.1. (American National Standards Institute, New York, 1986)

28. Gass JDM. *Stereoscopic Atlas of Macular Diseases: Diagnosis and Treatment.* Vol1, 1-49 (Mosby, St Louis, Missouri, 1997).

29. Hogan H, Alvarado JA, Wedell JE. *Histology of the Human Eye: An Atlas and Textbook.* 393-522 (WB Saunders, Philadelphia, 1971).

30. Chauhan DS, Marshall J. The interpretation of optical coherence tomography images of the retina. *Invest Ophthalmol Vis Sci.* 1999:40:2332-2342.

31. Toth CA, Drew GN, Boppart SA et al. A comparison of retinal morphology viewed by optical coherence tomography and by light microscopy. *Arch. Ophthalmol.* 1997; 115:1425-1428.

32. Muscat S, Parks S, Kemp E, Keating D. Repeatability and Reproducibility of Macular Thickness Measurements with the Humphrey OCT System. *Invest Ophthalmol Vis Sci.* 2002; 43:490-495.

33. Muscat S, McKay N, Parks S, Kemp E, Keating D. Repeatability and reproducibility of corneal thickness measurements by optical coherence tomography. *Invest Ophthalmol Vis Sci.* 2002; 43:1791-1795.

34. British Standards Institution. *Accuracy (trueness and precision) of measurement methods and results. General principles and definitions.* BS ISO 5725 part 1. (BSO, London, 1994).

35. British Standards Institution. *Accuracy (trueness and precision) of measurement methods and results. Basic methods for the determination of repeatability and reproducibility of a standard measurement method.* BS ISO 5725 part 2. (BSO, London, 1994).

36. Bland JM, Altman DG. Statistical methods for assessing agreement between two methods of clinical measurement. *The Lancet* 1986; 8:307-310

37. Hee MR, Puliafito CA, Duker JS, et al. Topography of diabetic macular edema with optical coherence tomography. *Ophthalmology* 1998; 15: 360-369.

38. Hee MR, Puliafito CA, Wong C, Reichel E, Duker JS, Reichel E, Rutledge B, Schuman JS, Swanson EA, Fujimoto JG. Quantitative assessment of macular

edema with optical coherence tomography. *Arch Ophthalmol.* 1995; 113(8): 1019-29.

39.   Otani T, Kishi S, Maruyama Y. Patterns of diabetic macular edema with optical coherence tomography. *Am J Ophthalmol.* 1999; 127(6):688-93.

40.   Koozekanani D, Roberts C, Katz SE, et al. Intersession repeatability of macular thickness measurements with the Humphrey 2000 OCT. *Invest Ophthalmol Vis Sci.* 2000; 41:1486-1491.

41.   Baumann M, Gentile RC, Liebmann JM, Ritch R. Reproducibility of retinal thickness measurements in normal eyes using optical coherence tomography. *Ophthalmic Surg Lasers.* 1998; 29:280-285.

42.   Massin P, Vicaut E, Haouchine B, Erginay A, Paques M, Gaudric A. Reproducibility of retinal mapping using optical coherence tomography. *Arch Ophthalmol.* 2001; 119:1135-1142.

43.   Schuman JS, Hee MR, Arya AV, Pedut-Kloizman T, Puliafito CA, Fujimoto JG, Swanson EA. Optical Coherence Tomography: a new tool for glaucoma diagnosis. *Curr Opin Ophthalmol* 1995; 6 (II):89-95.

44.   Pieroth L, Schuman JS, Hertzmark E, Hee MR, Wilkins JR, Coker J, Mattox C, Peduth-Kloizman R, Puliafito CA, Fujimoto JG, Swanson E. Evaluation of focal defects of the nerve fibre layer using optical coherence tomography. *Ophthalmology* 1999; 106(3):570-9

45.   Teesalu P, Tuulonen A, Airaksinen PJ. Optical coherence tomography and localized defects of the retinal nerve fiber layer. *Acta Ophthalmol Scand.* 2000; 78(1):49-52.

46.   Bowd C, Weinreb RN, Williams JM, Zangwill LM. The nerve fibre layer thickness in ocular hypertensive, normal, and glaucomatous eyes with optical coherence tomography. *Arch Ophthalmol.* 2000; 118(1):22-26.

47.   Schuman JS, Pedut-Kloizman T, Hertzmark E et al. Reproducibility of nerve fibre layer thickness measurement using optical coherence tomography. *Ophthalmology.* 1996; 103(11):1889-98.

48.   Jones AL, Sheen NJL, North RV, Morgan JE. The Humphrey optical coherence tomography scanner: quantitative analysis and reproducibility study of the normal human retinal nerve fibre layer. *Br J Opthalmol* 2001; 85:673-677.

49. Blumenthal EZ, Williams JM, Weinreb RN, Girkin CA, Berry CC, Zangwill LM. Reproducibility of nerve fibre layer thickness measurements by use of optical coherence tomography. *Ophthalmology* 2000; 107:2278-2282.

50. Bechmann M, Thiel MJ, Neubauer AS et al. Central corneal thickness measurement with a retinal optical coherence tomography device versus standard ultrasonic pachymetry. *Cornea.* 2001; 20(1):50-54.

51. Lattimore MR, Kaupp S, Schallhorn S, Lewis R. Orbscan Pachymetry: Implications of a Repeated Measures and Diurnal Variation Analysis. *Ophthalmology.* 1999; 106(5):977-981.

52. Harper CL, Boulton ME, Bennett D et al. Diurnal Variations in Human Corneal Thickness. *Br J of Ophthalmol.* 1996; 80:1068-1072.

53. Feng Y, Varikooty J, Simpson TL. Diurnal variation of corneal and corneal epithelial thickness measured using optical coherence tomography. *Cornea* 2001; 20(5):480-3.

54. Marsich MW, Bullimore MA. The Repeatability of Corneal Thickness Measures. *Cornea.* 2000; 19(6):792-5.

55. Ishikawa H, Gürses-Özden R, Hoh S, Dou H, Liebmann JM, Ritch R. Grayscale and proportion-corrected optical coherence tomography images. *Ophthalmic Surg Lasers* 2000; 31:223-228.

56. Muscat S, Fahad B, Parks S, Keating D. Optical coherence tomography and multifocal electroretinography of X-Linked juvenile retinoschisis. *Eye.*2001; 15: 796-99.

57. Muscat S, Sathish S, Sampat V, Kemp E, Parks S, Keating D. Optical coherence tomography in the diagnosis of sub-clinical serous detachment of the macula secondary to a choroidal nevus. *Ophthalmic Surgery and Lasers* 2001; 32(6):474-6.

58. Muscat S, Parks S, Kemp E, Keating D. Secondary retinal changes associated with choroidal naevi and melanomas documented by optical coherence tomography. *The British Journal of Ophthalmology* [In Press].

59. Massin P, Allouch C, Haouchine B, Metge F, Paques M, Tangui L, Erginay A, Gaudric A. Optical coherence tomography of idiopathic macular epiretinal membranes before and after surgery. *Am J Ophthalmol.* 2000; 130(6):732-9.

60. Wilkins JR, Puliafito CA, Hee MR, Duker JS, Reichel E, Coker JG, Schuman JS, Swanson EA, Fujimoto JG. Characterization of epiretinal membranes using optical coherence tomography. *Ophthalmology*. 1996; 103(12):2142-51.

61. Hoh ST, Greenfield DS, Mistlberger A, Liebmann JM, Ishikawa H, Ritch R. Optical coherence tomography and scanning laser polarimetry in normal, ocular hypertensive, and glaucomatous eyes. *Am J Ophthalmol*. 2000; 129(2):129-35.

62. Zangwill LM, Williams J, Berry CC, Knauer S, Weinreb RN. A comparison of optical coherence tomography and retinal nerve fibre layer photography for detection of retinal nerve fibre layer damage in glaucoma. *Ophthalmology*. 2000; 107(7):1309-15

63. Zangwill LM, Bowd C, Berry CC, Williams J, Blumenthal EZ, Sanchez-Galeana CA, Vasile C, Weinreb RN. Discriminating between normal and glaucomatous eyes using the Heidelberg Retina Tomograph, GDx Nerve Fiber Analyzer, and optical coherence tomography. *Arch Ophthalmol*. 2001; 119(7):985-93..

64. Soliman MA, Van Den Berg TJ, Ismaeil AA, De Jong LA, De Smet MD. Retinal nerve fiber layer analysis: relationship between optical coherence tomography and red-free photography. *Am J Ophthalmol*. 2002; 133(2):187-95

65. Greaney MJ, Hoffman DC, Garway-Heath DF, Nakla M, Coleman AL, Caprioli J. Comparison of optic nerve imaging methods to distinguish normal eyes from those with glaucoma. *Invest Ophthalmol Vis Sci*. 2002; 43(1):140-5.

66. Pons ME, Ishikawa H, Gürses-Öden R, Liebmann JM, Dou H, Ritch R. Assessment of retinal nerve fibre layer internal reflectivity in eyes with and without glaucoma using optical coherence tomography. *Arch Opthalmol*. 2000; 118:1044-7.

67. George NDL, Yates JRW, Moore AT. Clinical features in affected males with X-linked retinioschisis. *Arch Opthalmol*.1996; 114:274-280.

68. Kellner U, Brümmer S, Foerster MH, Wessing A. X-linked congenital retinoschisis. *Graefe's Arch Clin Exp Ophthalmol*. 1990; 228:432-7.

69. Manschot WA. Pathology of hereditary juvenile retinoschisis. *Arch Ophthalmolol* 1972; 88:131-138.

70. Yanoff M, Kertesz E, Zimmerman LE. Histopathology of juvenile retinoschisis. *Arch Opthalmol* 1968: 79:49-53

71. Kirsch LS, Brownstein S, de Wolff-Rouendaal. A histopathological, ultrastructural and immunohistochemical study of congenital hereditary retinoschisis. *Can J Opthalmol.* 1996; 31(6):301-10.

72. Peachey NS, Fishman GA, Derlacki DJ et al. Psychophysical and electroretinographic findings in X-linked juvenile retinoschisis. *Arch Ophthalmol.* 1987; 105:513-516

73. Parks SW, Keating D, Evans AL. Wide field functional imaging of the retina. *IEEE Medical Applications of Signal Processing* 1999; 107:91-6.

74. Gass JD. Idiopathic senile macular hole. Its early stages and pathogenesis. *Arch Ophthalmol* 1988; 106:629-639.

75. Gass JD. Reappraisal of biomicroscopic classification of stages of development of a macular hole. *Am J Opthalmol.* 1995; 119:752-9

76. Augsburger JJ, Vrabec TR. Impact of delayed treatment in growing posterior uveal melanomas. *Arch Opthalmol* 1993; 111:1382-6.

77. Ah-Fat FG, Damato BE. Delays in the diagnosis of uveal melanoma and effect on treatment. *Eye* 1998; 781-2.

78. Damato BE, Foulds WS. Tumour-associated retinal pigment epitheliopathy. *Eye.* 1990; 4:382-387.

79. Shields JA and Shields CL. *Intra-ocular tumours: a text and atlas.* Chapter 6. (W.B. Saunders Company, Pennsylvania, 1992.)

80. Shields JA and Shields CL. *Intra-ocular tumours: a text and atlas.* Chapter 9. (W.B. Saunders Company, Pennsylvania, 1992.)

81. Gonder JR. Augsburger JJ, McCarthy EF, Shields JA. Visual loss associated with choroidal naevi. *Ophthalmology* 1982; 89:961-965.

82. Gass JDM. Problems in the differential diagnosis of choroidal naevi and malignant melanomas. *Am J Opthalmol.* 1977; 83:299-323.

83. Shields CL, Cater J, Shields JA et al. Combination of clinical factors predictive of growth of small choroidal melanocytic tumours. *Arch Ophthalmol* 2000; 118:360-364.

84. Shields CL, Shields JA, Kiratli H, De Potter P, Cater JR. Risk factors for growth and metastasis of small choroidal melanocytic tumours. *Trans Am Ophthalmol Soc* 1995; 93:259-75

85. The Collaborative Ocular Melanoma Study Group. Factors predictive of growth and treatment of small choroidal melanoma. COMS Report no.5. *Arch Ophthalmol.* 1997; 115:1537-1544.

86. Schaudig U, Hassenstein A, Bernd A, et al. Limitations of imaging choroidal tumours in vivo by optical coherence tomography. *Graefe's Arch Clin Exp Ophthalmol* 1998; 236:588-592.

87. Haouchine B, Massin P, Gaudric A. Foveal pseudocyst as the first step in macular hole formation: a prospective study by optical coherence tomography. *Ophthalmology.* 2001; 108(1):15-22.

88. Azzolini C, Patelli F, Brancato R. Correlation between optical coherence tomography data and biomicroscopic interpretation of idiopathic macular hole. *Am J Ophthalmol.* 2001; 132(3):348-55.

89. Gaudric A, Haouchine B, Massin P, Paques M, Blain P, Erginay A. Macular hole formation: new data provided by optical coherence tomography. *Arch Ophthalmol.* 1999; 117(6):744-51.

90. Tanner V, Chauhan DS, Jackson TL, Williamson TH. Optical coherence tomography of the vitreoretinal interface in macular hole formation. *Br J Ophthalmol.* 2001; 85(9):1092-7.

91. Kishi S, Takahashi H. Related Articles Three-dimensional observations of developing macular holes. *Am J Ophthalmol.* 2000; 30(1):65-75.

92. Chauhan DS, Antcliff RJ, Rai PA, Williamson TH, Marshall J. Papillofoveal traction in macular hole formation: the role of optical coherence tomography. *Arch Ophthalmol.* 2000; 118(1):32-8.

93. Birch DG, Jost BF, Fish GE. The focal electroretinogram in fellow eyes of patients with idiopathic macular holes. *Arch Ophthalmol.* 1988; 106(11):1558-63.

94. Tiffany JM, Todd BS, Baker MR.Computer-assisted calculation of exposed area of the human eye. *Adv Exp Med Biol.* 1998; 438:433-9.

95. Koozekanani D, Boyer K, Roberts C. Retinal thickness measurements from optical coherence tomography using a Markov boundary model. *IEEE Trans. Medical Imaging.* 2001; 20(9):900-916.

96. Radharkrishnan S, Rollins AM, Roth JE et al. real-Time optical coherence tomography of the anterior segment at 1310nm. *Arch Ophthalmol* 2001; 119:179-85.

97. Podoleanu GH, Rogers JA, Jackson DA. Three dimensional OCT images from retina and skin. *Optics Express*. 2000; 7(9):292-298.

98. Rogers JA, Podoleanu A.G, Dobre GM, Jackson DA. Topography of volume measurements of the optic nerve using en-face optical coherence tomography. *Optics Express*. 2001; 9(10):533-545

99. Tearney GJ, Brezinski ME, Bouma BE et al. In vivo endoscopic optical biopsy with optical coherence tomography. *Science* 1997; 276(5321):2037-2039.

100. Tearney GJ, Brezinski ME, Southern JF, Bouma BE, Boppart SA, Fujimoto JG. Optical biopsy in human urological tissue using optical coherence tomography. *J of Urology*. 1997; 157(5):1915-1919.

101. Kobayashi K, Izatt JA, Kulkarni MD, Willis J, Sivak MV. High-resolution cross-sectional imaging of the gastrointestinal tract using optical coherence tomography: preliminary results. *Gastrointest Endosc* 1998; 47(6):516-523.

102. Sivak MV, Kobayashi K, Izatt JA et al. High-resolution endoscopic imaging of the GI tract using optical coherence tomography. *Gastrointest Endosc* 2000; 51(4 Pt 1):474-479.

103. Seitz U, Freund J, Jaeckle S et al. First in vivo optical coherence tomography in the human bile duct. *Endoscopy*. 2001; 33(12):1018-1021.

104. Das A, Sivak MV, Chak A. High-resolution endoscopic imaging of the GI tract: a comparitive study of optical coherence tomography versus high-frequency probe EUS. *Gastrointest Endosc* 2001; 54(2):219-24.

105. Gladkova ND, Petrova GA, Nikulin Nk et al. In vivo optical coherence tomography imaging of human skin: norm and pathology. *Skin Research and Technology* 2000; 6:6-16

106. Welzel J, Lankenau E, Birngruber R, Engelhardt R. Optical Coherence tomography of the human skin. *J Am Acad Dermatol*. 1997; 37(6):958-963

107. Otis LL, Everett MJ, Sathyam US, Colston BW. Optical coherence tomography: a new imaging technology for dentistry. *Journal of the American Dental Association*. 2000; 131:511-514.

108. Boppart SA, Brezinski ME, Bouma BE, Tearney GJ, Fujimoto JG. Investigation of developing embryonic morphology using optical coherence tomography. *Developmental Biology*. 1996; 177:54-63.

109. Boppart SA, Brezinski ME, Fujimoto JG. Optical coherence tomography in developmental biology. *Methods Mol Biol*. 2000; 135:217-233.

110. Pitris C, Brezinski ME, Bouma BE, Tearney GJ, Southern JF, Fujimoto JG. High resolution imaging of the upper respiratory tract with optical coherence tomography: a feasibility study. *Am J Respir Crit Care Med* 1998; 157(5 Pt 1):1640-1644.

111. Pitris C, Saunders KT, Fugimoto JG, Brezinski ME. High-resolution imaging of the middle ear with optical coherence tomography: a feasibility study. *Arch Otolaryngol Head Neck Surg.* 2001; 127(6):637-642.

112. Boppart SA, Goodman A, Libus J et al. High resolution imaging of endometriosis and ovarian carcinoma: feasibility for laparoscopic-based imaging. *Br J Obstet Gynaecol* 1999; 106(10):1071-1077.